Hammerli, Johannes (2014) ***Using microanalysis of minerals to track geochemical processes during metamorphism: examples from the Mary Kathleen fold belt, Queensland, and the Eastern Mt. Lofty Ranges, South Australia.*** **PhD thesis, James Cook University.**

Using microanalysis of minerals to track geochemical processes during metamorphism: Examples from the Mary Kathleen Fold Belt, Queensland, and the Eastern Mt. Lofty Ranges, South Australia

Thesis submitted by

Johannes Hammerli

February 2014

For the Degree of Doctor of Philosophy in the
School of Earth and Environmental Sciences of
James Cook University

Statement of Access

I, the undersigned author of this thesis, understand that James Cook University will make this thesis available for use within the university library and allow access in other approved libraries after its submission. All users consulting this thesis will have to sign the following statement:

> *In consulting this thesis I agree not to copy or closely paraphrase it in whole or in part without the written consent of the author; and to make proper public written acknowledgement for any assisstance which I have obtained from it.*

Beyond this, I do not wish to place any restrictions on access to this thesis.

Johannes Hammerli
February 2014

Declaration

I declare that this thesis is my own work and has not been submitted in any form for another degree or diploma at any university or other institute or tertiary education. Information derived from the published or unpublished work of others has been acknowledged in the text and a list of references is given.

Johannes Hammerli
February 2014

Statement of Contribution by Others

Nature of Assistance	**Contribution**	**Names and Affiliations of Co-Contributors**
Intellectual Support	Proposal writing	Carl Spandler, JCU
	Data Analysis	Carl Spandler, JCU Nick Oliver, JCU Tony Kemp, UWA Brian Rusk, WWU Poul Emsbo, USGS
	Editorial Assistance	Carl Spandler, JCU Nick Oliver, JCU Tony Kemp, UWA Brian Rusk, WWU Poul Emsbo, USGS
Financial Support	Stipend	IPRS
	Research funding	ARC Grant (DP 1095280) to C. Spandler, N. Oliver and T. Kemp

Statement of Contribution by Others

Chapter #	Details of publication(s) on which chapter is based	Nature and extent of the intellectual input of each author
1	Chemical Geology	I contributed to primary idea discussion
2	Journal of Metamorphic Geology	I contributed to primary idea discussion and sample collection
3	Earth and Planetary Science Letters	I contributed to primary idea discussion and sample collection

I confirm the candidate's contribution to this paper and consent to the inclusion of the paper in this thesis.

Name: Carl Spandler

Signature:

Date: 27-02-14

Statement of Contribution by Others

Chapter #	Details of publication(s) on which chapter is based	Nature and extent of the intellectual input of each author
1	Chemical Geology	I contributed to primary idea discussion

I confirm the candidate’s contribution to this paper and consent to the inclusion of the paper in this thesis.

Name: Poul Emsbo

Signature:

Date: 3/24/14

Chapter #	Details of publication(s) on which chapter is based	Nature and extent of the intellectual input of each author
1	Chemical Geology	I contributed to primary idea discussion
2	Journal of Metamorphic Geology	I contributed to primary idea discussion and sample collection

I confirm the candidate’s contribution to this paper and consent to the inclusion of the paper in this thesis.

Name: Nick Oliver

Signature:

Date: **21 Feb 2014**

Statement of Contribution by Others

Chapter #	Details of publication(s) on which chapter is based	Nature and extent of the intellectual input of each author
1	Chemical Geology	I contributed to primary idea discussion
2	Journal of Metamorphic Geology	I contributed to primary idea discussion

I confirm the candidate's contribution to this paper and consent to the inclusion of the paper in this thesis.

Name: Brian Rusk

Signature:

Date: 25/02/2014

Chapter #	Details of publication(s) on which chapter is based	Nature and extent of the intellectual input of each author
3	Earth and Planetary Science Letters	I contributed to development of concepts and idea discussion.

I confirm the candidate's contribution to this paper and consent to the inclusion of the paper in this thesis.

Name: Tony Kemp

Signature:

Date: 22 February 2014

Acknowledgments

There are many people who were involved or contributed in some way to my thesis work over the last four years. Although they cannot all be thanked here individually, their help is greatly appreciated.

I owe the greatest debt of thanks to my supervisors, Carl Spandler, Nick Oliver, Tony Kemp, and Brian Rusk. Firstly, a huge thanks to my primary supervisor Carl for all his support during the last 4 years. His wisdom on a wide range of subjects is truly remarkable. Carl was definitely one of the main reasons why my PhD was a very enjoyable and worthwhile experience. Thanks Nick for the fun time in the field and especially for all the accident-free dirt road racing and all your crucial advice throughout my PhD. Tony introduced me to the mysteries of radiogenic isotopes and he had to fly across the island to help me with isotope work, which is greatly appreciated and Brian introduced me to the world of porphyry systems which was interesting indeed. I also want to thank Christa Placzek to be my official secondary surpervisor when everyone else left JCU. I look forward to working with all you guys in the future.

Thanks to all the staff at SEES, especially Melissa, Beth, Bec, Jo and Judy, for all your time and help.

And thanks to my fellow PhD, honours and master students over the years, particularly Rob who provided plenty of advice and many fruitful and *endless* discussions including tectonics in PNG. Hannah thank you for being so awesome!

Also thanks to the staff of the Advanced Analytical Centre (Kevin, Shane, Yi, Gordon and Brendan) for assistance with analytical work.

And finally, my father for his support during my early years at university.

Abstract

Understanding the behaviour of major and trace elements during metamorphism is fundamental for our understanding of the geochemical evolution of the Earth's crust and the formation of orogenic orebodies. Furthermore, it is essential to know how key elements and radiogenic isotopes behave in metamorphic/hydrothermal systems in order to apply them meaningfully to solve important questions in geosciences. Metamorphic/hydrothermal reactions are most evidently preserved at the mineral scale, so in situ microanalytical techniques are best suited for tracing the record of metamorphism or hydrothermal alteration. In this thesis, I outline new analytical developments for in situ analysis of halogens in minerals and fluid samples, and of Sm-Nd isotopes in REE-rich minerals. These techniques, in conjunction with comprehensive bulk rock and mineral geochemistry and element distribution analysis, are then applied to well-characterised metamorphic rocks from the Adelaide Fold Belt and Mt Isa Inlier. Although fluid is an essential ingredient for mass transport during metamorphism, it is often difficult to identify the source of metamorphic/hydrothermal fluids. Traditionally, fluid inclusions have been used to gain insights into the source and composition of fluids. Until very recently, quantification of key elements such as bromine and chlorine in fluid inclusions relied almost solely on bulk rock analyses techniques (i.e., crush-leach). These methods do not allow distinction between different fluid inclusion generations that might hold crucial information on the evolution of a hydrothermal system and associated mineralization. The development of in situ LA-ICP-MS analysis of chlorine and bromine in fluid inclusions now allows for the targeting of individual fluid inclusions of a specific fluid type in a mineral. In this thesis these techniques were further tested and refined, and applied for the first time to a range of natural scapolite group minerals, minerals assumed to reflect the Cl/Br content of the coexisting hydrothermal fluids. The results show that fluid sources can be identified with a ~ 25 μm resolution in Cl and Br bearing minerals. This technique was applied on scapolite minerals from skarns, regional metamorphic rocks and a mineralized shear-zone of the Mary Kathleen Fold Belt in the Mt. Isa inlier. While scapolite minerals in skarns contain Cl/Br ratios typically associated with granitic fluids, metamorphic scapolite indicates that fluids were dominantly derived from basinal brines formed from sub-aerial evaporation of seawater beyond the point of halite saturation. This bittern fluid infiltrated the underlying sedimentary sequences prior to regional metamorphism. Zoned scapolite in the mineralized shear-zone records three discrete pulses of magmatic and metamorphic fluid, and it is suggested that fluid mixing may have assisted mineralization along and around this shear-zone.

To investigate element mobility during metamorphism, I studied the Eastern Mt. Lofty Ranges in South Australia. Metamorphic rocks of the Mt. Lofty Ranges have a relatively simple

metamorphic history, and metamorphic gradients and widespread up-temperature fluid flow has been documented previously. This allows monitoring of mineral and bulk rock compositional changes (or lack thereof) during metamorphism across a regional metamorphic gradient from ~350–400 ˚C to migmatite grade (~ 650–700 ˚C) at ~0.3–0.5 GPa, in a confined framework. The results show that, despite widespread up-temperature fluid flow, major elements and most trace elements are isochemical during metamorphism. These elements are effectively redistributed into newly formed major minerals or accessory phases. Monazite or allanite and xenotime control the whole rock concentration of REE whereas apatite and titanite are minor REEs hosts. The only non-volatile mobile elements are Zn, Pb, Cs and As whose concentrations decreased with increasing metamorphic grade. The Zn and Pb depletion was progressive with increasing temperature in staurolite-absent psammo-pelites, with losses of ~ 75% of the original Zn and ~ 50 % of the original Pb from the rocks from high-grade metamorphic zones. Microanalysis showed that biotite is a key mineral for Zn sequestration by concentrating >80 % of the Zn in the bulk rock. Zinc and Pb likely partitioned into a Cl-rich hydrothermal/metamorphic fluid that led to the observed depletion of Pb and Zn in the bulk rock. Simple mass balance calculations show that ~27 Mt of Zn and ~2.7 Mt of Pb were mobilized during prograde metamorphism, which is comparable to the amounts of base metals found in world class Pb-Zn deposits. Hence, prograde metamorphism of sedimentary rock packages is a viable base metal source for the formation of some Pb-Zn deposits, provided that the metamorphic fluid contains sufficient Cl to effectively mobilise metals from the metamorphic system into ore-forming environments. The observed As loss is consistent with the recrystallization of As-bearing pyrite to As-poor pyrrhotite, confirming previous studies. Cesium depletion in migmatites can be explained by the incompatibly of Cs in micas in high-grade metamorphic rocks. Significant element mobility during metamorphism is likely only achieved under conditions with high fluid flux.

In order to understand crustal evolutionary processes and crustal fractionation via for example melt production in migmatitic systems equivalent to the high-grade zone of the Eastern Mt. Lofty Ranges, geochemists widely rely on radiogenic isotopes. However recent claims of Nd and Sr isotope disequilibrium during anatexis question the reliability radiogenic isotopes. Microanalysis of REE-rich accessory minerals was used to investigate Nd isotope equilibration during metamorphism in order to assess to potential of disequilibrium situations during high-grade metamorphism. The results are used to demonstrate that apatite retains an original, probably detrital, highly variable Nd isotopic signature until at least 500 ˚C, before being isotopically homogenized. In contrast, allanite and titanite are equilibrated at temperatures as low as 350–400 ˚C. REE-rich accessory minerals in high-grade rocks (~600 ˚C) show very similar initial Nd isotope values at the time of metamorphism. I conclude that Nd isotope disequilibrium between crustal melts and metasedimentary sources is unlikely. Furthermore, in situ microanalysis of radiogenic isotopes can help to identify external melt components in migmatites that would not be resolvable by conventional bulk rock analysis.

Table of Contents

Chapter 1

Chapter 2

Chapter 3

Chapter 4

Published Papers

In situ quantification of Br and Cl in minerals and fluid inclusions by LA-ICP-MS: A powerful tool to identify fluid sources
(Chemical Geology)

Cl/Br of scapolite as a fluid tracer in the earth's crust: insights into fluid sources in the Mary Kathleen Fold Belt, Mt. Isa Inlier, Australia
(Journal of Metamorphic Geology)

Neodymium isotope equilibration during crustal metamorphism revealed by in situ microanalysis of REE-rich accessory minerals
(Earth and Planetary Science Letters)

.

Contents of Digital Appendices

Chapter 1:

- Compilation of all fluid inclusion analyses by LA-ICP-MS
- Calculated NaCl wt.% based on anion/cation coupling and Cl measured by LA-ICP-MS

Chapter 2:

- Compilation of EPMA and LA-ICP-MS analyses of scapolite

Chapter 3:

- Set-up for in situ LA-MC-ICP-MS analysis
- Compilation of Nd isotope analyses
- Methodology for LA-ICP-MS U-Pb dating of monazite
- Compilation of U-Pb ages of monazite
- Element distribution plots
- Sm-Nd isochron of sample AFB83

Chapter 4

- Whole rock concentrations of analysed sample
- F/Cl ratios in biotite
- Fe concentration of biotite vs. Zn content of biotite

Chapter 5:

- Methodology
- Plot of F and Cl concentration in biotite
- Results of HCl/H_2O activity ratio calculations

List of Tables

Chapter 1

Chapter 2

Chapter 3

Chapter 4

List of Figures

Chapter 1

Chapter 2

Chapter 3

Chapter 4

Chapter 5

Preamble

It is intended that the entire contents of this thesis will be published in internationally-recognised Earth science journals. At the time of submission, Chapters 1, 2 and 3 are published (see Appendix 1) and Chapter 5 is being prepared for submission by April, 2014.

This thesis consists of 5 chapters, and each chapter represents an independent body of work that is presented in a format similar to a published manuscript. Hence, the structure of this thesis has unavoidably led to repetitions of sections such as the geological settings and methodologies. However, it should be noted that the analytical methods applied vary from chapter to chapter. A single reference list follows Chapter 5. In this thesis reference to work presented in other chapters is made by referring to respective chapters, or if the chapter is published, to the respective publication.

Although each chapter represents a separate, stand-alone piece of work, all of the chapters together are related to the central theme of this thesis: understanding element mobility during metamorphism.

Subject of this Thesis

The geochemical recycling of crust during plate tectonic episodes is dependent on melt extraction, accumulation and emplacement, and on the gross changes that may accompany fluid flow during regional metamorphism. Whereas the final stages of crustal geochemical modification can be appreciated by the details of trace and radiogenic isotope geochemistry of igneous rocks, the initial elemental redistributions that accompany metamorphism, and thence the subsequent igneous evolution, are very poorly constrained. This thesis aims to establish a better understanding of element distribution and mobility during metamorphism through detailed investigations of rock samples on a regional-, bulk rock-, and mineral-scale. For this endeavour, my approach combines established petrological and geochemical techniques with innovative new micro-analytical tools that, in part, were developed through this project.

Over the last three decades, metamorphic petrologists have made significant progress in understanding mineral-to-mineral reactions during metamorphism and the role of volatile species (H_2O, CO_2) in these reactions (e.g., Holland & Powell 1990). Enhanced by recent application of geochronology to metamorphic reactions (e.g., Rasmussen et al. 2001; Gregory et al. 2009), detailed pressure-temperature-time paths can be constructed to understand tectonic processes. On the other hand, metamorphic petrologists on the whole have not embraced trace element and radiogenic isotope geochemistry to the same extent as the igneous petrologists. Furthermore, despite the general agreement of the presence of fluids during metamorphism, their sources are generally poorly constrained.

Studies into the how trace elements distribute between phases during metamorphism and fluid-rock interactions are in their infancy (e.g. Spandler et al. 2003; Spandler et al. 2007; Janots et al. 2008). Very few studies have utilized the fingerprinting power of trace elements and radiogenic isotopes for understanding metamorphic processes. Under conditions of high-grade metamorphism and crustal anatexis, bulk-rock radiogenic isotopes have been employed to track granite generation processes. However, experiments (Knesel & Davidson 2002) and studies of natural rocks (Tomasini & Davies 1997; Zeng et al. 2004; Jung 2005; Zheng et al. 2003) demonstrate radiogenic isotope (Sr, Nd, Pb) disequilibria between mineral phases or within single crystals in metamorphic rocks or during crustal anatexis, indicating that isotopic systematics of metamorphism and anatexis are considerably more complex that usually assumed. These issues directly impact on the reliability of isotopically-determined ages and source characteristics for granites and other igneous rocks. Progress on this front can be made if detailed isotopic studies of metamorphic rocks are conducted at the mineral scale.

The importance of fluids during metamorphism has been known for some time. Several examples of regional fluid flow during metamorphism have been documented (e.g. Cartwright et al., 1995; Oliver et al., 1998). Such large-scale hydraulic pumping systems (some extend to 100 km) might be crucial for the genesis of orogenic ore deposits. However, the origin of metamorphic fluids is often poorly constrained. One of the reasons is that until recently we lacked analytical tools to measure key elements such as Cl and Br as fluid tracers on a mineral and sub-mineral scale.

To better understand element mobility during metamorphism and crustal evolution, including the generation of new granitic crust, we need to address the following key questions:

- *How and where are trace elements, metals and radiogenic isotopes distributed prior to, and during metamorphism of crustal rocks?*
- *What controls the geochemical and isotopic compositions of anatectic melts that form during high-grade metamorphism?*
- *How reliable are isotope systems for crustal provenance studies?*
- *What is the origin of metamorphic fluids and how and what is their role in element mobility?*

Structure of this thesis

In order better understand fluid flow and fluid properties in metamorphic/hydrothermal environments we need a routine analytical method to measure key elements which can be used to track the fluid sources and reconstruct fluid pathways. However, such analytical tools have not existed until very recently. Chapter 1 focuses on the development and testing of in situ LA-ICP-MS analysis of Cl and Br in fluid inclusions and scapolite. This method was tested on scapolite from the Eastern Mt. Lofty Ranges, South Australia and on fluid inclusions from sphalerite from several Mississippi Valley Type deposits. In situ analysis of Br and Cl promises to resolve complex fluid-rock interaction histories on a sub-mineral scale. Furthermore, in situ LA-ICP-MS allows the simultaneous quantification of a range of trace elements and halogens so that direct conclusions on fluid origins, relative element concentrations and fluid mixing mechanisms can be drawn. Once this method was rigorously tested and assessed it was applied in Chapter 2 on a regional metamorphic suite in the highly mineralized Mt. Isa inlier, which underwent a complex history of fluid flow and fluid infiltration from different sources.

Chapter 3 investigates the mechanisms of radiogenic isotope homogenization during metamorphism. The approach taken involved in situ measurement of Nd isotope signatures by LA-MC-ICP-MS in REE-rich minerals that control the whole rock Nd budget. With knowledge of the pressure and temperature conditions at which REE-rich accessory phases homogenise, we can better utilise these minerals as chemical tracers and geochronometers of geological processes. Furthermore, it can be tested whether detrital REE-rich minerals with highly heterogeneous isotopic signatures can survive high-grade metamorphism, in which case isotopic disequilibrium during melt formation may result.

In Chapter 4, regional scale element mobility was investigated during HT/LP metamorphism in the Eastern Mount Lofty Ranges, South Australia. The previous 3 chapters provided crucial background information on the controlling factors influencing element mobility during metamorphism, such as fluid sources and recrystallization processes of key minerals. Chapter 5 focuses on a particular, significant new finding: large amounts of Zn and Pb are leached from metasedimentary rocks due to pervasive fluid flow during metamorphism. Although there is some overlap in scope and findings of the last 2 chapters of the thesis, Chapter 5 specifically evaluates the potential of metamorphic mobility of Pb and Zn as a source of metals for orogenic and sediment-hosted base metal ore deposits.

Chapter 1

In situ quantification of Br and Cl in minerals and fluid inclusions by LA-ICP-MS: A powerful tool to identify fluid sources

Published in *Chemical Geology*

Abstract

Bromine and chlorine are important halogens for fluid source identification in the Earth's crust, but until recently we lacked routine analytical techniques to determine the concentration of these elements in situ on a micrometer scale in minerals and fluid inclusions. In this study, I evaluate the potential of in situ Cl and Br measurements by LA-ICP-MS through analysis of a range of scapolite grains with known Cl and Br concentrations. I assess the effects of varying spot sizes, variable plasma energy and resolve the contribution of polyatomic interferences on Br measurements. Using well-characterised natural scapolite standards, I show that LA-ICP-MS analysis allows measurement of Br and Cl concentrations in scapolite, and fluid inclusions as small as 16 µm in diameter and potentially in sodalite and a variety of other minerals, such as apatite, biotite, and amphibole. As a demonstration of the accuracy and potential of Cl and Br analyses by LA-ICP-MS, I analysed natural fluid inclusions hosted in sphalerite and compared them to crush and leach ion chromatography Cl/Br analyses. Limit of detection for Br is ~8 µg g^{-1}, whereas relatively high Cl concentrations (> 500 µg g^{-1}) are required for quantification by LA-ICP-MS. In general, LA-ICP-MS fluid inclusion results agree well with ion chromatography (IC) data. Additionally, combined cathodoluminescence and LA-ICP-MS analyses on natural scapolites within a well-studied regional metamorphic suite in South Australia (Eastern Mt. Lofty Ranges) demonstrate that Cl and Br can be quantified with a ~25 µm resolution in natural minerals. This technique can be applied to resolve a range of hydrothermal geology problems, including determining the origins of ore forming brines and ore deposition processes, mapping metamorphic and hydrothermal fluid provinces and pathways, and constraining the effects of fluid–rock reactions and fluid mixing.

1. Introduction

Chlorine and bromine are common constituents of fluids derived from various sources and because they have relatively low abundances in the majority of silicate minerals, they can be used to trace the origin of fluids in sedimentary and hydrothermal/magmatic systems. Halogens are important ligands for metal transport in hydrothermal solutions, hence Br and Cl behaviours in hydrothermal environments may be crucial for ore forming processes. Numerous studies have investigated Cl and Br contents in hydrothermal fluids in various geological environments (e.g. Banks & Yardley, 1992; Böhlke & Irwin, 1992; Yardley et al., 1993; Banks et al., 2000a,b; Kendrick et al., 2001, 2002, 2008; Nahnybida et al., 2009). However halogen studies can be challenging especially if crucial samples lack fluid inclusions or contain multiple fluid inclusion generations, which limits effective use of routine bulk techniques. Br in particular is not easily measured by routine analytical tools such as electron probe microanalysis (EPMA) and quantification of iodine is limited by its low ppb abundance in most materials. Bromine and Cl concentrations in minerals and fluid inclusions have respectively been determined by instrumental neutron activation analyses (INAA) (e.g. Heinrich et al., 1993; Lieftink et al., 1993) and leachate ion chromatography analyses (e.g. Bottrell et al., 1988; Banks & Yardley, 1992; Yardley et al., 1993; Svensen et al., 1999; Nahnybida et al., 2009). Both, INAA and ion chromatography represent bulk analyses of fluid inclusions or minerals. The properties of different generations of fluid inclusions within a single mineral or chemical zoning in minerals cannot be resolved by these techniques. Other methods such as laser microprobe noble gas mass spectrometry (Böhlke & Irwin, 1992; Irwin & Reynolds, 1995; Irwin & Roedder, 1995; Kendrick et al., 2008; Kendrick, 2012), proton-induced X-ray emission (PIXE) (e.g. Heinrich et al., 1992; Ryan et al., 1993; Vanko et al., 2001), synchrotron X-ray fluorescence (SXRF) (e.g. Vanko et al., 2001; Foriel et al., 2004) or secondary ion mass spectrometry (SIMS) (e.g. Hauri, 2002) have been used to obtain halogen concentrations and ratios in minerals and fluid inclusions. However, these methods have not been applied extensively. Compared to the above techniques, LA-ICP-MS is now a widespread technique where Cl/Br is measured simultaneously, potentially with large range of other elements. Furthermore, LA-ICP-MS requires minimal sample preparation and is a very cost- and time effective method. Heinrich et al. (2003) assessed the potential of Cl and Br quantification by LA-ICP-MS and recently Seo et al. (2011) successfully demonstrated the feasibility of in situ LA-ICP-MS Br and Cl quantification. Leisen et al. (2012) also quantified Br by LA-ICP-MS, but were unable to determine Cl using their method. In many cases, minerals contain fluid inclusions belonging to several generations, each of which may represent very different stages of fluid evolution and/or fluid composition. A major advantage of fluid inclusion analyses by LA-ICP-MS is that single fluid inclusions in specific fluid inclusion assemblages can be easily targeted. Single fluid inclusion analyses have the unique benefit that fluid-mixing trends within one fluid generation can be recognized, whereas such information is lost by bulk crush and leach ion chromatography analyses.

Laser ablation inductively coupled plasma mass-spectrometry (LA-ICP-MS) can yield precise compositions of individual fluid inclusions (e.g., Audétat et al., 1998; Günther et al., 1998; Heinrich et al., 1999; Rusk et al., 2004; Klemm et al., 2007) and trace element compositions of minerals (e.g., Pearce et al., 1992; Heinrich et al., 2003; Spandler et al., 2011; Rusk et al., 2011). However, analysis of halogens by LA-ICP-MS is not standard practice, as halogens tend to have relatively low ionisation efficiencies that lead to lower analyte sensitivity, and thus increased detection limits. The energy required to positively ionise fluorine (17.42 eV) makes it impossible for quantification via an Ar (ionisation energy: 15.76 eV) plasma typically used in LA-ICP-MS systems. Bromine, Cl and I are not yet routinely measured by LA-ICP-MS, not only because of their high ionisation energies (Cl: 12.97 eV, Br: 11.81 eV, and I: 10.45 eV), but also because of the lack of suitable standard materials for these elements. Nevertheless, Seo et al. (2011) have demonstrated the feasibility of Cl and Br analyses by LA-ICP-MS. These authors present Cl and Br concentrations in fluid inclusions using scapolite as an external standard, but there are a range of potential analytical problems that remain to be tested, such as the extent of interferences between element signals, elemental fractionation during ablation and potential problems of matrix matching between sample materials and standards.

In this study, I assess the potential of determining in situ Br and Cl concentrations by LA-ICP-MS through analysis of several scapolite grains that have previously been studied for halogen contents (Lieftink et al., 1993; Kendrick, 2012). I compare LA-ICP-MS analyses of Br and Cl concentrations with existing and new microprobe data and with existing INAA and Noble Gas Method values (Lieftink et al., 1993; Kendrick, 2012). By using a homogenous scapolite that was previously characterised for Br and Cl by the Noble Gas Method (Kendrick, 2012), as the Br and Cl standards, I determine the accuracy and precision of the quantification of Cl, Br, and Cl/Br over a range of Cl and Br concentrations in scapolite, amphibole and sodalite. We evaluate the effects of interferences, down-hole fractionation, and plasma energies at different laser aperture sizes. As a demonstration of the method, we determine Cl/Br of a series of scapolite standards (Lieftink et al., 1993; Kendrick, 2012) and individual fluid inclusions from the Lucky Dog, Coy, and East Tennessee Mississippi Valley type (MVT) Pb–Zn deposits (Roedder, 1971; Viets et al., 1996; Wilkinson et al., 2009). The results compare well with those obtained by ion chromatography and the Noble Gas Method on the same samples. I also apply the method to metamorphic scapolite from the Adelaide Fold Belt (Eastern Mt. Lofty Ranges), South Australia, to show changes in fluid composition during scapolite formation.

2. Methods

To determine Cl and Br concentrations and ratios in situ in minerals and individual fluid inclusions, a homogenous standard with known concentrations of Cl and Br is needed. To test the accuracy of my data across a wide range of Cl and Br concentrations, I analysed 4 different scapolites for trace element concentrations using electron probe microanalysis (EPMA) and LA-ICP-MS. These scapolites were previously characterised for chemical homogeneity by SEM imaging, for major elements by EPMA and for halogen concentrations (Br, Cl and I) using the Noble Gas Method and INAA by Kendrick (2012) (SY, BB1 and BB2) and INAA by Lieftink et al. (1993) (DL137). Thirty-four electron probe analyses and over 230 LA-ICP-MS analyses at different spot sizes were carried out on polished grain mounts. To verify the chemical homogeneity of all of the scapolites analysed in this study, wavelength dispersive spectrometry (WDS) element maps of Ca, Na, Cl, and Si were acquired and SEM-CL images were used to identify subtle compositional variations that are not evident from transmitted light petrography. Scapolites SY, BB1, BB2 and DL137, several other Cl-bearing minerals (sodalite and hastingsite amphibole from Bancroft, Ontario, Canada and Little Chief Mine, Washington, USA, respectively) and scapolites from Tanzania, Canada, Switzerland and East Africa were also analysed with EPMA and LA-ICP-MS to compare results of these two methods across a wide compositional range.

2.1. Background

The two stable isotopes of bromine, ^{79}Br and ^{81}Br, are present in roughly equal proportions of 50.69% and 49.31% respectively. Chlorine has two stable isotopes, ^{35}Cl (75.78%) and ^{37}Cl (24.22%). The masses of the Cl and Br isotopes are therefore very close to stable isotopes of Ar (^{36}Ar, ^{38}Ar, and ^{40}Ar), and the biatomic 2(^{40}Ar)$^{+}$ molecule of mass 80. Because Ar is so abundant in the plasma of the ICP-MS, peak tailing of ^{36}Ar and ^{38}Ar has the potential to cause interference on ^{35}Cl and ^{37}Cl, and the combination of two ^{40}Ar ions causes a large peak at mass 80 whose peak tail could interfere with either stable isotope of Br. In addition, there are several potential interferences on ^{79}Br or ^{81}Br; the most significant being (^{40}Ar^{39}K)$^{+}$ interference with ^{79}Br and (^{65}Cu^{16}O)$^{+}$ and (^{41}K^{40}Ar)$^{+}$ interference with ^{81}Br signals. We have conducted a series of analytical tests to quantify the relative contributions from these interferences. No polyatomic species are likely to interfere significantly with ^{35}Cl as ^{70}Zn^{++} did not produce measurable ^{35}Cl when ablating sphalerite. The polyatomic species (^{36}Ar^{1}H)$^{+}$ and (^{23}Na^{14}N)$^{+}$ possibly interfere with ^{37}Cl. However due to the high backgrounds for ^{37}Cl I did not investigate these possible interferences any further in this study.

2.2. Characterisation of scapolite standards

2.2.1. EPMA analysis

Quantitative major element analysis of scapolite, sodalite and amphibole was carried out using a JEOL JXA 8200 superprobe, at the Advance Analytical Centre, James Cook University. Acceleration voltage and beam current were set to 15 kV, and 20 nA respectively. A defocused 5 μm beam was used to avoid potential diffusion of Na and Cl upon interaction with the electron beam. Counting times were 20 s on peak and 10 s on background for each element. The data were processed using φρz corrections and standardised against a set of well-characterised, in-house oxide (hematite) and silicate (albite, almandine, orthoclase, wollastonite, olivine), sulphate (barite) and tugtupite (chlorine) standards. The detection limit for Cl was ~120 μg g^{-1}.

2.2.2. CL analysis

Cathodoluminescence (CL) imaging was conducted at James Cook University on carbon-coated polished thin sections and grain mounts using a JEOL JSM5410LV SEM and a Robinson CL detector and photomultiplier. The photomultiplier covers the spectral range of 310 to 650 nm, thus is more sensitive in gathering light in the blue to ultraviolet range than in the red to infrared range. Instrument operating conditions were set to an accelerating voltage of 20 kV and a beam current of ~10 nA.

2.2.3. LA-ICP-MS

Trace elements in scapolite were analysed at the Advanced Analytical Centre at James Cook University using a Geolas 193 nm ArF excimer laser coupled with a Varian 820 quadrupole ICP mass spectrometer. Helium was used as the carrier gas in the ablation chamber and was mixed via a Y piece with Ar prior to introduction to the ICP to obtain maximum signal sensitivities. The ICP-MS was tuned to ensure robust plasma conditions sensitivity of Th $\approx$ U $\approx$ Pb; (e.g., Pettke et al., 2012) and low oxide production levels ($\leq$0.5% ThO) with the plasma power set at 1.4 kW. Prior to each analytical session the ICP-MS cones were cleaned and a dedicated set of teflon-lined sample tubing was installed. The mass spectrometer settings were optimized to maximise sensitivities for Br and Cl while maintaining multi element measurement capabilities. Typical gas backgrounds for ^{79}Br and ^{81}Br were ~1250 cps and 2850 cps, respectively, and 35,000–42,000 cps for ^{35}Cl. Dwell times were set to 20 ms for Cl, 30 ms for Br, and 10 ms for all other elements. LA-ICP-MS analyses of scapolite were carried out on polished 100 μm thick sections and polished grain mounts, using a laser energy density of 6 J/cm^2 and repetition rates of 5 Hz. The beam diameter varied between 24 and 120 µm. The following analytes were counted (typical detection limits for each element are in parentheses in µg g^{-1} for a 90 µm spot size): ^{23}Na (30), ^{25}Mg (1.4), ^{27}Al (1), ^{29}Si (365), ^{33}S (50), ^{35}Cl (230), ^{39}K (8), ^{43}Ca (91), ^{55}Mn (0.1) and ^{57}Fe (5) ^{79}Br (4), ^{81}Br(8).

I used scapolite sample BB1 (Kendrick, 2012) as a standard, based on the consistency of the data and the homogeneity of the sample and standard material availability (Table 1). External standard BB1 was used for Na, Al, Si, S, Cl, K, Ca, Fe and Br data reduction. (external standard: material with known concentrations of all elements of interest) while internal standardization of scapolites was made using ^{23}Na, based on electron probe microanalysis Na analysis (the internal standard is an independent constraint such as the absolute concentration of one element). Concentrations for external standardization were taken from Kendrick (2012) and BB1 was cross-checked by using SY and BB2 as standards (values form Kendrick (2012)) for BB1 analyses. All other elements were reduced via the software package "Glitter" (Griffin et al., 2008) with NIST SRM 612 and NIST SRM 610 glasses analysed for calibration using reference values taken from Spandler et al. (2011). For samples with very low Br (≤ 15 µg g^{-1}) and Cl (≤ 1000 µg g^{-1}) concentrations, the limits of detection (LOD) were calculated according to Eq. (6) in Pettke et al. (2012).

Table 1. EPMA measurements of scapolite reference material BB1 and other potential scapolite SRM minerals.

	BB1		BB1		BB2		BB2		SY		SY		DL137		DL137	
Source	1		**This study**		1		**This study**		1		**This study**		2		**This study**	
	(n=44)		(n=10)		(n=11)		(n=5)		(n=13)		(n=7)		(n=4)		(n=12)	
Wt.%	AVG	2σ	AVG	2σ	AVG	2σ	AVG	2σ	AVG	2σ	AVG	2σ	AVG	2σ	AVG	2σ
SiO_2	56.00	1.00	55.54	0.26	61.20	0.40	61.68	0.21	56.00	1.00	57.18	1.02	56.87	0.20	56.89	0.93
Al_2O_3	22.10	0.50	22.22	0.20	18.90	0.20	18.71	0.51	21.00	0.20	21.10	0.17	22.29	1.18	22.40	0.26
FeO	0.14	0.04	0.13	0.05	0.05	0.04	0.04	0.04	0.10	0.03	0.10	0.03	0.00	0.00	0.01	0.03
CaO	7.00	0.20	7.00	0.16	1.80	0.10	1.69	0.09	5.40	0.20	5.39	0.13	5.59	0.56	5.43	0.46
Na_2O	9.50	0.40	9.18	0.23	12.30	0.20	12.54	0.16	10.10	0.20	10.09	0.18	10.60	1.16	10.76	0.40
K_2O	1.40	0.10	1.50	0.11	1.30	0.10	1.34	0.06	1.40	0.10	1.47	0.06	0.17	0.10	0.24	0.07
SO_3	0.80	0.20	0.73	0.08	0.15	0.06	0.21	0.15	0.40	0.10	0.40	0.07	0.75	0.14	0.16	0.07
CO_2	0.59	0.07	0.90	0.13	0.00	0.00	0.00	0.00	0.33	0.14	0.51	0.10	n.d.	n.d.	0.34	0.26
Cl	3.10	0.10	3.04	0.10	4.00	0.10	4.12	0.05	3.50	0.20	3.52	0.06	3.81	0.12	3.81	0.22
–Cl=O	0.69	0.03	0.68	0.02	0.91	0.02	0.93	0.00	0.80	0.08	0.79	0.02	0.86	0.02	0.86	0.05
Total	99.00	2.00	99.55	0.61	98.80	0.70	99.38	0.86	98.00	1.00	98.96	1.24	99.24	1.14	99.19	0.66

1 = Kendrick (2012)
2 = Lieftink et al. (1993)
AVG = Average
n.d. = no data

2.3. Characterisation of fluid inclusions

2.3.1. Microthermometry

Microthermometric analysis of fluid inclusion was carried out at James Cook University using a Linkham THMSG-600 heating–cooling stage with a LinkhamTM TMS 91 temperature controller, mounted on an Olympus BX51 microscope. The heating–cooling stage was calibrated using synthetic CO_2–H_2O fluids (*T*mCO_2 = −56.6) and synthetic H_2O inclusions with critical density (*T*m(ice) = 0.0 °C; *T*h(tot) = 374 °C). Small sample chips from double polished thick-sections (ca. 200 µm thick) were cooled until the inclusion fluids were completely frozen. The samples were then gradually heated with rates of 40 °C/min until the ice started to melt. At this point the heating rate was lowered to 2 °C/min until the last ice melted (*T*m(ice)). Several cooling/heating cycles were conducted on most inclusions to ensure only stable transitions were recorded. Total homogenisation temperatures (*T*h(tot)) were measured by heating the chips with a rate of 40 °C/min. As Th(tot) was approached the heating was decreased to 2 °C/min. The precision of temperature measurements is ± 0.1 °C for Tm(ice), and ± 4 °C for *T*h. Ice melting temperatures were used to calculate salinities as NaCl wt.% equivalents according to Bodnar (1993).

2.3.2. LA-ICP-MS

I used the same LA-ICP-MS set up as for scapolite and the same procedure was followed as described above. All analysed fluid inclusions were hosted in sphalerite that ablates controllably using a 193 nm laser, thereby avoiding problems of host mineral fracturing or fluid inclusion explosions during ablation. Fluid inclusions within doubly polished sphalerite chips were analysed using a laser energy density of 8 J/cm^2 and a laser repetition rate of 5 Hz. The laser beam diameter varied between 24 and 44 µm depending on the inclusion size and depth within the sample. In all cases the smallest beam size required to ablate the entire volume of the fluid inclusion was selected. Fluid inclusions were analysed for the following analytes: ^{23}Na, ^{25}Mg, ^{33}S, ^{35}Cl, ^{39}K, ^{44}Ca, ^{55}Mn, ^{57}Fe, ^{65}Cu, ^{66}Zn (host mineral), ^{79}Br, ^{81}Br, and ^{208}Pb. Bracketing analysis of scapolite BB1 (Kendrick, 2012) and NIST SRM 610 and 612 glasses was used for external standardization of all analyses, employing the reference values of Spandler et al. (2011) for the NIST glasses, and (Kendrick, 2012) for scapolite BB1. Potassium, Na, Ca, Cl and Br concentrations were quantified using the scapolite BB1 standard as fluid inclusions contain K, Na, Ca concentrations similar to the BB1 standard, whereas all other (trace-) elements were quantified using the NIST glasses. Sodium concentrations, derived from microthermometry, were used as the internal standard. Contributions to the fluid inclusion signal from the host sphalerite were evaluated using Zn signals assuming that all Zn in the signal derive from the sphalerite host. All data reduction procedures were performed using the SILLS software (Guillong et al., 2008).

2.3.3. Ion chromatography

The solute compositions of fluid inclusions in sphalerite from the Lucky Dog, Coy, and East Tennessee deposits were determined using the bulk extraction ion chromatography method described in Hofstra and Emsbo (1993) and Viets et al. (1996). This analytical method has advantages over conventional crush-leach methods because it allows the analyses of very small samples that are crushed (~0.3 g), but not powdered, and only briefly leached with ultrapure water (conductance = 18 megohms/cm). This procedure minimizes leaching of ions from the host minerals and newly generated surface areas that promote adsorption of charged species. Moreover, this method permits an evaluation of contributed contaminates by (1) a pre-crush analysis to evaluate leaching from surfaces of host minerals, (2) an analysis immediately after the sample is crushed to determine ions released from fluid inclusions, and (3) a post-crush analysis to determine solutes from solid inclusions in host minerals. Analysis of concentrations matched in house aqueous standards, cross calibrated with USGS Standard Reference Samples, have a preci- sion of 2 to 3% and replicate analyses on the natural sphalerite refer- ence sample (c.f. LDAS-1 in Viets et al., 1996) are better than 10% RSD.

3. Calibration of Cl/Br by LA-ICP-MS

3.1. Interference and fractionation of Cl and Br during LA-ICP-MS analysis

3.1.1. Polyatomic interferences

I analysed atacamite ($Cu_2Cl(OH)_3$), which is 74.5 wt.% CuO and Br deficient to determine the magnitude of the interference of $(^{65}Cu^{16}O)^+$ on ^{81}Br. Measurement of atacamite with a 120 µm laser spot gave ^{81}Br values below the detection limit (8 µg g^{-1}), which confirms that there is no significant interference on ^{81}Br by $(^{65}Cu^{16}O)^+$. This reflects the low oxide production levels for which the plasma was tuned (see above). Analyses of series of Br-deficient, gem quality feldspar grains with compositions ranging from anorthite to orthoclase and Br- deficient biotite produced significant signals for ^{79}Br and ^{81}Br (Fig. 1), which we interpret to be due to polyatomic species $(^{40}Ar^{39}K)^+$ and $(^{40}Ar^{41}K)^+$, respectively. A linear positive relationship between the potassium concentration and counts of ^{79}Br and ^{81}Br is observed (Fig. 1). The magnitude of the interference is far greater for ^{79}Br, where ~13 wt.% K in feldspar leads to an apparent Br concentration of ~ 70µg g^{-1} for ^{79}Br, and ~ 15–20 µg g^{-1} for ^{81}Br. Analysis of Cl-absent biotite with a K content of ~8 wt.% leads to ^{79}Br and ^{81}Br concentrations ~ 50 µg g^{-1}, and ~ 8–18 µg g^{-1}, respectively. Analysis of anorthite with potassium content of ~ 3300 µg g^{-1} returned 7.7–8.1 ± 1.8 µg g^{-1} ^{79}Br, while ^{81}Br was below the detection limit. The smaller magnitude of K– Ar interference on ^{81}Br is consistent with the lower abundance of ^{41}K (6.7%) compared to ^{39}K (93.3%). Applying a slope of best fit through all of the data (Fig. 1), gives a zero K intercept of ~8.5 µg g^{-1} for ^{79}Br, and close to 0 µg g^{-1} for ^{81}Br (Fig. 1). These data indicate significant K–Ar interferences on the ^{79}Br and ^{81}Br signals that can be described according to the formulae:

$$^{79}Br_T = {}^{79}Br_M - (K_M/2000) - 8$$

$$^{81}Br_T = {}^{81}Br_M - (K_M/10000)$$

where T and M are true and measured element concentrations in µg g^{-1}, respectively. We analysed the same grains with plasma power settings of 1.2 kW and 1.4 kW, and no difference was observed in terms of the degree of interference. I also found no effect of varying laser spot size (between 120 and 60 µm diameter). While Leisen et al. (2012) did not observe ArK interferences with Br by measuring solutions with 1000 µg g−1 K, our results show that ArK interferes with both Br isotopes. However, based on the natural abundances of Ar and K isotopes, the expected interference on ^{79}Br should be 14 times higher than on ^{81}Br. Here, we only observe a ratio of ~4 for apparent ^{79}Br and ^{81}Br (~80 µg g^{-1} apparent ^{79}Br and ~20 µg g^{-1} apparent ^{81}Br at ~13 wt.% K; Fig. 1). Hence, we cannot exclude that another, as yet unrecognised, interference, contributes to the higher apparent ^{81}Br values and hence a lower ^{79}Br/^{81}Br ratio than expected. Nevertheless, I stress that the interference correction equations formulated here may not be directly applicable to analyses obtained on other LA-ICP-MS instruments, and we encourage analysts to further test potential polyatomic interferences with other analytical setups.

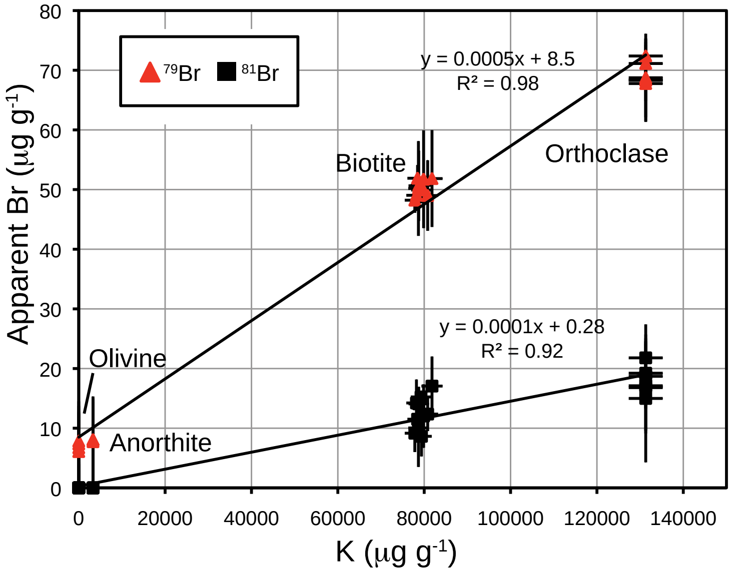

Fig. 1. Apparent ^{79}Br and ^{81}Br concentration versus K concentration of diffusion annealed San Carlos olivine (K and Br free), anorthite (3300 µg g^{-1} K), orthoclase (13,300 µg g^{-1} K) and biotite (~8000 µg g^{-1} K) as determined from both ^{79}Br and ^{81}Br signals. Lines of best fit and analysis of olivine indicate a "false positive" ^{81}Br signal of ~8.5 µg g^{-1}.

Analysis of K-deficient material such as San Carlos olivine annealed at 1300 °C for 25 days (see Spandler and O'Neill, 2010) does not show ^{81}Br concentrations above the LOD (~ 4 µg g^{-1}) (as calculated according to Pettke et al., 2012). On the other hand, ^{79}Br values in these analyses were determined to be 6 to 7.4 µg g^{-1}, which are well above the LOD of ~4 µg g^{-1}, but are consistent with the correction factor calculated above based on feldspar and biotite analyses. Interestingly, Seo et al. (2011) reported 9 µg g^{-1} ^{79}Br and 378 µg g^{-1} ^{35}Cl in quartz during their LA-ICP-MS study of halogen analysis of fluid inclusions, despite the fact that quartz should be devoid of Br and Cl.

We cannot conceive of any reasonable polyatomic or doubly-charged species that can explain these apparent ^{79}Br (~ 8 µg g^{-1}) and ^{35}Cl signals (Seo et al., 2011) in K-deficient minerals. After extensive petrographic (transmitted light and SEM) characterisation, we also exclude contamination of the analyses by micro-inclusions in the minerals as the source of these signals. Argon is by far the dominant component of the plasma, so one hypothesis is that the apparent ^{79}Br and ^{35}Cl signals are artefacts of Ar and Ar–Ar peak broadening caused by changes in plasma load during ablation. To test this idea, we collected ICP-MS peak scans from masses 32–38 and 77–83 of the gas background, and during ablation of Br- and Cl-free heat-treated San Carlos olivine. Comparison between the two sets of peak scans shows no changes to peak shape or height for masses 35 or 81, whereas, the 79 mass peak increases slightly (but does not change shape significantly) when ablating the olivine (Fig. 2). As a result, I can exclude an interference of ^{36}Ar peaks with ^{35}Cl or (^{40}Ar^{40}Ar)$^+$ interfering with ^{79}Br or ^{81}Br. The 79 mass peak increase is also not likely explained by a (^{40}Ar^{38}ArH)$^+$ interference as suggested by Seo et al. (2011) because our analytical set-up does not involve H_2 addition to the gas mixture and the ^{79}Br peak increase is only observed upon sample ablation. Due to (^{40}Ar^{39}K)$^+$ interference with ^{79}Br and K interference on (^{40}Ar^{41}K)$^+$ with ^{81}Br, in K-rich phases such as biotite, hornblende, or muscovite, a correction line for Br may need to be established at the beginning of an analytical session, by analysing Br-free K-rich mineral, in order to determine the magnitude of the interference on Br. Using BB1 scapolite, which contains 1.4 wt.% K_2O, as a standard should translate into an underestimate of ~2 µg g^{-1} in analysed K-deficient minerals. Nevertheless, in nearly all cases, this small difference will have little con- sequence for determination of fluid sources from Cl/Br ratios. It remains unresolved what causes the false positive signal of ~8.5 µg g^{-1} ^{79}Br when ablating Br-absent material. Therefore I suggest that in most situations ^{81}Br provides a more accurate quantification of actual Br concentrations than does ^{79}Br. This is especially the case for fluid inclusions that are typically enriched in K and have relatively low Br contents.

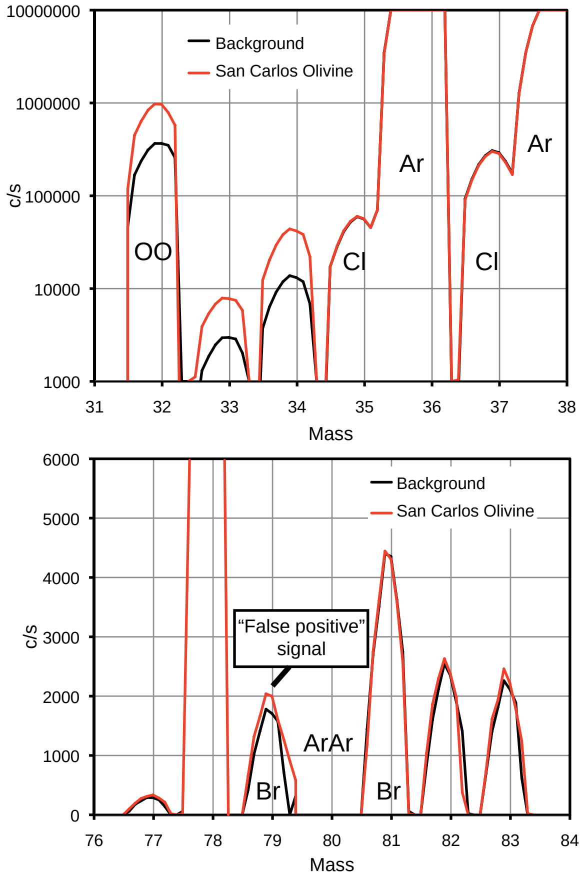

Fig. 2. Mass peak scans of background signals and diffusion annealed San Carlos olivine with a laser spot diameter of 120 µm. The peak at mass 80 is excluded, as it is a dominant Ar–Ar peak. Note the increase of the mass 79 peak upon sample ablation, where- as the mass 81 peak is unchanged. The increased peaks on masses 32, 33 and 34 during mineral ablation are ascribed to polyatomic interferences with oxygen.

3.1.2. Br and Cl fractionation

Fractionation of commonly analysed lithophile trace elements (e.g., REE, Sr, Ba, Th, U) during ablation, aerosol transport and ionisation is routinely monitored and controlled through laser and ICP-MS tuning (e.g., Kroslakova and Günther, 2007; Pettke, 2008). However, there has been little testing of halogen fractionation during LA-ICP-MS analysis. Guillong and Pettke (2012) reported a decrease in Na/Cl ratios with increasing fluid inclusion depth in the sample and deep drilling in scap- olite showed the same trend, which they interpreted to be fractionation between Na and Cl as a result of deep sample drilling. During deep drilling experiments on scapolite with 24 µm beam diameter, we also observe a progressive decrease in Na/Cl ratio and decreasing Na/Br, whereas no fractionation is observed between Si and Na (Fig. 3).

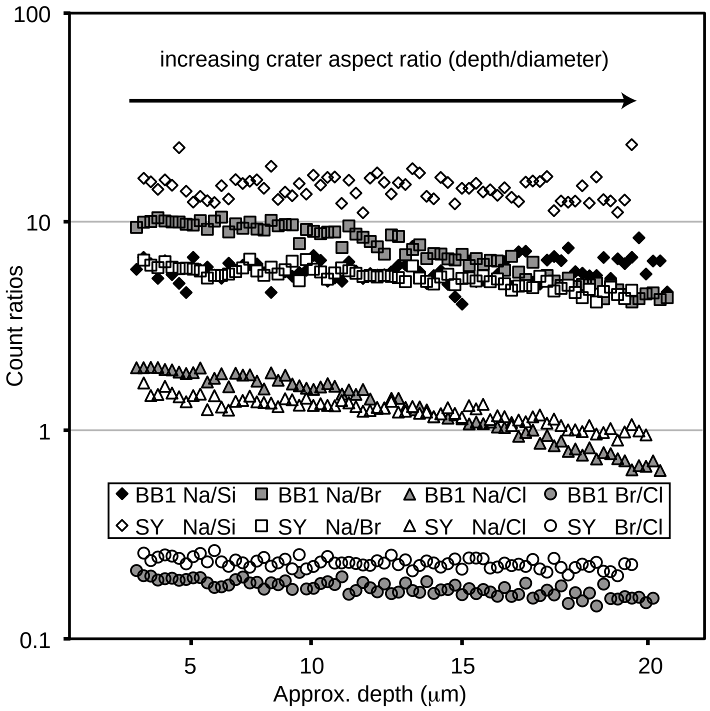

Fig. 3. Halogen fractionation during progressive drilling with increasing crater aspect ratios (depth/diameter) of scapolite with a 24-micrometer spot at 5 Hz. Scapolites SY and BB1 show different Br and Cl fractionation relative to Na. Count ratios of Na/Si indicate little down-hole fractionation of Na and Si.

The degree of fractionation is sample dependant (Fig. 3) and is not observed in analytical signals obtained using spot sizes > 60 μm due to the low crater aspect ratio (crater depth/crater diameter). The observed fractionation likely results from the higher volatility of Cl and Br relative to Na and possibly from Cl and Br escape from the crater (Garcia et al., 2009). The effect is most obvious only where count rates are lower, i.e. in analyses using small spot sizes, or in samples with low total concentrations of Cl and Br. Furthermore, at larger spot sizes the ratio of the depth to the width of the crater is much smaller so fractionation due preferential escape of volatile elements from a deep ablation crater is less significant. Nevertheless, the results (Figs. 4–6) show that the cumulative effect on Cl/Br ratios is negligible since Cl and Br do not fractionate significantly relative to each other (Fig. 7). These tests do highlight the importance of evaluating the potential of fractionation effects in acquiring, processing and interpreting LA-ICP-MS analytical signals. Because intra-element fractionation increases with ablation time (depth) and increasing crater aspect ratios, the most accurate element quantification is obtained by excluding deep analytical signals.

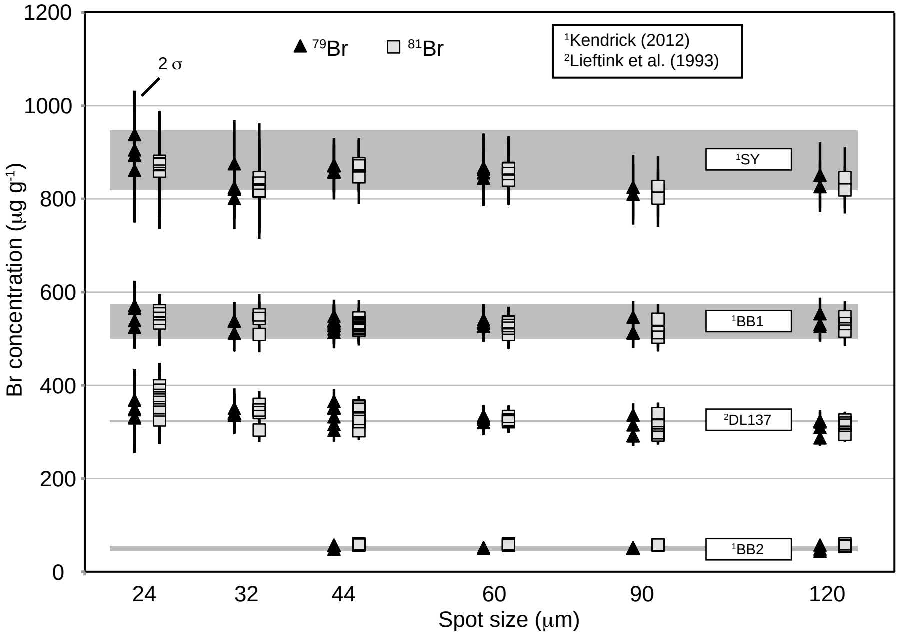

Fig. 4. LA-ICP-MS measurements of ^{79}Br and ^{81}Br with different spot-sizes compared to other analytical methods (INAA and Noble Gas Method). All analyses are well within the sigma 2 uncertainties of the INNA and Noble Gas Method values (grey bar).

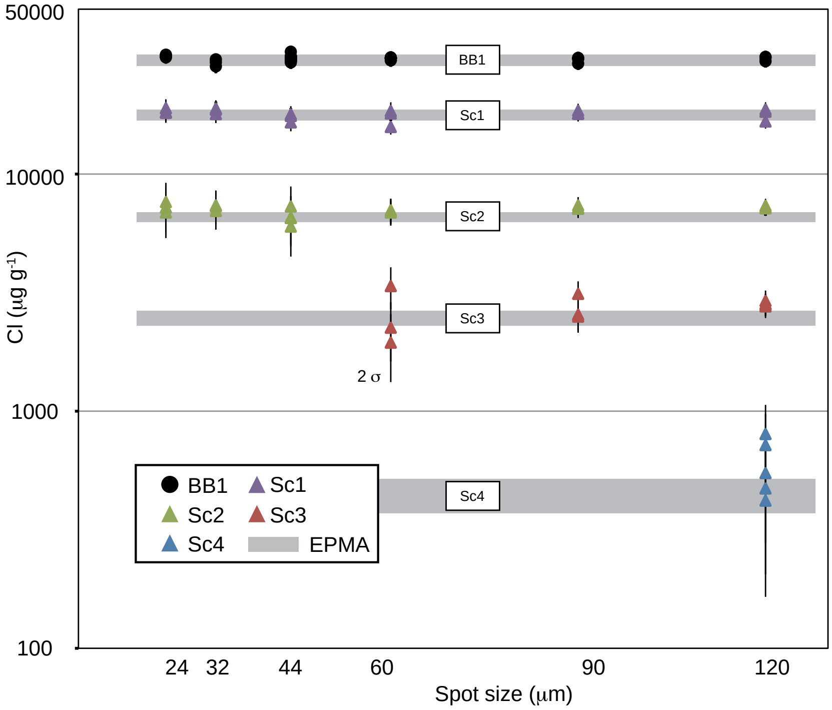

Fig. 5. Measured Cl concentrations of the BB1 and four scapolite (Sc1–4) samples with varying spot sizes. Grey bars are 2 sigma uncertainties of the EPMA analyses.

3.2. Quality of Cl and Br quantification by LA-ICP-MS

3.2.1. Cl quantification by LA-ICP-MS versus EPMA

To evaluate the accuracy of our Cl analyses by LA-ICP-MS, we analysed Cl-bearing minerals, including amphibole, sodalite and scapolite, with a broad range of chlorine contents from 450 µg g^{-1} to 7.32 wt.% as determined by EPMA. We carried out a total of 230 LA-ICP-MS analyses with variable spot sizes (24–120 µm). All samples were chemically homogenous with the exception of scapolite sample DL137, which has weak zonations in Na_2O and CaO (5.2–5.8 wt.% and 10.5–11.0 wt.%). Therefore, for sample DL137, Si was used as an internal standard while for all the other samples Na was employed as the internal standard (Si and Na concentrations from EPMA). Over the entire range of Cl values there is excellent agreement between the LA-ICP-MS and EPMA data (Fig. 6), although we note that the calculated detection limits of Cl by LA-ICP-MS (~500 µg g^{-1}) are higher than those achievable by EPMA (~120 µg g^{-1}) with the current settings.

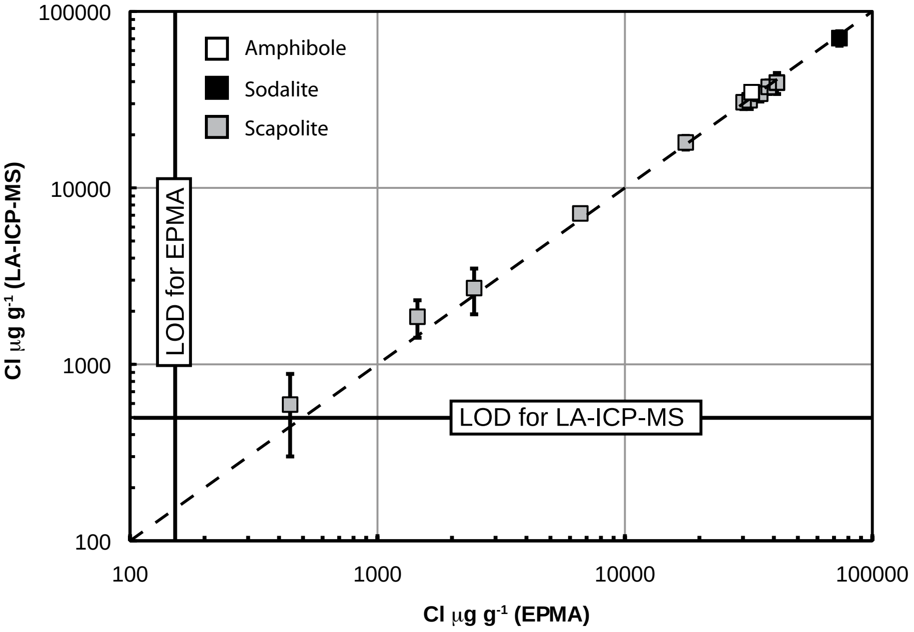

Fig. 6. Chlorine concentrations of one amphibole, one sodalite and a series of scapolite measured by EPMA versus Cl concentrations measured by LA-ICP-MS. Error bars indicate 2 sigma uncertainties. Representative limit of detection (LOD) for LA-ICP-MS and EPMA is shown for our set-up with a 120 µm spot size and 20 nA, respectively.

3.2.2. Scapolite as a Cl/Br standard

Scapolite makes an ideal standard for the quantification of Cl and Br in fluid inclusions (Seo et al., 2011) and minerals because it can contain relatively high concentrations of both Br and Cl (e.g. up to ~4 wt.% Cl). In addition, it has very small diffusion coefficients for halogens (Pan and Dong, 2003) and scapolite ablates well using a pulsed 193 nm laser. Scapolite is also cathodoluminescent, which potentially provides additional information on compositional zoning. Kendrick (2012) characterised halogen concentrations including Br and Cl in several scapolites using the Noble Gas Method and INAA. I analysed three of the same samples from the study of Kendrick (2012) (BB1, BB2, and SY1), and scapolite (DL137) described and analysed by INAA in Lieftink et al. (1993) to further evaluate the accuracy of LA-ICP-MS analysis of Cl and Br over a range of Cl and Br compositions. I chose BB1 as our standard reference scapolite as this material is readily available, has an intermediate Br concentration, and was shown by Kendrick (2012) and in this study to have a high degree of chemical homogeneity based on petrographic observations, WDS X-ray and CL mapping and multiple WDS quantitative analyses (Table 1). According to Kendrick's (2012) Noble Gas Method analyses, the Cl/Br ratio reproducibility uncertainty is ~6% (sigma 2) for BB1. The scapolite samples (BB2, SY and DL137) with known Br and Cl contents were also measured by EPMA (Tables 1 and 2) and LA-ICP-MS. While Kendrick (2012) documents the degree of homogeneity of samples BB1, BB2, and SY, no similar documentation exists for DL137 as only a few measurements were made (Lieftink et al., 1993). The EPMA measurements are in good agreement with previous analyses by Lieftink et al. (1993) and Kendrick (2012). For LA-ICP-MS analyses, we used a range of spot sizes from 24 to 120 μm to analyse ^{79}Br, ^{81}Br and ^{35}Cl concentrations. Our results show that, regardless of spot size or Cl and Br concentrations, the LA-ICP-MS data for Cl and Br are in excellent agreement with previously determined concentrations determined by INAA, the Noble Gas Method and EPMA (Figs. 4–7). The precision of the Cl and Br results is better than 10% in most cases (Table 2).

Table 2. Bromine and Cl concentrations of scapolite samples BB1, BB2, SY and DL137. Br and Cl values in this study are LA-ICP-MS values while Br and Cl of the other studies are a combination of INAA, the Noble Gas Method and EPMA.

	BB1		BB1		BB2		BB2		SY		SY		DL137		DL137	
Source	1		This study		1		This study		1		This study		2		This study	
	(n=56)		(n=28)		(n=20)		(n=12)		(n=44)		(n=20)		(n=1)		(n=27)	
	AVG	2σ	AVG	2σ	AVG	2σ	AVG	2σ	AVG	2σ	AVG	2σ	AVG	2σ	AVG	2σ
Br (μg g^{-1})	538	33	533	15	50	3	50	6	883	64	852	54	328	n.r.	300	32
Cl (wt.%)	3.10	0.10	3.07	0.17	4.00	0.10	3.94	0.25	3.50	0.20	3.40	0.17	3.81	0.12	3.73	0.40
Br/Cl x 10^{3} (mol)	7.7	0.4	7.7	0.5	0.55	0.03	0.58	0.11	11.2	0.5	11.2	0.9	3.8	0.1	3.9	0.6
Cl/Br (mol)	130	7	130	8	1818	94	1727	351	89	4	90	8	263	7	257	43

1 = Kendrick (2012)
2 = Lieftink et al. (1993)
AVG = Average

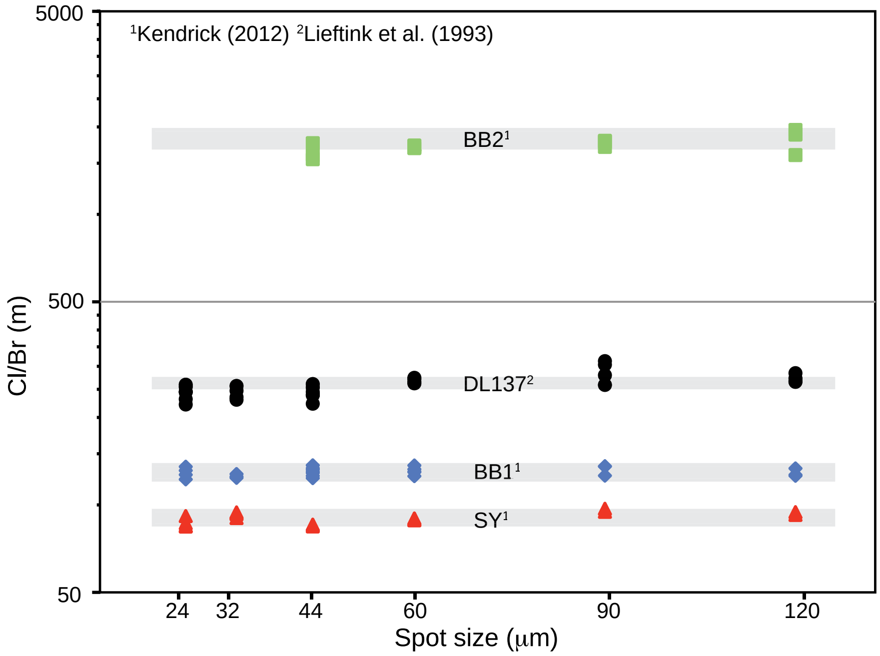

Fig. 7. Molar Cl/Br ratios with different spot sizes compared to INAA and the Noble Gas Method (Lieftink et al., 1993; Kendrick, 2012). Grey fields illustrate the sigma 2 uncertainties of the reference values (Lieftink et al., 1993; Kendrick, 2012).

3.3. Summary

Using scapolite as a standard, LODs of ~8 µg g^{-1} for Br and ~500 µg g^{-1} for Cl are routinely achievable by LA-ICP-MS analysis. Lower LODs are possible with spot sizes of greater than 120 µm. The analytical precision is insufficient to resolve depth-related change in Cl/Br making this technique applicable to the analysis of individual fluid inclusions or to compositionally zoned, halogen-bearing minerals. Nevertheless, care must be taken to monitor and control intra-element fractionation when measuring low concentrations of Br and Cl by LA-ICP-MS and we recommend using ^{81}Br (rather than ^{79}Br) to avoid false positive signals and to minimize the K–Ar interference on Br measurements. An important advantage of the LA-ICP-MS method is its rapid data accumulation, cost efficiency and that Cl and Br can be measured simultaneously with a list of other elements of in- terest in a single analysis. Fluids from different sources show distinct Cl/Br ratios that make Cl and Br quantification of particular interest for various fluid-related processes such as ore-formation or large- scale fluid flow. Below, we demonstrate the usefulness of this technique to the study of natural fluid inclusions from Mississippi Valley Type (MVT) ore deposits as well as on natural scapolite from a well-studied metamorphic suite.

4. Application of in situ Cl/Br quantification

4.1. Application to natural scapolites (Adelaide Fold Belt)

4.1.1. Geological background

In addition to fluid inclusions, in situ determination of Cl/Br ratios has important implications for various minerals that incorporate Br and Cl, such as apatite, amphibole, biotite, sodalite and scapolite. Scapolite group minerals may be excellent tracers for fluid sources since they are expected to mirror the CO_2, Cl and Br concentrations of the scapolite-forming fluids (Ellis, 1978; Pan and Dong, 2003). Scapolite and apatite are also strongly cathodoluminescent, and variations in CL intensity may reflect variations in Cl/Br ratio and thus fluid source. To demonstrate the potential of Cl and Br in scapolite as fluid tracers, I analysed scapolite in impure marble from the Eastern Mt. Lofty Ranges (Adelaide Fold Belt), South Australia. The studied marble occurs within the Milendella Mem- ber of the Cambrian Kanmantoo Group that mainly consists of silt- and sandstones (e.g. White, 1959; Kwak, 1977; Jago et al., 2003). Kwak (1977) suggested that scapolite in these rocks is a product of metamorphic fluids which evolved from evaporite-absent metamorphic rocks under greenschist/amphibolite facies metamorphism at a pressure of ~ 4–5 kbar. The protolith of the impure marble is limestone that was deposited at the height of a marine transgression during deposition of the 7–8 km thick sequence of turbiditic sediments of the Kanmantoo Group (Dyson et al., 1996; Preiss, 2000; Haines et al., 2001; Jago et al., 2003). There is no evidence of evaporitic horizons within this sedimentary sequence.

4.1.2. Results

Cathodoluminescence imaging of scapolite reveals a thin but distinct CL-bright rim surrounding a less luminescent core (Fig. 8). In a few cases, the rims are wide enough (>20 µm) to be analysed by LA-ICP-MS. The results show significantly lower molar Cl/Br ratios (~100–160) in the CL-bright rims compared to the CL-dark cores (Cl/Br = 257–300) (Fig. 8). I interpret these results to indicate that bittern brines (molar Cl/Br < 647) were present at the time of scapolite formation. The low Cl/Br of the scapolite rim indicates influx of an additional pulse of Br-enriched fluid at a relatively late stage, but prior to cessation of metamorphism. The lack of evaporative horizons within the stratigraphic sequence indicates that these bittern brine fluids are unlikely to be internally sourced. Rather, influx into the sedimentary package of externally-derived fluids must be considered, which I suggest may form the basis of fruitful research in the future (Chapter 2).

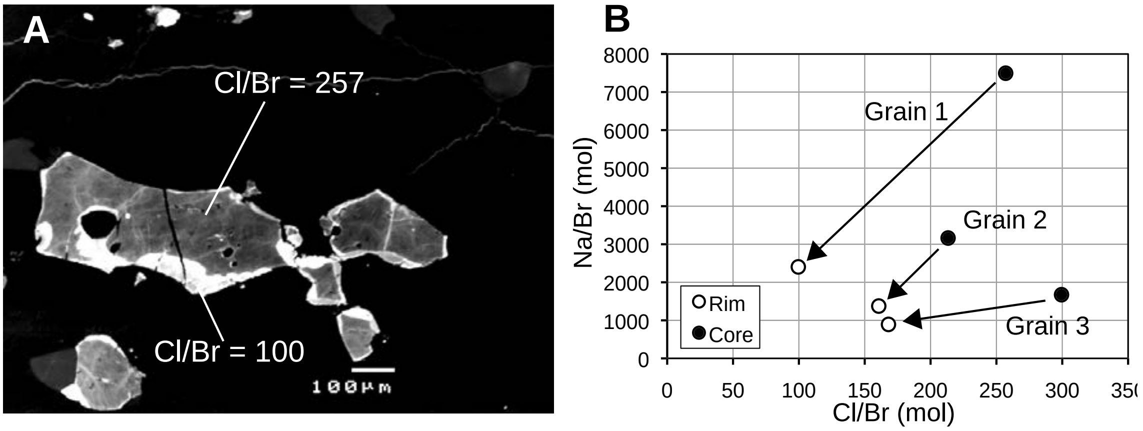

Fig. 8. A: Cathodoluminescence image of scapolite from a marble sample from the Eastern Mt. Lofty Ranges displaying bright rims with lower molar Cl/Br ratios than the darker core. B: Na/Br vs. Cl/Br ratios of scapolite from the Adelaide Fold Belt show an enrichment of Br in the rims.

4.2. Fluid inclusions

Fluid inclusions provide a direct source of information, on hydrothermal, sedimentary, and ore-forming fluids. Therefore fluid inclusions are of particular interest for understanding conditions and environments of ore formation. Here, I studied fluid inclusions hosted in sphalerite in samples from the Lucky Dog lead–zinc MVT deposit of the Tomahawk Creek subdistrict in Northern Arkansas (Viets et al., 1996; Wilkinson et al., 2009), the Coy Mine (Roedder, 1971; Viets et al., 1996), and the East Tennessee New Market Mine (Viets et al., 1996). Fluid inclusions in Lucky Dog sphalerite are primary and occur along growth zones and the average salinity based on microthermometry is ~ 22 wt.% NaCl equivalent (Table 3). Typically, these fluid inclusions appear dark in transmitted light, are equant in shape and range from 10 to 50 µm in diameter and contain 5–10 vol.% vapour and no daughter minerals were observed optically. However, LA-ICP-MS signals show that solids likely occur in some of the Lucky Dog fluid inclusions (see below). Coy Mine sphalerite contains scattered galena inclusions (~30 µm) and hosts fluid inclusions with sizes ranging from 15 to 30 µm in diameter with an average salinity determined by microthermometry of ~ 16 wt.% NaCl equivalent. These inclusions contain ~10 vol.% vapour and appear dark in transmitted light. No daughter minerals were observed. But as in Lucky Dog fluid inclusions, LA-ICP-MS signals suggest the presence of pyrite and galena in some of the fluid inclusions (see below). Fluid inclusions in East Tennessee New Market Mine sphalerite are 10 to 25 µm in diameter and appear black under transmitted light. Due to optical limitations, microthermometric measurements were conducted only on one fluid inclusion assemblage, giving ~ 23.6 wt.% NaCl equivalent. Total homogenization (*T*h(tot)) of all the measured inclusions occurred via bubble-point transition (liquid+vapour→liquid). Lucky Dog fluid inclusions homogenised between 113 and 121 °C, Coy Mine inclusions between 120 and 165 °C and fluid inclusions from the East Tennessee New Market Mine at ~150 °C (Table 3).

Table 3. Final ice melting temperatures (*T*fm(ice)) and total homogenisation temperatures (*T*h(tot)) via a bubble-point transition (liquid+vapour→liquid). The salinities (NaCl wt.% equivalent) are calculated according to Bodnar (1993).

Lucky Dog	T_{fm}(ice) ˚ C	T_h (tot) ˚ C	Salinity NaCl wt.% equi.
LD_1	-19.7	116	22.2
LD_3	-20.0	115	22.4
LD_4	-20.1	115	22.4
LD_12	-19.8	115	22.2
LD_13	-20.0	115	22.4
LD_15	-19.7	117	22.2
LD_16	-19.7	117	22.2
LD_17	-20.1	116	22.4
LD_18	-20.2	117	22.5
LD_19	-20.0	115	22.4
LD_20	-19.9	117	22.3
LD_21	-19.8	113	22.2
LD_23	-19.8	114	22.2
LD_24	-19.7	120	22.2
LD_25	-19.8	121	22.2
LD_26	-20.5	115	22.7
LD_27	-20.3	115	22.6
Average	-19.9	*116*	*22.3*
SD	0.2	*2*	*0.2*
Coy Mine			
CM_1	-11.9	125	15.9
CM_2	-11.7	122	15.7
CM_11	-11.5	165	15.5
CM_12	-11.2	121	15.2
CM_14	-11.9	120	15.9
CM_17	-12.3	141	16.2
CM_20	-12.5	132	16.4
CM_22	-11.9	129	15.9
Average	-11.9	*132*	*15.8*
SD	0.4	*15*	*0.4*

SD=Standard deviation

4.2.1. LA-ICP-MS measurements of fluid inclusions

Lucky Dog and East Tennessee New Market Mine sphalerite typically contain ~ 300–400 µg g^{-1} Fe, whereas Coy Mine sphalerite contains between 500 and 2000 µg g^{-1} Fe. All sphalerite samples have Pb contents of between 1 and 15 µg g^{-1}, and Mg, Mn and Cu contents of less than 10µg g^{-1}. Representative time-resolved LA-ICP-MS analysis signals of fluid inclusions in sphalerite are given in Fig. 9. The signal before and after the inclusion fluid was released is used to correct for contributions to the signal derived from the host mineral. Both Cl and Br are clearly quantifiable in all of the fluid inclusions analysed. While Cl and Br are clearly in the fluid phase, some of the LA-ICP-MS signals indicate that many of the inclusions contain Fe and Pb-bearing solids that are not always observed petrographically (Fig. 9b).

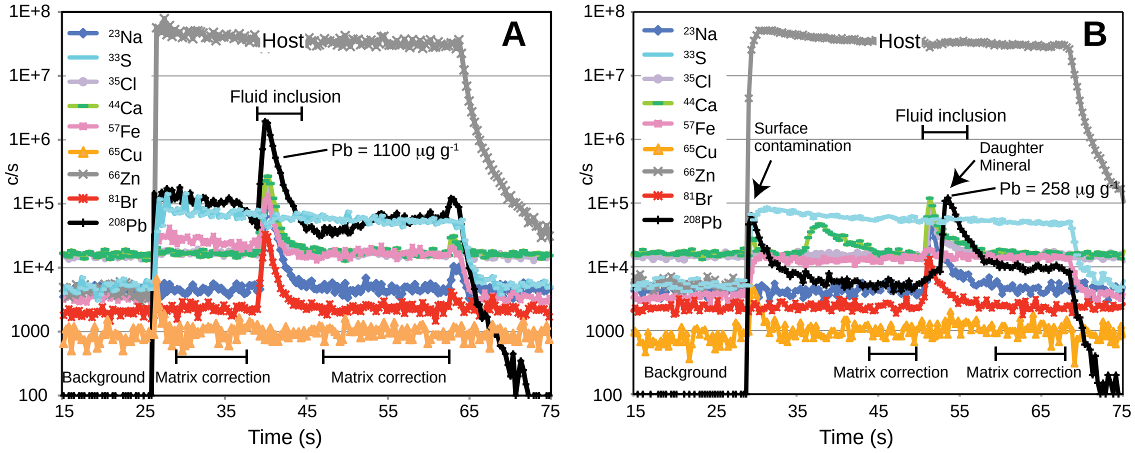

Fig. 9. Analytical signals of fluid inclusions hosted in sphalerite. The signal before and after the inclusion fluid was released was used for the matrix element correction. The sharp peaks in A suggest that all the components were present in the liquid phase while the late Pb peak in signal B is attributed to a Pb solid phase(s), most likely PbS. The S signal does not show a correlating with the Pb peak as the host (sphalerite) dominates the S signal.

4.2.2. Cl/Br quantification in fluid inclusions by LA-ICP-MS

Bromine and Cl concentrations in fluid inclusions in Lucky Dog sphalerite are very consistent. Most inclusions have Br contents between 600 and 700 μg g−1 (Tables 4, Appemdix A.1) and chlorine concentrations between 17 and 21 wt.% with an average of 20 wt.% Cl that results in an average molar Cl/Br ratio of 712±111 (2 sigma SD). Bromine concentrations in fluid inclusions from the Coy Mine sphalerite are much higher (2000–3200 μg g−1 Br) (Tables 4 and A.1) and Cl concentrations vary between 15 and 22 wt.% with two inclusions that show considerably higher Cl contents (~26.5 wt.%) that gives anaverage molar Cl/Br ratio of 170 ± 68 (2 sigma SD) (Table 4). Fluid inclusions hosted in East Tennessee New Market Mine sphalerite contain 2550–4600 μg g^{-1} Br while Cl contents are between 22 and 37 wt.% with the average molar Cl/Br ratio being 182 ± 60 (2 sigma SD) (Tables 4 and A.1). The high Cl content might be an artefact of deficient Na signal recording during analyses as too low internal standard intensities directly translate in overestimation of fluid inclusion element concentration (Pettke et al., 2012). It is also possible that salinities of fluid inclusions in the East Tennessee New Market Mine sample vary by a larger degree than that recorded by the limited number of microthermometry measurements. For the three samples the 2 sigma uncertainties for Cl/Br are more variable than the ~10% reproducibility of the standards. However, there is no systematic correlation between Br or Cl concentration and the crater aspect ratio (Fig. 10), suggesting that the variation in Cl/Br ratios is not significantly affected by this factor. Therefore, the Cl/Br variability in fluid inclusions most likely reflects real Cl/Br variations. Calculated NaCl wt.% from LA-ICP-MS measurements, with Na as the internal standard, agrees well with the NaCl wt.% equivalent calculated from microthermometry measurements for the very same individual fluid inclusions (see Appendix and Table A.2).

Table 4. Average molar ratios of crush and leach ion chromatography (IC) analyses and single fluid inclusions LA-ICP-MS measurements (this study). LD=Lucky Dog, CM=Coy Mine, ET= East Tennessee New Market Mine.

Sample	LA-ICP-MS Br (μg g^{-1})	LA-ICP-MS Cl (wt.%)	IC Na/Br [m]*	LA-ICP-MS Na/Br [m]	IC Cl/Br [m]	LA-ICP-MS Cl/Br [m]	IC Na/Cl [m]	LA-ICP-MS Na/Cl [m]	IC Ca/Mg [m]	LA-ICP-MS Ca/Mg [m]	IC K/Ca [m]	LA-ICP-MS K/Ca [m]
ET	3784 ± 1195	30.2 ± 9.1	95 ± 8	88 ± 34	206 ± 16	182 ± 60	0.46 ± 0.01	0.49 ± 0.16	5.56 ± 1.20	17.95 ± 3.33	0.19 ± 0.05	0.30 ± 0.06
CM	2577 ± 921	19.0 ± 6.7	95 ± 10	88 ± 42	209 ± 4	170 ± 68	0.46 ± 0.05	0.52 ± 0.18	2.19 ± 0.87	18.35 ± 6.48	0.47 ± 0.22	0.40 ± 0.18
LD	620 ± 157	19.5 ± 5.3	693 ± 112	499 ± 98	932 ± 112	712 ± 111	0.74 ± 0.04	0.70 ± 0.14	4.02 ± 1.04	6.13 ± 0.98	0.26 ± 0.06	0.15 ± 0.02

uncertainties represent 2 standard deviation

*molar ratio

Crush and leach ion chromatography (IC): ET (n=3), CM (n=5), LD (n=22); LA-ICP-MS: ET (n=13), CM (n=21), LD (n=23)

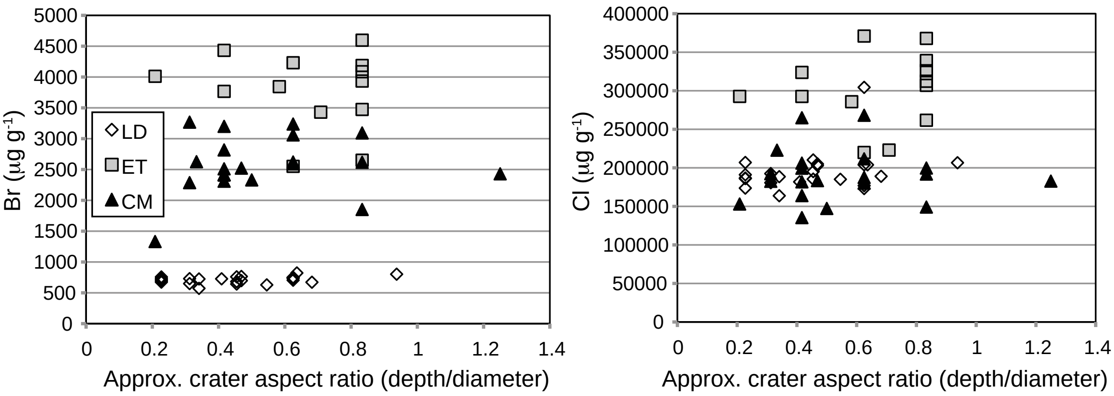

Fig. 10. Approximate crater aspect ratio (depth/diameter) of fluid inclusion analyses versus Cl and Br concentration (Table A1). LD = Lucky Dog, CM = Coy Mine, ET = East Tennessee New Market Mine.

4.2.3. Base-metal quantification in fluid inclusions

Lead concentrations in Lucky Dog fluid inclusions vary widely from < 1 to 400 μg g^{-1}; which is similar to the range reported by Wilkinson et al. (2009) for sphalerite-hosted fluid inclusions in the Northern Arkansas district (including Lucky Dog Mine) and sphalerite from the Midlands Basin orefield in Ireland. Fluid inclusions from the East Tennessee New Market Mine show similar levels (33 μg g^{-1} to 620 μg g^{-1} with one outlier of 1490 μg g^{-1}) while Coy Mine fluid inclusions show more variable Pb concentrations (< 0.2 to ~ 9000 μg g^{-1}). Manganese concentrations are generally low with Coy Mine inclusions containing the highest concentrations (up to 130 μg g^{-1} (Table A.1)). Copper concentrations vary considerably within the three samples. Lucky Dog fluid inclusions contain <1.6 to 135 µg g^{-1} Cu, Coy Mine fluid inclusions between < 7 and 250 µg g^{-1} and fluid inclusions from the East Tennessee New Market Mine contain < 22–974 µg g^{-1} Cu. Iron concentrations, if detectable are between 26 and 740 µg g^{-1} in Lucky Dog inclusion while Coy Mine and East Tennessee New Market Mine inclusions contain up to several 1000 µg g^{-1} Fe and some inclusions in the Coy Mine sample contain up to 3.3 wt.% Fe (Table A.1). Magnesium concentration is fairly uniform in all three samples and is usually between 1000 and ~2000 µg g^{-1}. Calcium varies in Lucky Dog inclusions between 1.7 and 3.2 wt.% while Coy Mine and East Tennessee New Market Mine inclusions show generally higher Ca values, 4.2–9.4 wt.% and 1.7–7.3 wt.%, respectively (Table A.1). The lowest K values are found in Lucky Dog inclusions (0.23–0.41 wt.%) while fluid inclusions from the other samples mostly contain K concentrations be- tween 1 and 2 wt.% (Table A.1). Fig. 11 shows that there is no significant correlation between Pb concentration and Cl/Br and between Pb and other base metals in solid-absent fluid inclusions. Final ice melting temperatures (*T*m) and *T*h(tot) are not correlated with any base metal concentrations or Cl/Br values.

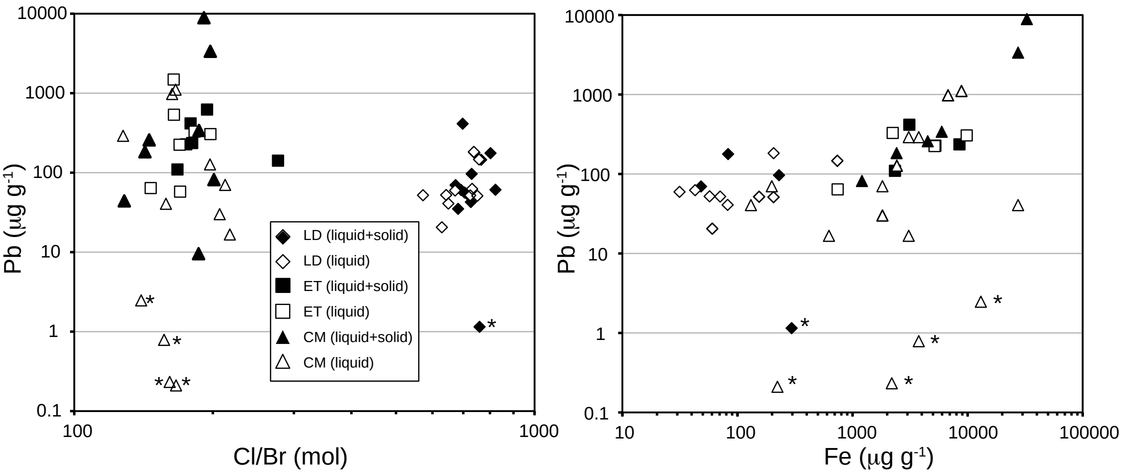

Fig. 11. Lead vs. molar Cl/Br ratios and Fe versus Pb concentration. Filled black symbols represent fluid inclusions that are interpreted to contain solid PbS minerals (see text and Fig. 9). Empty symbols stand for seemingly solids-absent fluid inclusions. * Analyses with Pb below LOD. For these analyses, we use the LOD, which represents maximum Pb contents. LD=Lucky Dog, CM=Coy Mine, ET=East Tennessee New Market Mine.

4.2.4. Comparison between crush and leach IC and LA-ICP-MS measurements

The average molar Na/Br ratio of single fluid inclusions determined by LA-ICP-MS analyses in the East Tennessee New Market Mine and Coy Mine samples is in good agreement with the bulk crush and leach ion chromatography analyses (Table 4, Fig. 12). Individual fluid inclusions also show similar molar Cl/Br ratios to those obtained by crush and leach (Table 4, Fig. 12). Likewise the average molar Na/Cl values of the individual fluid inclusions are all within 10% of those acquired by IC for all deposits (Table 4 and Fig. 12). In inclusions from Lucky Dog, molar Na/Br and Cl/Br values obtained by bulk crush and leach are higher than those acquired by LA-ICP-MS (Table 4, Fig. 12). Potassium-based interferences on the LA-ICP-MS Br signal can be ruled out as a reason for the lower LA-ICP-MS Cl/Br values because the fluid inclusions contain ≤2 wt.% K, which equates to a negligible correction of ~2 µg g^{-1} ^{81}Br. Furthermore, no correlation between the crater aspect ratios (depth/diameter) and Cl/Br ratios of fluid inclusions was observed (Fig. 10) which can explain lower Cl/Br ratios. As demonstrated above, Cl concentrations measured by LA-ICP-MS are consistent with EPMA values, especially when Cl concentrations exceed 10,000 µg g^{-1}. It is therefore unlikely that Cl concentrations were underestimated by LA-ICP-MS. Hence, the difference in Cl/Br ratios in the Lucky Dog sample might be explained by multiple generations of fluid inclusions that might not be present in every sphalerite grain. Barrie et al. (2009) demonstrated that sphalerite can incorporate significant amounts of Cl in its crystal structure. However, my analyses did not show any evidence of Cl concentrations in the sphalerite hosts. Nevertheless, at this stage it cannot be excluded that Cl concentrations in sphalerite are elevated locally, which may lead to higher Cl/Br ratios measured by the IC method. K/Ca and Ca/Mg ratios also vary significantly between the two methods, with Ca/Mg values determined by ion chromatography being significantly lower than LA-ICP-MS values (Table 4, Fig. 12). Mineral inclusions of dolomite within the sphalerite might affect the Mg and Ca numbers derived by crush and leach ion chromatography, whereas Ca and Mg contamination is not expected to affect in situ single fluid inclusion analyses by LA-ICP-MS.

4.2.5. Discussion of fluid sources

The major solutes in high salinity (>15 wt.%) basinal brines could be derived from residual brine formed by sub-aerial evaporation be- yond the point of halite saturation that infiltrated down into underlying sedimentary sequences or from the dissolution of evaporite minerals, primarily halite, in the subsurface. Solute ratios help discriminate between the two possible brine sources for modern basinal brines (Rittenhouse, 1967; Carpenter, 1978). Bromine is relatively incompatible in halite (Holser, 1979), so progressive seawater evaporation and halite deposition will evolve residual brine with progressively decreasing Cl/Br, Na/Br, and Na/K ratios, which can be plotted as evaporation arrays as shown in Fig. 12. Alternatively, if the fluid solutes are derived from the dissolution of halite, the Cl/Br and Na/Br ratios will systematically increase depending on the original fluid composition and the amount of halite dissolved. For example, if meteoric water dissolves pure NaCl containing about ~70 µg g^{-1} Br (Holser, 1979), the molar Cl/Br and Na/Br ratios will be ~20,000 and the Na/Cl ratio will be 1. Fluid compositions that represent both end-members, as well as mixtures of them, are recognized in modern sedimentary basins, but the primary source of salt in most basins – even those filled with salt – is residual brine (Moldovanyi and Walter, 1922; Carpenter, 1978; Kharaka et al., 1987; Walter et al., 1990; Hanor, 1994, 1997).

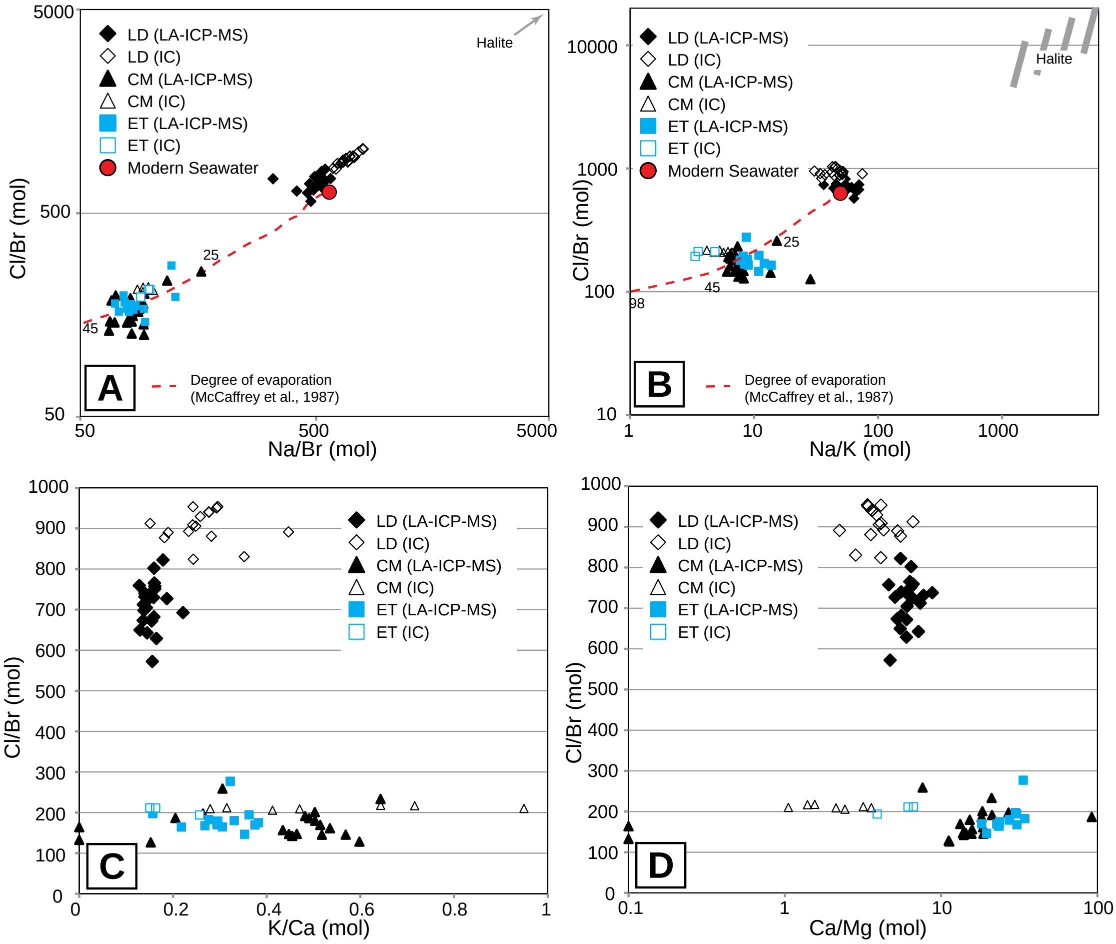

Fig. 12. A) + B) Molar Cl/Br vs. Na/Cl and Na/K ratio of crush and leach ion chromatography (IC) and LA-ICP-MS. The halite data and the simplified evaporation curve are taken from McCaffrey et al. (1987) and modern seawater composition from Mottl and Holland (1978). C)+D) Molar Cl/^{81}Br ratios vs. molar K/Ca, Ca/Mg ratios, respectively, in individual fluid inclusions analysed by LA-ICP-MS are shown as diamonds, squares and triangles and bulk crush and leach analyses are shown as empty symbols. LD=Lucky Dog, CM=Coy Mine, ET=East Tennessee New Market Mine.

Understanding of modern sedimentary brine systems has been fundamental to the interpretation of MVT fluid inclusion data. The majority of data from the world's MVT deposits plot in a relatively small compositional field near the seawater evaporation line suggesting that the primary salinity source for fluids that formed MVT deposits was dominantly evaporatively-concentrated seawater. Only a few deposits show evidence for halite dissolution as a primary source for the parent fluid and thus residual brines are considered fundamental to the genesis of MVT deposits (e.g. Kesler et al., 1995; Stoffell et al., 2008; Appold and Wenz, 2011). However, a contribution of organically derived Br has recently been identified in other Pb–Zn deposits as a reason for decreased Cl/Br rather than purely evaporitic processes (Kendrick et al., 2011). Here, we cannot exclude an organic Br input but as Cl/Br and major elements follow the seawater evaporation line reasonably well, we consider the organic Br component as a minor fraction if present.

In this study, both LA-ICP-MS and IC data indicate that the compositions of fluid inclusions in the Coy Mine and East Tennessee New Market Mine samples are highly evaporated seawater (Fig. 12). The Lucky Dog sphalerite, however, has Cl/Br ratios greater than seawater indicating that halite dissolution had contributed to the halogen budget of the mineralizing fluid. The concentrations of Pb, Cu, and Fe in fluid inclusions from all deposits vary widely. Lead values, for example, vary over five orders of magnitude in Coy Mine and East Tennessee New Market Mine samples. In contrast, Mn values are generally low and do not show the extent of variability of the other base metals. The LA-ICP-MS peak intensity versus time profiles (e.g., Fig. 9b) and peak shapes imply that many inclusions with high metal values contained mineral inclusions including pyrite or galena (Figs. 9b, 11; Supplementary Table A.1). These minerals likely represent solids that were accidentally trapped in the inclusions during inclusion sealing by the host mineral and were present in the fluid prior fluid entrapment, or represent crystallites on mineral surfaces around which fluid inclusions formed with progressive mineral growth. I argue that solids do not represent daughter minerals as Pb concentrations vary over several magnitudes that make it unlikely that daughter minerals precipitated from a homogenous fluid upon P and T decrease. Even so, some of the highest measured Pb concentrations are in inclusions where accidentally trapped solids are not obvious and the LA-ICP-MS signals show no evidence of solid phases (Fig. 9a) so that the Pb appears to be giving the appearance that Pb is dissolved within the fluid. Yet, Pb concentrations in seemingly solid-absent fluid inclusions do not correlate with other element concentrations (Fig. 11) or elemental ratios (Fig. 13) while base metals in fluid inclusions with suspected solids correlate positively with each other (Fig. 11).

Recognition of high Pb values in MVT sphalerite fluid inclusions has been the subject of recent interest (e.g. Klemm et al., 2004; Stoffell et al., 2008; Wilkinson et al., 2009; Appold and Wenz, 2011). The range and variability of concentrations of Pb and other base metals reported in these studies are similar to those reported here. Appold and Wenz (2011) discussed the difficulties involved in generating and maintaining Pb-rich fluids in sphalerite-saturated brine because of the low solubility of galena. This has led to the proposal that fluid mixing might explain these Pb enriched fluids in MVT deposits (e.g. Klemm et al., 2004; Stoffell et al., 2008; Appold and Wenz, 2011). In fact, the broad range of Pb concentration within single samples is interpreted to support the mixing of oxidized Pb rich ore fluid with a second fluid rich in dissolved S species (Appold and Wenz, 2011). Moreover, metal contents in sphalerite hosted inclusions are reported to be several orders of magnitude greater than those hosted in ore-related quartz and dolomite, which is interpreted to be due to periodic influx of anomalously metal-rich fluids into systems otherwise dominated by barren fluids (Wilkinson et al., 2009). Such processes may be critical to ore formation in MVT deposits.

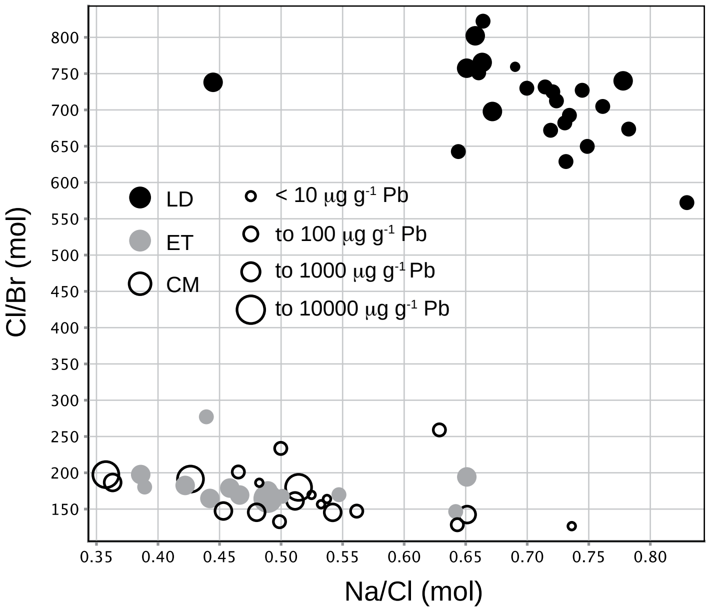

Fig. 13. Molar Cl/Br ratios vs. molar Na/Cl ratios of individual fluid inclusions analysed by LA-ICP-MS. The size of symbols denotes the Pb concentration of the fluid inclusions. LD = Lucky Dog, CM = Coy Mine, ET = East Tennessee New Market Mine.

Fluid mixing is often invoked to be an overarching control on ore deposition (cf. Leach et al., 2010); a claim that is supported by fluid inclusion studies that document the presence of several fluid types within single minerals (e.g. Klemm et al., 2004). By contrast, the *T*h(tot), *T*m(ice), and major solute composition of fluid inclusions are strikingly similar within the samples examined here and by Viets et al. (1996). We also do not observe variable Cl/Br ratios in individual sam- ples or a Cl/Br correlation with Pb (Fig. 13) or other metal concentra- tions. However, the occurrence of entrapped solids in a few samples from our study demonstrates clear evidence for the accidental entrap- ment of galena and other ore phases. In total, these features suggest that fluid inclusions in sphalerite examined here are samples of (post)-mixing fluids, and not premixing "endmember" fluids. It is interesting to note that samples with high Pb levels and sharp peaks (thus no evidence of fluid inclusion hosted solids; e.g. Fig. 9a) are more common in sphalerite that contain scattered micro-inclusions of galena. Togeth- er, these observations raise the possibility of the entrapment of Pb-rich metastable solid phases or fine metal-sulphide colloids at a scale finer than resolvable with current technology formed in the ore zone and heterogeneously trapped in the inclusions. It this case, we cannot ascribe the high Pb contents found in some of the fluid inclusion to be solely due to Pb dissolved in the fluid phase. It is also significant that the concentrations of trace elements that do not form sulphides such as Mn, Mg and Ba are relatively homogeneous within samples. Taken together our results suggest that the very high metal values measured in sphalerite may be more reflective of processes of ore deposition than the original metal concentration of the ore fluid. While these results are inconclusive, our new method demonstrates a new tool that may ultimately answer these important questions in the formation of MVT deposits.

5. Conclusions

I have tested the potential of in situ LA-ICP-MS analyses of Br and Cl in minerals and fluid inclusions. The results show that with minor modifications on the LA-ICP-MS set-up, Cl and Br can be successfully measured with a high accuracy and precision. Analytical results obtained by bulk crush and leach IC (fluid inclusions), EPMA, INAA, and the Noble Gas Method (minerals) compare well with results obtained by single LA-ICP-MS measurements, even using laser spot diameters as small as 24 µm. However, when Br is measured in K-bearing phases, corrections due to polyatomic interferences on the Br signal are required. Furthermore, an unknown positive signal 79 (^{79}Br) upon material ablation is always present. For this reason we suggest to use ^{81}Br values rather than ^{79}Br. Intra ele- ment fractionation of Br and Cl has to be considered and assessed when drilling deep ablation pits with small spot-sizes.

By analysing Cl and Br together with a list of elements in fluid inclusions by LA-ICP-MS, we demonstrated the advantage of individual fluid inclusion analyses over bulk inclusion methods. In the case of fluid inclusions hosted in sphalerite from different MVT deposits, fluid inclusions with accidentally trapped minerals reflect samples of heterogeneous (post)-mixing fluid that was present at the time of sphalerite formation.

In combination with micro-imaging techniques (e.g. CL), mineral zoning and related Cl/Br variations can be resolved on a sub-mineral scale in halogen-bearing minerals. This capability has huge potential to resolve fluid evolution and fluid origin in complex igneous, metamorphic, and hydrothermal systems.

Chapter 2

Cl/Br of scapolite as a fluid tracer in the earth's crust: insights into fluid sources in the Mary Kathleen Fold Belt, Mt. Isa Inlier, Australia

Published in *Journal of Metamorphic Geology*

Abstract

A combination of analytical methods, including trace element analysis of Br in scapolite by LA-ICP- MS, was employed to unravel the fluid–rock interaction history of the Mary Kathleen Fold Belt of northern Australia. Halogen ratios in the metamorphic and hydrothermally derived scapolite from a range of rock-types record interaction between the host rocks and magmatic-hydrothermal fluids derived from granite plutons and regional metamorphism. The results show that halite-dissolution supplied at best only minor chlorine to fluids in the Fold Belt. Chlorine/bromine ratios in metamorphic scapolite indicate that fluids were dominantly derived from basinal brines formed from sub-aerial evaporation of seawater beyond the point of halite saturation. This bittern fluid infiltrated the underlying sedimentary sequences prior to regional metamorphism. Zoned scapolite in a major late meta- morphic mineralized shear-zone records three discrete pulses of magmatic and metamorphic fluid, and it is suggested that fluid mixing may have assisted mineralization along and around this shear-zone. As a crucial prerequisite for halogen fluid tracer studies using scapolite, we find in our samples that Cl and Br do not fractionate when incorporated in scapolite. Furthermore, unaltered rims of heavily retrogressed scapolite show indistinguishable Cl/Br signatures compared with fresh grains from the same sample indicating retrograde metamorphism did not significantly affect Cl and Br signatures in scapolite group minerals.

1. Introduction

Studies of the composition and origin of fluids in the Earth's crust are critical to understanding many geological processes, including mass and heat transfer, metamorphism, alteration and the formation of hydrothermal ore deposits. The composition and origin of geological fluids can be determined through the analysis of halogens in fluid inclusions and in minerals (e.g. Banks & Yardley, 1992; Bo€hlke & Irwin, 1992; Yardley et al., 1993; Irwin & Roedder, 1995; Banks et al., 2000a,b; Kendrick et al., 2001, 2008; Nahnybida et al., 2009; Hammerli et al., 2013). For example, biotite can be used for HCl/HF estimates in hydrothermal fluids (e.g. Munoz & Swenson, 1981), Cl contents in amphibole have been used to explain fluid–rock interaction processes during metamorphic cycles (e.g. Xiao et al., 2005), and apatite has been used to trace OH, F and Cl of hydrothermal and magmatic systems (e.g. Boudreau et al., 1993; Brenan, 1994). Scapolite group minerals have also been used to constrain Cl and CO_2 compositions and origins of coexisting fluids (e.g. Ramsay & Davidson, 1970; Kwak, 1977; Moecher & Essene, 1991; Oliver et al., 1992; Cartwright & Oliver, 1994; Pan et al., 1994; Jiang et al., 1994; Moecher et al., 1994; Faryad, 2002; Pan & Dong, 2003; Satish-Kumar et al., 2006).

In addition, Cl/Br ratios of scapolite are potentially powerful fluid tracers, as scapolite Cl/Br ratios are likely to mirror the Cl/Br ratio present in the coexisting fluid at the time of scapolite formation (Pan & Dong, 2003) and Cl/Br ratios are distinct for different fluid sources(e.g. Böhlke & Irwin, 1992). Furthermore, scapolite occurs in a range of bulk rock compositions, and at a wide range of metamorphic, hydrothermal and igneous conditions (e.g. Shaw, 1960a,b; Orville, 1975; Kwak, 1977; Goff et al., 1982; Pan et al., 1994; Satish-Kumar et al., 2006) that makes it in particular useful for fluid source tracking. Nevertheless, except for Pan & Dong (2003) no other studies have applied Cl/Br ratios in scapolite as a fluid tracer. One of the reasons is the difficulty of Br quantification, as it cannot easily be measured by routine analytical methods such as electron probe microanalysis (EPMA). However, recent technique developments now allow Br and Cl quantification by LA-ICP-MS, with detection limits for Cl and Br of ~500 and ~8 $\mu g\ g^{-1}$ respectively (Seo et al., 2011; Hammerli et al., 2013). An additional advantage of LA-ICP-MS is that scapolite grains can be measured in situ at the micrometre scale, and a range of other trace elements can be simultaneously obtained.

In this study, I examine the relationships between Cl and Br contents and the mineral chemistry of scapolite to assess whether scapolite Cl/Br ratios reflect fluid Cl/Br ratios, as suggested by Pan & Dong (2003). Cathodoluminescence (CL)-imaging is combined with EPMA and in situ LA-ICP-MS analyses of Cl and Br, together with other trace elements. The potential of scapolite geochemistry for elucidating hydrothermal processes is demonstrated by investigating regional metamorphic and metasomatic scapolite from the Mary Kathleen Fold Belt (MKFB) of the

Mount Isa Region, Australia. This region has undergone a complex and protracted hydrothermal history (Oliver, 1995), is host to significant Cu, U and REE mineralization, and is one of the most extensive scapolite-bearing districts worldwide. Despite extensive previous study, many geological aspects of the region remain unresolved, such as sources of the fluids that led to the widespread skarn formation (Cartwright & Oliver, 1992; Oliver et al., 1994), the source of the Cu-U-REE mineralizing fluid(s) (Oliver et al., 1999), and the nature and patterns of fluid flow during regional metamorphism.

2. Halogens in scapolite group minerals

The scapolite formula is best described by $M_4(T_{12}O_{24})A$, where M represents Na, K, Ca, Sr, Ba and Fe^{2+}, T represents Si, Al and Fe^{3+}, and A stands for Cl, CO_3, SO_4 or Br. Minerals of the scapolite group generally fall into the simplified non-linear solid-solution between marialite $Na_4(Al_3Si_9O_{24})Cl$ and meionite $Ca_4(Al_6Si_6O_{24})CO_3$ (Sokolova & Hawthorne, 2008), although there can be significant substitution of Na for K, Sr and/or Ba for Ca, Fe^{3+} for Al, Br and/or OH for Cl and SO_4 for CO_3. Compositions of natural scapolite is commonly expressed as meionite equivalent% (Me% = 100 [∑(divalent cations/4)], where high meionite numbers generally correlate with increased CO_2 and/or S contents, while low meionite numbers typically reflect high Cl contents (e.g. Teertstra & Sherriff, 1997).

Scapolite chemistry on the A site (Cl, CO_3, Br, SO_4 and H_2O) is influenced by the following: (i) fluid compositions; (ii) site occupancy and charge balance issues arising from Ca–Na–Al coupled substitutions; and (iii) P–T conditions and coexisting minerals (Haughton, 1971; Orville, 1975; Ellis, 1978; Kwak, 1977; Moecher & Essene, 1991; Teertstra & Sherriff, 1997; Sokolova & Hawthorne, 2008). Information about fluid chemistry can be obtained for a given P–T and mineral assemblage if the effects of site occupancy and solid solution can be isolated from potential controls of the fluid chemistry such as quantitative calculations of the salt content of the coexisting fluids (Ellis, 1978; Oliver et al., 1992).

3. Geological Background

The MKFB is part of the Proterozoic Mt Isa inlier of Queensland, Australia, and consists of metasiltstone, metaquartzite, calc silicate rock and marble of the Corella formation (e.g. Matheson & Searl, 1956; Oliver et al., 1994) intruded by the 1740–1730 Ma Lunch Creek Gabbro and Burstall Granite (Page, 1983). There are three major phases of hydrothermal activity: (A) early syn-intrusive contact metasomatism (Domain A, Fig. 1); (B) regional metamorphism, including circulation of saline fluids (Domain B, Fig. 1); and (C) infiltration of mineralizing fluids during late-stage shearing (Domain C, Fig. 1). The abandoned Mary Kathleen U and REE mine and several Cu-, Au-, U- and REE-prospects, including the Elaine Dorothy prospects south of the Mary Kathleen mine (Fig. 1), are evidence that some of the fluids transported significant quantities of Cu, Au, U and REE.

Intrusion of the Burstall Granite at 1740–1730 Ma (Page, 1983) is thought to have resulted in banded and massive garnet–clinopyroxene skarns (e.g. Matheson & Searl, 1956) that partially replace and cut many of the calcareous rock types proximal to the granite (Domain A, Fig. 1). The current outcrop pattern supports the interpretation of skarn formation via fluids derived from the upper surface of the Burstall Granite, although it is considered to be too small to produce the amount of fluid needed for the observed widespread skarn development (Cartwright & Oliver, 1994). Therefore, it is possible that the more extensive Wonga Batholith (c. 1780–1740 Ma; Neumann et al., 2009) residing at deeper crustal levels contributed fluids to hydrothermal systems (Oliver et al., 1994). Due to structural partitioning, regional metamorphism did not recrystallize earlier metasomatic rocks in close proximity to the granite. Hence, scapolite close to the Burstall Granite occurs in radial acicular needles in skarn layers (Fig. 2) or as veins and irregular blebs in felsic dykes. These scapolite assemblages likely formed during contact metamorphism. The large-scale fluid flow direction and fluid sources for skarn formation are not yet resolved with certainty, although Cartwright & Oliver (1992, 1994) and Oliver et al. (1994) used oxygen isotope and mineralogical data to formulate a model involving both skarn-forming fluids emanating directly from granites, and a component of up-temperature fluid flow that operated during the peak of contact metamorphism. Cartwright & Oliver (1992, 1994) constrained the fluid composition to be aqueous with relatively low mol.% of CO_2 ranging from 0.05 in distal rocks to ~0.12 proximal to the Burstall Granite

Low-P (3–4 kbar) amphibolite facies metamorphism occurred at c. 1580 Ma (Rubenach et al., 2008) and is preserved within Domain B (Fig. 1). This event included major deformation phases that produced N–S trending tight to isoclinal folds and local refolding, as well as localized shearing, including the development of the Mary Kathleen Shear-zone adjacent to the U-REE orebody (e.g. Holcombe et al., 1991; Oliver et al., 1999). Fluid flow during regional metamorphism was focused and structurally controlled rather than pervasive (Oliver & Wall, 1987). At 100 m to 20 km scales, lozenge-shaped bodies of pre-regional metamorphic intrusive and contact metamorphic rocks (Fig. 1) show moderate to excellent internal preservation of features related to the intrusion, such as magmatic textures, contact metamorphic assemblages and weak deformation. These bodies are surrounded by deformed rocks that experienced minimal contact metamorphism prior to later regional metamorphism (Oliver et al., 1990; Oliver, 1995). Moreover, regional metamorphic temperatures did not exceed those of contact metamorphism in rocks close to the Burstall Granite

(Cartwright & Oliver, 1994). Oliver et al. (1992) examined regionally metamorphosed scapolite-bearing rocks (that were unaffected by contact metamorphism) from the northern MKFB (samples CFM) some 30 km north of the Mary Kathleen Syncline (MKS) (Domain B, Fig. 1). The variable distribution of scapolite modes and chemistry in these rocks, as well as variations on a mm- and outcrop scale in fluid *X*NaCl, *X*CO_2, *X*HCl and *X*FeCl/MgCl determined from scapolite, amphibole and biotite were interpreted as a close reflection of halite–calcite ratios in the original pre-metamorphic sedimentary rock, consistent with the chemistry of the fluid having been rock-buffered during regional metamorphism (Oliver et al., 1992).

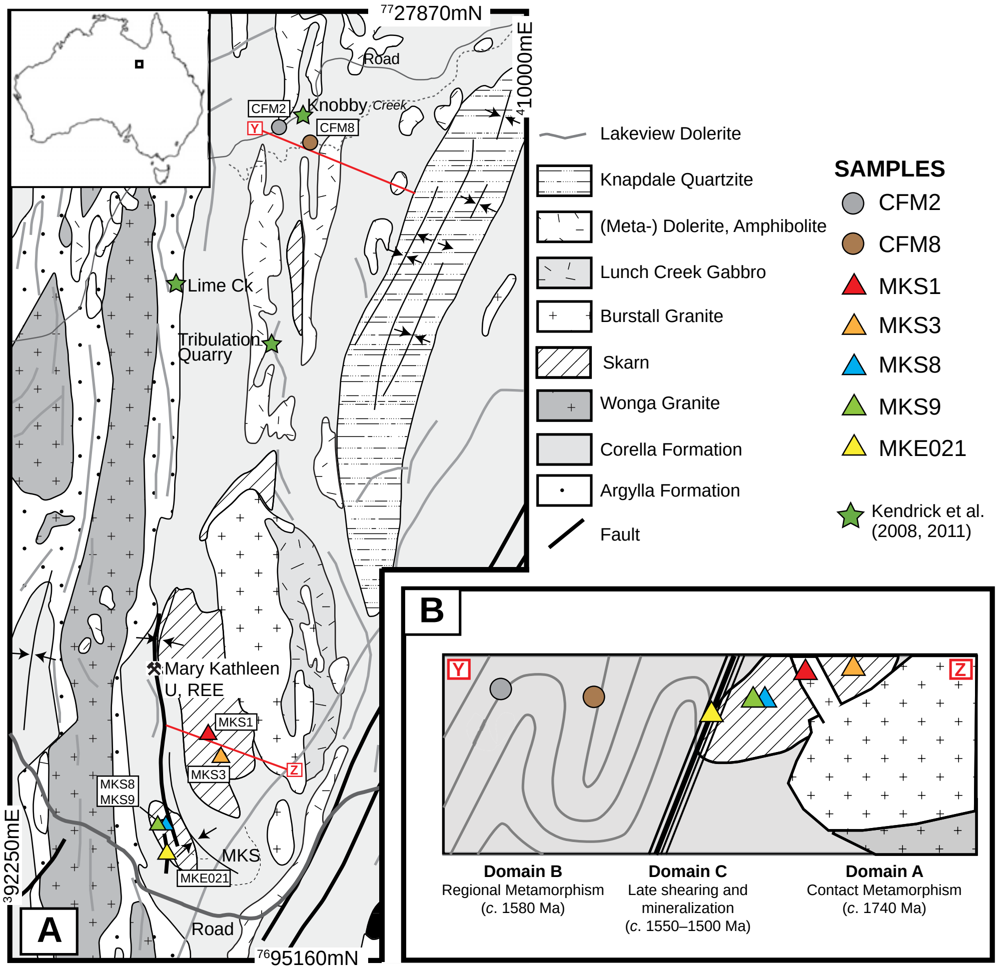

Fig. 1. (a) Sample location in the Mary Kathleen Fold Belt and location of the abandoned U-REE mine (modified after Oliver et al., 1999). Green star symbols show the locations of fluid inclusion samples studied by Kendrick et al. (2008, 2011). (b) Schematic cross-section Y-Z with interpolated sample locations. Domain A represents dominantly contact metamorphic scapolite, Domain B represents regional metamorphic scapolite, while Domain C represents scapolite from late-stage regional metamorphic shear-zones.

Late-stage shearing and associated Au, Cu, REE mineralization (c. 1525 Ma; Sha, 2013) in the Elaine Dorothy District (Fig. 1; MKE021) represent the final stage of hydrothermal activity in the study area (Domain C). Fluid inclusion data of such late hydrothermal activity suggest that the mineralizing fluid had a magmatic component, which likely was related to A-type granite emplacement (Kendrick et al., 2011).

4. Scapolite samples from the MKFB

A series of samples were collected that represent the three main scapolite associations and ages (Fig. 1). The samples of the first contact metamorphic phase at c. 1740 Ma (metasomatic Domain A; Fig. 1) include scapolite–garnet–quartz veins (MKS1) in Burstall Granite dykes, banded skarns of garnet, clinopyroxene, scapolite with or without K-feldspar (MKS3), scapolitite (i.e. a rock composed of >90% of scapolite) formed by replacement of gabbro (MKS8) and adjacent scapolite-bearing amphibolite (MKS9). Scapolitites are most likely a product of extensive gabbro alteration as gabbro fragments within scapolitites are observed in the field. All of these samples are from the MKS (Fig. 1) and have previously been described by Oliver et al. (1994, 1999). The scapolite-bearing metasedimentary rocks (Domain B) were collected from north of the MKS from the same localities as samples described in Oliver et al. (1992) (Fig. 1, labelled CFM). In contrast to the samples from the MKS, some samples of metamorphic rocks from the northern MKFB have scapolite porphyroblasts aligned within and locally cross-cutting the 1580 Ma regional metamorphic foliations. These were considered by Oliver et al. (1992) to be unrelated to pre-regional metamorphic intrusions. Scapolite, biotite and apatite from the biotite-rich Mary Kathleen shear-zone (MKE021; Domain C; Figs 1 & 2) associated with Elaine Dorothy U-REE-Cu prospect (Sha, 2013) were also studied to gain information about fluid compositions late in the Isan Orogeny, at a time of U-REE-Cu mineralization.

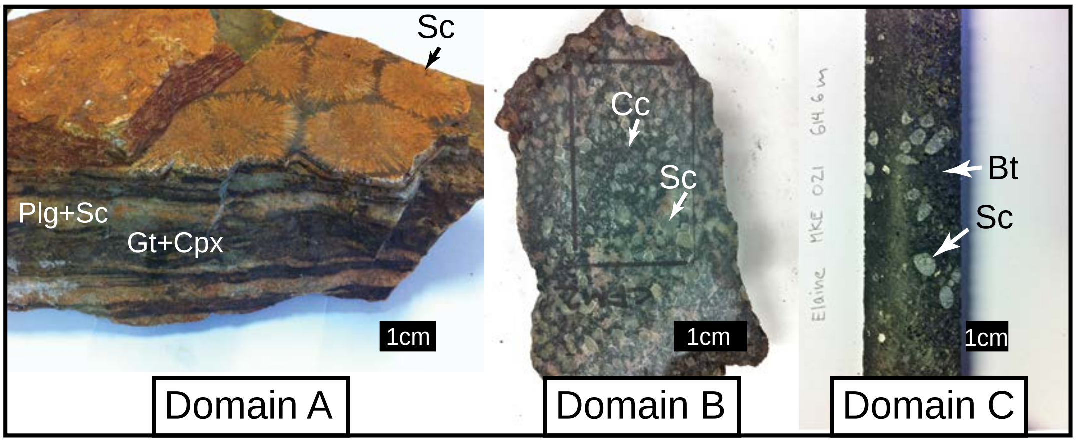

Fig. 2. Domain A scapolite in skarns is layer bound (albite and scapolite) and exhibits radial or oblate sprays of crystals (arrowed). Domain B scapolite occurs in metamorphosed impure, carbonate-rich calc silicate rocks (see mineralogy in Table 3) as scattered porphyroblasts. Scapolite in the shear-zone sample (Domain C) is hosted in a biotite matrix; the precursor rock may have been amphibolite.

5. Methods

5.1 Electron probe microanalysis

Quantitative major element analysis of scapolite, biotite, apatite and amphibole was carried out using a JEOL JXA 8200 superprobe in WDS mode, with 15 kV acceleration voltage and a 5 μm beam with 20 nA beam current, housed at the Advanced Analytical Centre, James Cook University (JCU). A defocused beam of 5 lm was used to avoid potential diffusion of Na and Cl by the beam. This technique was verified by our previous study (Hammerli et al., 2013). Counting times were 20 s on peak and 10 s on background for each element. The data were processed using the φqz method for matrix correction (Armstrong, 1991) and standardized against a set of well-characterized, in-house oxide (hematite), silicate (albite, almandine, orthoclase, wollastonite, olivine), sulphate (barite) and tugtupite (chlorine) standards.

5. 2 Cathodoluminescence imaging

Cathodoluminescence imaging was carried out at the Advanced Analytical Centre, JCU on carbon-coated polished thin sections using a JEOL JSM5410LV SEM and a Robinson CL detector and photomultiplier. By covering the spectral range of 310–650 nm, the photomultiplier is more sensitive in gathering light in the blue to ultraviolet range than in the red to infrared range. Instrument operating conditions were set to an accelerating voltage of 20 kV and a beam current of ~10 nA.

5.3 LA-ICP-MS

All LA-ICP-MS analyses were conducted using a Varian 820 quadrupole ICP-MS coupled with a GeoLas Pro 193 nm ArF Excimer laser system from Lambda Physik, at the AAC, JCU. Ablation was conducted in a He atmosphere and the ICP-MS was tuned to ensure robust plasma conditions (sensitivity of Th ≈ U ≈ Pb) (e.g. Pettke et al., 2012) and low oxide production levels (<0.5% ThO). Prior to each analytical session the ICP-MS cones were cleaned and a dedicated set of Teflon-lined sample tubing was installed. Analyses of scapolite were carried out on polished 100 lm thick sections, using a laser energy density of 6 J cm^{-2} and repetition rates of 5–10 Hz. The beam diameter varied between 44 and 120 μm. The following elements were analysed (typical detection limits for each element are in parentheses in μg g^{-1} for a 90 μm spot size): ^{23}Na (30), ^{25}Mg (1.4), ^{27}Al (1), ^{29}Si (365), ^{33}S (50), ^{35}Cl (230), ^{39}K (8), ^{43}Ca (91), ^{55}Mn (0.1) ^{57}Fe (5), ^{65}Cu (0.3), ^{66}Zn (0.3), ^{81}Br (8.5), ^{85}Rb (0.01), ^{88}Sr (0.04), ^{89}Y (0.05), ^{93}Nb (0.05), ^{133}Cs (0.01), ^{137}Ba (0.01),

^{139}La (0.01), ^{140}Ce (0.01), ^{141}Pr (0.01), ^{146}Nd (0.02), ^{147}Sm (0.03), ^{153}Eu (0.03), ^{157}Gd (0.03), ^{163}Dy (0.05), ^{165}Ho (0.04), ^{167}Er (0.04), ^{171}Yb (0.04), ^{175}Lu (0.05), ^{208}Pb (0.005), ^{232}Th (0.001), ^{238}U (0.001). Scapolite standard BB1 (Kendrick, 2012; Hammerli et al., 2013) was used for Na, Al, Si, S, Cl, K, Ca, Fe and Br data reduction with the same set-up as described in Hammerli et al. (2013). We used the revised Br concentrations of BB1 of Kendrick et al. (2013) which are ~19% lower than previously reported (Kendrick, 2012). Hammerli et al. (2013) compared Br and Cl quantification by LA-ICP-MS with various other methods using the standards (SY, BB1 and BB2) described in Kendrick (2012). Measured Cl/Br shows an internal consistency for these standards, whereas Cl/Br ratios of fluid inclusions determined by LA-ICP-MS were ~20% too low compared to ion chromatography (see Hammerli et al., 2013 for more details). Hence, the new Br values from Kendrick et al. (2013) result in an excellent agreement between the LA-ICP-MS and fluid inclusion ion chromatography data. All other analysed elements were standardized using NIST612 and NIST610 glass reference materials with values from Spandler et al. (2011) and were reduced via the software package 'Glitter' (Griffin et al., 2008).

6. Results

6.1 Mineralogy and CL-textures in scapolite of the MKFB

Domain A

Scapolite in garnet–scapolite veins in the Burstall Granite (MKS1, Fig. 1) is xenomorphic, unaltered and shows no CL-zoning. Scapolite in banded skarns (MKS3) occurs in plagioclase-rich layers (~1 mm– 1 cm) that alternate with green-brownish garnet– pyroxene layers (~1–5 mm) (Fig. 2, Table 1), and lacks any distinct CL-zoning. K-feldspar is less common than plagioclase and is commonly absent in plagioclase–scapolite layers. The scapolitized gabbro sample (MKS8) contains ~90% scapolite with distinct CL zoning (Fig. 3c) with only minor amounts of K-feldspar and albite (Table 1). The CL-weakly luminescent inner scapolite zones are interpreted to be relict cores with higher calcic contents than the intermediate and bright areas (Table 2). The adjacent amphibolite sample MKS9 has minor scapolite (Table 1) without distinct CL zoning despite variable luminescence between individual grains. Calcic amphibole (possibly hastingsite, Oliver et al., 1992) is the most abundant mineral (~70%), while clinopyroxene (~10 modal %) occurs as relicts within calcic amphibole. K-feldspar (microcline) is rare and occurs in pockets between amphibole grains, commonly close to scapolite.

Domain B

The regional metamorphic sample CFM2 (Fig. 1) contains idiomorphic, poikiloblastic scapolite with quartz, calcite and titanite inclusions (Figs 2 & 3b). In some cases, the CL-images reveal patchy textures in scapolite but the differences between weakly luminescent and CL-bright zones are not as clear as in the Domain A samples and there are no significant compositional differences (Fig. 3; Table 2). Sample CFM8 (Fig. 1) contains xenomorphic scapolite grains that are most prominent within K-feldspar and calcite-rich layers, but they are also present in the calcic amphibole-rich layers. Scapolite grains show little variation in CL-intensity other than thin (<10 μm) CL-bright rims (Fig. 3a).

Domain C

Scapolite from the late metamorphic biotite shear- zone (MKE021) is present as large (up to 10 mm), unaltered idiomorphic grains surrounded by biotite (Fig. 2). CL imaging reveals three distinct zones in some grains (Fig. 3d): the core zone (Zone 1); a thin dark zone mantling the core (Zone 2); and a brighter outer rim (Zone 3). Also present is heavily retrogressed scapolite with well-preserved outer rim zones and cores zones that have reacted to calcite, biotite, quartz and K-feldspar. Comparatively large (up to 1 mm) apatite grains occur in minor amounts, and often contain a CL-bright core and one or two distinct rim zones. K-feldspar is only present as a minor phase.

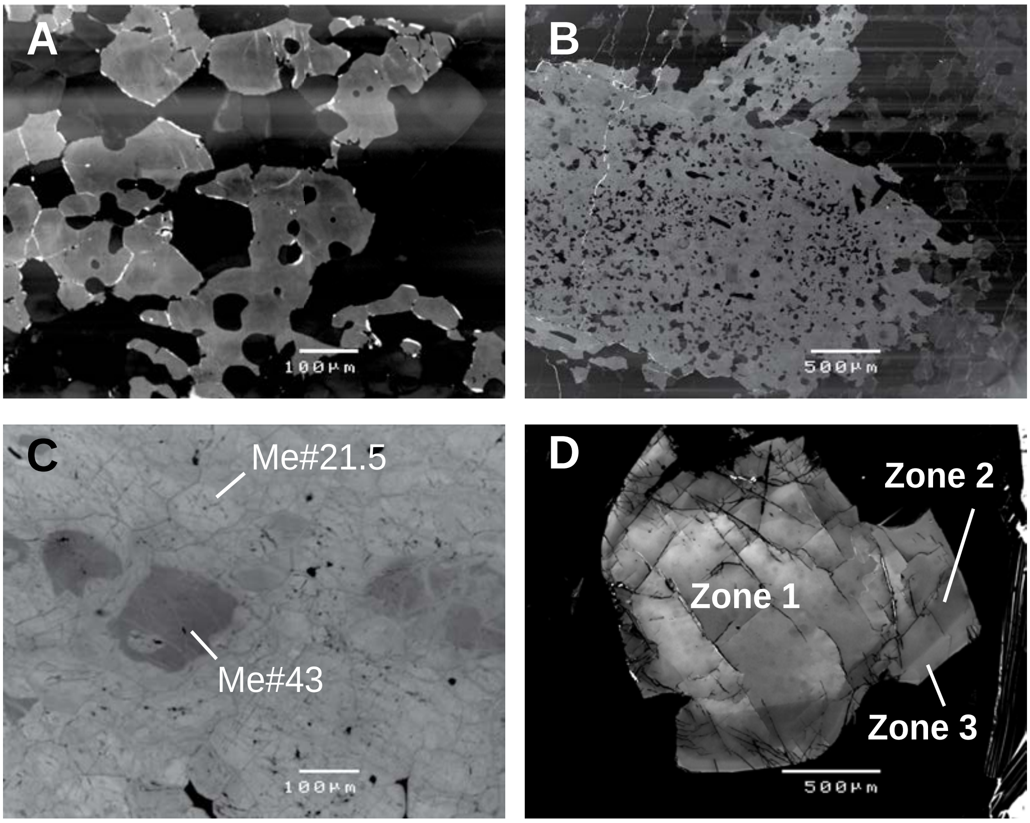

Fig. 3. Cathodoluminescence (CL) images of scapolite grains from Domains A and B. (a) Fine-grained, xenomorphic scapolite in Domain B regional metamorphic sample CFM8 showing thin CL-bright rims. (b) Poikiloblastic, idiomorphic scapolite with quartz inclusions from sample CFM2 (Domain B). (c) Scapolite in the scapolitite sample (MKS8, Domain A) contains CL-weakly luminescent relict cores with a meionite component of 43% surrounded by CL-bright scapolite with a meionite component of ~21.5%. (d) Zoned Domain C shear-zone scapolite from the Elaine Dorothy Cu-U-REE prospect (MKE021).

Table 1. Mineral assemblages in the investigated samples.

Sample	Type	Mineral Assemblage
MKS1	Garnet-scapolite veinlet in Burstall Granite Dyke	**gt, sc**
MKS3	Banded Skarn	**gt, cpx, sc, pl,** ti, ap
MKS8	Scapolitite	**sc**, pl, kf, ti
MKS9	Amphibolite	**hbl, cpx, sc, kf,** ti, ap
CFM8	Meta-calc-silicate (Breakfast Creek)	**cc, hbl, kf, sc, cpx, qz**, ti, ap
CFM2	Impure marble (Paddymilon location)	**cc, cpx, hbl, qz, sc, kf**, ti, ap, to
MKE021	Biotite shear zone	**bt, sc,** ap, py ± kf

gt=andradite-grossular, sc=scapolite, cpx=diopside–hedenbergite, pl=albite, ti=titanite, ap=apatite, kf=K-feldspar, qz=quartz, hbl=hornblende, to=tourmaline, py = pyrite

6.2 Major element chemistry and Cl/Br quantification in scapolite from the MKFB

Representative scapolite analyses of the three domains are given in Table 2 and all EPMA and LA-ICP-MS analyses can be found in the electronic repository. Whereas K_2O contents in analysed scapolite is generally low (<1.3 wt% K_2O), meionite components can vary significantly on a sample and subgrain scale.

Domain A

Domain A (contact metamorphic) scapolite has meionite components in the range of ~20–30% (Fig. 4; Table 2). Exceptions are the CL-weakly luminescent cores in MKS8 scapolite and scapolite from amphibolite sample MKS9 that contain meionite components of ~40% and ~60% respectively (Fig. 4; Table 2). Chlorine is the major anion that fills the A-site in Domain A scapolite. The exceptions also include the amphibolite sample MKS9 that has scapolite with up to 2 wt% SO_3 and up to 3 wt% CO_2 (meionite component ~63%) (Table 2; Fig. 4), and CL-weakly luminescent zones in MKS8 scapolite (scapolitite) that have low Cl (~2 v. ~3–3.5 wt%), higher CO_2 and SO_3 contents and higher meionite components (~43%) than the CL-weakly luminescent and intermediate zones (Table 2). Scapolite from the scapolitite sample has low molar Cl/Br values (<570) and zones with an intermediate brightness have Cl/Br ratios as low as 280 (Table 2). Molar Cl/Br ratios are in the range 410–510 in scapolite from sample MKS9, 850–1230 in vein sample MKS1, and 440–1250 in the skarn sample MKS3 (Table 2; Fig. 10).

Domain B

Domain B regional metamorphic scapolite is tyoially higher in CO_2 concentrations (~3.5 wt. %), and a higher meionite content (~55–65%) than Domain A scapolite Fig. 4; Table 2), although Oliver et al. (1992) reported a larger range from a greater number of outcrops. Molar Cl/Br ratios in domain B scapolite vary considerably from sample to sample. Sample CFM2 has the lowest Br concentrations of all samples (<30 $\mu g\ g^{-1}$) and has molar Cl/Br ratios of ~900–400, whereas CFM8 scapolite contains distinctly lower Cl/Br ratios, ranging from 300 to 520 (Table 2).

Domain C

Most shear-zone scapolite (MKE021) has a meionite component between 30% and 35% (Table 2; Fig. 4). The three internal zones within the scapolite grains have similar major element geochemistry; although SO_3 concentrations in Zone 2 (~0.8 wt%) are elevated compared to the other zones (~0.1 wt%) and Cl concentrations are usually slightly lower in Zone 2 (~2.6 wt%) than in Zones 1 and 3 (~2.9 wt%) (Table 2). Molar Cl/Br ratios differ between the three internal zones: The cores (Zone 1) show molar Cl/Br ratios of ~950–1330 while Zone 2 contains lower molar Cl/Br ratios (~390–640). The outer rim (Zone 3) shows similar molar Cl/Br ratios to Zone 1 (1330– 1700).

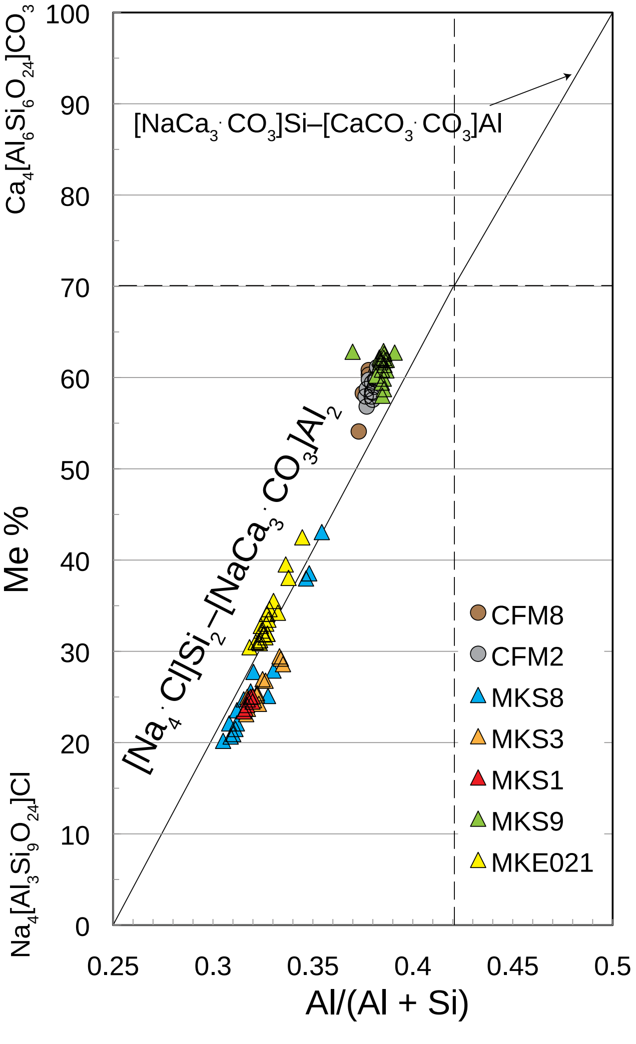

Fig. 4. Meionite % v. Al/(Al + Si) of scapolite with the solid line showing $[Na_4 \cdot Cl]Si_2$ – $[NaCa_3 \cdot CO_3]Al_2$ and $[NaCa_3 \cdot CO_3]$ Si – $[Ca_4CO_3]Al$ non-linear substitutions separated by the intersection of the dashed lines at Me = 75%, and Al/ (Al+Si) = 0.42. Our samples plot between 20% and 65% meionite and follow the $[Na_4 \cdot Cl]Si_2$ – $[NaCa_3 \cdot CO_3]Al_2$ substitution mechanism of Hassan & Buseck (1988).

Table 2. Representative scapolite analyses by EPMA, with Br and Cl concentrations determined by LA-ICP-MS. BB1 is the external standard used for quantification of Br and Cl concentrations by LA-ICP-MS. Assuming H_2O-free scapolite compositions, the calculated CO_2 values represent maximum concentrations (Teertstra & Sherriff, 1997).

Sample	**MKS1A**	**MKS3**	**MKS8**	**MKS8**	**MKS8**	**MKS9**	**MKS9**	**CFM2**	**CFM2**	**CFM8**		**MKE021**	
CL-texture[1]	homo.	homo.	CL-bright	CL-inter.	CL-w.l.	CL-bright	CL-w.l.	CL-bright	CL-w.l.	homo.	Zone1	Zone 2	Zone 3
(wt. %)													
SiO_2	56.6	56.2	56.5	57.1	52.1	47.9	48.3	49.9	50.0	50.2	55.5	54.8	55.7
Al_2O_3	22.3	22.5	23.4	22.3	24.3	26.1	25.7	26.0	25.7	25.3	22.7	22.6	23.0
FeO	0.12	0.07	0.01	0.10	0.04	0.05	0.26	0.06	0.07	0.07	0.02	0.10	0.07
CaO	6.39	6.47	6.06	6.05	10.7	15.5	15.2	14.5	14.6	13.6	8.19	8.87	8.38
Na_2O	10.2	10.2	9.45	9.68	7.49	4.68	4.70	5.47	5.37	6.08	9.14	9.07	9.39
K2O	1.07	1.19	0.85	0.95	0.55	0.62	0.62	0.42	0.48	0.50	0.83	0.74	0.83
Cl	3.87	3.91	3.05	3.43	2.19	0.87	0.83	1.07	1.06	1.30	2.90	2.58	2.89
SO_3	0.00	0.02	0.06	0.39	1.67	1.51	1.98	0.34	0.28	0.04	0.10	0.81	0.10
CO_2 (calc)[2]	0.37	0.31	1.33	0.69	1.36	2.92	2.71	3.43	3.46	3.28	1.44	1.42	1.50
Total	100.9	100.9	100.7	100.8	100.3	100.2	100.4	101.2	101.0	100.4	100.8	101.0	101.9
–O=Cl	0.87	0.88	0.69	0.77	0.49	0.20	0.19	0.24	0.24	0.29	0.65	0.58	0.65
Total	100.07	100.03	99.99	99.99	99.82	99.99	100.16	100.98	100.77	100.07	100.13	100.42	101.20
#Meionite	24.7	24.7	25.1	24.7	43.1	62.7	62.6	58.3	58.7	54.1	31.9	34.1	31.9
Br ($\mu g\ g^{-1}$)	60–100	65–160	140–160	150–290	120–180	40–60	40–60	17–29	17–29	30–100	50–80	95–130	35–60
Cl (wt.%)	3.4–3.8	3.2–3.9	3.0–3.6	3.4–3.7	2.2–2.6	0.9–1.2	0.9–1.2	0.8–1.2	0.8–1.2	0.6–1.5	2.7–3.5	2.2–3.1	2.7–3.4
Molar Cl/Br	850–1230	440–1250	450–540	280–570	450–550	410–510	410–510	900–1400	900–1400	300–520	950–1330	390–640	1330–1700

[1] Cathodoluminescence texture: homo.=homogeneous, inter. = intermediate, w.l. = weakly luminescent

[2] CO_2 calculated based on total anion and cation budget, assuming H_2O-free compositions

6.3 Retrograde alteration of scapolite and implication for Cl/Br values

Large areas of the MKFB underwent post-regional metamorphic albitization that retrogressed or altered scapolite (Oliver, 1995) and may have affected Cl/Br ratios. Samples from the biotite shear-zone (MKE021, Figs 1 & 2) contain both heavily altered and fresh scapolite grains, even within the same sample. Figure 5 exhibits euhedral, altered scapolite that recrystallized to feldspar, calcite, quartz and biotite. However, grain rims in contact with biotite seem to be unaffected, which gives the opportunity to compare Cl/Br signatures of fresh scapolite grains with the still intact rims of heavily altered grains. Molar Cl/Br values (650–850) of the intact rims of the heavily retrogressed scapolite are very similar to those of fresh scapolite (720–860) (Fig. 5), which indicates that alteration did not affect the Cl/Br signatures in the intact rims of altered scapolite. This supports very limited diffusion in scapolite grains, as also observed in experiments of Pan & Dong (2003). In other rocks containing strongly altered scapolite, it may thus be possible to still extract useful Cl/ Br data.

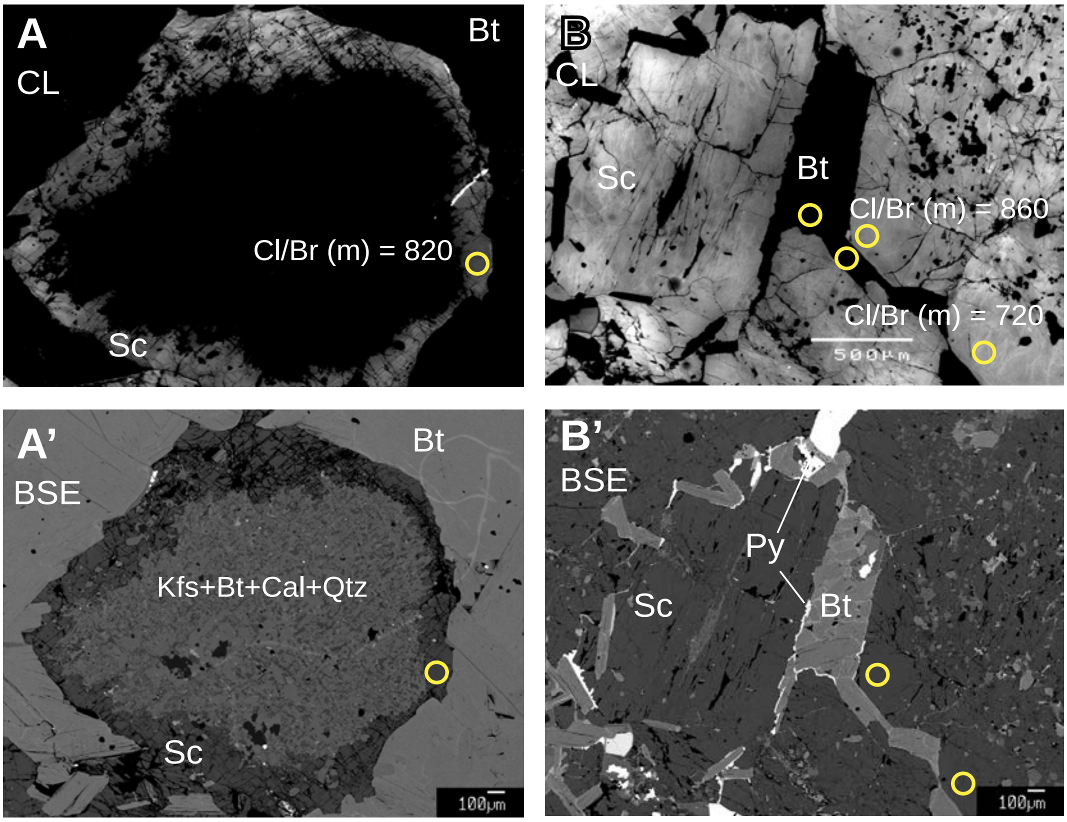

Fig. 5. (a) CL and (a′) BSE images of a Domain C (shear-zone) scapolite with alteration of the core zone clearly evident. (b) CL and (b′) BSE images of unaltered scapolite together with biotite and late pyrite fillings. Yellow circles denote the locations of 90 µm diameter laser ablation spots. All images are from sample MKE021.

6.4 Trace elements in scapolite and apatite from the MKFB

Lithophile trace element concentrations were measured in scapolite from each of the three domains. Figure 6 presents REE patterns of Domain A contact metasomatic (MKS1, MKS3, MKS8) and Domain B regional metamorphic scapolite (CFM2, CFM8). Trace element patterns in Domain A scapolite vary significantly between samples despite their similar major element chemical compositions (Table 2). Scapolite in the felsic dyke-hosted vein sample MKS1 is enriched in HREE and shows a negative Eu anomaly, whereas MKS3 skarn scapolite (with impure limestone precursor) is depleted in HREE, and has a positive Eu anomaly. Compared to scapolite in sample MKS1 and MKS3, those in amphibolite sample MKS8 are generally elevated in LREE (Fig. 6b). Weakly luminescent, Ca-rich scapolite in sample MKS8 (Fig. 6b) has elevated REE contents with a negative Eu anomaly compared to CL-intermediate and CL-bright zones, whereas strongly luminescent CL-bright scapolite contains the lowest REE concentrations (Fig. 6b).

Compared to Domain A scapolite, trace element patterns in metamorphic scapolite from the northern MKFB (Domain B) are rather uniform without significant enrichment or depletion in HREE or distinct Eu anomalies (Fig. 6a). Trace element concentrations in Domain C shear- zone scapolite (MKE021) vary on the subgrain scale. In general, all three zones have similar trace element patterns with REE patterns that are LREE enriched with distinct positive Eu anomalies when compared to the Domain B scapolite. However, Zone 2 in the Domain C scapolite is enriched in REE compared to the Zone 1 (core) and Zone 3 (rim) scapolite and contains slightly higher meionite component (~34%) (Fig. 6c; Tables 2 & 3). Shear-zone apatite, on the other hand, has a distinct negative Eu anomaly (Fig. 6d). Apatite rims are relatively enriched in REE, Th, U and Y compared to their cores (Table 3; Fig. 6d).

Table 3. Major element (measured by EPMA), and trace element (measured by LA-ICP-MS) concentrations of zoned scapolite, apatite and biotite from the biotite shear-zone of Domain C (MKE021).

Scapolite	**Zone 1**	**Zone 2**	**Zone 3**	**Apatite**	**Core**	**Rim**	**Biotite**	
Sample	6b_3_3	6b_3_1	6b_3_4	Sample	6b_ap8	6b_ap8	Sample	6b_6bt1
(wt. %)								
SiO_2	55.5	54.8	55.7	CaO	55.0	55.0	SiO_2	40.7
Al_2O_3	22.7	22.6	23.0	SiO_2	0.36	0.07	Al_2O_3	13.2
Na_2O	9.14	9.07	9.39	P_2O_5	40.2	40.1	Na_2O	0.17
CaO	8.19	8.87	8.38	SO_3	0.03	0.11	K_2O	9.3
FeO	0.02	0.10	0.07	Cl	0.14	0.13	FeO	10.7
K_2O	0.83	0.74	0.83	F	4.55	4.15	MnO	0.04
SO_3	0.10	0.81	0.10	Total	100.3	99.5	MgO	20.1
Cl	2.80	2.90	2.78				TiO_2	0.11
Total	99.2	99.9	100.2				Cl	0.24
							F	1.42
(µg g^{-1})							Total	95.9
^{7}Li	<3.66	<4.46	12.1	^{7}Li	41.05	3.3		
^{35}Cl	26801	30272	26624	^{35}Cl	1550	1003		
^{65}Cu	1.74	<1.47	1.7	^{65}Cu	<3.05	<1.38		
^{66}Zn	2.77	2.93	<2.21	^{66}Zn	6.85	<1.49		
^{71}Ga	8.94	11.3	8.18	^{71}Ga	6.72	9.66		
^{81}Br	59.1	130	35.1	^{81}Br	<39.6	<15.2		
^{85}Rb	5.22	9.96	10.27	^{85}Rb	124	<0.07		
^{88}Sr	75.9	74.3	72.75	^{88}Sr	71.7	66.3		
^{89}Y	1.20	2.66	1.51	^{89}Y	438	1070		
^{93}Nb	0.02	<0.00	<0.02	^{93}Nb	0.90	<0.03		
^{133}Cs	<0.01	0.05	0.20	^{133}Cs	1.73	0.02		
^{137}Ba	33.4	27.0	29.7	^{137}Ba	25.0	0.77		
^{139}La	1.30	4.72	1.82	^{139}La	27.1	252		
^{140}Ce	4.78	15.77	6.36	^{140}Ce	152	1175		
^{141}Pr	0.89	2.55	1.14	^{141}Pr	40.3	254		
^{143}Nd	4.66	12.18	5.66	^{143}Nd	289	1421		
^{147}Sm	1.06	2.27	1.20	^{147}Sm	122	419		
^{151}Eu	0.72	1.15	0.78	^{151}Eu	21.8	66.6		
^{157}Gd	0.61	1.47	0.69	^{157}Gd	134	366		
^{159}Tb	0.06	0.13	0.08	^{159}Tb	16.6	43.1		
^{163}Dy	0.30	0.56	0.35	^{163}Dy	88.6	223		
^{165}Ho	0.05	0.12	0.05	^{165}Ho	16.2	40.5		
^{167}Er	0.15	0.28	0.11	^{167}Er	47.6	116		
^{171}Yb	0.08	0.20	0.11	^{171}Yb	44.4	112		
^{175}Lu	0.00	0.02	0.01	^{175}Lu	7.10	17.4		
^{208}Pb	1.88	0.99	1.66	^{208}Pb	0.29	2.36		
^{232}Th	<0.001	<0.001	0.00	^{232}Th	1.41	16.3		
^{238}U	<0.001	0.001	0.02	^{238}U	2.82	25.0		

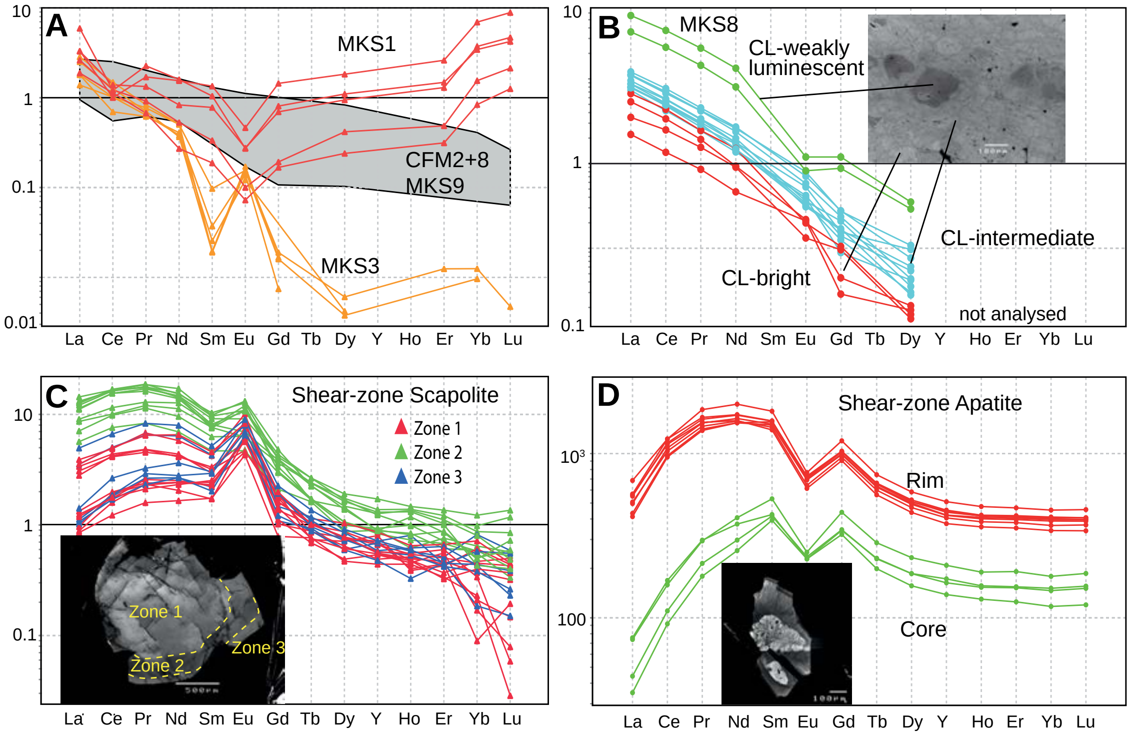

Fig. 6. Rare earth element (REE) patterns of scapolite and apatite normalized to C1 Chondrite (Taylor & McLennan, 1985). (a) REE pattern of scapolite from the Domain A scapolite (MKS1 and MKS3) and Domain B scapolite (CFM8). Scapolite from the Burstall granite dyke (MKS1) shows a negative Eu anomaly and higher HREE concentrations compared to scapolite in banded skarns (MKS3). The relatively low HREE content of MKS3 scapolite may be due to co-precipitation with HREE-sequestering garnet. Metamorphic scapolite grains (CFM8 and CFM2) and MKS9 scapolite (grey field) display flat REE patterns with a decline towards the HREE and no Eu anomaly. These three samples were formed under rock-buffered hydrothermal alteration conditions, so their REE patterns likely represent protolithic REE concentrations. (b) CL-weakly luminescent, intermediate and CL-bright textures in scapolite from the scapolitite sample (MKS8). CL-weakly luminescent cores contain elevated REE concentrations and a negative Eu anomaly. (c) Zoned scapolite from the Elaine-Dorothy shear-zone (Domain C; sample MKE021). The three zones have similar REE patterns, including distinct positive Eu anomalies, but Zone 2 is markedly enriched in REE compared to Zone 1 and 3. (d) Core and rims zones of apatite from the shear-zone sample (MKE021) have similar REE patterns, but the rim zone has elevated REE concentrations.

7. Discussion

7.1 Scapolite as a reliable fluid tracer

Ellis (1978) showed in experiments that the Cl/ (Cl + CO_3) composition of scapolite is determined by the fluid composition in calcite-buffered systems. Although we lack data for the K_D dependence on P–T, it is assumed that the experiments and conclusions of Ellis (1978) at 750 °C and 4 kbar are applicable in amphibolite facies conditions. In this case, the equation below can be solved for $X\mathrm{NaCl}_{\mathrm{Fl}}$ to obtain an approximation on the NaCl fraction in the coexisting fluid, in the presence of calcite.

$$K_D = \frac{X\mathrm{cc}_{\mathrm{Sc}} \times X\mathrm{NaCl}_{\mathrm{Fl}}}{X\mathrm{NaCl}_{\mathrm{Sc}}}$$

where K_D is the equilibrium constant, $X\mathrm{cc}_{\mathrm{Sc}}$ is the activity of $CaCO_3$ in scapolite, $X\mathrm{NaCl}_{\mathrm{Sc}}$ is the activity of NaCl in scapolite and $X\mathrm{NaCl}_{\mathrm{Fl}}$ is the activity of NaCl in the fluid as (NaCl/(NaCl + H_2O). Ellis (1978) has shown that activity coefficients in this system are close to 1, so for our calculations component activities are interchanged with component mole fractions, where $X\mathrm{NaCl}_{\mathrm{Fl}}$ is expressed as NaCl/ (NaCl + H_2O). Using the method of Ellis (1978), calculations by Oliver et al. (1992), and results of this study (Domain B scapolite), the regional metamorphic fluid NaCl mole fraction (NaCl/(NaCl + H_2O)) is calculated to be between ~0 and ~0.6, which corresponds to EqAn (equivalent anorthite content = 100(Al–3)/3) values ranging from 70 to 20 (Fig. 7). Oliver et al. (1992) further reported variations in calculated fluid HCl and XFeCl/ XMgCl activities based on biotite and amphibole chemistry. Effects of temperature on the fluid–scapolite exchange equilibria are likely to be insignificant in this case, as a wide range in scapolite compositions is observed at outcrop scale. The observation of coexisting calcite and scapolite in the Domain B samples means that the compositional variation in scapolite can be used to track the effect of bulk rock composition, Na–Ca–K solid solution and halogen/CO_2 ratios in scapolite. This has been shown by Oliver et al. (1992), and is supported by the results from this study, where variable scapolite compositions reflect variable XNaCl and $X\mathrm{CO}_2$ activities in the fluid (Fig. 7).

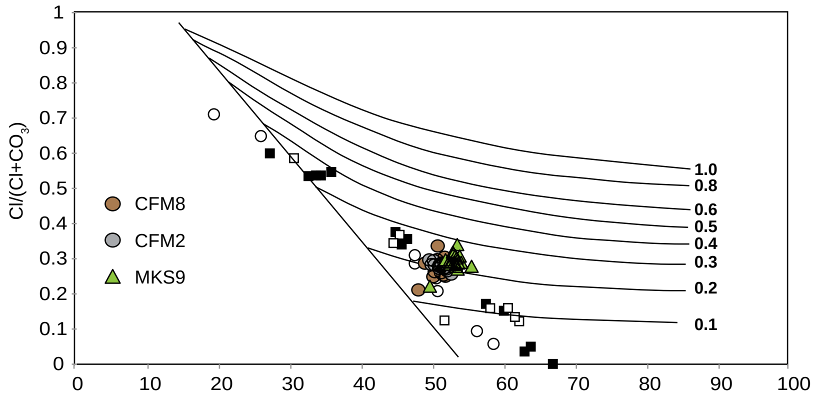

Fig. 7. Lines of equal NaCl/(NaCl + H_2O) in fluid coexisting with scapolite over a range of scapolite composition expressed as EqAn and Cl/(Cl + CO_3) (after Ellis, 1978). Black symbols represent data from Oliver et al. (1994).

In rock-buffered hydrothermal environments, the chemical composition of the rock has potential to influence or control the coexisting fluid chemistry, including halogens, because of the coupled non-binary solid-solution between marialite $Na_4(Al_3Si_9O_{24})Cl$ and meionite $Ca_4(Al_6Si_6O_{24})CO_3$. We use the term rock-buffered here to describe systems in which mm- to cm-scale rock layers attempted to approach local equilibrium (e.g. Evans et al., 2013) during a series of reactions governed primarily by the composition of the rock layer, in response to increasing P–T (although there may be complexity at smaller scales). I use the term fluid-buffered to describe systems in which the primary rock composition does not control the approach to local equilibrium; rather the system is controlled by the fluid volume and composition. Combinations of these two processes are likely at mm to metre scales if there is a variable fluid supply during metamorphism.

To use Cl/Br ratios of scapolite as a tool to directly determine the Cl/Br ratios in the coexisting fluid would thus require that no fractionation occurs between Cl and Br during incorporation into scapolite, unlike Cl/CO_2 fractionation that occurs due to the coupled solid solution. The results (Fig. 8) show that there is no correlation between molar Cl/Br ratios (~200–1700) and molar Na/Ca ratios (~0.25–2), or K (~0.2–1 wt%) or Cl contents (~0.5–4 wt%) of MKFB scapolite. These results imply that Cl/Br ratios in scapolite are independent of major solid solution substitutions (Ca, Na and K) and Cl concentration. There is also general agreement between the Cl/Br ratios of scapolite and MKFB fluid inclusions from related hydrothermal episodes (Kendrick et al., 2008, 2011; Fig. 10). I am therefore confident that Cl and Br fractionation upon incorporation in scapolite was insignificant in this case, and hence, Cl/Br ratios of the scapolite are reliable monitors of fluid compositional variations. This result supports the findings of Pan & Dong (2003), but I stress that more experimental work is needed to examine the controls of Cl and Br partitioning into scapolite over a range of pressure and temperatures conditions and over a range of scapolite and fluid compositions. In the meantime, it is stressed that independent evaluations of Cl and Br fractionation need to be undertaken on a cases by case basis before conclusions on fluid chemistry can be drawn from the halogen geochemistry of scapolite.

Fractionation of Cl/Br due to precipitation or dissolution of other minerals that also incorporate halogens needs to be considered when interpreting halogen ratios in scapolite or fluid inclusions. The potential for such fractionation effects is likely only in rock-buffered systems with low fluid/rock ratios, which means the hydrothermal fluid regime and mineral paragenesis need to be carefully defined and characterized before accurate interpretations of mineral chemical data can be made. In this case, the approach of in situ analysis with a retained textural context allows a linkage between mineral paragenesis and scapolite chemistry, which means that such fractionation effects can be evaluated.

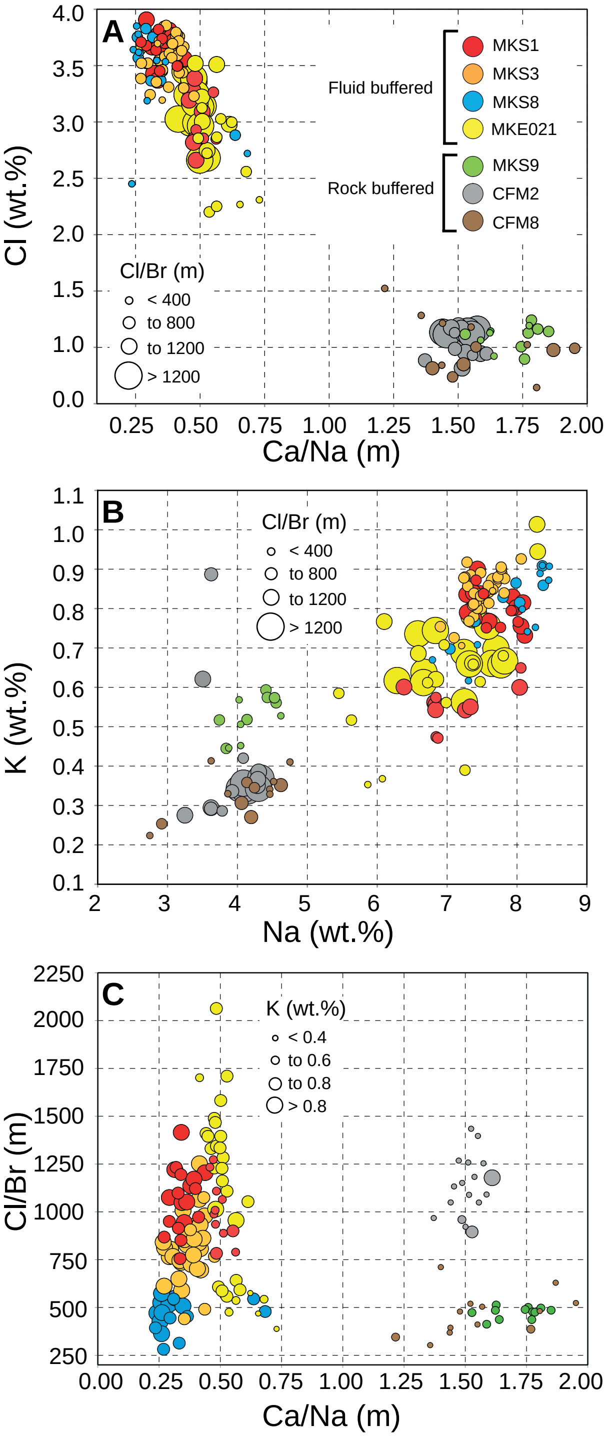

Fig. 8. (a) Chlorine concentration v. molar Ca/Na ratio of scapolite grains, with increasing data symbols size representing higher molar Cl/Br ratios. Fluid-buffered and rock-buffered scapolite plots in different areas, but molar Cl/Br ratios are independent of the scapolite Ca/Na and Cl content. (b) Potassium concentration v. Na concentration of scapolite from fluid-buffered and rock-buffered environments. The positive correlation between K and Na suggests that both cations occupy the same site in the scapolite crystal lattice. Cl/Br ratios do not vary systematically with K concentration, indicating that there is no Cl/Br fractionation with increased K incorporation. (c) Molar Cl/Br ratios v. molar Ca/Na ratios of scapolite. Increasing sizes of data symbols represent higher K concentrations. Again, no relationships between the Cl/Br and Ca/Na, or Cl/Br and K concentration are observed.

7.2 Scapolite formation in the MKFB

Domain B metasedimentary tocks (CFM2 and CFM8, Fig. 1) contain calcite, quartz and K-feldspar but are plagioclase free (Table 1). A possible scapolite-forming reaction in these samples might be plagioclase + calcite + $NaCl_{fluid}$ = scapolite whereby plagioclase has been fully consumed. In this case, the meionite-rich scapolite compositions reflect a low Cl/ CO_2 ratio in the fluid and a calcic bulk composition (Fig. 4; Table 2). The absence of plagioclase in these samples (Table 1) assigns the bulk rock composition to the scapolite + halite + calcite stability field (Fig. 9). Scapolite from sample MKS9 from Domain A has similar meionitic values as Domain B scapolite. As no calcite or plagioclase is present in this sample, the estimated bulk rock composition cannot be plotted adequately in Fig. 9.

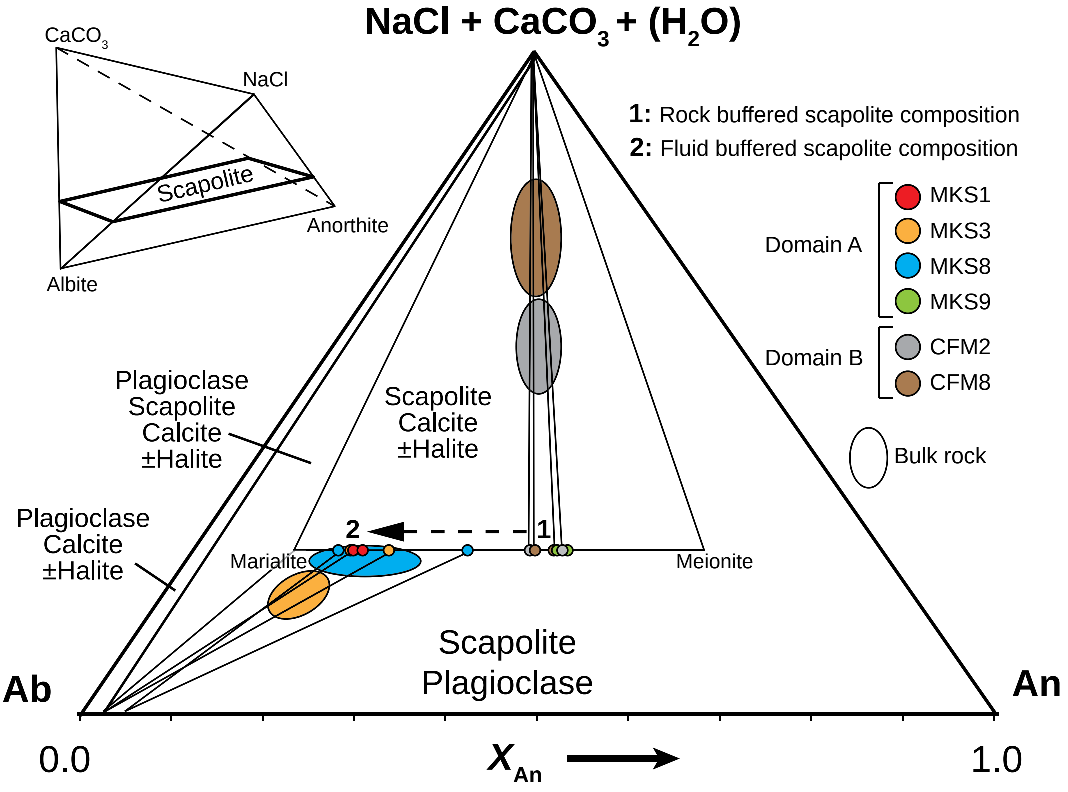

Fig. 9. Modified projection of the Ab–An– NaCl–$CaCO_3$ tetrahedron (insert) parallel to the NaCl–$CaCO_3$ edge (Orville, 1975). The stability field of scapolite and plagioclase is shifted towards lower anorthite numbers for our data (550–650 °C at 2–4 kbar, Oliver, 1995) compared to the equilibrium phase relations at 750 °C and 4 kbar of Orville (1975). Coloured fields represent estimated bulk rock compositions, calculated from estimated modal abundance and compositions of minerals in each rock sample. A change in bulk rock composition and scapolite composition (1 →2) was observed when comparing scapolite produced under rock- buffered v. fluid-buffered conditions (see text).

The texturally preserved clinopyroxene to amphibole breakdown reaction might suggest scapolite-forming processes such as clinopyroxene + H_2O + $NaCl_{fluid}$ = calcic amphibole + scapolite, which may have allowed Ca buffering by excess clinopyroxene and amphibole, hence resulting in scapolite with a relatively high meionite component (Fig. 4; Table 2). The banded skarn sample (MKS3, Figs 1 & 2) within Domain A does not contain any calcite or quartz (Table 1). Scapolite usually occurs in discrete layers together with albite. Initially, scapolite could have formed via the reaction albite + calcite + NaClfluid → scapolite + anorthite, followed by $NaCl_{fluid}$ + anorthite → marialitic scapolite + albite. This would explain the observed mineral assemblage and also the negative Eu anomaly, as simultaneous plagioclase formation could have acted as a Eu sink. With calcite and anorthite being consumed or absent, the NaCl-rich fluid could have buffered the Na-content of the scapolite. Scapolite within the scapolitite sample (MKS8) accounts for ~90 vol.% of the rock. Hence, the estimated bulk rock composition overlaps with the scapolite chemistry. Gabbro fragments within highly scapolitized rocks can be observed in the field, which suggests that scapolitite is an end product of intense fluid– gabbro interaction, via reactions similar to that above.

Oliver et al. (1992) proposed internal rock buffering in Domain B as a reason for the compositional spread of scapolite shown in Fig. 7, although my more limited sampling of regional metamorphic scapolite (Domain B) showed mostly Ca-rich compositions. In contrast, scapolite in samples MKS1, MKS3 & MKS8 (Figs 1 & 2) in the metasomatic Domain A are NaCl-rich (Figs 4 & 8). This means that in the case of CFM2 and CFM8 in the regional metamorphic Domain B, calcite buffers the scapolite composition in terms of its Ca content, whereas in sample MKS1, MKS3 and MKS8, scapolite was most likely to be fluid-buffered. A fluid-buffered system leads to a very similar scapolite and bulk rock composition as shown in Fig. 9. CL images and EPMA measurements of scapolite cores in sample MKS8 may be reflecting the change from rock-buffered conditions to fluid-buffered conditions as the rims are richer in Na (Figs 3 & 9; Table 2).

7.3 Cl/Br signatures of fluids from different sources

Studies aimed to determine the source and origin of salinity in fluids, using fluid inclusions, have shown that fluid sources can be distinguished on the basis of Cl/Br ratio. Molar Cl/Br ratio is usually between ~700 and 1800 for granite related fluids (e.g. Böhlke & Irwin, 1992; Irwin & Roedder, 1995; Kendrick et al., 2001; Nahnybida et al., 2009; Fig. 10), and studies of fluid inclusions in diamond and mid ocean ridge basalts (Jambon et al., 1995; Johnson et al., 2000) provide molar Cl/Br ratios of between ~500 and 1000 for mantle-derived fluids. Evaporation of seawater (molar Cl/Br ~647) first precipitates $CaCO_3$ in the form of aragonite followed by gypsum. Once the salinity of seawater has been concentrated up to 10–12 times by evaporation, halite starts to precipitate, which leads to Br enrichment in the residual fluid and consequently low molar Cl/Br ratios (<650) due to the incompatibility of Br in halite (e.g. Holser, 1979; McCaffrey et al., 1987). Such high-Br residual fluids are typically called bittern brine fluids. While bittern brine molar Cl/Br ratios are lower than seawater (<650), typically ~200–300 (e.g. Kesler et al., 1995), fluids that derived their salinity from halite dissolution processes, show significantly higher (>>650, in some cases >3700; Böhlke & Irwin, 1992) Cl/Br and Na/Br ratios than those of seawater (e.g. Kesler et al., 1995). Because halite precipitation leads to fractionation between Cl and Br, the Cl/Br ratio in scapolite can be used to determine the degree of evaporation of the original seawater and/or the halite dissolution component in a fluid, as long as the effects of metamorphism and hydrothermal processes can be isolated.

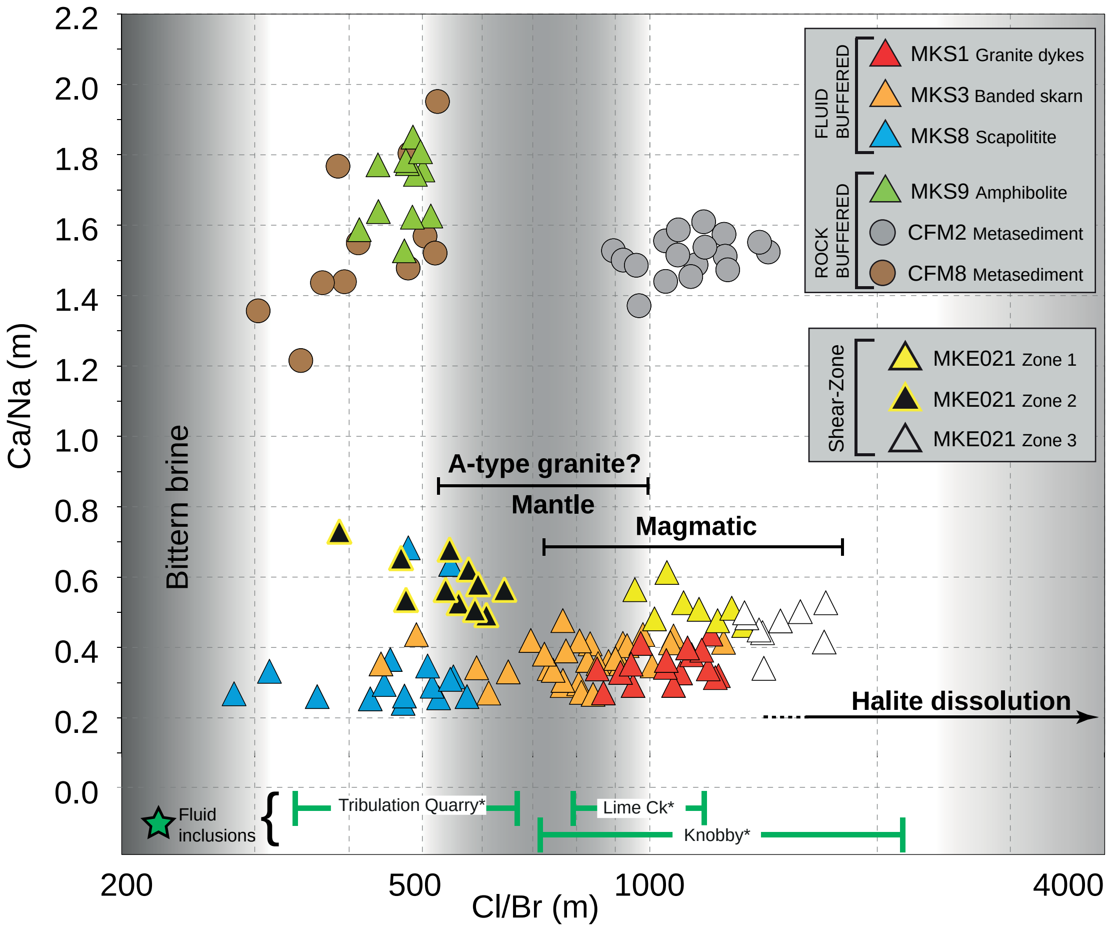

Fig. 10. Molar Ca/Na ratios v. molar Cl/Br ratios of fluid-buffered (MKS1, MKS3 and MKS8) scapolite and rock-buffered scapolite (MKS9, CFM2 and CFM8). Rock buffering leads to high Ca/Na ratios in scapolite. The Ca/Na variation in CFM8 might be due to small-scaled local equilibria. The fluid-buffered scapolite compositions fall on a fluid mixing trend between magmatic and bittern brine fluid. Fields of molar Cl/Br ratios of typical magmatic fluids (e.g. Bo€hlke & Irwin, 1992; Irwin & Roedder, 1994; Kendrick et al., 2011), mantle fluids (Johnson et al., 2000), Br-enriched bittern brine fluids and typical halite dissolution fluids (McCaffrey et al., 1987) are shown as shaded areas. Data on fluid inclusions from the MKFB are from Kendrick et al. (2008, 2011).

The Cl/Br signatures of scapolite in samples MKS1 and MKS3 from Domain A (Figs 1 & 2) plot along a mixing line between a granitic fluid source and a bittern brine fluid (Fig. 10). Chlorine/bromine values in scapolite of garnet–scapolite veins in the Burstall Granite plot closer to a 'pure' granitic fluid source with a fairly small bittern brine component. The amphibolite sample (MKS9, Fig. 1) plots in a narrow field of <650 Cl/Br, which indicates that the scapolite forming fluid contained a major bittern brine component. Cl/Br values from scapolitite sample (MKS8) cover a broader range extending between the magmatic and bittern brine fields (Fig. 10). The implication of this range of data is that intrusion of the original felsic and mafic rocks resulted in circulation of bittern brines and local admixture of magmatic/hydrothermal fluids that subsequently formed scapolite (see below).

Chlorine/bromine signatures of Domain B regional metamorphic scapolite vary considerably between each sample. The Cl/Br signatures in sample CFM8 are consistent with a major bittern brine component in the scapolite forming fluid with molar Cl/Br ratios in the range ~300–500. Sample CFM2 on the other hand contains much higher Cl/Br values (~900–1500) that apparently plot in the magmatic field (Fig. 10). Although the rock-buffered mineral assemblages and textures at these localities preclude the major involvement of fluids derived from intrusions (Oliver et al., 1992), it is possible that some of the scapolite compositions were inherited from contact metamorphism. Another possibility is the mixing of the bittern brine with Br-depleted pore-water and/or interaction with traces of halite crystals within the sedimentary layers that leads to elevated Cl/Br ratios. Fluid inclusion data from post-regional metamorphic calcite pods in samples from three locations within the northern MKFB (Kendrick et al., 2008, 2011; Figs 1 & 10) show that bittern brine was still present in the region at the time of post-regional metamorphic thermal events (Tribulation Quarry; Fig. 10) or that the low Cl/Br fluids (320–670) were generated upon scapolite albitization. Furthermore, Cl/Br analyses of fluid inclusions in two scapolite-bearing metasedimentary rocks from Knobby (Heinrich et al., 1993) have molar Cl/Br ratios of 580 and 730. These ratios are too low for them to have been derived from halite dissolution; they more likely represent a major bittern brine component during regional metamorphism. The observed Cl/Br ratios in fluid inclusions from the Knobby quarry show a broad range (Cl/Br = 710– 2500) and overlap with signatures of typical magmatic fluids (Fig. 10). Hence, it seems that the scapolite at Knobby retained its original metasedimentary Cl/Br signatures and was not recrystallized by late magmatic fluids. Cl/Br values (770–1110) from fluid inclusions in the Lime Creek samples have been interpreted as likely being basinal (bittern brine) fluids with a halite component (Kendrick et al., 2008, 2011).

Shear-zone scapolite (Domain C) shows three internal zones with distinct Cl/Br ratios. The grain cores show Cl/Br ratios that are very similar to those in the granite dykes (MKS1). Hence, the cores likely represent scapolite formed from a granitic fluid that also led to scapolite formation in the granite dykes (e.g. MKS1). Cl/Br ratios in Zone 2 of the scapolite are indicative of a bittern brine component, but also fall partially within the Cl/Br field of mantle fluids (molar Cl/Br ~500–1000) and are strikingly similar to post-regional metamorphic fluid inclusion Cl/Br values from the Tribulation Quarry (Kendrick et al., 2011). However, a pure mantle origin of these fluids seems to be unlikely. Neodymium isotopes of post-metamorphic (1540–1515 Ma) granitic, doleritic and gabbroic intrusions in the region show a clear crustal component that is interpreted as a result of magma mingling and mixing (Pollard, 1997; Pollard et al., 1998). Kendrick et al. (2007, 2011) suggested, based on halogen and noble gas data, the presence of fluids derived from A-type granites and they ruled out a pure mantle late-orogenic fluid (Kendrick et al., 2007, 2011). Late, unexposed mafic components of the Williams and Naraku Batholith equivalents could be a main source of the mantle-like component seen in scapolite (internal Zone 2) from the shear-zone (see below). The source of the bittern brine component (Cl/Br ratios <500) was possibly halogen release and recycling upon albitization (Oliver, 1995) of metamorphic scapolite. The outer rim (Zone 3) of the shear-zone scapolite shows the highest Cl/Br ratios that match late Isan-fluids recorded in fluid inclusions in the Knobby Quarry (Kendrick et al., 2011), which fall into the typical granite Cl/Br field (Fig. 10). Mixing of these different fluid types may have been one of the processes that resulted in precipitation of associated U-REE minerals (Sha, 2013).

The highest molar Cl/Br ratios in scapolite from skarns occur in garnet–scapolite veinlets, and cores of shear-zone scapolite (Zone 1). They are all around ~1250, which is very close to the ratio proposed for typical magmatic–hydrothermal systems (~1200, St. Austell Granite fluids) observed in fluid inclusions by Böhlke & Irwin (1992).

My Cl/Br results indicate that scapolite formation during regional metamorphism involved fluid with a major component of bittern brine. Simple mass balance calculations show that in the case of CFM2, the maximum volume proportion of halite dissolution fluid is ~0.1 (10 vol.%) when taking an average molar Cl/Br ratio of ~10,000 for halite (e.g. McCaffrey et al., 1987). For the sample with lower molar Cl/Br values (CFM8), the halite component in the fluid, if present, would be ~2 vol.% of the total salinity to produce the observed molar Cl/Br ratios. The halite component might be even smaller than our estimates if the fluids were affected by gravitational Cl/Br fractionation (Bons & Gomez-Rivas, 2013). This interpretation is in contrast to Oliver et al. (1994) and Ramsay & Davidson (1970) who proposed in situ production of NaCl-rich fluids by halite dissolution within the sediments.

Using these new data, I conclude that halite dissolution only played a minor role in scapolite formation, which implies that interaction of Br-enriched bittern brine fluid with metasedimentary rocks led to scapolite formation during regional metamorphism. However, to produce Br-enriched bittern brines, halite components had to be extracted from the original fluid to fractionate Br and Cl. Halite precipitates from seawater at a concentration factor of ~10.6 (McCaffrey et al., 1987). It follows that the amount of extracted halite must have significantly exceeded the required 2 x 10^9 m^3 of halite calculated by Oliver et al. (1994) to produce the amount of scapolite present in the MKFB. Because only small amounts of halite, if at all, were directly involved in the formation of saline metamorphic fluids it is likely that most halite layers were removed (i.e. by erosion or tectonism) before the onset of regional metamorphism, or that the fluid was derived externally. Kendrick et al. (2008) studied halogen content in fluid inclusions in the same region and reached similar conclusions that a halite horizon must have been present prior to regional metamorphism and fluid/halite interaction was limited during metamorphism. They also conclude that residual bittern brine was the dominant fluid type in the MKFB.

7.5 Trace elements in scapolite and apatite

Scapolite from the MKFB contains detectable levels of a large suite of trace elements including REE, Sr, Pb, Ba, Rb and Y (Fig. 6; Table 3), which is consistent with the findings of Satish-Kumar et al. (2006). The presence of trace elements in scapolite permits further testing for scapolite formation processes (e.g. via Eu anomalies) and for the provenance of fluids (e.g. via Sr and Nd isotopes). There are few data available concerning trace element uptake by scapolite (Shaw, 1960b; Romer et al., 1996; Satish-Kumar et al., 2006) and there is a need to better understand the major element compositional and environmental (e.g. P, T) controls on trace element incorporation. Nevertheless, REE concentrations on a sample and sub-mineral scale evaluated with other petrographic and chemical (e.g. Cl/Br) criteria allow qualitative assessment of fluid sources and compositions. Positive Eu anomalies in scapolite (MKS3, MKE021; Fig. 6) support feldspar involvement in scapolite forming reactions such as scapolitization of anorthite via Ca/NaCl exchange and Eu inheritance. Owing to the strong preference of garnet for HREE, the REE patterns in scapolite can potentially be used to resolve the relative timing of garnet/scapolite formation in skarns in a similar way that REE patterns of zircon are used to infer concurrent zircon and garnet growth (e.g. Rubatto, 2002; Rubatto & Hermann, 2007). The two samples proximal to the Burstall Granite (Domain A; MKS1, MKS3, Figs 1 & 11) both contain garnet (Table 1). The HREE-depletion (negative slope in REE) in banded skarn scapolite (MKS3) suggests that scapolite formed together with garnet. Scapolite in sample MKS1 (garnet–scapolite vein in Burstall Granite dykes) shows a positive REE slope (HREE-enriched) that likely indicates that formation of scapolite and garnet was not coeval (MKS1). The differences in REE concentrations on a sub mineral scale (MKS8, MKE021) suggest the presence of fluids of different compositions during various stages of scapolite formation. The Ca-enriched weakly luminescent cores in sample MKS8 have higher trace element concentrations than the Na-rich intermediate and bright zones (Table 2; Fig. 6). These differences might be due to higher REE partition coefficient in Ca-rich scapolite. However, no experimental data for REE partitioning in scapolite exists to date. The Cl/Br ratios in the different zones are very similar (Table 2), so I infer that the fluid source remained the same during the course of scapolite formation. The relatively uniform REE pattern of Domain B scapolite from two samples (Fig. 6a) indicates that this scapolite generation has equilibrated with a common REE-controlling assemblage. Zoned scapolite from the shear-zone (MKE021) indicates initial formation from a fluid with relatively low REE, Th and U concentrations (Zone 1, core) followed by a fluid enriched in REE, Th and U (Zone 2 in scapolite), which was subsequently followed by a third fluid (Zone 3) of similar trace element composition to the fluid recorded in Zone 1 of the scapolite. The Cl/Br ratios of the REE enriched Zone 2 are significantly lower (bittern brine component) than those of the core (Zone 1) and the outer rim (Zone 3), which are indicative of a major magmatic fluid component.

Similar to scapolite, the core zone of apatite from the shear-zone sample is relatively depleted in REE compared to the enclosing apatite rim. It appears that two of the three hydrothermal events recorded in shear-zone scapolite are also recorded in shear-zone apatite, with the equivalent of the outer scapolite zone not present/preserved in the apatite. Together with the high F content of biotite (Table 3; see also Sha, 2013) in the shear-zone and Cl/Br ratios in shear-zone scapolite, it is possible that the second major fluid pulse represented a mixture between bittern brine and F-bearing fluid derived from magmatic rocks such as A-type granite (e.g. Whalen et al., 1987; Sha, 2013).

8. Fluid evolution model

Scapolite in banded skarns and in veinlets (MKS3, MKS1) in the Burstall Granite (i.e. Domain A) do not seem to be affected by regional metamorphic fluids but retained their signatures from granitic fluids. The bittern brine component present in some of the skarn scapolite suggests the presence of bittern brine fluid in the sedimentary rocks during the Burstall Granite emplacement. Up-temperature fluid flow during contact metamorphism (Cartwright & Oliver, 1994) led to a restricted mixing of out-flowing granite-derived hydrothermal fluid and bittern brine in the endoskarns (Figs 10 & 11), while samples further away from the intrusion (exoskarns; MKS8, MKS9) show a smaller magmatic fluid component (Fig. 10).

Mora & Valley (1989) found considerable variations in biotite and scapolite compositions on a layer scale in metamorphic rocks of the Wallace formation, Idaho. These authors attributed these variations to channelled flow of fluid of heterogeneous composition. Furthermore, halite-bearing layers were assumed to be responsible for the observed compositional variations, and skeletal halite crystals in protolithic rocks were cited as support for derivation of NaCl-rich fluids from halite dissolution during metamorphism (Mora & Valley, 1989). Although Oliver et al. (1992) did not find direct evidence of halite in protoliths around the MKFB, they inferred that com positional variations in scapolite compositions were a consequence of initial variations in halite–$CaCO_3$ ratios in the protolith. However, the new results indicate that the NaCl-bearing fluid was introduced from a bittern source, most likely during diagenesis, which is similar to the conclusions of studies by Heinrich et al. (1993) and Kendrick et al. (2008). Chlorine/ bromine signatures of fluids along grain boundaries are thought to be resistant to modification, even during metamorphism (Yardley, 1997). In a similar scenario to that of Mora & Valley (1989), I suggest that the observed compositional variations of Domain B scapolite and biotite at the sample scale (see also Oliver et al., 1992) were produced by low fluid-flux, layer-bound, channelled fluid flow in combination with rock buffering. I imply that variable mineralogy and different mineral modal abundances led to the evolution of a heterogeneous fluid along the layer-bound channels (Fig. 11). In this case, rock- buffered mineral assemblages were preserved at low fluid/rock ratios, with a major component of bittern brine fluid controlling the Cl/Br in scapolite. The variation of Cl/Br ratios seen in fluid inclusions (Heinrich et al., 1993; Kendrick et al., 2008, 2011) and, to some degree, in scapolite (Fig. 10) suggests that traces of halite might have been present at the time of scapolite formation after most of the evaporite deposits had eroded, but before regional metamorphism (Fig. 11b).

Scapolite in the shear-zone at the Elaine-Dorothy Prospect experienced three fluid pulses with a magmatic fluid, followed by bittern brine/A-type granite REE-rich fluid, and a late magmatic fluid pulse. The last two fluid pulses may have had a major contribution from fluid exsolved during crystallization of a deep-seated A-type magma body of equivalence to the c. 1550–1500 Ma Williams Naraku Batholith of the Eastern Fold Belt (e.g. Oliver et al., 2004, 2008) (Fig. 11c). Halogen and noble gas analysis of fluid inclusions that represent late-orogenic (1550– 1500 Ma) fluids (Kendrick et al., 2007, 2008, 2011), and C and O stable isotope studies on calcite pods dated at c. 1555–1521 Ma (Oliver et al., 1993) have also been interpreted to have a fluid component sourced from a deep-seated intrusion. These results are consistent with a c. 1525 Ma age obtained from hydrothermal titanite associated with the shear-zone mineralization (Domain C) at Elaine Dorothy (Sha, 2013). Collectively, these data indicate that late magmatic-derived fluids had a significant role in mineralization in the MKFB.

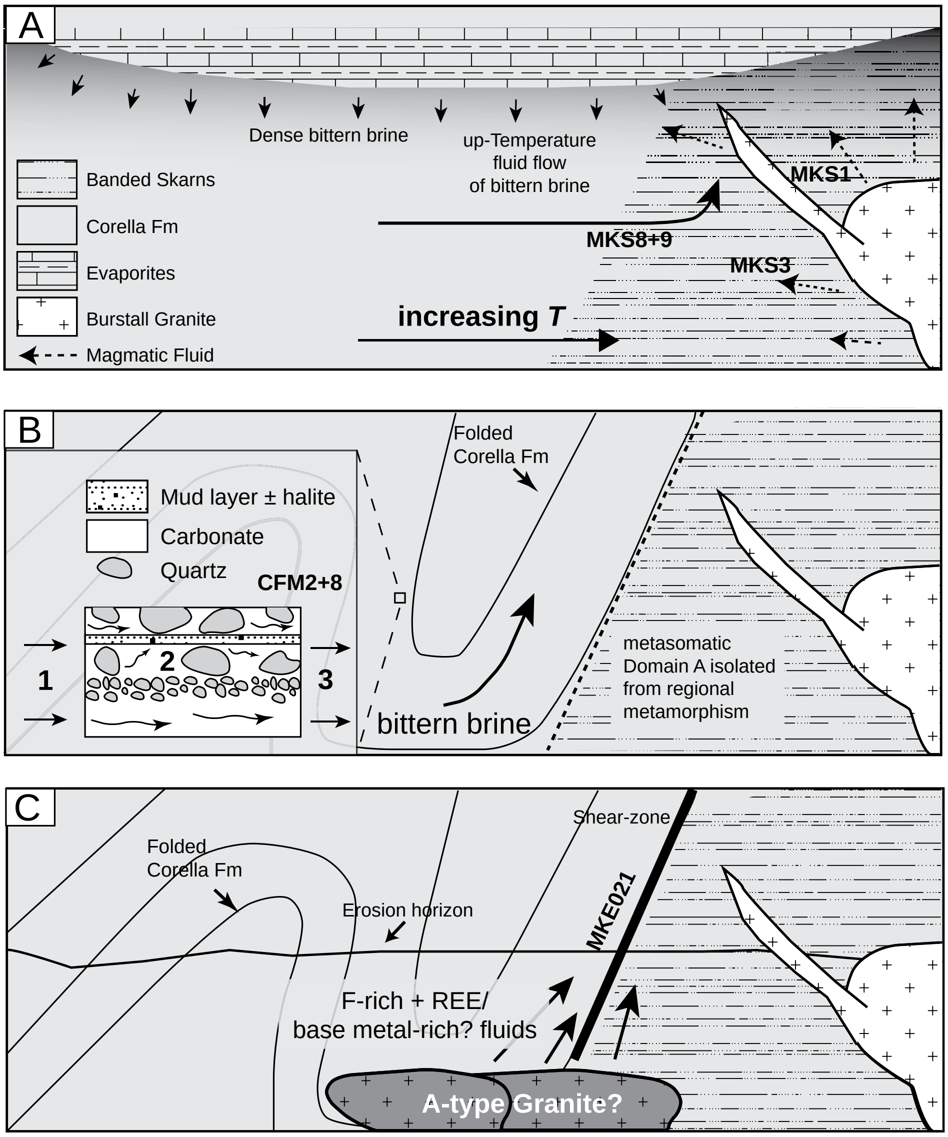

Fig. 11. Schematic overview of three stages of fluid flow and metamorphism within the MKFB. (a) c. 1740 Ma; dense bittern brine formed as residues of saline surface water evaporation flux into deeper sediments. Intrusion of the Burstall Granite acts as heat source for contact metamorphism, which leads to up-temperature fluid flow of the bittern brine. The proximal regions of the Burstall Granite are also infiltrated by magmatic fluids exsolved from the intrusion, which results in fluid mixing at the bittern brine–magmatic fluid interface. The banded skarns are the result of the Fe-rich magmatic fluids interaction with carbonate-rich sediments. This process is represented by Domain A in Fig. 1b. (b) c. 1580 Ma; regional metamorphism and deformation (Domain B in Fig. 1b) causes upright isoclinal folding. Most of the evaporites had been eroded at that stage and only traces of halite (at best) remained in the now metamorphosed sedimentary sequence. Regional metamorphism of the metasedimentary rocks that had not been affected by prior contact metamorphism lead to release of fluid with 'bittern brine' signatures and layer-bound fluid- mineral reactions: (1) bittern brine fluid interacts with sediment layers of different compositions, (2) possible traces of halite may have led to fluid alteration at a layer-scale, (3) variable fluid flux and fluid/rock reaction under rock-buffered conditions lead to variable fluid compositions (e.g. variable Cl concentrations and Cl/Br ratios) at a sample scale Crustal scale shear-zones (e.g. Mary Kathleen shear-zone) was likely activated during these events. (c) c. 1525 Ma; deep-seated A-type intrusions (possible equivalents of the William Naraku Batholith) exsolve F-rich fluids that flow into reactivated shear-zones (Domain C in Fig. 1b). Fluid–rock reaction and/or fluid mixing with bittern brines from the country rock may have led to U + REE + base metal mineralization in and around the shear-zones (e.g. Elaine Dorothy prospect).

9. Conclusions

My studies support the findings by Pan & Dong (2003) that little to no fractionation of Br and Cl occurs upon incorporation into scapolite, but further experimental work is needed to see if this relationship can be applied universally to scapolite. Chlorine and Br contents in scapolite are unlikely to be reset during retrograde metamorphism or metamorphic events that do not exceed temperatures of previous events. We confirm the findings by Oliver et al. (1992) that the bulk rock composition can buffer the scapolite composition; however, our Cl/Br analyses show that halite played a minor role during scapolite formation in metamorphic scapolite in the MKFB. Cl/Br ratios suggest that evaporite-derived bittern brine fluids were the main fluid type that led to scapolite formation during regional metamorphism.

Chlorine/bromine ratios together with trace element concentrations in zoned shear-zone scapolite suggest that at least three fluid pulses: (magmatic, bittern brine/magmatic, magmatic) used the shear-zone (Domain C) as their path. These fluids of the same hydrothermal episodes are likely to be preserved as fluid inclusions in late/post-orogenic carbonate pods (Kendrick et al., 2011). Hence, our results indicate that scapolite is an excellent monitor for fluid sources and mixing processes in complex hydrothermal systems.

Chapter 3

Neodymium isotope equilibration during crustal metamorphism revealed by in situ microanalysis of REE-rich accessory minerals

Published in *Earth and Planetary Science Letters*

Abstract

Radiogenic isotopes are widely used to investigate crustal evolutionary processes, however recent claims of Nd and Sr isotope disequilibrium during anatexis question the reliability of such information. We have conducted an in situ Sm-Nd isotope study of apatite, allanite, titanite, xenotime and monazite in metasedimentary rocks of different metamorphic grade to test Nd isotope equilibrium during metamorphism. Our results show that apatite retains an original, probably detrital, highly variable Nd isotopic signature until at least 500 ˚C before being isotopically homogenized, irrespective of textural context within the rock. Once equilibrated, apatite retains its Nd isotope signature throughout anatexis. In contrast, allanite and titanite are equilibrated at temperatures as low as 350 – 400 ˚C. REE-rich accessory minerals in high-grade rocks (~600 ˚C) show very similar initial εNd values at the time of metamorphism. We conclude that under these metamorphic conditions Nd isotope disequilibrium between crustal melts and metasedimentary sources is unlikely. Intra-grain Nd isotope zoning of monazite indicates that partial melting was open system, involving the injection of externally-derived melt into migmatites. This process, likely to be common in anatectic terranes but not always obvious at hand-specimen scale or from bulk rock geochemical data, can produce isotope variation that could potentially be misinterpreted as disequilibrium between the melt and its protolith

1. Introduction

Crustal melting has a crucial role in the chemical differentiation and stabilisation of continental crust (e.g., Brown, 2010; Sawyer et al., 2011). Nevertheless, there are very few crustal sections where anatexis and the emplacement of large granitic bodies can be directly linked. Geochemists must, therefore, rely on radiogenic isotope analysis (particularly Sm-Nd and Lu-Hf) of igneous rocks to deduce the source and timing of crustal melting (e.g., Patchett and Ruiz, 1989; Maas et al., 1991; McCulloch and Bennett, 1994; Griffin et al., 2000; Zheng et al., 2004; Hawkesworth and Kemp, 2006; Kemp et al., 2007; Condie et al., 2009; Pietranik et al., 2013), and to test large-scale tectonic reconstructions (e.g. McLennen et al., 1990; Wendlandt et al., 1993; Maboko, 2000, Zhang et al. 2007; Dorais et al., 2012). However, the claim of Nd isotope disequilibrium between crustal protoliths and melts (Barbero et al., 1995; Ayres and Harris, 1997; Davies and Tommasini, 2000; Zeng et al., 2005; Perini et al., 2009; Macera et al., 2011) raises important questions about the reliability of the Sm-Nd isotope system for geochronology and for tracing magma sources. This is because the Nd isotope ratio of the melt might not accurately reflect the crustal source rocks, as is widely assumed. Such a situation could potentially lead to erroneous reconstructions of crustal growth and differentiation history.

The Nd and Sm budget of continental rocks is strongly controlled by the accessory phases allanite ($(LREE,Ca,Y)_2(Al, Fe^{3+})_3(SiO_4)(OH)$) and monazite ($(LREE,Th)PO_4$), and to a lesser extent by titanite ($CaTiSiO_5$), apatite ($Ca_5(PO_4)_3(OH,F,Cl)$), and xenotime (YPO_4) (e.g. Spear and Pyle, 2002; Janots et al., 2008). While apatite is a common detrital phase in low-grade metasediments, titanite commonly breaks down during diagenesis or low-grade metamorphic conditions to form Ti-oxides, carbonates and quartz (e.g. Aldahan and Morad, 1988; Morad, 1988). Similarly, allanite is easily weathered (e.g., Price et al., 2005) and is therefore inferred to represent metamorphic growth in most cases (e.g., Gieré and Sorensen, 2004). Factors that govern the stability of monazite in low-grade crustal rocks are not fully understood. Recent work shows that monazite stability in pelitic/psammitic rocks is strongly linked to the behaviour of allanite, as well as to the bulk rock Al/Ca ratio and the pressure of metamorphism (Spear, 2010; Janots et al., 2007, 2008). During prograde metamorphism in Buchan and Barrovian regional metamorphic terrains, detrital monazite is expected to break down to allanite at or near the biotite isograd (e.g., Wing et al., 2003). Higher-grade metamorphism then leads to allanite breakdown and metamorphic monazite formation, typically in the temperature range 500–600 ˚C, leaving monazite as the main LREE host in high-grade metamorphic rocks (Janots et al., 2007, 2008; Spear, 2010; Wing et al., 2003). However, a few studies have shown that the monazite-allanite-monazite transition does not always proceed to completion, as detrital monazite can survive low-grade metamorphism (Rubatto et al., 2001; Krenn et al., 2008).

The dissolution of apatite and monazite during partial melting is sensitive to the conditions of melting (Ayres and Harry, 1997; Zeng et al., 2005). Temperature is the most important factor controlling apatite and monazite solubility in water saturated conditions (e.g., Harrison and Watson, 1984; Pichavant et al., 1992, Kelsey et al., 2008) although monazite dissolution is also closely linked to the water activity (Rapp and Watson, 1986; Montel, 1993; Wolf and London, 1995). It follows that under relatively low temperature, H_2O-rich conditions, the melt obtains its Nd signature mostly from monazite whereas under H_2O-poor conditions the Nd contribution from apatite becomes more significant. Apatite has intrinsically higher Sm/Nd ratios than monazite (e.g., Zeng et al., 2005), and so with time will evolve to relatively radiogenic ^{143}Nd/^{144}Nd. Enhanced apatite dissolution during anatexis can thus lead to derivative melts with elevated ^{143}Nd/^{144}Nd compared to those whose Nd budget is controlled by monazite. However, to generate isotopic disequilibrium between the source rock and the melt, the source has to be isotopically heterogeneous. This means that there needs to be differences in ^{143}Nd/^{144}Nd ratios between the accessory phases in the rock at the time of melting (Barbero et al., 1995). One way to obtain Nd isotope heterogeneities in metamorphic rocks is to preserve heterogeneous detrital Nd signatures in REE-rich accessory phases; e.g., from enclosure by refractory minerals (e.g., monazite inclusions in biotite or quartz), provided that diffusion is slow compared to the time-scale of melting (Ayres and Harris, 1997; Krenn et al., 2008). Furthermore it is also critical that the melt generation, extraction and crystallisation process is short-lived so as to inhibit diffusive Nd isotope re-equilibration between the protolith and melt (Baker, 1989; Zhang et al., 2010 and therein). Despite an awareness of the prerequisites for isotopic disequilibria between source rock and anatectic melt, little is known about the conditions and processes that preserve isotopic heterogeneities during high-grade metamorphism and partial melting.

Recent analytical developments now allow in situ Nd isotope analysis of REE-rich minerals on a sub grain scale (McFarlane and McCulloch, 2007; Yang et al., 2008; Fisher et al., 2011). In situ microanalysis has many advantages over previous studies that utilise bulk-rock Nd isotope data, as it allows assessment of isotope disequilibrium among and between minerals of individual rock samples. Understanding these isotopic inter-phase relationships might be the key for investigating the putative Nd isotope disequilibrium during crustal anatexis.

Here, I present the first systematic test of Nd isotope equilibration during prograde metamorphism of metasedimentary rocks in which the Nd isotope compositions of coexisting accessory minerals allanite, monazite, titanite, apatite and xenotime were measured from petrographic thin sections by laser ablation MC-ICPMS. This reveals the micro-scale variations in these minerals while preserving their textural context within the rock. I found that REE-rich minerals acquire similar initial Nd isotope ratios at temperatures much lower than that required for anatexis, thus ruling out Nd isotope disequilibrium between melt and residue. Our sub-mineral scale approach also allows identification of external melt components with different Nd isotope compositions, which otherwise could be incorrectly interpreted as evidence for disequilibrium.

2. Geological Setting

The metasedimentary samples examined in this study derive from the Delamerian Orogen as exposed in the eastern Mount Lofty Ranges, South Australia (Fig. 1). Samples were collected from the Early Cambrian Kanmantoo Group, which consists of a turbiditic metasedimentary sequence of psammitic and less abundant pelitic protoliths, with intercalated limestone (c.f. Jago et al., 2003 and therein). Detrital zircon age spectra (Gibson and Ireland, 1996) and low ^{143}Nd/^{144}Nd (Foden et al., 2002) indicate diverse, Precambrian continental sediment sources. The Kanmantoo Group underwent regional metamorphism (0.3-0.5 GPa) during the Cambro-Ordovician Delamerian Orogeny, resulting in the formation of a broad and coherent metamorphic zonation (Dymoke and Sandiford 1992; Sandiford et al. 1995, Turner et al, 2009 and therein). The metamorphic grades were established by Arnold and Sandiford (1990), Dymoke and Sandiford (1992) and Cartwright et al. (1995) via mineral assemblages of metapelitic rocks and P-T modelling. Peak metamorphic temperatures varied between ~350 and 700 ˚C over a distance of ~ 55 km, with an average metamorphic field gradient of ~6–7 ˚C/km (e.g., Cartwright et al., 1995).

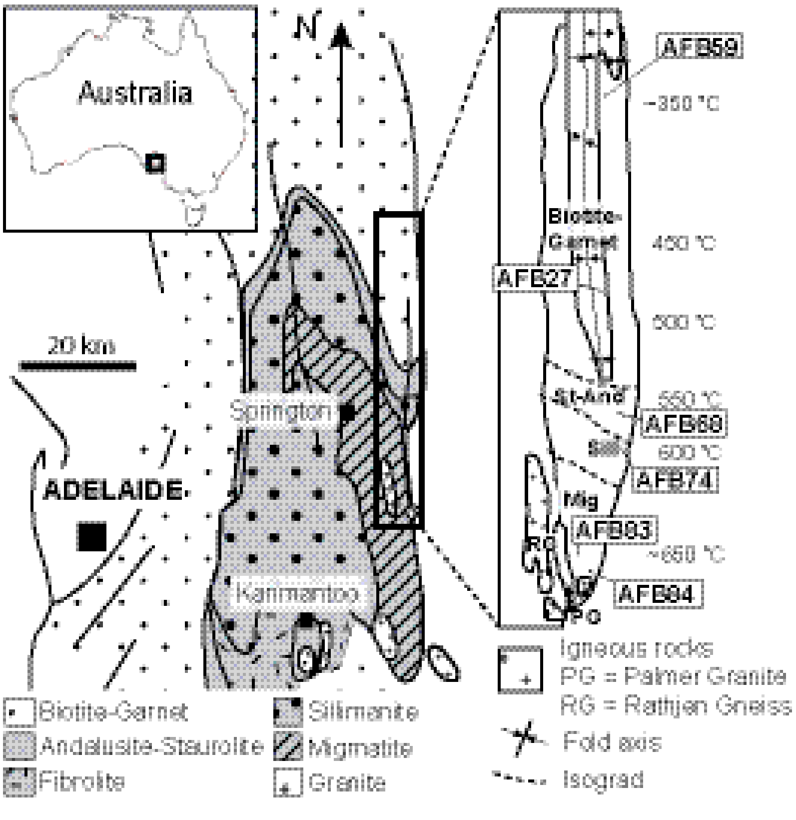

Figure 1: Map of the Eastern Mount Lofty Ranges, South Australia, showing the location of samples with respect to metamorphic zonation (modified after Dymoke and Sandiford, 1992; Oliver et al. 1998; Cartwright et al., 1995).

The metamorphic sequence progrades inwards from low-grade (~350–400 ˚C) greenschist facies rocks in the north to an upper amphibolite facies (~650–700 ˚C) migmatitic core in the southern part of the orogen (Fig. 1). The prograde sequence starts at the biotite zone, which is followed successively by the staurolite-andalusite, and fibrolite/sillimanite zones, before reaching the highest grade at the onset of partial melting in the migmatite zone (Fig. 1). Peak metamorphic assemblages are well preserved and show limited retrogression. Syn-orogenic granitic plutons and widespread dolerites (now metabasites) conceivably provided the heat for high temperature metamorphism, which culminated in extensive (10-25%) partial melting in the presence of excess aqueous fluid (Cartwright et al., 1995). Notably, most syn-metamorphic granitic intrusions are isotopically distinct (εNd ~ -6) from the surrounding Kanmantoo Group metasedimentary rocks (εNd ~ -12 at the time of granitic emplacement) and thus cannot be derived exclusively from such sources (Foden et al., 2002). Geological relationships (see Foden et al., 2002), place a time window on the metamorphism of between c. 525 and 485 Ma, although emplacement of the pre-/ syn-metamorphic Rathjen Gneiss at ~514 Ma, the oldest and largest felsic igneous body in the region, (Foden et al., 1999) may date the onset of high T metamorphism.

3. Samples

A suite of Kanmantoo Group samples that record prograde metamorphic temperatures ranging from ~350 ˚C to ~650–700 ˚C were studied in detail (Fig. 1). In order to compare mineral assemblages we chose rocks with similar psammo-pelitic bulk rock chemistry (see appendix Table A-1). Psammo-pelites/greywackes tend to be coarser-grained than pelites and, hence, more readily permit the study of accessory phases in low-grade metamorphic rocks. A relatively pelitic sample (AFB68, with 16.3 wt.% Al_2O_3, 64 wt.% SiO_2) from the andalusite-staurolite zone was included to investigate the effect of bulk composition on the stability of accessory minerals. All samples, besides pelitic sample AFB68, are chemically rather similar in major (70–75 wt. % SiO_2, 11.4–13.9 wt.% Al_2O_3, 2–4 wt.% K_2O, 0.87–3.4 wt.% CaO, see Appendix Table A-1) and trace element contents (e.g., 30–88 μg g $^{-1}$ Nd; Table 1).

Table 1: Mineral assemblages in the studied samples with modal abundances of the major mineral phases and bulk rock Nd content. Modal abundances of major phases were calculated via mineral / whole rock chemistry budgeting using a similar methodology to that of Spandler et al. (2003).

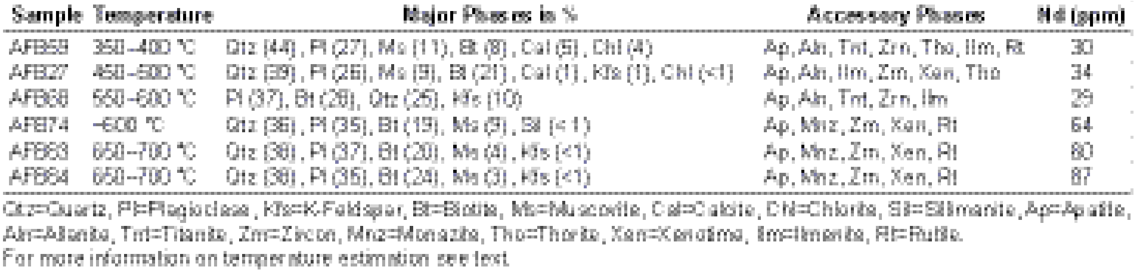

Sample	Temperature	Major Phases in %	Accessory Phases	Nd (ppm)
AFB59	350–400 °C	Qtz (44), Pl (27), Ms (11), Bt (8), Cal (5), Chl (4)	Ap, Aln, Tnt, Zrn, Tho, Ilm, Rt	30
AFB27	450–500 °C	Qtz (39), Pl (26), Ms (9), Bt (21), Cal (1), Kfs (1), Chl (<1)	Ap, Aln, Ilm, Zrn, Xen, Tho	34
AFB68	550–600 °C	Pl (37), Bt (28), Qtz (25), Kfs (10)	Ap, Aln, Tnt, Zrn, Ilm	29
AFB74	~600 °C	Qtz (36), Pl (35), Bt (19), Ms (9), Sil (< 1)	Ap, Mnz, Zrn, Xen, Rt	64
AFB63	650–700 °C	Qtz (38), Pl (37), Bt (20), Ms (4), Kfs (<1)	Ap, Mnz, Zrn, Xen, Rt	80
AFB64	650–700 °C	Qtz (38), Pl (35), Bt (24), Ms (3), Kfs (<1)	Ap, Mnz, Zrn, Xen, Rt	87

Qtz=Quartz, Pl=Plagioclase, Kfs=K-Feldspar, Bt=Biotite, Ms=Muscovite, Cal=Calcite, Chl=Chlorite, Sil=Sillimanite, Ap=Apatite, Aln=Allanite, Tnt=Titanite, Zrn=Zircon, Mnz=Monazite, Tho=Thorite, Xen=Xenotime, Ilm=Ilmenite, Rt=Rutile.
For more information on temperature estimation see text

Sample AFB59 represents the lowest grade metamorphic rock studied (biotite zone ~350 ˚C). It is a calcite-bearing, plagioclase-rich psammite (AFB59), which contains biotite, muscovite and a minor chlorite component (Table 1). The average grain size of the major mineral phases is ~ 100–200 µm. This sample lacks monazite but contains sub-idiomorphic, complexly zoned allanite (≤ 200 µm) (Fig. 2c), while a (Th,U)SiO4 phase, probably thorite, is present as minute (< 10 µm) grains. Titanite is present as tabular grains (Fig. 2), typically < 100 µm in size, and apatite occurs as rounded, sometimes zoned (Fig. 2b) grains with a maximum size of ~ 200 µm. Zircon is present as idiomorphic grains and can reach 200 µm in length. All accessory phases in this sample are located interstitially between other mineral phases or occur at triple junctions.

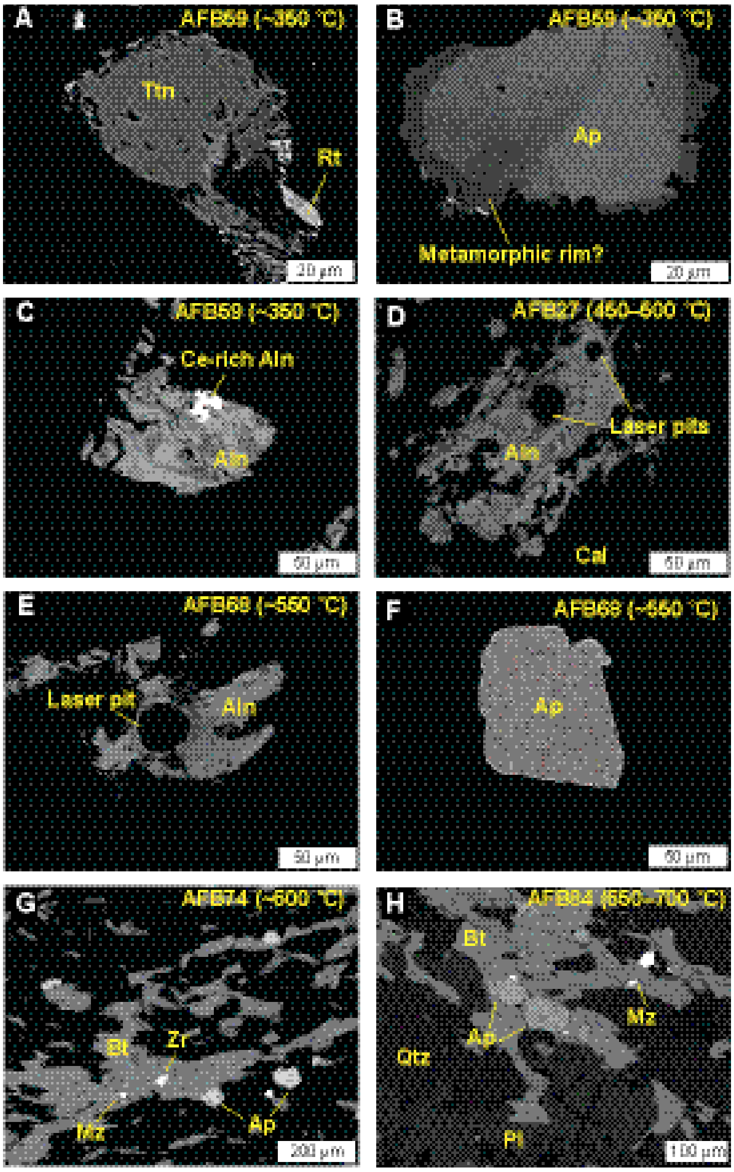

Figure 2: Backscattered electron images of (A) titanite replacing rutile (AFB59), (B) apatite grain with possible metamorphic rim, (C) allanite with a high Ce-zone (AFB59), (D) allanite in sample AFB27 with a complex zonation pattern, (E) allanite in the Ca-richer sample AFB68, (F) sub-idiomorphic apatite grain without zonation, (G) Monazite fully enclosed in biotite and partially biotite-mantled apatite in sample AFB74 that represent the mineral assemblage before partial melting starts, (H) Apatite and monazite inclusions in biotite of migmatite sample AFB84. Dark material is a mixture of plagioclase, quartz and K-feldspar with no visible grain boundaries in the BSE images.

Sample AFB27 from the biotite-garnet zone (450–500 ˚C) contains quartz, biotite, plagioclase and muscovite as the major mineral assemblage. K-feldspar and calcite are present in minor amounts. The average grain size of the major mineral phases is ~100–200 µm. Complexly zoned allanite, up to 200 µm in size (Fig. 2d), is present in calcite-rich layers. Titanite is absent, but small, irregular blebs (< 10 µm) of a (Th,U)SiO4 mineral are probably thorite. Apatite occurs as rounded grains up to 200 µm in diameter and idiomorphic zircons (≤ 200 µm) are scattered throughout the sample. As with AFB59, apatite and the other accessory phases are not found as inclusions but occur at the grain boundaries of the major minerals.

Sample AFB68, from the staurolite-andalusite zone (~560 ˚C), contains a higher CaO content (2.8 wt. %) than samples from the biotite-garnet zone (AFB27; 0.9 wt.% CaO) and sillimanite zone (AFB74, 1.2 wt.% CaO) (Appendix Table A-1). The major mineral phases are plagioclase, biotite, quartz and lesser K-feldspar. The average grain size is between 150¬–200 µm, where the K-feldspars are typically coarser-grained than the other major minerals. The accessory mineral assemblage includes apatite, zircon, titanite, and allanite. The allanite grains in this sample may be complexly zoned and are up 150 µm in size (Fig. 2e). No evidence for retrograde allanite formation was found. Titanite is present as sub-idiomorphic grains, only a few of which exceed 50 µm in size. Subidiomorphic homogeneous apatite (Fig. 2f) and euhedral zircon are typically smaller (≤ 100 µm) than in the previous samples. None of these accessory phases form inclusions in other minerals.

Sample AFB74, a gneissic rock from the fibrolite/sillimanite isograd (~600 ˚C) consists mainly of plagioclase and quartz, followed by biotite and muscovite, while fibrolitic sillimanite is minor (Table 1). This represents the mineral assemblage at P-T conditions immediately below the onset of partial melting. The average grain size of quartz and plagioclase is between 150 and 250 µm, whereas muscovite and biotite plates can reach sizes of ~500 µm. Rutile, zircon, apatite, xenotime and monazite are present as accessory phases. Monazite occurs as small grains (typically < 30 µm), and commonly in clusters, a texture interpreted to result from the reaction of allanite to monazite (e.g., Janots et al., 2007). Monazite grains may be enclosed by biotite (Fig. 2) but also occur interstitial to other minerals. Apatite occurs as rounded grains, typically ~100 µm in size, that are commonly partially (but never fully) enclosed by biotite (Fig. 2g). Zircons are present as euhedral grains (≤ 100 µm) while xenotime occurs as small (≤ 20 µm) sub-idiomorphic crystals. The two samples (AFB83 and AFB84) from the migmatite zone attained temperatures of ~650 to 700 ˚C, corresponding to the onset of fluid-present anatexis (Cartwright et al., 1995). Sample AFB84 is a typical stromatic migmatite with well-defined leucosomes that make up ~25% of the sample, whereas the segregation between leucosome and residual material is less pronounced in sample AFB83, making estimation of the amount of leucosome difficult. Sample AFB83 was collected ~1.5 km to the west of the outcropping Rathjen Gneiss (Fig. 1). This rock contains folded pegmatitic veins that consist of K-feldspar, quartz, plagioclase and minor biotite and muscovite. These veins make up ≤ 5% of the outcrop, lack a complementary melanosome and may be externally derived. Their grain-size varies from centimentre- to millimetre-sized on an outcrop-scale, as typifies pegmatites in high-grade metamorphic rocks. The major minerals in both migmatite samples (AFB83 and AFB84) are plagioclase, quartz, biotite and minor muscovite and K-feldspar (Table 1). The average grain size in sample AFB83 ranges between 200–300 µm for most major minerals, whereas biotite can reach ~500 µm. The average grain size in sample AFB84 ranges from 300–400 µm with biotite up to 600 µm in length. Accessory phases were studied in leucosome and residual parts of the migmatites. Both samples contain apatite grains that reach 250 µm in diameter and some are fully enclosed by biotite (Fig. 2h) or feldspars, or they are located interstitially. Enclosed apatite grains are rounded, whereas interstitial apatite can be xenomorphic. Similarly, monazite grains (≤ 150 µm) occur both as inclusions in biotite, feldspars or quartz, and at grain boundaries between major mineral phases. Xenotime is present as sub-idiomorphic crystals, commonly enclosed in major mineral phases, and can reach ~35 µm in size.

4. Methods

4.1 Element budgeting via mineral and whole-rock geochemistry

Mineral trace element analyses were conducted in situ on polished thin sections by LA-ICP-MS using a Varian 820 quadrupole ICP-MS coupled with a GeoLas Pro 193 nm ArF Excimer laser system at the Advanced Analytical Centre, JCU. Ablation was conducted in He atmosphere and the ICP-MS was tuned to ensure robust plasma conditions (sensitivity of Th≈U≈Pb) (e.g., Pettke, 2008) and low oxide production levels (<0.5 % ThO). Analyses of minerals were carried out on polished 100 µm thick sections, using a laser energy density of 6 J/cm^2 and repetition rates of 10 Hz. The beam diameter varied between 24 and 120 micrometers as dictated by the size of the mineral. All element concentrations were externally standardized using NIST SRM 612 and NIST SRM 610 glass reference materials with concentration values taken from Spandler et al. (2011), and internally standardized using ^{43}Ca for titanite and apatite, ^{31}P for monazite and xenotime, and ^{29}Si for zircon. Final concentrations were calculated using the software package "Glitter" (van Achterbergh et al., 2001; Griffin et al., 2008). Neodymium distribution budgets for each sample were calculated by multiplying the average Nd content of each mineral by the respective mineral modal proportion (calculated using least squares regression), and then normalizing to bulk rock Nd content (see Appendix for further details). The calculated mineral proportions agree with petrographic observations of several thin sections per sample. For all studied samples, the least-squares calculations show low residuals ($\sum r^2 < 1$) that reflect accurate mineral phase proportion calculations (see appendix for details, Fig. A-2).

4.2 In situ Sm-Nd isotope microanalysis

In situ isotopic analyses were carried out at the Advanced Analytical Centre at James Cook University (JCU) in Townsville, using a ThermoScientific NEPTUNE MC-ICP-MS coupled to a Geolas 193 nm ArF excimer laser. The faraday cup configuration is the same as that used by McFarlane and McCulloch (2007) and is presented together with other instrumental parameters in the Appendix (Table A-2). In situ laser ablation analyses were conducted on polished thin sections over 60 seconds with spot sizes of 16–90 µm, pulse rates of 4 Hz and a laser energy density at the sample site of 5-6 J/cm^2, as determined by an energy meter. Ablation was carried out in He (typical flow rate ~0.9 l/min), which was combined with Ar (~0.8 l/min, optimized daily) and N_2 (~0.005 l/min) prior to transport into the torch. Interference and mass bias corrections were made according to the method of Fisher et al. (2011). The ^{147}Sm/^{144}Nd ratios were calibrated against a synthetic LREE-rich silicate glass (^{47}Sm/^{144}Nd = 0.2451; Fisher et al. 2011), which was routinely analysed throughout each session. Sample mineral ^{143}Nd/^{144}Nd ratios were further normalized to bracketing analyses of Nd-doped glass (JNdi-1, TIMS ^{143}Nd/^{144}Nd = 0.512098 ±13, Fisher et al., 2011).

We used three apatite grains as quality control material: Ap1 and Ap2 from Yang et al. (2008) and Durango Apatite. Our ^{143}Nd/^{144}Nd results for Ap1 and Ap2 of 0.511316 ± 39 (2SD) and 0.510958 ±45 (2SD), respectively, agree well with those reported by Yang et al. (2008) (Ap1 = 0.511342 ± 31 (2SD) and Ap2 = 0.510977 ± 39 (2SD)). Our analyses of Durango Apatite gave ^{143}Nd/^{144}Nd values of 0.512468 ± 39 (2SD), which is in good agreement with the ratios acquired by LA-MC-ICP-MS reported in Foster and Vance (2006) (0.512469 ±25) (2SD) and by Fisher et al. (2011) (0.512463 ± 48), and the TIMS value of 0.512489 ± 12 (Fisher et al., 2011). Our ^{143}Nd/^{144}Nd result for the LREE glass is 0.512098 ± 29 (2SD) is indistinguishable from the value determined by TIMS (0.512098 ±13, Fisher et al., 2011).

4.3 Whole Rock Sm–Nd isotope analysis

Whole rock isotope analyses were performed at the University of Adelaide with a Finnigan MAT262 thermal ionization mass spectrometer (TIMS), in static and quadruple cup dynamic measurement modes following the routine described in Wade et al., (2006). The measurements were corrected for mass fractionation by normalization to ^{146}Nd/^{144}Nd = 0.7219. Reference material JNdi-1 yielded ^{143}Nd/^{144}Nd = 0.512074 ± 20 (2SD) (n=5). Whole rock ^{143}Nd/^{144}Nd ratios were normalized to the TIMS value of JNdi-1 (0.512098 ±13, Fisher et al., 2011). All age and isochron calculations were produced with Isoplot/Ex (Ludwig, 2003).

5. Results

5.1 Trace elements

Titanite and allanite show a narrow range of REE patterns within low-grade metamorphic zones (see Appendix Fig. A-1). In contrast, apatite grains in low-grade (< 500 ˚C) samples have a wide range of trace element concentrations (e.g., 30 – 3000 μg g $^{-1}$ Nd), although this greatly contracts at temperatures above 550 ˚C (Fig. 3). Despite variation from sample to sample, the Nd concentration in apatite at ≥ 550 ˚C is mostly < 1000 μg g $^{-1}$. The same striking "homogenization-effect" can be observed for all the other REE and Sr in apatite (Fig. 3; see Appendix Fig. A-3).

Titanite, allanite and monazite are important Nd hosts (Fig. 3). Allanite and monazite sequester ~2.5 wt.% and ~10 wt.% Nd, respectively, whereas titanite contains < 3000 μg g $^{-1}$ Nd in the lowest-grade sample (AFB59) and < 400 μg g $^{-1}$ in the metapelitic sample at ~ 550 ˚C (AFB68). Trace element distribution calculations show that in low-grade rocks (< 500 ˚C) and in the Ca-enriched sample (AFB68; ~560 ˚C), allanite is the main Nd host. In low grade-rocks (< 500 ˚C), titanite (21 %) and apatite (14 %) are major contributors to the bulk rock Nd concentration. At higher metamorphic grades, however, the importance of titanite and apatite as Nd hosts decreases dramatically (≤ 6%), where upon more than 90 % of the bulk rock Nd is stored in allanite or monazite (Fig. 3c). Zircon is a very minor contributor to the whole-rock Sm-Nd budget, limiting the capacity of this phase to cause melt-residue disequilibrium for Nd isotopes (c.f., Paterson et al., 1992). Zircon, together with xenotime and $ThSiO_4$ phases, collectively host 4 % or less of the bulk rock Nd content (Fig 3c). Major mineral phases such as feldspars and micas host <1% of the total Nd and their potential influence on Sm-Nd isotope systematics can therefore be disregarded (see appendix Fig. A-2).

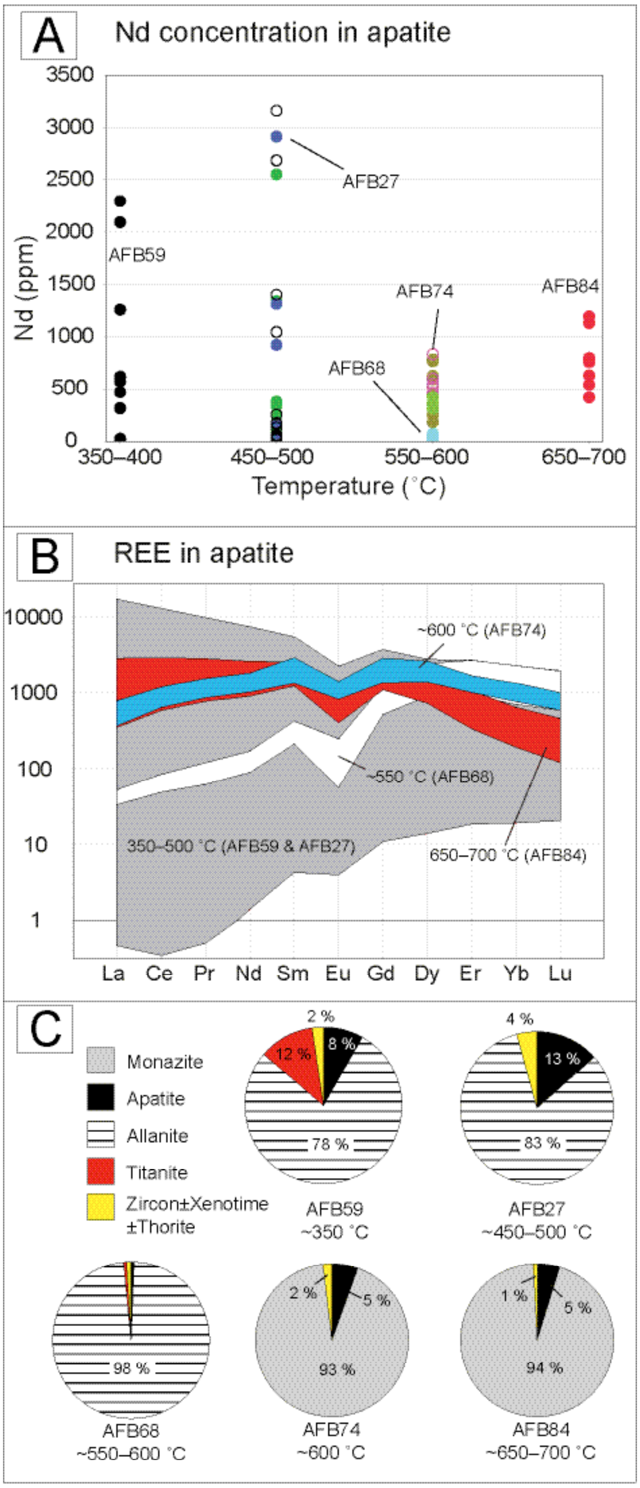

Figure 3: A) The Nd concentration in apatite from the prograde sample suite. Each colour represents an individual sample. Samples from which Nd isotopes were measured are labelled. B) chondrite-normalised REE patterns of apatite in metasedimentary samples as a function of metamorphic grade (normalizing values of Taylor and McLennan, 1985). Sample AFB68 that has a higher Ca-content and contains allanite has apatite with a positive REE slope, which suggests LREE fractionation during apatite recrystallization and allanite resorption. C) Proportion of whole rock Nd hosted by the accessory phases based on modal abundances determined by bulk rock – accessory phase budgeting.

5.2 Nd isotope analysis

Figure 4 plots the εNd values at 500 Ma of the various accessory phases as a function of inferred metamorphic temperature. Apatite in low-grade rocks exhibits a wide range of values that spans almost 30 epsilon units. However, as observed with the trace element concentrations, apatite becomes isotopically equilibrated for Nd at temperatures ~500-550 ˚C (Figs. 3, 4). Unlike apatite, titanite and allanite show homogenous initial $\varepsilon Nd_{(500)}$ values in the lowest-grade sample (AFB59) (Fig. 4, Table 2). In the higher-grade sample (AFB74) monazite also has homogeneous initial εNd, irrespective of textural context within the rock.

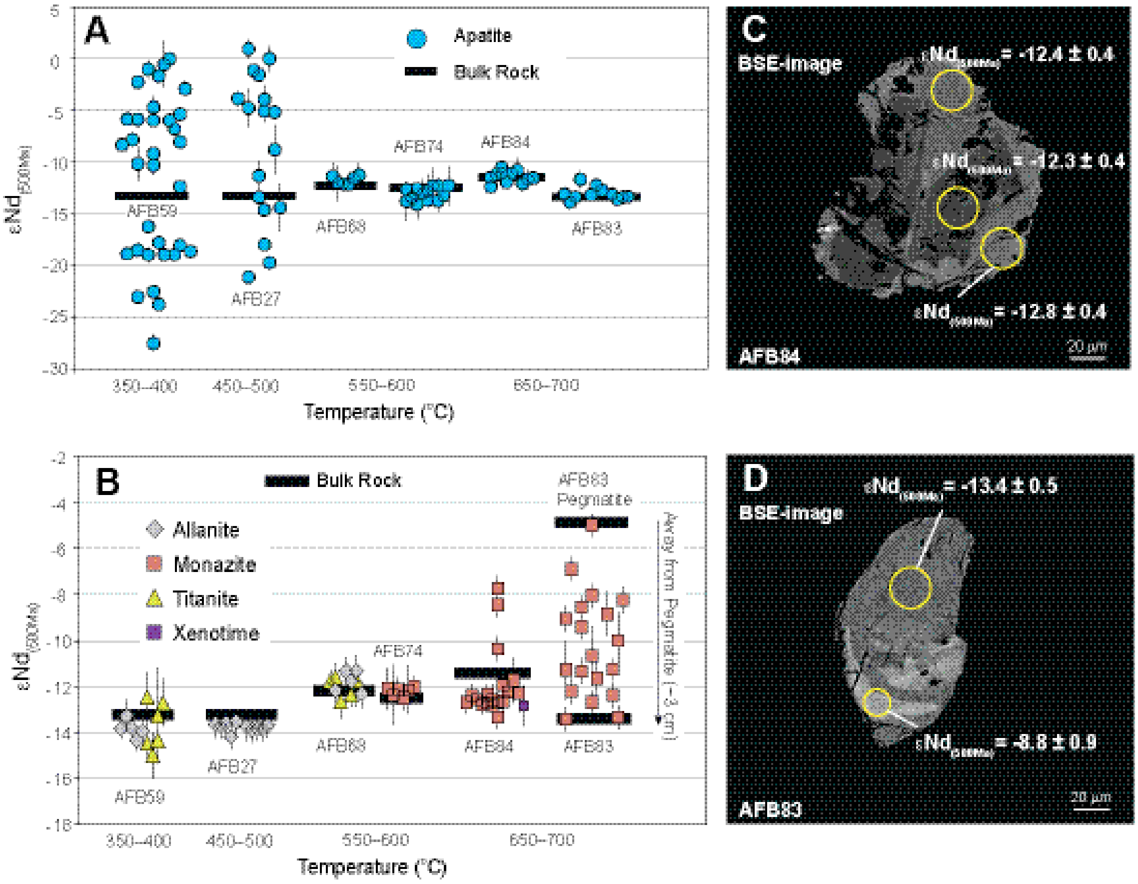

Figure 4: A) and (B) Variation of εNd values in (A) apatite, and (B) other REE-rich accessory phases upon prograde metamorphism. 'AFB83 Pegmatite' refers to the pegmatite vein hosted in migmatite AFB83. Error bars are 2 sigma. C) Zoned but isotopically homogeneous monazite from sample AFB84. D) Zoned, isotopically heterogeneous monazite from sample AFB83. The high εNd in the overgrowth records interaction between host rock monazite and relatively radiogenic externally-derived pegmatite melt. Initial Nd ratios were corrected back to 500 Ma ($\varepsilon Nd_{(500Ma)}$) which is the best estimate of the peak metamorphic age (Foden et al., 2002) and is consistent with the Sm-Nd isochron (Fig. 5).

The situation is, however, more complicated for the migmatites. In migmatite sample AFB83, there is a systematic relationship between the εNd values of monazite and the distance of the analysed grain from the pegmatite vein within the rock. Those grains farthest (> 3 cm) from the vein have low εNd values (~ -13) that overlap those of coexisting apatite and typical Kanmantoo Group metasedimentary rocks (Table 2, Fig. 4). Monazite grains closer to the pegmatite vein have overgrowths with relatively radiogenic Nd, approaching the whole rock ^{143}Nd/^{144}Nd of the vein (εNd$_{(500Ma)}$ ~ -5). Monazite grains actually located within the vein have the same Nd isotope signature as the bulk pegmatite (Fig. 4). U-Pb ages of monazite in AFB83 are ~ 500 Ma, irrespective of their Nd isotope signatures and location within the migmatite sample, thus precluding relict inherited monazite as being the cause of the heterogeneity (see Appendix Fig. A-4 and Table A-3). The whole rock Nd data are consistent with this pegmatite vein (Table 2) having been injected from igneous bodies similar to that represented by the nearby (~ 1.5 km) Rathjen Gneiss (εNd ~5.5; Foden et al., 2002), rather than being generated by melting of the host metasedimentary sequence. In migmatite sample AFB84 there is no obvious externally-derived leucosome (former melt) present, and most of the monazite has very similar εNd$_{(500Ma)}$ (Fig. 4). However, we identified a single monazite grain that has considerably higher ^{143}Nd/^{144}Nd (Fig. 4), despite the core and rim yielding indistinguishable U-Pb ages (~ 500 Ma, see Appendix Table A-3). The euhedral shape and large size (~ 400 µm) of this grain implies crystallization from melt. We attribute this Nd isotope variation to reflect a small, but otherwise cryptic, component of externally derived melt in sample AFB84.

Table 2: Average initial εNd values (± 2σ) of various accessory phases compared to that of their corresponding bulk rocks. Monazites from sample AFB83 represent those furthest away from the pegmatite vein (>3 cm) and for sample AFB84 the zoned, radiogenic monazite grain (Fig. 4) has been excluded.

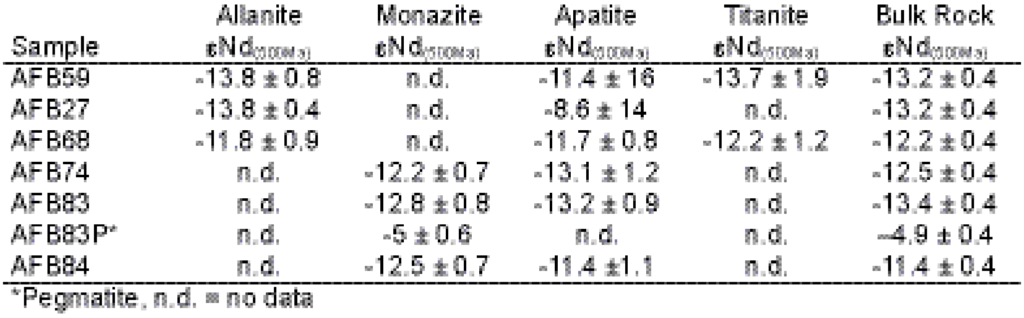

Sample	Allanite εNd$_{(500Ma)}$	Monazite εNd$_{(500Ma)}$	Apatite εNd$_{(500Ma)}$	Titanite εNd$_{(500Ma)}$	Bulk Rock εNd$_{(500Ma)}$
AFB59	-13.8 ± 0.8	n.d.	-11.4 ± 16	-13.7 ± 1.9	-13.2 ± 0.4
AFB27	-13.8 ± 0.4	n.d.	-8.6 ± 14	n.d.	-13.2 ± 0.4
AFB68	-11.8 ± 0.9	n.d.	-11.7 ± 0.8	-12.2 ± 1.2	-12.2 ± 0.4
AFB74	n.d.	-12.2 ± 0.7	-13.1 ± 1.2	n.d.	-12.5 ± 0.4
AFB83	n.d.	-12.8 ± 0.8	-13.2 ± 0.9	n.d.	-13.4 ± 0.4
AFB83P*	n.d.	-5 ± 0.6	n.d.	n.d.	–4.9 ± 0.4
AFB84	n.d.	-12.5 ± 0.7	-11.4 ±1.1	n.d.	-11.4 ± 0.4

*Pegmatite, n.d. = no data

The initial Nd isotope ratios of the in situ mineral analyses agree with that of the corresponding bulk rock – notable exceptions being apatite in the low-grade samples (Table 2, Fig. 4), monazite relatively close to the pegmatitic vein (sample AFB83) and the slightly lower initial Nd ratios of monazite in sample AFB84. On an Sm-Nd isochron diagram, analyses of monazite (excluding the strongly zoned grain), apatite and xenotime of migmatite sample AFB84 define an array corresponding to an age of 512±22 Ma (Fig. 5), which falls within the permissible time-window for metamorphism (~514–485 Ma, Foden et al., 1999, 2002). In contrast, sample AFB83 yields a poorly defined Sm-Nd isochron due largely to the scattered Nd isotopic signatures of constituent monazite (Appendix Fig. A-5).

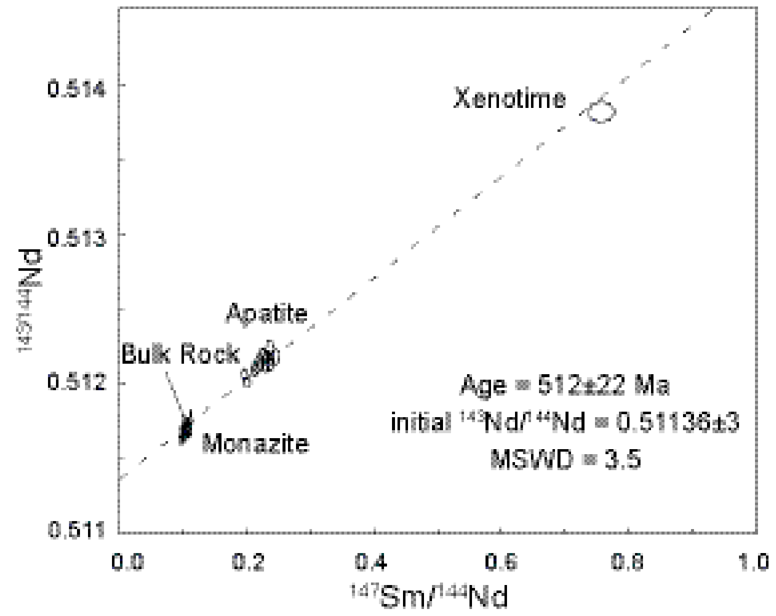

Figure 5: Sm-Nd isochron diagram for migmatite sample AFB84. Data ellipses represent 2 sigma uncertainties. In this case, the additional data from the rare xenotime grains with high Sm/Nd helps define a robust Nd isotope isochron.

6. Discussion

6.1 Nd-bearing accessory phase relations

The lowest-grade sample (AFB59) contains autogenic titanite that most likely formed via the reaction calcite + Ti-oxide + quartz = titanite. This mechanism is supported by the observed mineral assemblage and by overgrowths of titanite on rutile (Fig. 2a). Rounded apatite grains with heterogeneous REE contents are probably of detrital origin and have not been homogenized at these low metamorphic grades. The growth of sub-idiomorphic allanite most likely followed the monazite-allanite transformation during diagenesis or low-grade metamorphism, as suggested by Janots et al. (2007; 2008). Sample AFB27 (~450–500 ˚C) contains the largest allanite crystals found in the studied samples. The presence of allanite in this rock agrees with the proposed stability field of allanite in rocks of similar chemical compositions (e.g., Spear, 2010; Wing et al., 2003; Janots et al., 2007, 2008). Apatite in the same sample still preserves REE heterogeneity, suggesting that it was not fully homogenised at temperatures between 450 and 500 ˚C. The higher CaO contents in sample AFB68 (~560 ˚C) extended the stability field of allanite towards higher temperatures (Spear, 2010) and also stabilised titanite. The restricted range of REE concentration between apatite grains in AFB68 and the absence of zoning (Fig. 2f) suggests that this phase recrystallised at ~550 ºC. The reappearance of monazite at ~ 600 ˚C (AFB74) agrees with the proposed allanite decomposition reaction at temperatures below 600 ˚C for similar bulk rock compositions (Janots et al., 2007, 2008; Spear, 2010). Furthermore, the presence of small xenotime grains is also consistent with the allanite-monazite transformation (e.g., Janots et al., 2008). As with sample AFB68, apatite shows a relatively homogenous REE pattern that suggests that apatite has been recrystallised.

As the studied samples represent typical psammo-pelitic metasedimentary rocks, and the observed Nd-bearing accessory mineral assemblages conform to stability relations expected for the metamorphic conditions and compositions, the evaluation of trace element distribution and isotope homogenization are relevant for numerous metasedimentary suites and associated melt production upon anatexis.

6.2 Nd isotope homogenization between accessory phases

The scattered trace element concentrations and $\varepsilon Nd_{(500Ma)}$ values in apatite in the low-grade samples strongly suggests that apatite retains its original detrital geochemical signature during metamorphism, up to at least 500 ˚C. On the other hand, the very similar and homogeneous Nd-isotope signatures of early metamorphic phases allanite and titanite at lower temperatures (350–400 ˚C) are consistent with equilibration. Despite the relatively radiogenic Nd contained by detrital apatite in low-grade rocks (≤ 500 ˚C), the Nd isotope ratios of the early metamorphic phases agree well with bulk rock data (Fig. 4). The implication is that apatite contains insufficient Nd in this case to exert a strong influence on the whole rock Sm-Nd budget (Fig. 3c). However, apatite might have been involved in the formation of early metamorphic REE-bearing phases via reactions such as: 1) detrital Mz + detrital Ap = Aln + Ap, or 2) MREE-rich detrital Ap + Rt + Cc + Pl = Tit + Ap. If these reactions take place at similar P-T conditions, isotopic equilibration between early metamorphic phases would be facilitated.

Despite the overall small fraction of Nd hosted in apatite, it remains possible that in sedimentary packages with much higher apatite fractions, the initial Nd values in early metamorphic accessory phases might not reflect bulk rock Nd signatures due to retention of radiogenic Nd in unequilibrated detrital apatite. The homogeneous Nd isotope signature of allanite in the lowest-grade sample (AFB59), together with petrographic observations and the fact that the isotope signatures agree reasonably well with the bulk rock data, implies that allanite formed at low metamorphic temperatures (≤ 350 ˚C). Most allanite forming reactions at low metamorphic grades consume detrital monazite and produce apatite (e.g., Janots et al., 2008). However, the analysed apatite grains appear to have retained detrital Nd isotope and REE signatures up to 500 ˚C (Figs. 3a,b, 4), that is well above the formation of first autogenic allanite. According to element budget calculations, the modal abundance of apatite is at least 3 times higher than monazite. We calculate that a maximum of 25 % new apatite can be formed upon phosphorous release by detrital monazite dissolution prior to allanite formation at temperatures < 350 ˚C (assuming that no phosphorous is lost via a fluid). Such newly formed apatite might occur as isotopically non-resolvable rims on pre-existing apatite grains (Fig. 2b), or as small grains of a minor new apatite population.

The isotopic homogeneity between titanite and allanite can be explained by the concurrent formation of these minerals within a certain temperature window (≤350 ˚C). Neodymium isotopes fully equilibrate amongst Nd-bearing accessory phases in the temperature range 500–550 ˚C (Fig. 4) when allanite is expected to break down to monazite, and detrital apatite recrystallises (Nutman, 2007; Janots et al., 2008; Spear, 2010). I suggest that the Nd-isotope equilibration in apatite at ≥ 500 ˚C, together with the observed homogenization of REE, is controlled by apatite recrystallization, thus allowing chemical and isotopic exchange with co-existing REE-rich phases. This interpretation assigns only a subsidiary role for diffusion in chemical/isotopic equilibration, which is in accord with expected slow rates of REE diffusion in apatite at these temperatures (Cherniak, 2000). However, in the relatively pelitic, Ca-rich sample AFB68, which contains stable allanite at ~550 ˚C, coincident allanite/monazite transformation and apatite recrystallization can be ruled out. The homogeneous trace element pattern and Nd isotope values of apatite show that apatite must have homogenized at an earlier stage, independently from allanite-monazite transition reactions (Figs. 3, 4). The LREE-depleted REE pattern in these apatite grains suggests that apatite loses LREE during recrystallization (Figure 3b). Allanite would be the most likely new host for released LREE; however, we were not able to resolve LREE zoning on individual allanite grains to confirm this.

The indistinguishable εNd values (within analytical uncertainty) of monazite grains enclosed by biotite or located between quartz and feldspar in migmatite leucosomes (AFB84) provides a strong argument against preservation of heterogeneous initial ^{143}Nd/^{144}Nd of enclosed accessory phases in minerals that do not participate significantly in melting reactions (c.f. Bea et al., 1994; Perini et al., 2009). The reason for this is that monazite becomes homogenous with the same age-corrected Nd isotope composition as the bulk rock at temperatures well below the onset of partial melting. In metapelites of Barrovian metamorphic sequences, garnet commonly forms at temperatures < 550 ˚C and garnet porphyroblasts could potentially enclose apatite grains with detrital isotope signatures. However, my results show that monazite and/or allanite control the

Nd budget, to which apatite is only a minor contributor. Armouring of isotopically heterogeneous apatite by garnet is therefore unlikely to cause isotope disequilibrium between anatectic melts and restitic material.

The Nd isotope systematics of monazites in migmatite AFB83 appear to record variable interaction between the relatively radiogenic injected pegmatite melt and the host migmatite (Fig. 4b,d). This observation, together the identification of relatively radiogenic rims on zoned monazite in sample AFB84, demonstrates the capacity of externally derived melt to infiltrate and modify the chemical and isotope composition of host rocks at a sub-grain scale. Indeed, the slightly higher whole rock εNd value of AFB84 relative to most monazite in the same sample plausibly reflects the influence of a small, but pervasive external melt component. Care is therefore required in the assignment of “isotopic disequilibrium” during melting, and in evaluating mass balance constraints between melts and apparent source rocks.

This study shows that REE-rich accessory phases in metasedimentary rocks, although initially markedly heterogeneous in Nd isotope composition, are isotopically equilibrated at <600 ˚C at ~0.3–0.5 GPa. Minimum-temperature melts formed via fluid induced melting at ≥650 ˚C will therefore reflect the Nd isotope composition of their metasedimentary protolith. Clemens (2005) and Brown (2013) suggest that the more common and relevant process for granitic melt production in the crust involves fluid-absent or dehydration melting. In such systems, the breakdown of hydrous minerals such as micas liberates the H_2O necessary for melt production. Importantly, however, in this scenario, higher temperatures are required for melting. In metapelitic rocks, muscovite schists partially melt at 750˚C at 0.6 GPa, whereas higher temperatures are needed to generate melt in biotite-schists (e.g., Patino-Douce and Harris, 1998). In both cases, the solidus has a positive slope in P-T space, which means that at higher pressures even higher temperatures are required to produce melt. Experiments have shown that at ~ 0.5 GPa metagreywackes undergo melting at ≥800 ˚C (e.g., Stevens et al., 1997). Clemens (2006) concludes that significant partial melting in most fertile metasedimentary rock types occurs at temperatures of around 850 ˚C. A much larger temperature window would therefore be available for subsolidus isotopic homogenization amongst accessory phases than observed in our study. The implication is that melt-source equilibration for Nd isotopes may be the general case for anatexis of metasedimentary rocks, over a range of crustal P-T conditions and irrespective of the type of melting reaction.

7. Conclusions

My results suggest that Nd isotope disequilibrium between a metasedimentary protolith and melt is very unlikely under most crustal anatectic conditions. Neodymium isotopes in such systems remain faithful tracers of source composition and average crustal residence age. REE-rich accessory phases are sensitive monitors of the injection of externally-derived melt into migmatites, as is commonly inferred in anatectic terranes (e.g. Sawyer, 1991) – the resulting isotopic variations in the rock reflect open-system melting, not disequilibrium between Nd-hosting phases during anatexis. The injected pegmatite vein in sample AFB83 represents an example of external melt that isotopically modified its migmatitic host. This finding has important implications for geochemical mass balance studies of migmatites where it is assumed that leucosomes were generated in situ (e.g., Johannes et al., 1995; Ayres and Harris, 1997) – clearly, it is critical to characterise leucosomes isotopically before mass balance calculations are conducted. Moreover, our results show that in situ Nd isotope analysis can pinpoint pervasive infiltration of externally-derived melt into migmatitic rocks (potentially from different layers of the sedimentary pile), which cannot be easily resolved otherwise (e.g., by bulk rock analysis). Neodymium isotopes in REE-rich accessory minerals may therefore offer a means to further understand the scale and mechanism of melt transfer through deep crustal terranes (e.g., Weinberg, 1999).

This study also sheds new light on the behaviour of apatite during prograde metamorphism. The data suggest that apatite recrystallization in metasedimentary rocks may not always be mutually linked to monazite/allanite reactions and/or transitions. Furthermore, apatite appears to be a relatively robust mineral in high-grade rocks that is less sensitive to external melt infiltration - at least under the HT/LP conditions investigated here. Lastly, the discovery that apatite preserves its detrital Nd isotope signature up to ~500 ˚C also encourages sediment provenance studies where apatite is used to trace the sediment source based on initial Nd isotope ratios (e.g., Foster and Carter, 2007), even where the host rock has undergone a moderate degree of metamorphism.

Chapter 4

Element redistribution and mobility during upper crustal metamorphism of metasedimentary rocks: An example from the Eastern Mount Lofty Ranges, South Australia

Abstract

In this paper, I present a detailed study on element mobility during prograde metamorphism in the eastern Mt. Lofty Ranges, South Australia. Mineral and bulk rock compositions were monitored across a regional metamorphic gradient from ~350–400 ˚C to migmatite grade (~ 650–700 ˚C) at ~0.3–0.5 GPa, where pervasive up-temperature fluid flow during metamorphism has been proposed previously. The results show that major and rare earth elements and most other trace elements are isochemical during metamorphism as they are effectively redistributed into newly formed major minerals or accessory phases. Monazite or allanite and xenotime control the whole rock concentration of REE whereas apatite and titanite are minor REEs hosts. The only non-volatile mobile elements are Zn, Pb, Cs and As whose concentrations decreased with increasing metamorphic grade. The Zn and Pb depletion was progressive with increasing temperature in staurolite-absent psammopelites, with losses of ~ 75% of the original Zn and ~ 50 % of the original Pb from the rocks from high-grade metamorphic zones. Arsenic contents decrease rapidly at the greenschist/amphibolite facies boundary, while Cs depletion is observed at the transition to migmatite grade.

1. Introduction

Understanding the behaviour of major and trace elements during prograde metamorphism is fundamental for our understanding of the geochemical evolution of the Earth's crust and the formation of orogenic orebodies. Geochemical alteration accompanying prograde regional and contact metamorphism has been addressed in numerous studies (e.g. Shaw, 1954; Schwarcz, 1966; Wodzicki, 1971; Ronov et al., 1977; Ferry, 1983; Haack et al., 1984; Giére et al., 1988; Oliver et al., 1994; Ague, 1994; Moss et al. 1995; Roser and Nathan, 1997; Masters and Ague, 2005; Pitcairn et al., 2006; Corrie and Kohn, 2008; Garofalo, 2012), but, there is no overall consensus for element mobility during metamorphism, with the exception of general agreement of the mobility of volatile phases, such as H_2O and CO_2. Several studies have claimed that elements are mobile during progressive metamorphism of sedimentary rocks. Haack et al. (1984) reported loss of Cu, Tl, Ba, Pb, Bi, Hg, Sr, Zn and Cd between the biotite isograd and partial melting in regional metamorphosed pelites (0.3–0.6 GPa) of the Damara Orogen, South West Africa, while Ague (1994) proposed loss of Si, P, Na and potentially Ca and Sr with increasing metamorphic temperatures during Barrovian metamorphism of Wepawaug Schists, Connecticut, USA, as well as an enrichment of Mn, Zn, K and Ba in high-grad metamorphic metapelites. Pitcairn et al. (2006) investigated a suite of Alpine and Otago schists in New Zealand that reach upper amphibolite facies (~ 1 GPa) and found a systematic depletion of Au, Ag, As, Sb, Hg, Mo and W during metamorphism, while no systematic change in concentrations of the other trace elements or major elements was observed. Roser and Nathan (1997) evaluated element mobility in psammites and pelites during lower greenschist to amphibolite facies metamorphism of a turbiditic sequence of the Greenland Group, New Zealand, and except for a depletion of Ba and As in high-grade metamorphic rocks, little compositional contrast between rocks from different metamorphic grades was observed. Furthermore, they attributed Ca and Sr enrichment to subsequent homogenization of minor calcareous horizons within the sedimentary sequence. Apart from heavy rare earth elements (HREE) enrichment upon increasing metamorphic grade, Ronov et al. (1977) described regional metamorphism as a generally closed system, and Moss et al. (1995, 1996) argued that only volatile components are mobilised during metamorphism. These authors suggest that differences in concentration ratios during between pelitic rocks of different metamorphic grade is due to protolith variability. More recently, Garofalo (2012) inferred near isochemical behaviour of a suite of HP metamorphic schists at a regional scale. The only elements that potentially showed mobility with metamorphism were Si, B and Li.

Notwithstanding any intrinsic fluid flux variations (and hence variable element mobility potential) that might be expected across the spectrum of regional metamorphism in different tectonic and thermal regimes (e.g., Oliver, 1996; Oliver et al., 2006), all the above studies were confronted with the uncertainty of the chemical variation of protoliths of a prograde metamorphic suite that complicate interpretations of element mobility during metamorphism (e.g., Moss et al., 1995, 1996; Cardenas et al., 1996; Cullers, 2002). Thus, information on element mobility due to metamorphism can only be obtained if the affect of protolithic variability on element concentrations can be identified and accounted for. Bulk rock analyses combined with mineral chemistry studies permit a better evaluation of element (re-) distribution, element loss, and/or element gain during metamorphism, as elements and their host minerals can be monitored across metamorphic grades. This approach has been successfully used to investigate element mobility during high-pressure subduction-related metamorphism (e.g., Spandler et al., 2003; Korh et al., 2009) and relatively high temperatures (> 500 ˚C) metamorphism of pelites and migmatites (e.g. Bea et al., 1994; 1996; Bingen et al., 1996Bea and Montero, 1999). In contrast, only a few studies have addressed bulk rock chemistry behaviour together with major and trace element (re-) distribution on a mineral and sub-mineral-scale during prograde metamorphism at upper crustal conditions (e.g., Lebedev and Nagaytsev, 1980; Pitcairn et al. 2006, 2010).

Studies of accessory phases (Bea and Montero, 1999; Pyle et al., 2001; Wing et al., 2003; Fitzsimons et al., 2005; Janots et al., 2008; Berger et al., 2009) have shown a strong link between bulk rock compositions and stablility of accessory phases Therefore, studying element distribution/ mobility in mineral phases not only helps to identify potential processes that lead to element enrichments, but they are also crucial to define stability fields of accessory phases that are used as U-Pb geochronometers (e.g. monazite, allanite, zircon, apatite, titanite, xenotime) and isotope tracers (such as Nd, Sr, and Hf) to appropriately constrain crustal evolution processes.

This study focuses on element mobility in a suite of LP/HT rocks from the Mt. Lofty Ranges, (South Australia), which underwent widespread up-temperature fluid flow during metamorphism (Cartwright et al., 1995; Oliver et al., 1998). The presence of fluid is essential for element mobility during metamorphism. The documented widespread up-temperature fluid flow towards the migmatitic core of the Eastern Mt. Lofty Ranges (Fig. 1) during metamorphism (Cartwright et al., 1995 and Oliver et al., 1998) permits an excellent opportunity to investigate element mobility in a prograde metamorphic sequence. I monitor the compositions of major elements and a comprehensive set of trace elements in each mineral phase during progressive metamorphism. This allows unique insight into element (re-) distribution amongst mineral phases that can be compared with bulk rock properties upon progressive metamorphism. I also discuss the conditions most favourable (e.g., pervasive fluid flow) for element mobility during prograde metamorphism.

2. Geological Background

The samples studied in this contribution come from the Kanmantoo Group in the Eastern Mount Lofty Ranges, South Australia (Fig. 1), which consists of a rapidly deposited turbiditic metasedimentary sequence of psammitic and lesser pelitic protoliths with intercalated limestone (c.f. Jago et al., 2003 and therein). Detrital zircon age spectra (Gibson and Ireland, 1996) and low 143Nd/144Nd (Foden et al., 2002, Hammerli et al., 2014a) indicate diverse, Precambrian continental sediment sources. The Kanmantoo Group sediments underwent regional low pressure (0.3-0.5 GPa) metamorphism during the Cambro-Ordovician Delamerian Orogeny that was caused by convergent tectonism along the paleo-Pacific margin of Gondwana resulting in the formation of a broad and coherent metamorphic zonation (Dymoke and Sandiford 1992; Sandiford et al. 1995, Turner et al, 2009 and therein). The metamorphic grade distribution around a high-grade migmatitic core were established in studies by Offler and Fleming (1968), Arnold and Sandiford (1990), Dymoke and Sandiford (1992) and Cartwright et al. (1995) via mineral assemblages in metapelitic and carbonate rocks and pressure-temperature modelling.

Over ~ 55 km, metamorphic temperatures range from 350–400 ˚C to ~650–700 ˚C, resulting in an average metamorphic field gradient of ~6–7 ˚C/km (e.g. Cartwright et al., 1995). The metamorphic sequence progrades from low-grade (~350–400 ˚C) biotite zone greenschist facies rocks in the north and west, through a staurolite-andalusite zone, to an upper amphibolite facies (~650–700 ˚C) core in the the firbrolite/sillimanite zone in the southern and eastern part of the belt, that locally reached migmatite grades (Fig. 1). Rock samples preserve peak metamorphic mineral assemblages with limited retrogression. Syn-orogenic granitic plutons and abundant dolerites (now metabasites) are found within the highest-grade rocks and may have contributed directly to the thermal budget (see Foden et al., 2002 and therein). Cartwright et al. (1995) and Oliver et al. (1998) studied oxygen and carbon isotopes systematics in metapelites, metapsammites and metacarbonates across two prograde traverses (Fig. 1). The large isotopic shifts, affecting every rock type, were inferred to indicate widespread pervasive up-temperature fluid flow towards the high-grade metamorphic (migmatitic) core of the Fold Belt. Both studies estimated total time-integrated fluid fluxes of ~ 10^5 m^3/m^2. The scale of the shifts, the paucity of skarns, and the absence of distinct isotopic breaks expected for down-temperature fluid flow preclude widespread infiltration of fluid derived from crystallizing igneous bodies. The presence of a free fluid phase during peak metamorphism led to extensive (10 to 25%) partial melting under fluid saturated conditions (e.g., Cartwright et al., 1995 and therein). Geological relationships and geochronology (see Foden et al., 1999; 2002) together with the emplacement of the pre-/syn-metamorphic Rathjen Gneiss at ~514 Ma, the oldest and largest igneous body in the region, sets the time frame for metamorphism between ~514 Ma and ~485 Ma. This is also consistent with the Sm-Nd isochron age of 512 Ma determined on accessory metamorphic minerals by Hammerli et al. (2014).

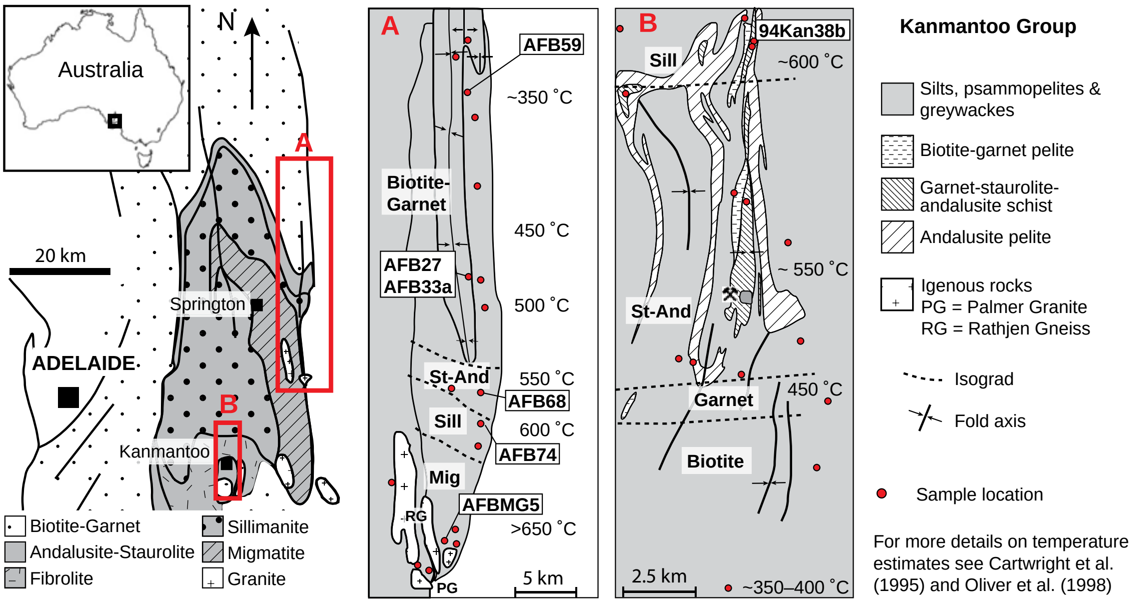

Figure 1: Map of the Eastern Mount Lofty Ranges. Detailed map shows the isogrades, lithologies and sample locations of the A) northern suite (AFB) and B) the southern suite (94Kan) (modified after Dymoke and Sandiford, 1992; Oliver et al. 1998; Cartwright et al., 1995).

3. Samples

Samples from the investigated suites may be termed "psammo-pelites", and have a greywacke-like composition, reflected in relatively low Al concentrations (high Si/Al ratios). Hence, key pelitic indicator minerals for the respective metamorphic grade, e.g., garnet or staurolite, are only locally present. Most prograde metamorphic reactions are multi-variant, involve recrystallization of (and local exchange reactions within and between) existing major mineral phases (see Bucher et al., 2011 and therein). However, we observed that low-grade rocks (<500 ˚C) commonly contain small amounts of calcite (<5%) and local chlorite, both absent in rocks from intermediate metamorphic grades (≥ 500˚C, Fig. 2). Calcite most likely disappeared via the following reaction: muscovite + calcite + quartz = K-feldspar + plagioclase + H_2O + CO_2, and chlorite was consumed by the reaction; chlorite + (detrital) K-feldspar = biotite + muscovite + quartz + H_2O. In the more aluminous variants, the consumption of chlorite also likely led to the formation of local andalusite and the subsequent formation of sillimanite via chlorite + muscovite = andalusite + biotite + H_2O in higher-grade rocks (Yardley, 1989).

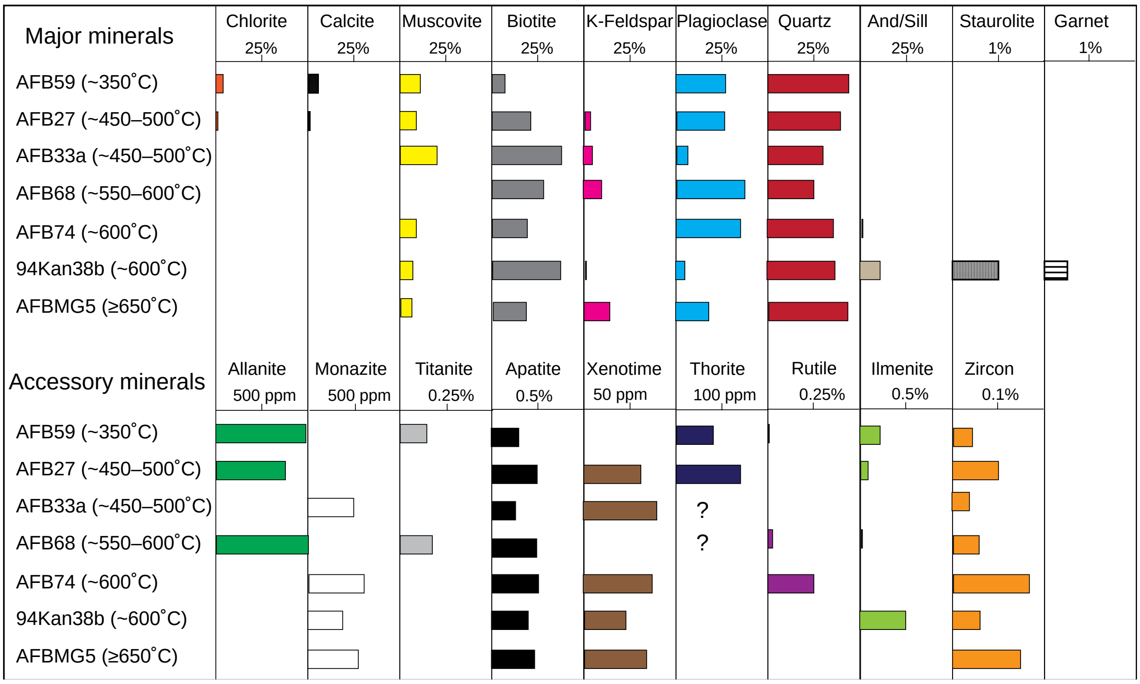

Figure 2: Mineralogy of key samples. Percentages show modal abundance of minerals. Scale for major minerals ranges from 0 to 50% (except staurolite and garnet: 0-2%). And/Sill = Andaulsite or sillimanite. Percentages and ppm for accessory minerals start from 0 and range to 1000 ppm for allanite and monazite, to 0.5 % for titanite and rutile, to 1% for apatite and ilmenite, to 0.2 % for zircon and to 100 ppm for xenotime.

Forty-nine samples from the lower greenschist facies to the upper amphibolite facies were studied for whole rock analyses. We sampled the same metamorphic suite (n=35, samples labelled AFB) described in Cartwright et al. (1995) and reanalysed (n=14) samples from Oliver et al. (1998) (samples labelled 94Kan) that represent a prograde profile that also encompasses the Kanmantoo Cu-deposit (Fig. 1). The samples collected from the northern part of the metamorphic belt (Cartwright et al., 1995) are generally psammo-pelitic in composition as described, and they cover a temperature range from ~350–400 ˚C to the onset of partial melting at ≥650 ˚C. The composition of the lithologies in the southern suite is more variable and samples, tending to more pelitic compositions, and cover a temperature range from ~400 ˚C to ~600 ˚C (Fig. 1). The Kanmantoo Cu-deposit is hosted within the southern suite and in order to avoid complications with external element enrichments (i.e. during ore genesis), we only investigated samples distal to the ore body (Fig. 1). Major and minor element compositions of all samples are presented in the appendix (Table A-1).

I chose 7 samples (AFB59, AFB27, AFB33, AFB68, 94Kan38b, AFB74, AFBMG5) that are representative for the chemical spectrum of psammo-pelites in the region for detailed investigation of element distribution amongst minerals and corresponding bulk rock element budgets. Samples AFB59, AFB27, AFB74, and AFBMG5 are more psammitic (SiO_2=69.6–73.2 wt.%, Al_2O_3=11.4–

13.9 wt.%, Table 1) than sample AFB33, AFB68 and 94Kan38b (Al_2O_3 = 14–19 wt. %, Table 1). Sample AFB59 was collected from the zone of the lowest metamorphic grade (biotite zone ~350 ˚C) investigated in this study and represents a homogeneous, fine-grained (100–200 µm) calcite-bearing plagioclase-rich psammite (AFB59). The major minerals besides plagioclase and quartz are calcite, biotite, muscovite and a small chlorite component (Table 2, Fig. 2). Accessory phases present in this sample include sub-idiomorphic, complexly zoned allanite grains (≤ 200 µm), while small (< 10 µm) grains of a $(Th,U)SiO_4$ phase, probably thorite, are present in trace amounts. Apatite occurs as rounded grains (~ 200 µm) and titanite is present as tabular grains, typically < 100 µm in size. Trace amounts of euhedral zircon (≤ 200 µm) are also present.

Sample AFB27 and AFB33 come from the biotite-garnet zone (450–500 ˚C). AFB27 represents a fine-grained (~100–200 µm), slightly foliated psammopelite sample with a major mineral assemblage that includes quartz, biotite, plagioclase and muscovite. K-feldspar and calcite are present in minor amounts (Table 2, Fig. 2). Accessory phases include complexly zoned allanite (≤ 200 µm), small, irregular $(Th,U)SiO_4$ grains (< 10 µm) of probable thorite, rounded grains of apatite (≤ 200 µm) and euhedral zircon (≤ 200 µm). Accessory phases are not found as inclusions but occur at grain boundaries between various other mineral phases. Sample AFB33 represent a fine-grained (≤ 100 µm), layered pelite with biotite, quartz, plagioclase, and K-feldspar as the major minerals. Xenomorphic monazite (≤ 15 µm), apatite (≤ 60 µm), zircon (≤ 60 µm), xenotime (≤ 30 µm) and rutile (≤ 60 µm) occur as accessory phases (Table 2, Fig. 2).

Sample AFB68 from the staurolite-andalusite zone (~570 ˚C) represents a step up in metamorphic grade. The major mineral phases are plagioclase, biotite, quartz and lesser K-feldspar. The grain sizes vary between 100 to 150 µm, whereas K-feldspar is typically coarser grained. Apatite, zircon, titanite, allanite, and ilmenite occur as accessory minerals. Sub-idiomorphic allanite grains (~ 100 µm) can be complexly zoned. Apatite and zircon grains are typically smaller (< 100 µm) than in the previous samples and titanite is present as sub-idiomorphic grains (~ 50 µm). Despite their relatively small size, apatite, titanite and allanite have not been found as inclusions in other mineral phases.

Sample AFB74 and 94Kan38b were collected from the sillimanite zone (~600 ˚C) in the northern and southern suites, respectively. Sample AFB74 is medium-grained ≤ 500 µm and exhibits a gneissic texture with biotite-rich bands. The major mineral assemblage consists of plagioclase, quartz, biotite and muscovite; sillimanite, mostly fibrolitic, occurs as a subsidiary mineral phase (Table 2, Fig. 2). This sample represents the mineral assemblage before the onset of partial melting. The accessory phases are rutile, zircon, apatite, xenotime and monazite. Monazite (< 30 µm) commonly occurs in clusters, sometimes as inclusions in biotite and frequently interstitially between other mineral phases. Apatite (~100 µm) is present as rounded grains that can be partially (but never fully) enclosed by biotite. Zircon (≤ 100 µm) occurs as euhedral grains and xenotime appears as small (≤ 20 µm) sub-idiomorphic minerals. Sample 94Kan38b comes from the southern part of the high-grade zone (Fig. 1) and contains medium-grained (100–300 µm) quartz, biotite, plagioclase, K-feldspar, muscovite, andalusite, subordinate fine-grained sillimanite, and staurolite and garnet porphyroblasts. This rock contains the highest Al concentration (19.3 wt. % Al_2O_3) of the samples studied in detail (Table 1). Apatite (≤ 500 µm), monazite (≤ 100 µm), xenotime (≤ 40 µm), zircon (≤ 100 µm), and ilmenite (≤ 200 µm) represent the accessory mineral assemblage (Table 2, Fig. 2).

Table 1: Bulk rock composition of samples studied in detail.

Sample	AFB59	AFB-27	AFB-33a	AFB68	94Kan38b	AFB-74	AFBMG5
Temp. (°C)	350–400	450–500	450–500	550–600	550–600	550–600	≥650
SiO_2 wt.%	72.55	70.43	61.01	63.74	61.72	69.62	73.16
TiO_2 wt.%	0.43	0.69	0.87	0.82	0.81	0.86	0.53
Al_2O_3 wt.%	11.39	12.91	14.84	16.28	19.29	13.91	11.81
Fe_2O_3 wt.%	2.51	4.54	9.31	5.73	7.96	4.50	5.08
MnO wt.%	0.07	0.08	0.07	0.07	0.08	0.04	0.03
MgO wt.%	1.25	2.11	4.57	2.57	3.21	2.21	1.52
CaO wt.%	3.14	0.87	0.19	2.76	0.41	1.15	0.96
Na_2O wt.%	3.37	3.00	0.70	2.71	0.79	3.79	1.88
K_2O wt.%	2.07	3.50	6.15	4.20	4.12	2.66	3.88
P_2O_5 wt.%	0.12	0.20	0.12	0.19	0.16	0.22	0.20
LOI wt.%	3.09	1.24	1.95	0.68	1.52	0.39	0.69
($\mu g\ g^{-1}$)							
Cu	14.8	7.2	8.6	18.6	37.5	6.4	3.7
Zn	47.5	44.2	58.2	29.7	79.9	22.1	13.2
Ga	12.0	n.a.	n.a.	21.3	24.5	n.a.	14.0
Ge	2.4	2.1	2.0	2.1	n.a.	2.2	n.a.
As	1.3	1.2	1.0	1.0	0.5	0.9	b.d.
Rb	77.2	120.1	338.9	167.8	169.1	118.4	155.5
Sr	189.9	118.9	33.3	157.7	37.1	107.3	171.8
Y	24.0	31.0	32.9	32.2	35.5	36.8	37.0
Zr	167.4	342.4	174.6	206.1	212.3	580.2	436.9
Nb	7.7	14.4	20.5	14.6	16.8	21.6	11.0
Mo	0.8	2.9	2.1	1.3	1.3	2.3	1.1
Sn	5.6	4.6	7.6	6.9	5.7	6.5	4.8
Sb	1.4	1.4	1.3	1.4	0.8	1.0	0.9
Cs	3.4	2.8	8.7	4.1	4.6	3.7	1.7
Ba	547.8	1151.4	1064.1	991.1	508.7	481.4	922.0
La	39.6	38.5	53.5	49.1	47.6	71.8	67.6
Ce	64.6	76.6	102.1	65.0	97.6	147.9	132.8
Pr	7.3	9.0	11.6	7.4	11.1	17.1	14.7
Nd	29.5	34.1	44.2	28.7	41.5	64.4	56.4
Sm	5.9	6.6	8.4	5.7	7.9	11.4	9.8
Eu	1.2	1.2	1.8	1.5	1.8	1.9	1.7
Gd	5.1	5.6	6.9	4.9	6.8	8.5	8.2
Tb	0.8	0.8	0.9	0.8	1.0	1.1	1.2
Dy	4.3	5.2	5.9	5.6	6.3	6.9	7.0
Ho	0.9	1.1	1.1	1.2	1.3	1.4	1.4
Er	2.5	3.1	3.1	3.6	3.5	3.7	4.0
Tm	0.3	0.4	0.4	0.5	1.0	0.5	1.0
Yb	2.2	3.0	2.8	3.5	3.4	3.7	3.5
Lu	0.3	0.5	0.4	0.5	0.5	0.6	0.5
Hf	4.7	9.2	4.7	6.1	5.7	14.7	12.3
Pb	10.2	9.0	3.8	6.5	5.8	8.9	6.3
Th	11.1	18.3	10.5	17.8	21.1	27.8	24.8
U	1.9	3.3	3.0	3.7	3.5	5.0	3.9

n.a. = not analysed

I selected sample AFBMG5 from the migmatite zone (~650–700 ˚C, Fig. 1) for detailed trace element distribution studies. The major mineral phases in this sample are plagioclase, K-feldspar, quartz, biotite and minor muscovite (Table 2). Biotite can reach 600 µm in length while the other major minerals range between 300 and 400 µm. The accessory minerals include apatite (≤ 250 µm) and monazite grains (≤ 150 µm). Both minerals can be fully enclosed in major minerals, or are located in the interstices of major minerals. Fully enclosed apatite grains are rounded, whereas interstitial apatite can be xenomorphic; no morphological difference with textural setting was observed for monazite (sub-idiomorphic grains). As with apatite and monazite, sub-idiomorphic xenotime (≤ 35 µm) is often enclosed in major mineral phases such as feldspars.

Biotite and apatite can be used as fluid composition monitors (e.g., Munoz, 1984; Zhu & Sverjensky, 1991; Coulson et al., 2001), and apatite is a ubiquitous mineral phase throughout the metamorphic suite and has a huge potential for crustal provenance studies (Henderson et al., 2010; Hammerli et al., 2014a). Therefore, I conducted detailed geochemical studies on these two minerals in additional samples from each metamorphic zone.

Table 2: Mineralogy of samples studied in detail. Calculated modal abundances (see text for details) of major mineral phases are given in brackets.

Sample	Metamorphic Facies	Temp. (˚C)	Mineralogy
AFB59	Greenschist	350–400	Qtz (44), Pl (27), Ms (11), Bt (7), Cal (5), Chl (4), Ap, Ilm, Tnt, Zrn, Tho, Rt
AFB27	Upper Greenschist*	450–500	Qtz (39), Pl (26), Bt (21), Ms (9), Kfs (3), Cal (1), Chl (<1), Ap, Aln, Zrn, Ilm, Tho, Xen
AFB33a	Upper Greenschist*	450–500	Bt (38), Qtz (30), Ms (20), Pl (6), Kfs (5), Ap, Mag, Ilm Zrn, Xen
AFB68	Mid Amphibolite	550–600	Pl (37), Bt (28), Qtz (25), Kfs (10), Rt, Ap, Aln, Tnt, Mag, Ilm, Zrn
AFB74	Mid Amphibolite	550–600	Qtz (36), Pl (35), Bt (19), Ms (9), Sil (0.5), Ap, Rt, Zrn, Mnz, Xen
94Kan38b	Mid Amphibolite	550–600	Qtz (37), Bt (37), And (11), Ms (7), Pl (5), St (1), Kfs (0.5), Grt (0.5), Ilm, Ap, Mnz, Xen
AFBMG5	Upper Amphibolite	650–700	Qtz (43), Bt (18), Pl (18), Kfs (14), Ms (6), Ap, Zrn, Xen

**Transition zone upper Greenschist facies to lower Amphibolite facies*

4. Methods

A JEOL JXA 8200 superprobe in WDS mode, with 15 kV acceleration voltage and 20 nA beam current, housed at the Advanced Analytical Centre, James Cook University (JCU) was used for quantitative major element analysis of all the major silicates phases and apatite. A 5 µm diameter defocused beam was used to avoid potential diffusion of Na and Cl by the beam. Counting times were 20 seconds on peak and 10 seconds on background for each element. The data were processed using φρz corrections (Armstrong, 1991) and standardised against a set of well-characterized, in-house oxide (hematite) and silicate (albite, almandine, orthoclase, wollastonite, olivine), sulfate (barite), tugtupite (chlorine), and Sr-fluorite (fluorine) standards. Accurate analysis of apatite can be challenging due to Cl and F migration during analysis (McCubbin et al. 2010). I applied an offline calculation that corrects signal intensities for potential F and Cl migration in a similar way to that described in McCubbin et al. (2010). Allanite analyses were performed using single-element phosphates for REE standardisation with analytical accuracy checked against analysis of in-house allanite standards.

Rock samples were milled to fine powder in a tungsten carbide ring mill and then analysed for major and selected trace elements at the Advanced Analytical Centre, JCU by conventional X-ray fluorescence (XRF) using a Bruker-AXS S4 Pioneer XRF Spectrometer on fused beads and pressed powder pellets, respectively. Further trace element analysis on bulk rock samples were carried out at the Advanced Analytical Centre at JCU, following a similar methodology to that of Holm et al. (2013). Rock powders were mixed with 12:22 borate flux at a sample to flux ratio of 1:6 and fused to glass after heating to 1050 ^{0}C. The fused samples were then mounted into epoxy pucks and analyzed for a range of trace and major elements by LA-ICP-MS using a Varian 820 quadrupole ICP-MS coupled with a GeoLas Pro 193 nm ArF Excimer laser system. Ablation was conducted in He atmosphere and the ICP-MS was tuned to ensure robust plasma conditions (sensitivity of Th≈U≈Pb) (e.g., Pettke, 2008) and low oxide production levels (<0.5 % ThO), using a laser energy density of 6 J/cm^2 and repetition rates of 10 Hz. The beam diameter was set at 120 micrometers and 3 analyses per sample were conducted. All elements were externally standardized using NIST SRM 612 and NIST SRM 610 glass reference materials with concentration values taken from Spandler et al. (2011), using SiO_2 contents obtained by XRF as the internal standard. The Glitter software package (Van Achterbergh et al., 2001) was used for data processing.

The same laser ablation ICP-MS system was used for trace element analysis in minerals. The beam diameter varied between 16 and 90 micrometers and analyses were standardized using bracketing analysis of NIST SRM 612 and NIST SRM 610 glasses. The analyses were internally standardized using ^{43}Ca for titanite and apatite, ^{31}P for monazite and xenotime, and ^{29}Si for other silicate minerals. Final concentration values were performed using the SILLS software (Guillong et al., 2008). SILLS allows the identification of optically non-resovlavle inclusions that can result in elevated concentrations of trace elements, which can lead to misleading results (see appendix). Glass reference (NIST SRM 612 and 610) values for external standardization were taken from Spandler et al. (2011). LA-ICP-MS analyses for monazite and allanite were compared with EPMA analysis and showed good agreement between the two methods (see appendix). Quantitative Zn analysis by LA-ICP-MS can be compromised by potential ^{26}Mg and ^{40}Ar interference (^{26}Mg^{40}Ar)$^+$ with the ^{66}Zn signal. We assessed the degree of ^{26}Mg^{40}Ar$^+$ interference with ^{66}Zn by monitoring the apparent Zn signal while ablating a pure MgO waver as well as San Carlos Olivine. Our results show that ~ 0.2 µg g^{-1} Zn is erroreously simulated per 1 wt.% Mg. All Zn analyses have been corrected for this interference accordingly.

Element distribution budgets for each sample were calculated by multiplying the average element content of each mineral by the respective mineral modal proportion, and then normalizing to bulk rock element content. The mineral modal proportions were calculated via least-squares regressions (using Solver in Micrsoft Excel), using mineral and bulk-rock compositions. The calculated mineral proportions agree with petrographic observations in thin sections. The sum of the square of the residuals are low ($\sum r^2 < 1$) for all samples, which reflects precise mineral phase proportion calculations.

5. Results

5.1 Whole rock chemistry

5.1.1 Major elements

The major- and trace element compositions of the seven samples studied in detail are given in Table 1. Major and minor element compositions of all the other samples are listed in the appendix. The SiO_2 content of all the samples ranges from 50 to 78 wt. % (southern suite (94Kan) = 50–72 wt. %, northern suite (AFB) = 59–78 wt. %) and the Al_2O_3 concentrations vary between 11 and 23 wt. % (94Kan: 12–23 wt. %, AFB: 11–19 wt. %). The K_2O (2–6 wt.%) and the CaO content (< 4 wt. %) of the studied samples are similar in both sampling suites. Samples from the lower grades (~350–450˚C) have loss of ignition (LOI) values between 0.5 and 6 wt. %, while samples from higher metamorphic grades typically have LOI values of < 2 wt.% with samples from the migmatite zone having the lowest LOI values (Fig. 3). Besides the expected decreasing LOI numbers with increasing grade, no systematic variation between major elements, element ratios (K_2O/Al_2O_3, Na_2O/Al_2O_3) and estimated temperatures is observed (Fig. 3). This indicates isochemical behaviour for major element retention during metamorphism, even for elements such as Na and K that are often assumed to have a high mobility potential under elevated temperatures and high H_2O activity. Despite these results, systematic bulk-rock $\delta^{18}O$ depletions were recorded in all rock types during up-temperature fluid flow (Cartwright et al., 1995, Oliver et al., 1998), and changes to alkalis and metals were pronounced in the 100m-scale alteration zones around the Kanmantoo orebody (Oliver et al., 1998).

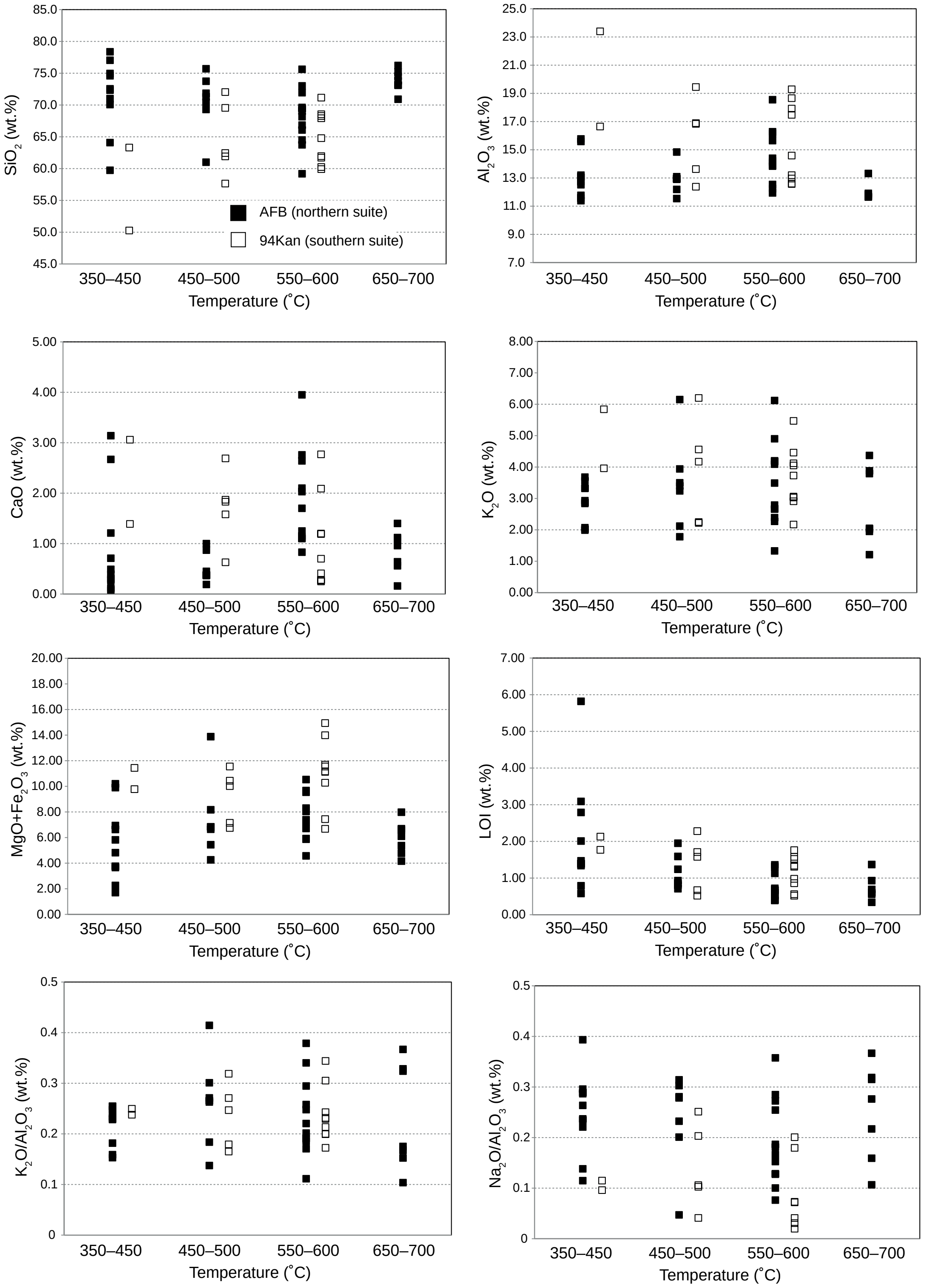

Figure 3: Major element composition (bulk rock) of the northern suite (AFB, filled squares) and the southern suite (Kan94, empty squares). No systematic major element loss or gain can be observed throughout metamorphism.

5.1.2 Trace elements

Figure 4 shows whole rock analysis of the studied samples normalized by the average post-Archean Australian Shale (PAAS) composition (Taylor and McLennan, 1985). We modified the Cs, Nb and TiO_2 values of the PAAS reference numbers as recommended in Plank and Langmuir (1998). The average normalised values of both suites show a reasonably flat trace element pattern, with average compostions around 1.

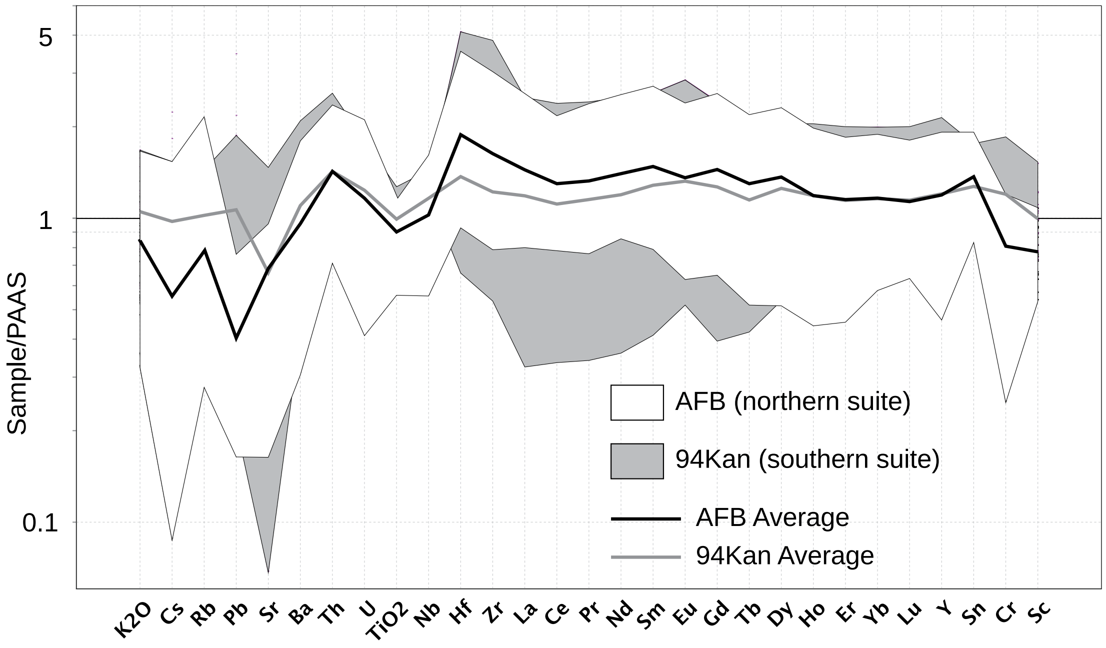

Figure 4: Grey and whit fields show range of whole rock compositions of the southern and northern metamorphic suite (94Kan and AFB). The whole rock analyses were normalized by Post-Archean Australian Shale values (Taylor and McLennan, 1985) modified for TiO_2, Nb and Cs as suggested by Plank and Langmuir (1998). Solid lines show the average for each suite (black line: northern suite (AFB), grey line: southern suite (94Kan).

As with major elements concentrations (Fig. 3), the REE and most other trace element contents in bulk rock analyses vary between rocks samples, but independant of the metamorphic grade (Fig. 5). For example, Ce varies in low-grade metamorphic rocks from 44 to 172 μg g^{-1} and from 68 to 152 μg g^{-1} in migmatites, while Zr contents in low-grade rocks range from 108 to 608 μg g^{-1} and from 214 to 626 μg g^{-1} in migmatites. Strontium concentrations in low-grade rocks from the northern suite range from 95 to 190 μg g^{-1} and migmatites contain between 68 and 152 μg g^{-1} Sr, whereas Sr contents in the southern sample suite (94Kan samples) are more variable (Fig. 5).

There are several trace elements, namely Cs, Pb, As and Zn, whose concentrations do change considerably and systematically during prograde metamorphism (Fig. 6). Cesium concentrations in rocks that underwent ~350–600 ˚C range from ~0.5 to 11 μg g^{-1} and no correlation with temperature can be seen. However, migmatites (≥650 ˚C) contain considerably lower Cs concentrations and plot in a narrow range between 1 and 2 µg g^{-1} (Fig. 6). To account for protolithic variations we normalized Cs concentrations by the bulk rock K_2O content, as most of the Cs is accommodated in K-rich mineral phases (see below), nevertheless, even with K normalization, the same trend of low Cs values in migmatites is observed (Fig. 6).

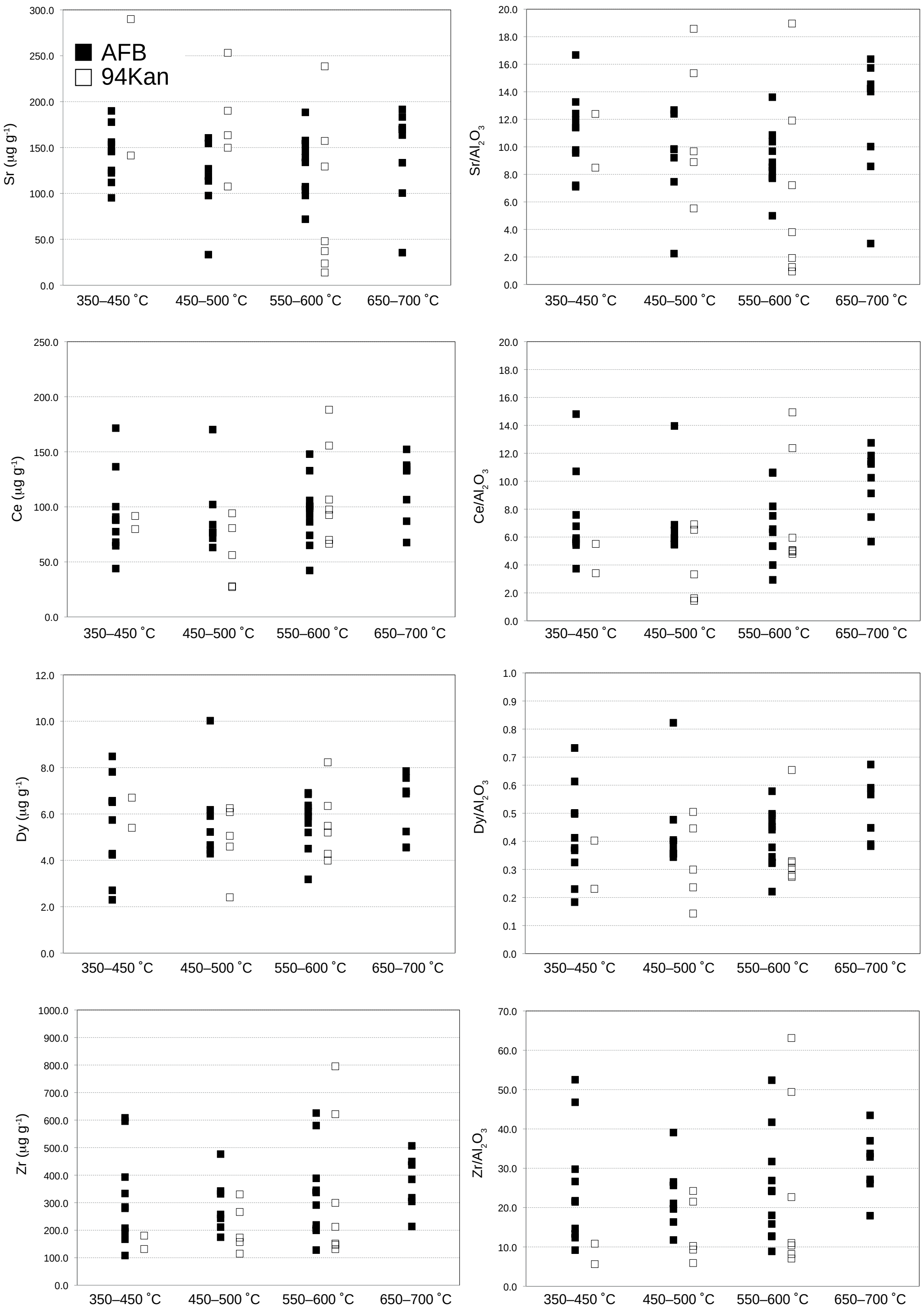

Figure 5: Immobile trace elements. Filled squares represent samples from the northern suite (AFB) and empty symbols represent samples from the southern transect (94Kan).

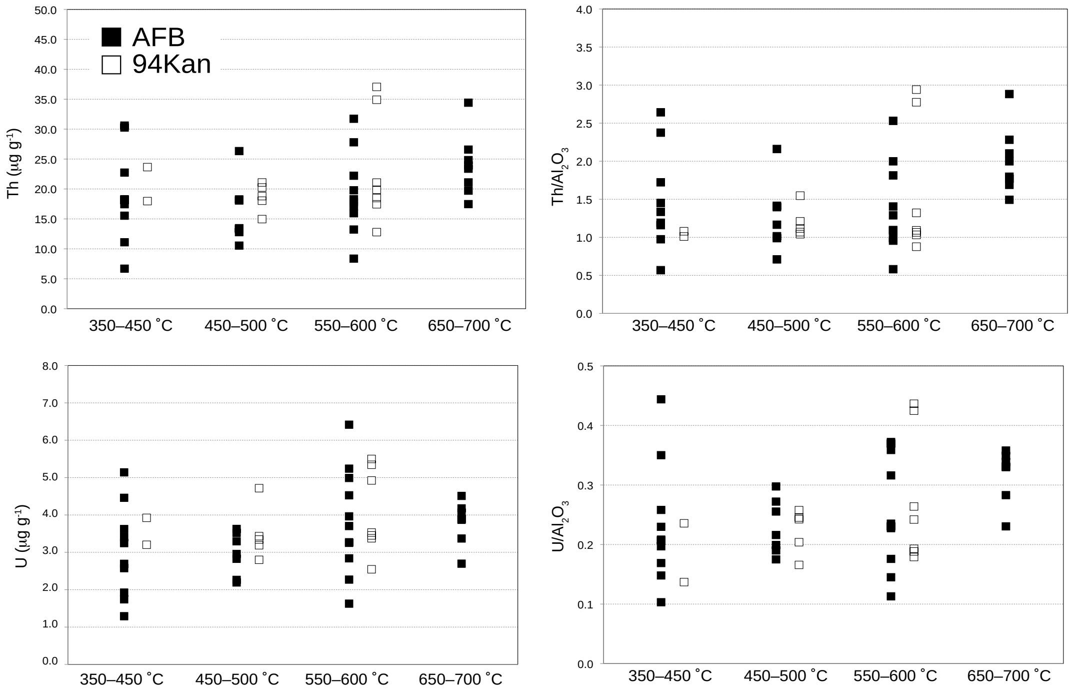

Figure 5 (continued)

Samples in the temperature range 450–500 ˚C from the northern suite (AFB) show significantly higher As contents (1–11 μg g^{-1}) than samples from higher metamorphic grades (~ 550–650 ˚C, 1–2.5 μg g^{-1} As). After this decrease in As concentrations, no noticeable changes of As concentrations can be observed with increasing temperatures (Fig. 6). Samples from the southern suite (Kan94) show a similar trend, however, besides for one sample, the As concentrations seem to decrease at higher temperatures (550–600 ˚C) (Fig. 6). To account for possible protolithic variations, especially for the pelite/psammite component of the individual samples, we normalized As values with the Al_2O_3 content of the sample (Fig. 6). However, the normalized values show the same pattern, and therefore protolithic variations within the different metamorphic zones can be ruled out as a reason for As depletion at 450–500 ˚C.

The Pb concentration in the lowest-grade rocks in the northern suite is between 4–15 μg g^{-1} whereas migmatites contain < 8 μg g^{-1} Pb. Samples from the southern suite contain 25–30 μg g^{-1} Pb in low-grade zones and < 20 μg g^{-1} in samples metamorphosed to temperatures > 450 ˚C. To account for protolithic variations we normalized the Pb values by dividing them by K_2O + CaO as it is assumed that Pb replaces K and Ca in silicates and carbonates (e.g. Haack et al., 1984; Cherniak, 1995). We also normalized Pb concentrations by Al_2O_3 to account for the pelitic component in the samples (see Chapter 5). However, normalization does not change the pattern of decreasing Pb concentrations during metamorphism (Fig. 6).

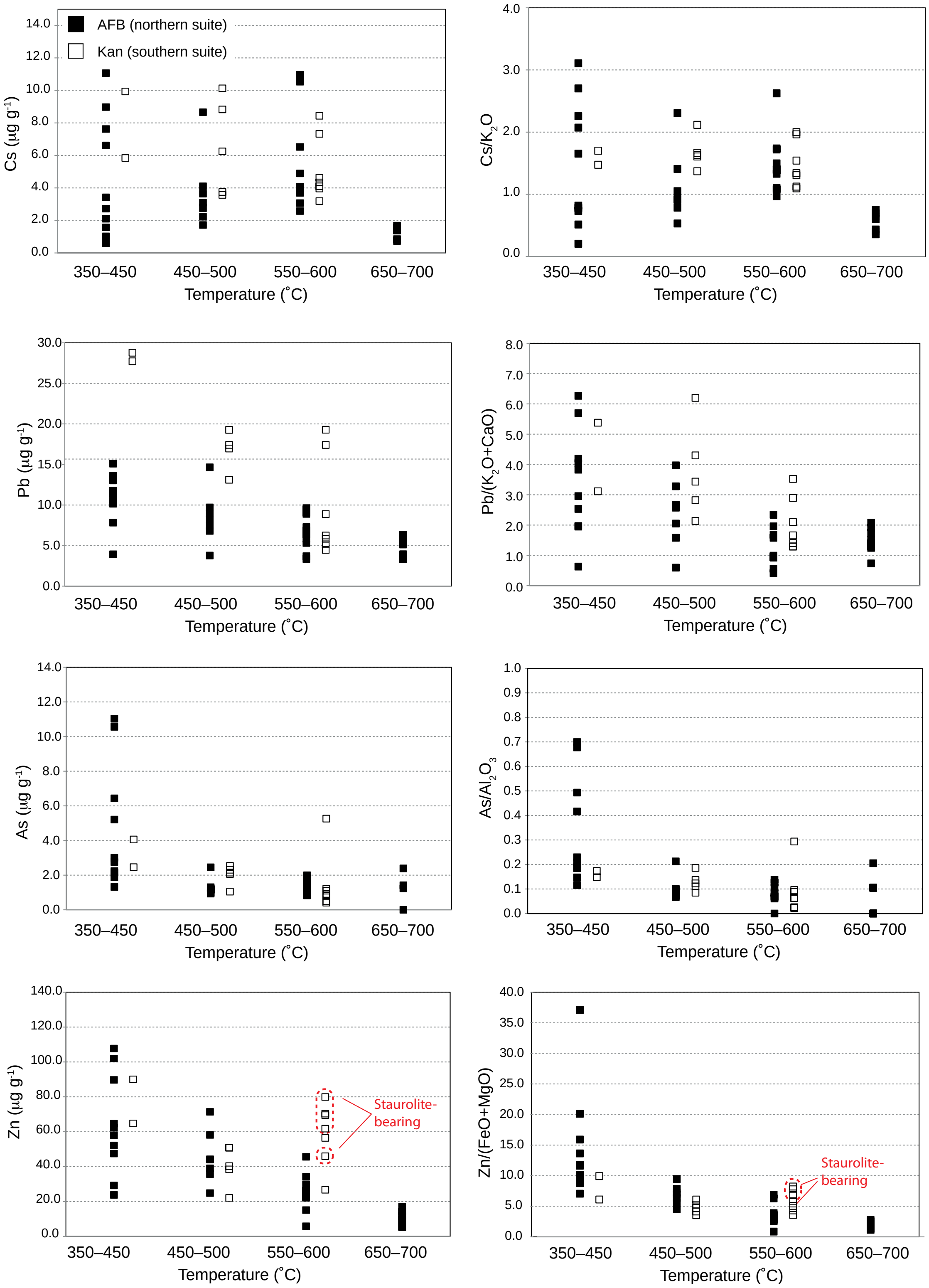

Figure 6: Whole rock concentrations (in µg g^{-1}) of mobile trace elements during prograde metamorphism. Filled squares represent samples from the northern suite (AFB); empty squares stand for samples from the southern suite (94Kan). To account for protolithic variations, trace elements were normalized with major elements (see text).

Zinc concentrations in rocks from the northern suite show a clear trend of Zn depletion during prograde metamorphism. Low-grade rocks contain up to 108 µg g^{-1} Zn whereas intermediate-grade rocks typically contain < 70 µg g^{-1} Zn and migmatites contain < 20 µg g^{-1} Zn. Zinc is mainly hosted in Fe and Mg rich minerals (see below), hence, Zn values normalized by Fe+Mg account for protolithic variations and by dividing Zn concentrations by Al_2O_3 we account for variable pelitic components in the samples (see Chapter 5). Yet, the normalized Zn values show the same trend of decreasing Zn concentrations during metamorphism in samples from the northern suite (AFB) (Fig. 6). Samples from the southern suite show a different Zn vs. temperature pattern (Fig. 6). In contrast to the northern suite, Zn contents do not decrease during metamorphism (~400–600 ˚C). Samples from the temperature range 550–600 ˚C show higher Zn concentrations than samples from the northern suite from the same metamorphic grade. Most of the samples with high Zn concentrations at these temperatures contain staurolite (Fig. 6) that possibly explains the difference Zn concentration patterns of the two suites (see discussion).

5.2 Element distribution / Mineral composition

5.2.1. Feldspars

In samples with relatively high feldspar contents (e.g., AFB68, AFB74 and AFBMG5, Table 2, Fig. 2) plagioclase and K-feldspar contain several tens of µg g^{-1} Pb (Table 3, Figs. 7 & 8), and so are the major host of Pb, whereas micas are the most important Pb host in samples with low feldspar contents (see below). In all our samples, feldspars are the most important hosts for Sr containing several hundreds of µg g^{-1} (e.g., AFBMG5 ~400–500 µg g^{-1} Sr, Table 3) with plagioclase incorporating slightly more Sr than K-feldspar if both minerals are present (Table 3). K-feldspar is often found to be the major Ba host with concentrations of several thousands of µg g^{-1} (e.g., ~ 4900 µg g^{-1} in sample AFB68, Table 3) while less Ba is hosted in plagioclase (< 200 µg g^{-1}, Table 3). K-feldspar also hosts considerable amounts of Rb (~200–250 µg g^{-1}) with plagioclase typically containing less than 1 µg g^{-1} Rb (Table 3). The concentration of REE and other trace elements in feldspars is generally at the sub-µg g^{-1} level or were fond to be below the analytical limit of detection (LOD), so these mineral have a negligible contribution to the overall budget of these elements in the rock (< 1%, Figs. 7–9 Table 3).

Table 3: Composition of feldspar and calcite during metamorphims. For each sample the compositional range (min. to max.) is given. SiO_2, Al_2O_3, Na_2O and K_2O are given in wt.%, trace elements are in μg g^{-1}. (b.d. -= below detection)

Sample	AFB68	AFBMG5
Mineral	K-feldspar	K-feldspar
Temp. (°C)	550–600	≥ 650
	(n=5)	(n=5)
SiO_2	64.49±0.51	65.43±0.30
Al_2O_3	17.97±0.06	18.87±0.12
CaO	b.d.	0.01 ±0.001
Na_2O	0.62±0.04	1.58±0.27
K_2O	16.07±0.15	14.52±0.61
Li	b.d.	≤1.7
V	b.d.	b.d.
Cu	b.d.	b.d.
Zn	1.6–2.6	≤4.80
As	b.d.	b.d.
Rb	192–220	233–253
Sr	215–308	434–505
Y	0.17–0.61	0.12–0.18
Zr	0.26–0.64	b.d.
Nb	b.d.	b.d.
Mo	b.d.	b.d.
Sb	b.d.	b.d.
Cs	0.72–0.86	0.62–0.81
Ba	3913–4913	4735–5063
La	0.07–0.16	0.45–0.64
Ce	0.05–0.30	0.30–0.56
Pr	b.d.	0.01–0.06
Nd	b.d.	0.02–0.21
Sm	b.d.	b.d.
Eu	0.53–0.92	0.67–74
Gd	0.06–0.10	b.d.
Dy	b.d.	b.d.
Er	b.d.	b.d.
Yb	b.d.	b.d.
Lu	b.d.	b.d.
Hf	0.09–0.12	0.03–0.05
Ta	0.05–0.11	0.02–0.04
Pb	29.3–41.6	24.4–26.1
Th	0.01–0.03	b.d.
U	0.01–0.03	b.d.

Sample	AFB59	AFB27	AFB33a	AFB68	94Kan38b	AFB74	AFBMG5
Mineral	Plagioclase	Plagioclase	Plagioclase	Plagioclase	Plagioclase	Plagioclase	Plagioclase
Temp.	~350°C	450–500	450–500	550–600	550–600	550–600	≥650°C
	(n=4)	(n=4)	(n=3)	(n=3)	(n=1)	(n=4)	(n=4)
SiO_2	68.77±0.57	66.61±0.6	68.85±1.1	60.47±0.39	64.06±0.67	65.51±0.38	64.09±0.07
Al_2O_3	19.22±0.17	21.71±0.5	19.63±0.36	24.24±0.18	22.65±0.46	21.71±0.20	23.17±0.14
CaO	0.26±0.26	0.1±0.05	0.41±0.33	6.67±0.39	3.85±0.38	2.68±0.19	4.06±1.56
Na_2O	11.66±0.21	11.2±0.3	11.62±0.36	8.05±0.14	9.53±0.11	10.35±0.16	9.36±0.08
K_2O	0.06±0.02	0.08±0.02	0.08±0.01	0.18±0.03	0.07±0.01	0.16±0.02	0.31±0.01
Li	≤5.20	b.d.	b.d.	b.d.	0.45	b.d.	b.d.
V	0.32–7.08	b.d.	0.58–5.95	b.d.	b.d	b.d.	b.d.
Cu	b.d.	b.d.	b.d.	b.d.	b.d	b.d.	b.d.
Zn	≤5.07	b.d.	≤2.91	b.d.	b.d	b.d.	b.d.
As	b.d.	b.d.	b.d.	b.d.	b.d	b.d.	b.d.
Rb	0.21–37.32	≤0.58	2.74–22.9	0.79–4.73	b.d.	0.05–0.14	0.29–0.48
Sr	142–397	68.6–87.4	219–261	276–339	253	214–252	487–501
Y	0.06–1.30	≤0.47	≤0.04	0.39–1.31	0.15	0.07	0.32–0.40
Zr	≤1.18	b.d.	n.d.	<0.16	b.d.	b.d.	b.d.
Nb	≤0.35	≤0.02	0.08–0.10	b.d.	b.d.	b.d.	b.d.
Mo	b.d.	b.d.	n.d.	b.d.	b.d.	b.d.	b.d.
Sb	≤0.48		0.16–0.20	b.d.	b.d.	b.d.	b.d.
Cs	≤3.89	0.01–0.02	0.04–0.25	0.02–0.06	0.06	bb	b.d.
Ba	5.94–153	3.46–5.25	15.8–130	33.7–47.3	168	111–184	71.0–79.06
La	0.03–1.47	0.04–0.15	≤0.05	0.93–1.15	0.81	0.63–0.68	2.74–3.14
Ce	0.05–1.64	0.04–0.18	≤0.05	≤1.29	1.30	0.93–1.08	3.97–4.65
Pr	0.01–0.32	0.01–0.02	≤0.005	≤0.12	0.11	0.09–0.10	0.36–0.42
Nd	≤1.28	b.d.	≤0.02	≤0.34	0.37	0.20–0.29	1.03–1.23
Sm	≤0.17	b.d.	≤0.83	≤0.05	0.07	0.03–0.06	0.14–0.15
Eu	≤0.08	0.02	0.02–0.31	0.97–1.27	0.42	0.04–0.05	0.73–0.77
Gd	≤0.18	b.d.	≤0.40	<0.07	0.03	0.03–0.05	0.09–0.16
Dy	≤0.13	b.d.	≤0.09	≤0.06	0.04	0.01–0.02	0.05–0.11
Er	≤0.14	b.d.	≤0.03	≤0.02	0.04	b.d.	0.03–0.05
Yb	≤0.16	b.d.	≤0.05	b.d.	b.d.	b.d.	b.d.
Lu	≤0.02	b.d.	b.d.	b.d.	b.d.	b.d.	b.d.
Hf	≤0.07	b.d.	b.d.	b.d.	b.d.	b.d.	b.d.
Ta	0.01–0.03	bb	0.01–0.04	b.d.	b.d.	b.d.	b.d.
Pb	3.33–8.94	3.03–4.31	6.93–8.33	8.06–8.79	24.25	17.6–20.4	7.76–8.00
Th	≤0.05	b.d.	≤0.02	<0.07	b.d.	b.d.	b.d.
U	≤0.03	b.d.	0.03–0.19	0.01	0.01	b.d.	b.d.

5.2.2 Calcite

In calcite-bearing low-grade samples, calcite can be the main Pb host by sequestering ~ 30 µg g^{-1} Pb (Figs. 7 & 9, Table 3). Furthermore, calcite can host 300–1000 µg g^{-1} Sr, up to ~13 µg g^{-1} HREEs, and smaller amounts of LREE (Table 3), which means that calcite controls large proportion of the bulk rock's Sr budget and significant amounts (up to 20%) of the bulk rock HREE content (Figs. 7 & 9), despite only being a minor phase in the these rocks (Table 2; Fig. 2).

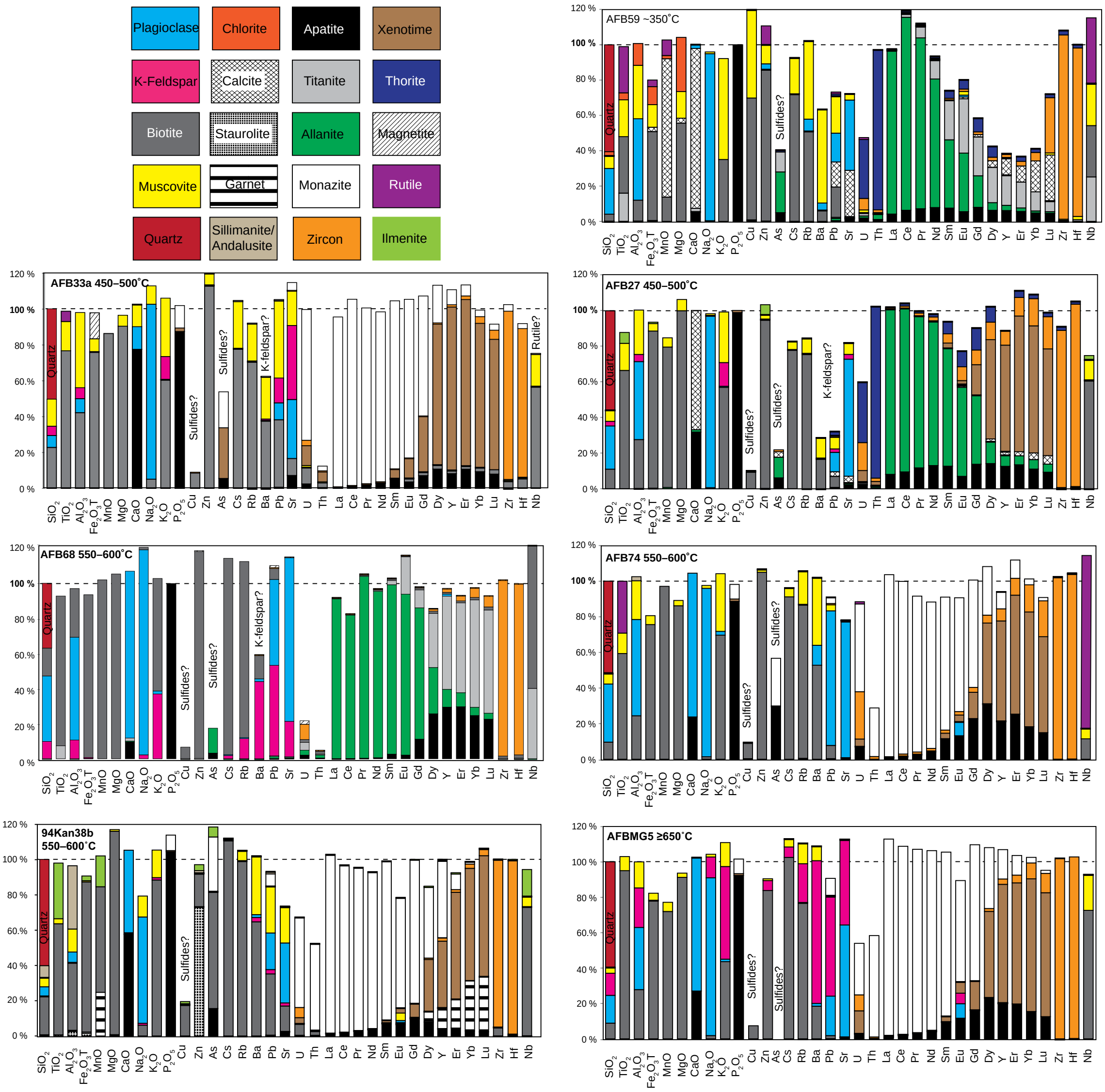

Figure 7: Element distribution amongst mineral phases. The 100 % line represents the bulk rock composition.

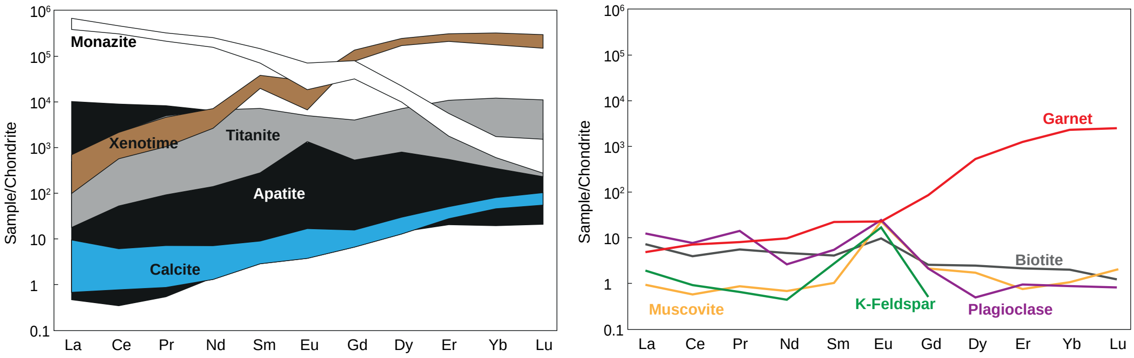

Figure 8: Trace element contents of major and minor mineral phases normalized against chondrite (McDonough and Sun, 1995). Fields cover all the concentrations measured in the respective minerals so that the apatite field contains measurements of detrital grains, resulting in a large field. Only the highest measured concentrations of REE are shown for garnet, micas and feldspar as trace element contents in theses phases are often below the limit of detection (also LREE in garnet).

5.2.3 Biotite and Muscovite

Together with apatite, biotite is the major host for Cl and F. Chlorine contents in biotite from samples > 450 ˚C are higher than in lower-grade samples, which is reflected by lower F/Cl ratios in biotite (see appendix). Biotite in low-grade samples (<500 ˚C) contains <0.12 wt.% Cl and <0.4 wt.% F, while biotite from higher metamorphic grades (> 500 ˚C) contain more Cl (≤0.33 wt.%) and similar concentrations of F as in low-grade samples. Our results show that the biotite composition follows the "Mg-Cl avoidance rule" (Munoz, 1984, Fig. 14); whereas the F-Fe avoidance is not evident in our data set. TiO_2 contents vary between 1.3 and 3.5 wt. % with biotite in high-grade rocks generally containing > 2 wt. % TiO_2.

Biotite is an important host for trace elements as it contains ≥ 90 % of the bulk rock Zn in most rocks and is the major host for Rb, Cs and Li (bulk rock Li was not measured, but micas are the only minerals found to host significant amounts of Li, Figs. 7, 9, Table 4). Zinc concentrations in biotite decrease with increasing metamorphic grade (Fig. 10, Table 4); also reflected in the bulk rock compositions (Fig. 6). Biotite from low-grade samples contain up to 900 µg g^{-1} Zn whereas samples from intermediate metamorphic grades contain ~ 150 µg g^{-1} Zn and biotite in migmatites contains low Zn concentrations (~ 50 µg g^{-1}) (Fig. 10, Table 4). The Zn content of biotite seems to be independent of the biotite major element composition (see appendix Fig. A-3), also reported in Tischendorf et al. (2001). Lead concentrations in biotite follow a very similar pattern to that of

Zn with a decrease towards higher metamorphic temperatures. Biotite from metamorphic zones > 500˚C generally contain less Pb (< 2µg g^{-1} Pb) than biotite in samples from low metamorphic grades (2–50 µg g^{-1} Pb; Fig. 10, Table 4). In K-feldspar-poor mineral assemblages, biotite and muscovite are the most important Ba hosts (Fig. 7). Together with other Ti-bearing minerals (rutile, ilmenite and titanite), biotite and muscovite are major Nb and Ta hosts that accommodate several µg g^{-1} Ta and several tens of µg g^{-1} Nb (Table 4). The high affinity of Nb for biotite results in biotite being the most important Nb (and most likely Ta) host in rutile-absent assemblages (Fig. 7, Table 4). We found that micas can host several tens to hundreds of µg g^{-1} Cu in low-grade samples, whereas the Cu contents in samples in high-grade rocks are in the µg g^{-1} range (Table 4). Concentrations of other trace elements are low and contribute < 1 % to the bulk rock inventory (Table 4, Fig. 7).

Muscovite essentially hosts a similar suite of trace elements as biotite, although muscovite can contain higher concentrations of Ba, Sr and Pb than biotite (Table 4). Trace elements in muscovite follow a very similar pattern during metamorphism to that of biotite. A decline in Pb and Zn concentrations from low metamorphic grades (6–40 µg g^{-1} Pb, up to 80 µg g^{-1} Zn) to high-grade zones (< 1µg g^{-1} Pb, <10 µg g^{-1} Zn) is observed (Table 4).

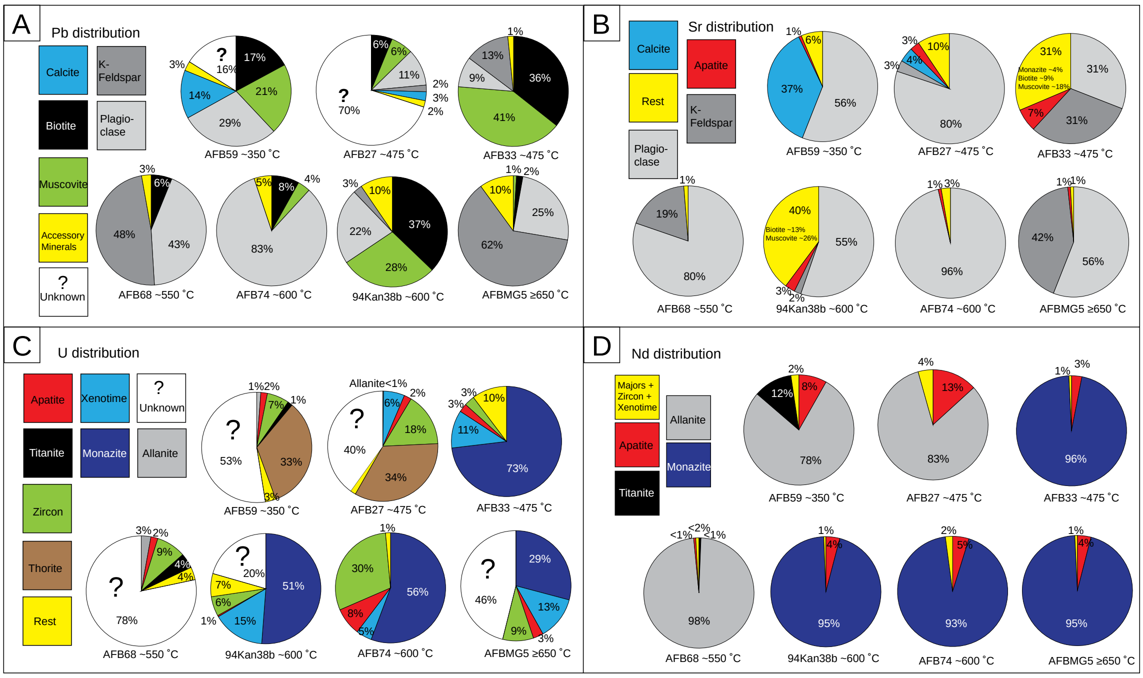

Figure 9: Distribution and whole rock budget of A) Pb, B) Sr, C) U, and D) Nd.

Table 4: Composition of muscovite and biotite during metamorphism. Given are the ranges of compositions measured in each sample.

Sample	**AFB59**	**AFB27**	**AFB33**	**94Kan38b**	**AFB74**	**AFBMG5**
Mineral	**Muscovite**	**Muscovite**	**Muscovite**	**Muscovite**	**Muscovite**	**Muscovite**
Temp. (˚C)	**~350**	**450–500**	**450–500**	**550–600**	**550–600**	**≥650˚C**
wt.%	(n=2)	(n=5)	(n=4)	(n=3)	(n=5)	(n=5)
SiO_2	47.43±0.58	47.38±0.60	47.21±0.68	46.76±0.45	46.66±0.30	47.27±0.24
TiO_2	0.98±0.24	0.95±0.11	0.73±0.13	0.33±0.02	1.12±0.19	0.81±0.02
$Al2O_3$	30.75±2.36	32.3±0.72	31.82±1.12	35.98±0.37	33.99±0.24	33.41±0.23
K_2O	10.56±0.25	10.54±0.38	10.27±0.08	9.20±0.07	9.77±0.32	10.10±0.16
Na_2O	0.31±0.09	0.29±0.02	0.37±0.15	1.34±0.03	0.68±0.06	0.56±0.05
FeO	2.87±1.13	2.00±0.24	3.38±0.93	0.77±0.10	2.58±0.10	3.81±0.10
MgO	1.68±0.71	1.410.32	1.43±0.40	0.43±0.07	0.79±0.12	0.71±0.01
MnO	b.d.	0.04±0.02	b.d.	b.d.	b.d.	0.02±0.02
Cl	b.d.	b.d.	b.d.	b.d.	0.04±0.03	b.d.
F	b.d.	b.d.	b.d.	b.d.	b.d.	0.10±0.01
$\mu g\ g^{-1}$						
Li	53.2–66.2	11.0–34.7	15.1–41.6	2.54–3.19	11.5–15.7	6.82–7.19
V	209–222	69.4–207	108–230	250–294	251–298	187–192
Cu	64.6–69.72	≤5.05	b.d.	≤2.85	b.d.	b.d.
Zn	42.0–50.8	9.96–25.1	6.92–76.8	3.82–4.22	4.22–6.89	1.78–2.77
As	b.d.	b.d.	b.d.	b.d.	b.d.	b.d.
Rb	294–319	22.4–231	363–620	136–143	241–268	338–367
Sr	43.0–80.7	21.4–116	10.3–53.6	96.0–125	8.98–18.3	18.7–24.34
Y	0.15–1.14	0.13–0.73	b.d.	0.05–0.07	b.d.	0.04–0.09
Zr	2.75–15.9	2.89–8.72	1.95–2.61	0.37–0.38	1.30–1.69	2.38–3.48
Nb	14.5–18.3	6.56–41.2	19.5–32.1	12.9–14.9	4.5–22.13	41.6–45.2
Mo	≤0.87	b.d.	b.d.	b.d.	0.15–0.30	0.81–1.42
Sb	0.88–1.24	≤0.26	b.d.	b.d.	b.d.	≤0.02
Cs	3.63–8.91	0.41–3.91	4.60–35.0	0.62	1.89–2.80	1.25–1.73
Ba	2327–2876	1246–2393	389–3072	2407–2419	1431–2453	1211–1507
La	0.18–0.22	≤0.17	b.d.	≤0.01	b.d.	≤0.17
Ce	0.20–0.35	≤0.26	≤0.06	b.d.	b.d.	≤0.26
Pr	0.06	≤0.08	b.d.	b.d.	b.d.	≤0.05
Nd	≤0.28	≤0.31	b.d.	b.d.	b.d.	≤0.12
Sm	≤0.14	≤0.06	b.d.	b.d.	b.d.	≤0.03
Eu	0.06–0.38	0.03–0.11	≤0.21	0.92–1.27	0.02–0.05	0.03–0.06
Gd	≤0.42	≤0.11	b.d.	b.d.	b.d.	b.d.
Dy	≤0.42	≤0.21	b.d.	b.d.	b.d.	b.d.
Er	≤0.12	≤0.11	b.d.	b.d.	b.d.	b.d.
Yb	≤0.14	≤0.17	b.d.	b.d.	b.d.	b.d.
Lu	0.02–0.05	≤0.03	b.d.	b.d.	bb	b.d.
Hf	0.24–1.27	0.17–0.54	0.07–0.18	0.04	0.11–0.13	0.16–0.23
Ta	0.28–1.15	0.24–1.68	1.51–2.66	0.61–0.73	0.14–1.47	1.80–2.26
Pb	6.22–31.6	4.26–9.26	3.88–20.4	20.2–23.9	2.56–4.82	0.79–1.12
Th	0.08–0.83	0.10–0.67	≤0.05	b.d.	b.d.	≤0.01
U	0.05–0.46	0.04–0.27	≤0.24	b.d.	b.d.	≤0.01

Sample	**AFB59**	**AFB27**	**AFB33**	**AFB68**	**94Kan38**	**AFB74**	**AFBMG5**
Mineral	**Biotite**	**Biotite**	**Biotite**	**Biotite**	**Biotite**	**Biotite**	**Biotite**
Temp. (˚C)	**~350**	**450–500**	**450–500**	**550–600**	**550–600**	**550–600**	**≥650˚C**
wt.%	(n=6)	(n=4)	(n=4)	(n=7)	(n=4)	(n=4)	(n=7)
SiO_2	36.87±0.83	36.75±0.54	36.90±0.38	36.59±0.33	36.02±0.39	36.14±0.40	36.01±0.25
TiO_2	2.11±0.15	2.18±0.13	1.77±0.09	2.54±0.25	1.38±0.06	2.70±0.17	2.81±0.10
Al_2O_3	16.12±0.25	16.85±0.49	16.54±0.32	16.34±0.32	19.58±0.38	18.34±0.20	18.26±0.22
K_2O	9.48±0.34	9.83±0.15	9.87±0.18	19.29±0.31	9.85±0.06	9.98±0.07	9.71±0.16
Na_2O	0.20±0.09	0.08±0.02	0.10±0.03	9.82±0.18	0.13±0.02	0.30±0.04	0.20±0.02
FeO	19.37±0.43	19.03±0.69	18.78±0.18	9.78±0.27	16.42±0.37	18.28±0.34	21.74±0.26
MgO	10.52±0.27	10.02±0.25	10.94±0.18	0.13±0.04	10.01±0.10	10.21±0.28	7.72±0.06
MnO	0.15±0.04	0.23±0.06	0.16±0.2	0.26±0.04	0.05±0.02	0.18±0.02	0.08±0.02
F	0.05±0.03	0.15±0.09	0.15±0.02	0.15±0.02	0.13±0.06	0.23±0.10	0.27±0.04
Cl	0.05±0.03	0.03±0.01	0.11±0.01	0.24±0.03	0.11±0.11	0.05±0.02	0.23±0.02
$\mu g\ g^{-1}$							
Li	184–214	78.7–102	75.8–104	45.6–72.2	21.3–53.3	123–130	69.1–91.1
V	124–189	178–222	120–133	299–679	221–255	291–339	224–254
Cu	28.3–913	≤3.73	1.54–2.64	3.8–18.9	18.5–374	≤5.58	≤2.20
Zn	348–896	235–312	125–214	101–152	23.6–57.9	161–167	47.6–51.6
As	b.d.	b.d.	≤0.72	b.d.	b.d.	b.d.	b.d.
Rb	561–621	393–478	533–742	563–654	278–494	534–560	639–720
Sr	1.00–3.36	0.48–3.02	4.73–15.5	0.69–3.53	0.91–43.99	0.82–1.39	0.53–1.90
Y	0.07–0.37	0.07–1.65	1.30–2.02	0.33–2.74	0.27–2.92	0.04–0.08	≤0.20
Zr	≤1.69	≤10.1	16.0–21.1	2.44–8.26	3.57–28.4	0.34–1.58	0.26–1.17
Nb	22.5–41.3	40.2–46.0	27.2–35.2	38.6–68.8	25.9–40.1	2.56–24.2	42.0–46.9
Mo	≤0.64	0.20–0.25	0.28–0.34	0.47–0.86	0.40–0.77	0.14–0.18	0.55–0.83
Sb	≤0.56	≤0.25	0.29–0.38	b.d.	≤0.19	b.d.	b.d.
Cs	16.1–37.5	7.75–12.9	13.3–22.3	15.5–18.8	6.2–16.7	17.64–18.65	8.69–9.97
Ba	271–692	795–1089	889–1362	412–603	697–1217	1189–1512	730–1008
La	0.03–0.30	≤0.11	0.06–0.13	0.31–1.06	0.12–1.67	0.01–0.04	0.01–0.17
Ce	0.05–1.41	0.01–0.20	0.16–0.31	0.90–2.40	0.12–3.77	0.01–0.08	0.01–0.30
Pr	0.01–0.22	≤0.05	0.03–0.06	0.19–0.53	0.03–0.47	≤0.01	≤0.05
Nd	0.04–0.70	≤0.18	0.20–0.36	0.93–1.32	0.15–2.08	≤0.06	≤0.21
Sm	≤0.11	≤0.13	0.15–0.27	0.05–0.64	0.05–0.47	≤0.03	≤0.02
Eu	≤0.02	≤0.03	0.07–0.12	0.01–0.07	0.01–0.54	b.d.	≤0.02
Gd	≤0.17	≤0.13	0.28–0.47	0.13–0.37	≤0.53	b.d.	≤0.05
Dy	≤0.14	≤0.21	0.30–0.49	0.03–0.72	0.04–0.63	b.d.	≤0.02
E1	≤0.05	≤0.20	0.12–0.21	0.02–0.34	≤0.33	b.d.	b.d.
Yb	≤0.03	≤0.22	0.16–0.21	0.02–0.32	≤0.32	b.d.	b.d.
Lu	b.d.	≤0.32	0.02–0.03	≤0.01	≤0.1	b.d.	b.d.
Hf	≤0.22	0.03–0.54	0.58–0.76	0.04–0.82	0.15–1.14	0.04–0.09	0.03–0.13
Ta	0.71–3.17	2.34–3.37	2.18–3.18	1.83–5.51	1.82–2.97	0.06–2.19	3.23–4.15
Pb	6.58–52.9	1.85–3.19	3.63–3.92	0.93–2.88	2.46–11.4	3.34–3.80	0.41–0.71
Th	0.11–0.25	0.14–0.65	0.52–1.06	0.45–8.9	0.12–3.1.5	b.d.	≤0.01
U	≤0.18	≤0.47	0.47–0.99	0.04–0.52	0.06–0.46	≤0.02	0.01–0.06

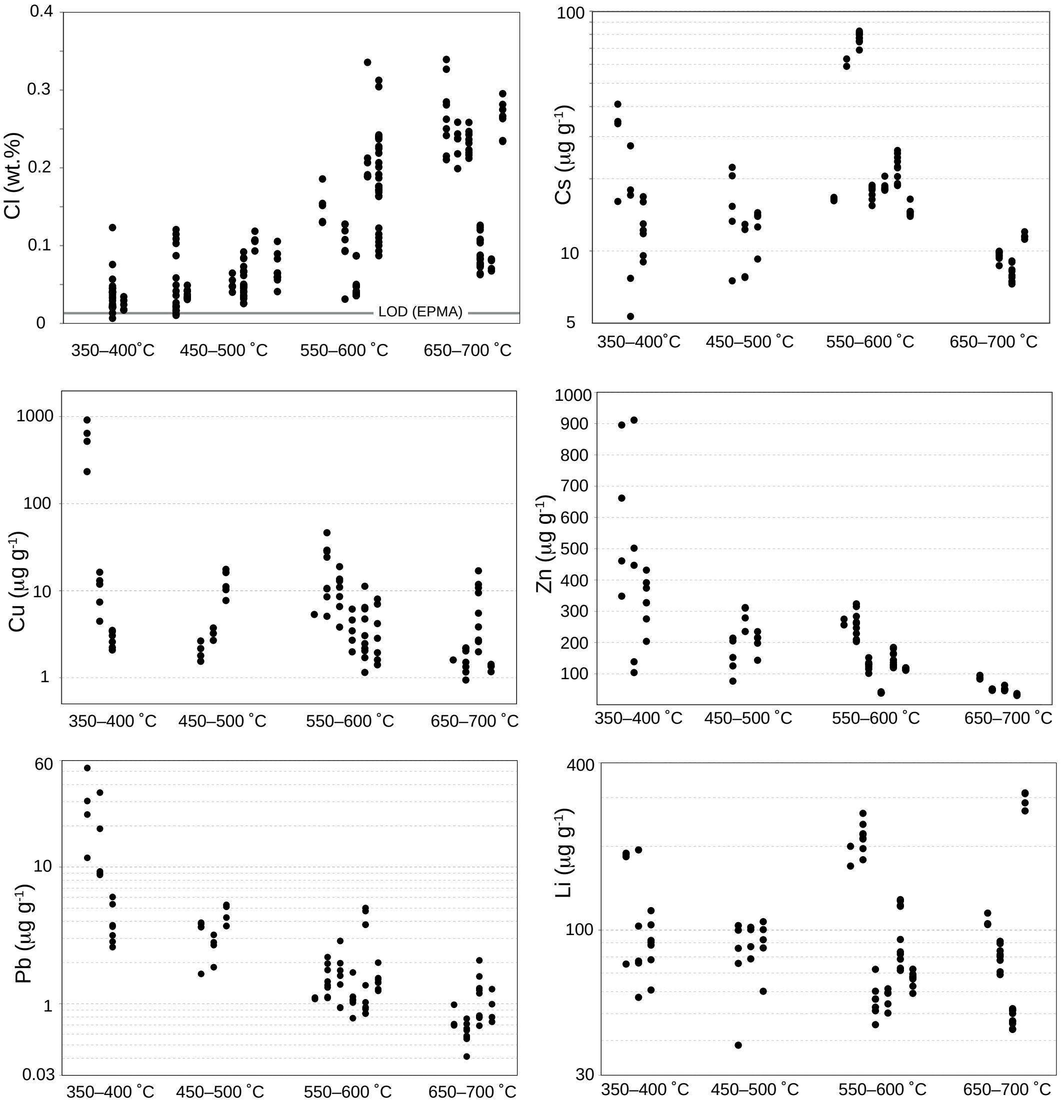

Figure 10: Trace elements in biotite from samples across the range of metamorphic grades. Individual samples are separated horizontally.

5.2.4 Garnet, staurolite and andalusite/sillimanite

Sample 94Kan38b is the only sample studied in details that contains garnet, staurolite, andalusite and small amounts of fibrolite (Table 2, Fig. 2). Garnet incorporates significant amounts of Y and HREE (Fig. 7, Table 5) with the garnet rims being enriched in REE compared to the grain cores (Table 5). The contribution to the whole rock Fe and Mg content is small due to the small modal fraction (~0.05) of garnet in the studied samples; however, a considerable amount of the bulk rock Mn is hosted in garnet (~20 %, Fig. 7). Staurolite in this sample is the main host for Zn, containing ~ 5300 µg g^{-1} and thus hosts ~75% of the bulk rock Zn (Fig. 7). Other trace elements are present in low concentrations and have little impact on the bulk rock composition (Table 5). Andalusite does not accommodate any significant concentrations of trace elements and fibrolitic sillimanite was too fine-grained to conduct meaningful trace element analysis by LA-ICP-MS.

5.2.5 Apatite

In all the analysed samples, irrespective of the metamorphic grade, apatite is the most important host for P (>90%, Fig. 7) and, together with biotite, is the only mineral that accommodates detectable Cl and F. A steady increase of the Cl concentration during metamorphism in apatite can be observed, leading to lower F/Cl ratios in apatite grains from high-grade samples (Fig. 11). The whole suite of REE is present in apatite with the middle rare earth elements (MREE and Y) being present in the highest concentrations compared to the other REEs (Fig. 7 and Table 5). However, compared to allanite and monazite, apatite contributes relatively small amounts of REE to the overall whole rock budget. On the other hand, apatite can be an important host for As (Fig. 7) with As concentrations generally decreasing with increasing metamorphic grade (Table 5, Fig. 11).

Apatite shows a broad range of REE compositions at low temperatures (≤ 500 ˚C) which notably contracts at temperatures > 500 ˚C (Figs. 8, 11, Table 5), as also reported by Hammerli et al. (2014). A similar trend can be seen for Sr and Pb, Sr concentrations in apatite range from ~200 to 1600 µg g^{-1} at low grade and ~ 70 to 250 µg g^{-1} at high grade. Lead contents vary between ~3 and 30 µg g^{-1} in low-grade samples, and high-grade samples typically contain < 6 µg g^{-1} Pb (Table 5, Fig. 11). The concentration of Th in apatite decreases during prograde metamorphism. Yttrium, on the other hand, is slighly enriched in apatite from higher metamorphic zones (Fig. 11, Table 5).

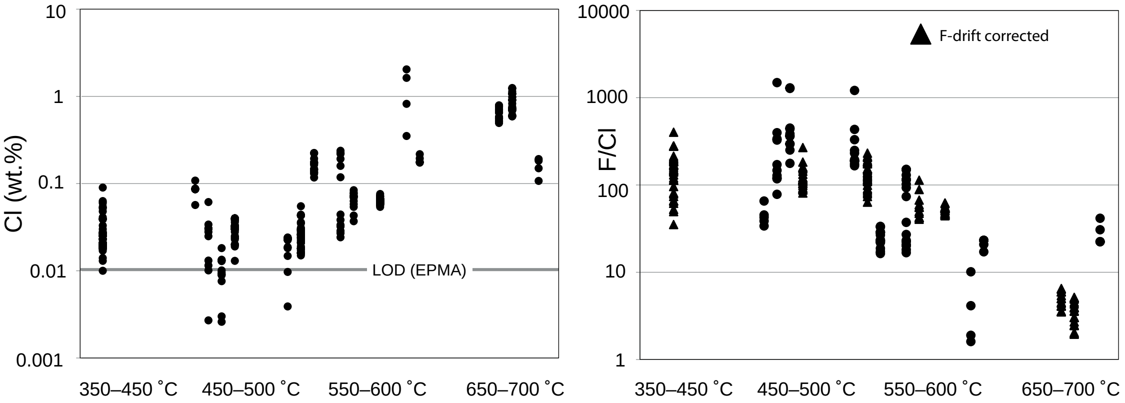

Figure 11: Trace elements in apatite across the metamorphic gradient. Individual samples are separated horizontally.

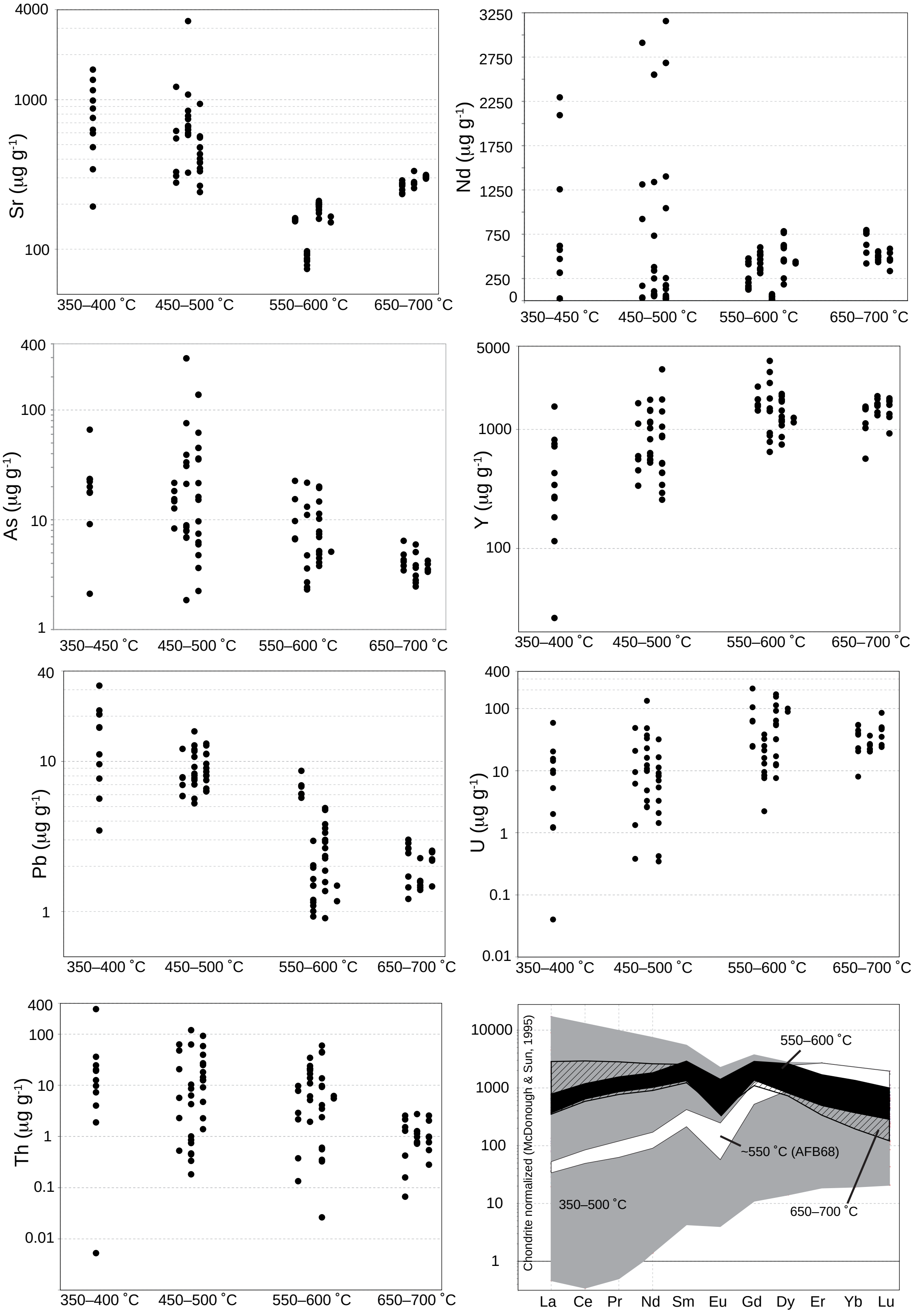

Figure 11 (continued)

Table 5: Composition range of apatite, titanite and garnet during metamorphism.

Sample	AFB59	AFB33	AFB27	AFB68	94Kan38	AFB74	AFBMG5
Mineral	Apatite	Apatite	Apatite	Apatite	Apatite	Apatite	Apatite
Temp. (˚C)	~350	450–500	450–500	550–600	550–600	550–600	≥650˚C
wt.%	(n=11)	(n=12)	(n=6)	(n=10)	(n=4)	(n=4)	(n=8)
CaO	55.94±0.56	55.78±0.32	56.17±0.37	55.52±0.42	54.87±0.69	55.16±0.83	56.84±0.28
P_2O_5	39.36±1.00	39.74±0.66	40.38±0.83	39.54±48	38.77±0.59	39.37±0.78	40.97±0.31
FeO	0.05±0.03	0.13±0.05	0.14±0.07	0.17±0.07	0.24±0.06	0.21±0.09	n.a.
MnO	0.04±0.04	0.07±0.03	0.09±0.03	0.07±0.03	0.19±0.1	0.25±0.07	n.a.
F	3.92±0.22	3.67±0.18	3.97±0.24	3.81±0.24	3.33±0.20	3.72±0.19	3.97±0.15
Cl	0.03±0.01	0.08±0.02	0.02±0.01	0.04±0.01	1.21±0.76	0.05±0.01	0.23±0.03
$\mu g\ g^{-1}$							
Li	≤3.67	≤3.47	≤1.33	b.d.	0.15–2.37	b.d.	b.d.
V	≤28.1	≤38.9	0.54–0.99	≤1.53	b.d.	0.45–3.86	≤0.36
Cu	≤15.3	≤2.98	b.d.	b.d.	0.82–131?	≤0.90	b.d.
Zn	≤7.98	b.d.	≤1.15	b.d.	18–25?	b.d.	≤3.54
As	2.12–66.1	1.85–75.8	8.33–21.7	≤4.74	2.45–37.6	4.40–18.5	2.45–5.95
Rb	≤2.05	≤3.80	≤0.52	≤1.94	0.015–1.69	0.1–0.7	≤0.38
Sr	193–1587	325–3351	309–1218	73.7–97.0	218–228	148–154	256–333
Y	26.1–1555	601–1458	337–1658	887–3760	306–378	1327–1498	1314–1901
Zr	0.10–14.9	≤3.19	≤9.48	≤3.75	≤19.7	0.14–0.58	≤2.63
Nb	≤0.28	≤0.74	≤0.47	≤0.33	≤0.20	≤0.11	b.d.
Mo	≤0.18	≤0.52	≤0.13	b.d.	≤2.16	0.11–0.44	b.d.
Sb	≤0.23	≤0.89	b.d.	b.d.	b.d.	≤0.03	b.d.
Cs	b.d.	≤0.05	b.d.	b.d.	≤0.14	≤0.03	b.d.
Ba	0.33–4.93	0.30–2.24	0.12–1.26	≤2.46	3.04–7.14	≤0.41	0.14–1.21
La	0.11–2129	10.9–515	5.35–2385	3.29–11.9	120–179	65.6–107	115–187
Ce	0.21–5191	44.2–2180	20.2–5420	9.64–49.8	351–548	318–460	428–633
Pr	0.05–608	8.56–511	4.06–756	1.80–10.1	60.2–83.4	66.7–89.1	76.9–104
Nd	0.64–2295	50.8–2551	28.5–2912	12.0–73.62	311–421	436–529	435–557
Sm	0.69–377	28.8–763	15.8–430	8.79–60.1	117–145	202–251	181–216
Eu	0.23–63.7	11.2–69.6	3.31–37.9	2.57–6.39	23.0–30.9	40.2–48.1	37.1–43.7
Gd	2.36–313	71.7–674	33.6–284	39.1–229	146–161	288–390	256–312
Dy	3.46–266	107–746	54.7–340	111–600	107–126	330–418	301–385
Er	3.25–155	53.5–425	32.6–201	85.0–429	31.0–38.5	163–176	135–199
Yb	3.11–62.3	34.0–413	26.3–164.6	67.6–356	16.1–26.6	117–120	86.3–139
Lu	0.51–15.9	4.02–15.2	3.12–20.9	9.00–50.00	1.89–3.33	13.9–15.2	9.89–17.5
Hf	≤0.28	≤0.09	≤0.16	≤1.83	0.06–0.84	≤0.04	≤0.12
Ta	≤0.02	≤0.12	b.d.	≤0.22	≤0.05	≤0.01	b.d.
Pb	3.46–31.9	5.25–15.8	5.87–12.1	0.93–2.95	2.70–4.83	5.03–6.46	1.39–2.27
Th	0.01–308	0.18–120	0.53–62.8	1.93–34.4	0.76–31.8	0.12–1.86	0.72–2.74
U	0.04–59.0	2.58–133	0.38–48.8	2.22–38.4	2.39–3.73	23.0–57.8	20.4–36.7

Sample	AFB59	AFB68
Mineral	Titanite	Titanite
Temp. (˚C)	~350˚C	550–600
wt.%	(n=9)	(n=6)
SiO_2	30.96±0.31	30.77±0.23
TiO_2	34.25±1.60	35.83±1.01
Al_2O_3	3.17±1.13	2.38±0.30
CaO	28.6±0.35	28.17±0.23
FeO	0.58±0.18	0.35±0.06
$\mu g\ g^{-1}$		
Li	≤19.2	b.d.
V	400–574	288–412
Cu	≤48.1	2.75–8.20
Zn	≤37.9	≤5.35
As	34.7–112	≤2.16
Rb	≤26.8	0.32–3.40
Sr	10.4–25.0	4.31–22.9
Y	1018–3993	6124–12606
Zr	187–840	29.7–331
Nb	444–1680	1364–5296
Mo	≤1.63	≤0.72
Sb	0.89–9.92	≤1.21
Cs	0.04–2.74	0.08–0.51
Ba	1.63–167	0.30–2.35
La	17.0–116	4.19–16.3
Ce	303–1301	31.5–142
Pr	109–454	8.49–29.1
Nd	767–2986	63.4–159
Sm	308–1052	41.1–136
Eu	87.1–278	73.4–229
Gd	277–787	105–525
Dy	194–921	305–1726
Er	87.2–458	309–1711
Yb	55.7–306	393–1923
Lu	5.62–24.2	64.0–269
Hf	10.7–37.7	2.92–13.8
Ta	41.9–98.8	93.7–259
Pb	1.13–190	0.83–4.57
Th	0.56–20.3	6.46–93.3
U	1.93–25.8	35.9–248

Sample	94Kan38b	94Kan38b
Mineral	Garnet Core	Garnet Rim
Temp. (˚C)	550–600	550–600
wt.%	(n=3)	(n=3)
SiO_2	38.00±0.34	38.15±0.37
Al_2O_3	21.0±0.21	21.21±0.22
CaO	1.75±0.18	0.88±0.15
MgO	2.45±0.11	2.62±0.12
MnO	5.75±0.15	6.44±0.05
FeO	30.10±0.72	30.21±0.68
$\mu g\ g^{-1}$		
Li	16.1–16.7	9.18–14.29
V	32.5–33.3	32.1–43.9
Cu	b.d.	b.d.
Zn	14.8–16.8	13.6–15.8
As	b.d.	b.d.
Rb	0.10–0.11	0.07
Sr	2.15–3.11	0.04–0.57
Y	752–1018	538–896
Zr	6.20–7.88	3.86–8.30
Nb	0.08–0.11	0.01–0.02
Mo	0.61–0.62	0.77–0.82
Sb	b.d.	b.d.
Cs	b.d.	b.d.
Ba	b.d.	b.d.
La	0.82–1.14	b.d.
Ce	3.14–4.34	b.d.
Pr	0.55–0.74	b.d.
Nd	3.19–4.40	0.04–0.09
Sm	2.49–3.02	0.42–0.77
Eu	1.27–1.17	0.49–0.81
Gd	16.0–16.9	6.13–11.2
Dy	126–129	61.3–105
Er	193–198	98.0–148
Yb	361–367	146–198
Lu	60.0–60.8	22.3–31.1
Hf	0.13–0.18	0.09–0.25
Ta	0.04	0.01
Pb	0.11–0.17	0.02–0.04
Th	0.34–0.48	≤0.05
U	0.20–0.22	0.02–0.09

5.2.7 Allanite, monazite, xenotime and zircon

Allanite and monazite are the major hosts for LREE, and monazite can be an important host for U (Figs. 7–9). In samples from low metamorphic grades (< 500 ˚C), minute grains (< 10 µm) of thorite are the most important hosts of the rocks U and Th content, as well as a considerable proportion of the LREE (Figs. 7 & 8). Monazite and allanite are also the main hosts for Eu, accounting for >70 % of the bulk rock Eu budget in most cases (Fig. 7, Table 6). Arsenic contents in monazite and allanite are relatively high, but cover a small range from 315 to 490 µg g^{-1} in monazite and from 120 to 190 µg g^{-1} in allanite, irrespective of the metamorphic grade (Table 6). Allanite commonly incorporates several thousand µg g^{-1} Sr whereas - with the exception of sample AFB33a (~ 3000 µg g^{-1} Sr) - monazite hosts <150 µg g^{-1} Sr (Table 6) and, hence, very little of the bulk rock Sr budget (Fig. 7). In general, REE, Pb, Th and U concentrations in allanite and monazite are variable on a mineral-scale (Table 6, Table 7). Nevertheless, the overall REE, Th, and U concentrations in monazite (Th: ~3100–45300 µg g^{-1}, U: ~810–5300 µg g^{-1}) and allanite (Th: ~42–844 µg g^{-1}, U: ~9–123 µg g^{-1}) do not vary systematically with metamorphic grade, as a similar similar concentration ranges is observed in all the studied samples (Table 6). Xenotime, if present, is the main host for Y and HREE, accommodating ≥50% of bulk rock inventory of these elements (Figs. 7, 8, Table 6). Zircon hosts >95% of the bulk rock Zr and Hf content and can also be an important host for HREE (~30%) and U (up to 20%) (Figs. 7 & 8).

5.2.8 Titanite and Ti (Fe-) oxides

Where present, titanite is a major host for Nb (up to ~5300 µg g^{-1}, Table 5, Fig. 7), Ta (up to ~250 µg g^{-1}, Table 5) and U (up to 190 µg g^{-1}). REE concentrations in titanite vary by an order of magnitude (Fig. 8, Table 5), which is most likely due to cryptic mineral zoning. Titanite is a major host for Y, containing up to ~12000 µg g^{-1}, while Zr and Hf concentrations are < 1000 µg g^{-1} and a few 10s of µg g^{-1}, respectively (Table 5). Titanite can also be an important host for HREE. Titanite grains from sample AFB59 (~350˚C) generally contain higher concentrations of LREE and lower concentrations of HREE than titanite found in sample AFB68 (550–600 ˚C). Furthermore, titanite from the lower-grade sample seems to be depleted in Y and Nb compared to titanite in sample AFB68 (Table 5). Rutile contains high concentrations of high field strength elements (HFSE: Ti, Nb, Ta, Zr, Hf), including up to ~13000 µg g^{-1} Nb and ~730 µg g^{-1} Ta, and also has elevated concentrations of U and Th. However, with the exception of Nb and Ta, rutile hosts a small fraction of the bulk rock HFSE content, due to the low modal fraction (Fig. 7). Ilmenite incorporates elevated concentrations of Nb and Ta (~1300 and ~80 µg g^{-1}, respectively) and also contains ~ 4300 µg g^{-1} Zn. However, as with rutile, the modal abundance of ilmenite is low (Fig. 2) and, hence, ilmenite only hosts a minor proportion of the bulk rock's inventory of these elements (e.g. < 10 % of the bulk-rock Zn). REE concentrations in ilmenite are typically <1 µg g^{-1} and are therefore not of significance for our study (Fig. 7).

Table 6: Compositional range of allanite, monazite and xeontine during metamorphism.

Sample	AFB59	AFB27	AFB68
Mineral	Allanite	Allanite	Allanite
Temp. (˚C)	~350	450–500	550–600
wt.%	(n=4)	(n=6)	(n=5)
SiO_2	33.4	34.39±2.6	33.50±0.30
TiO_2	0.14±0.09	0.21±0.04	0.15±0.08
Al_2O_3	16.96±0.38	17.54±0.50	19.86±0.32
CaO	12.89±0.59	10.42±0.67	12.62±0.50
FeO	10.81±0.54	11.74±1.13	10.31±0.52
MgO	0.38±0.16	0.18±0.04	0.41±0.15
MnO	0.35±0.14	0.45±0.07	0.30±0.13
$\mu g\ g^{-1}$			
V	747–1057	1118–2280	255–335
Cu	38.3–127	n.d.	3.35–61.0
Zn	88.4–122	70.4–91.9	44.7–60.2
As	275–389	159–195	122–189
Rb	3.67–16.8	≤0.53	1.01–2.58
Sr	1246–1999	949–3025	743–1441
Y	726–954	1865–2878	2606–3277
Zr	23.4–505	3.91–24.1	17.8–237
Nb	0.50–1.17	0.11–27	0.47–2.27
Mo	≥1.02	≤0.81	≤0.52
Sb	6.05–7.30	1.94–26.5	0.52–1.32
Cs	0.23–0.63	b.d.	0.09–0.12
Ba	6.55–27.3	0.50–5.08	17.3–47.8
La	32330–47199	39939–49453	41110–47883
Ce	67404–91617	81978–93525	66451–89914
Pr	6585–9323	7590–9950	8564–9344
Nd	20923–27968	33171–37621	25809–33840
Sm	2063–3221	4635–6087	5266–7162
Eu	387–509	643–924	973–1520
Gd	857–1293	2143–3115	3482–4024
Dy	181–197	612–940	1318–1385
Er	46.6–65.0	154–234	220–300
Yb	21.6–31.5	148–240	122–169
Lu	2.52–4.01	23.0–30.9	13.1–17.8
Hf	1.10–16.5	0.37–2.85	1.16–17.9
Ta	0.03–0.18	≤0.06	0.09–0.56
Pb	72.2–220	21.1–72.2	28.0–284
Th	234–533	133.0–254	41.5–844
U	13.5–52.8	8.66–14.8	93.1–123

Sample	AFB33a	94Kan38	AFB74	AFBMG5
Mineral	Monazite	Monazite	Monazite	Monazite
Temp. (˚C)	450–500	550–600	550–600	≥650˚C
wt.%	(n=3)	(n=4)	(n=5)	(n=4)
P_2O_5	30.5	30.4	30.5	29
$\mu g\ g^{-1}$				
As	347–435	317–422	315–438	378–490
Rb	183–683	3.13–38.1	1.52–60.6	0.36–0.53
Sr	2672–3244	61.5–134	43.6–89.2	18.0–107
Y	48041–5717	7199	5812–6123	10489–11820
Zr	4650–20198	21.6–53.0	3.68–19.89	2.10–3.23
Nb	10.1–41.4	0.17–3.52	0.15–0.91	0.26–0.28
Cs	3.96–5.48	0.89–1.22	0.07–2.84	b.d
La	89626–109873	90379–130142	106189–132388	115257–157411
Ce	189575–236929	185971–246499	202504–259150	234320–278913
Pr	19481–25793	19794–27249	20317–27665	25766–29579
Nd	70611–98166	71691–99160	70512–99975	93510–114662
Sm	12763–19412	13134–21295	10301–18875	15477–17591
Eu	2718–3931	2080–2982	1653–2381	1029–2404
Gd	7986–10611	9252–15640	6248–11640	10532–12295
Dy	2408–2535	3366–5403	2283–4042	4201–4538
Er	281–485	440–651	470–796	747–883
Yb	124–277	96.4–135	161–237	150–256
Lu	14.3–37.3	6.72–9.92	13.6–19.6	12.2–20.9
Hf	97.9–412	0.62–1.76	0.25–0.62	≤0.15
Ta	1.09–5.27	0.05–30	0.04–0.12	0.05–0.06
Pb	515–573	1044–1447	302–943	274–1931
Th	3125–6055	26844–31773	4824–25020	6443–45314
U	934–2157	3926–4936	2755–5797	811–3318

Sample	AFB33a	AFB74	AFB27	94Kan38b	AFBMG5
Mineral	Xenotime	Xenotime	Xenotime	Xenotime	Xenotime
Temp. (˚C)	450–500	550–600	450–500	550–600	≥650 ˚C
wt.%	(n=1)	(n=1)	(n=3)	(n=1)	(n=1)
P_2O_5	38.6	38.6	38.6	38.6	38.6
$\mu g\ g^{-1}$					
Y	374043	275661	297578–383931	385240	366002
Zr	12807	117	1281–8678	2968	353
Nb	9.4	0.8	b.d.	3.4	1.8
La	291	23	108–163	49	42
Ce	1284	374	345–643	552	422
Pr	276	185	96.4–174	241	196
Nd	2658	2719	1192–1937	3116	2666
Sm	5415	4621	2881–5564	5296	4469
Eu	2548	944	371–496	971	1583
Gd	26683	16759	15260–18013	20702	19384
Dy	57893	41383	46914–59283	57328	50274
Er	36321	33198	37841–46625	48794	40951
Yb	28143	31876	34635–37695	51144	39266
Lu	3621	3996	4395–4839	7180	5491
Hf	290	3.9	210–259	44.	7.2
Ta	1.9	4.9		0.9	0.7
Pb	231	b.d.	952	111	46
Th	7224	0.5	567–6083	3115	1019
U	4087	2711	2947–3288	11764	7345

5.2.9 Element distribution coefficients

In samples from high-grade metamorphic zones (>600 ˚C) pertrographic observations indicate complete recrystallization of most mineral phases, it is inferred that chemical equilibrium was, or was very nearly reached during metamorphism. In these cases, we calculate approximate element distribution coefficients from the composition of mineral pairs according to the formula $D_i=X_i/Y_i$, where D_i is the distribution coefficient, and X_i and Y_i represent the concentration of an element (i) in respective minerals (Table 7). We chose sample AFB74, AFB112, and AFB126 from the sillimanite zone and sample AFBMG5 and AFBMG6 from the migmatite zone for element distribution calculations. Our results show that distribution of Pb between muscovite and biotite is close to unity, except for sample AFBMG5 where considerably more Pb is sequestered in biotite (Table 7). Plagioclase incorporates less Pb than K-feldspar (Table 3) resulting in distribution coefficients ($D_{Pb}=Pl_{Pb}/Kfs_{Pb}$) between 0.27 and 0.40 (Table 7). Barium preferentially partitions into K-feldspars over muscovite by a factor of 3 to 5, and into muscovite over biotite by a factor of 1.5 and 2 (Table 7). Distribution coefficients between biotite and muscovite (Bt/Ms) are ~0.1 to ~0.15 for Cs and Li, and between 0.03 and 0.05 for Zn. Distribution coefficients for Ta and Nb between muscovite and biotite are more variable (~0.3–1.1 and 0.2–0.9, Table 7).

Table 7: Distribution coefficients calculated from LA-ICP-MS analyses

Pb distribution coefficients (D_{Pb})		**Ms/Bt**	**Bt/Pl**	**Bt/Kfs**	**Pl/Kfs**	**Ms/Pl**	**Ms/K**
Temperature	Sample						
~ 600 ˚C	AFB74	0.96	0.18			0.18	
~ 600 ˚C	AFB112	0.89	0.13	0.04	0.27	0.14	0.0
~ 600 ˚C	AFB126	1.01	0.13	0.05	0.40	0.14	0.0
≥ 650 ˚C	AFBMG5	1.53	0.07	0.02	0.31	0.04	0.0
≥ 650 ˚C	AFBMG6	0.91	0.18			0.17	

Ba distribution coefficients (D_{Ba})		**Ms/Bt**	**Bt/Pl**	**Bt/Kfs**	**Pl/Kfs**	**Ms/Pl**	**Ms/K**
Temperature	Sample						
~ 600 ˚C	AFB74	1.52	8.8			13.2	
~ 600 ˚C	AFB112	1.85	12.8	0.12	0.01	23.8	0.2
~ 600 ˚C	AFB126	1.99	16.2	0.12	0.01	32.2	0.2
≥ 650 ˚C	AFBMG5	1.56	11.6	0.18	0.02	18.2	0.2
≥ 650 ˚C	AFBMG6	1.78	7.7			14.0	

Rb distribution coefficients (D_{Rb})		**Ms/Bt**	**Bt/Pl**	**Bt/Kfs**	**Pl/Kfs**	**Ms/Pl**	**Ms/K**
Temperature	Sample						
~ 600 ˚C	AFB74	0.45					
~ 600 ˚C	AFB112	0.45		2.58			1.1
~ 600 ˚C	AFB126	0.44		2.30			1.0
≥ 650 ˚C	AFBMG5	0.53		2.74			1.4
≥ 650 ˚C	AFBMG6	0.45					

Distribution coefficients Ms/Bt		**Cs**	**Zn**	**Li**	**Nb**	**Ta**
Temperature	Sample					
~ 600 ˚C	AFB74	0.12	0.03	0.11	1.08	0.65
~ 600 ˚C	AFB112	0.10	0.05	0.12	0.31	0.20
~ 600 ˚C	AFB126	0.10	0.04	0.13	0.45	0.28
≥ 650 ˚C	AFBMG5	0.16	0.04	0.09	0.97	0.58
≥ 650 ˚C	AFBMG6	0.12	0.05	0.15	1.00	0.88

6. Discussion

6.1 Major elements

The studied samples do not show correlations between major element concentraions and metamorphic grades, even when the variation in protolith is accounted for. The decline of LOI values of our samples during prograde metamorphism (Fig. 3) confirms the expected decrease of volatile phases during metamorphism, but there are no correlations between major element concentrations and metamorphic grades. Hence, despite widespread up-temperature fluid flow during metamorphism (e.g. Cartwright et al., 1995; Oliver et al., 1998), the metamorphic evolution can be regarded as an essentially isochemical process for major elements as no discernable mass transfer of major elements is observed.

6.2 Immobile trace elements

The average bulk rock Hf, Zr, U and Th values are slightly higher than the PAAS reference values (Fig. 4), which is considered to reflect a higher protolithic zircon content in the studied samples. The relatively low Pb and Sr values in the AFB samples can be explained by the lower carbonate content of samples from the northern suite. The range of trace elements in each metamorphic zone is consistent with the variable concentrations of major elements, and the modal variability of trace elements (Figs. 2, 3). Variations in the concentration of REE and other trace elements, including Zr, Hf, Th and U, correlate with the bulk rock P_2O_5 content (Fig. 12), which is consistent with P- and Zr-bearing minerals such as apatite, monazite and zircon controlling the trace element inventory of these rocks. Moreover, concentrations of P_2O_5, REE and other trace elements (e.g., U, Th) are not correlated with metamorphic grade, which means that the concentration of most trace element is controlled by varying fractions of heavy minerals (e.g., apatite, monazite, zircon, xenotime) in the protolith sediment (Figs. 2, 7, 12). This is similar to what Ronov et al. (1977) proposed, that variations of rock forming- and trace elements are inherited from the primary facies. Such variations in mineral fraction are also expressed be by the non-systematic variations of accessory phase fractions in samples from various metamorphic-grades (Fig. 2). Furthermore, our results show no systematic change in concentrations of Ba, Rb, Cu, Sc, Mo, Sn, HFSE and Sb during metamorphism. High-field strength minerals are often considered to be immobile elements, as they are only effectively soluble in F-rich fluids, with very high fluid fluxes, that are rarely found in metamorphic environments (e.g., Jiang et al., 2005, Rapp et al., 2010). In this case it seems that the above elements are completely redistributed during mineral resorbtion or recrystallization processes during prograde metamorphism.

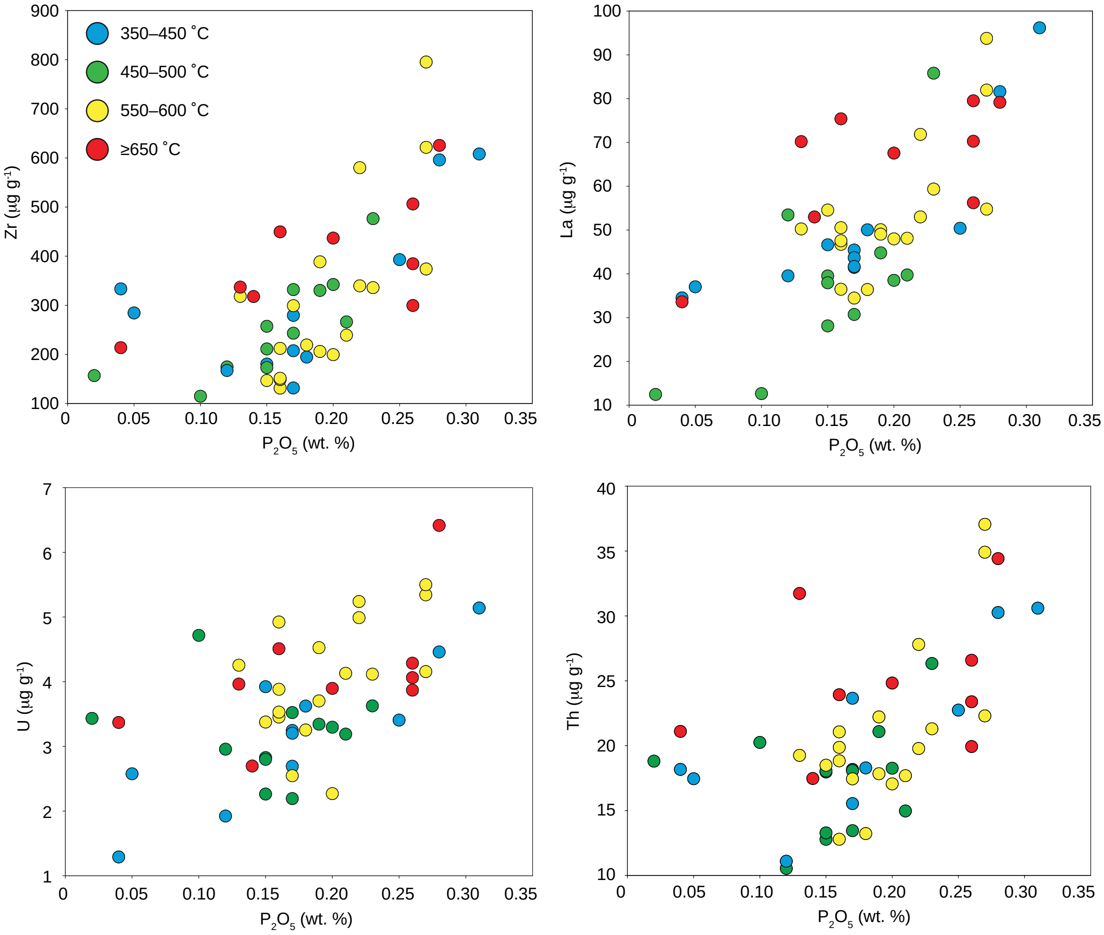

Figure 12: Whole-rock trace element (Zr, La, U, Th) concentrations in µg g^{-1} versus whole rock P_2O_5 (wt.%) contents.

6.3 REE redistribution

The results show that the vast majority of REE, Th and U are hosted in the accessory phases allanite, monazite, apatite, xenotime, titanite and zircon (Fig. 7, see also Bea et al. 1996). Hence it is fundamental to understand the behaviour of these trace element-rich accessory minerals during metamorphism. Several studies have shown that the stability of the above phases strongly relates to bulk rock composition (e.g., Janots et al., 2007, 2008; Spear, 2010). Despite lacking sub-greenschist facies samples (< 300 ˚C), petrographic observations and homogeneous isotopic Nd signatures in allanite from the lowest-grade sample (AFB59; Hammerli et al. 2014) strongly suggest that the transition from detrital monazite to metamorphic allanite follows the predictions by Janots et al., (2007, 2008) and Spear (2010). Allanite is stable up to ~500 ˚C (AFB27) and ~ 550–600 ˚C in the Ca-enriched sample (AFB68), which agrees well with the proposed stability field of allanite in rocks of similar chemical compositions (e.g. Wing et al., 2003; Janots et al., 2007, 2008; Spear, 2010). The reappearance of monazite at ~ 600 ˚C (AFB74, 94Kan38b) agrees with the proposed allanite break down reaction at temperatures below 600 ˚C and the subsequent monazite formation for similar bulk rock compositions (Janots et al., 2007, 2008; Spear, 2010). Furthermore, xenotime is present as small grains that have been inferred to be products of allanite-monazite transformation reactions (e.g. Janots et al., 2008). Figure 7 shows that REEs are recycled into the above minerals during following metamorphic reactions during sub-greenschist metamorphism: detrital monazite + chlorite + calcite ± hematite = allanite + apatite + thorite + biotite. The allanite-monazite transformation in the upper greenschist/lower amphibolite facies most likely occured via a reaction similar to apatite + allanite + thorite = monazite + xenotime + plagioclase ± magnetite. The poor budgeting of REE (mostly HREE) in sample AFB59 is most likely due to minute HREE-rich grains such as xenotime that are too fine-grained to be identified and analysed.

Complete apatite recrystallisation takes place at temperatures <550–600 ˚C (e.g., sample AFB68) when sample scale heterogeneity in apatite trace element concentrations is reduced (Fig. 11) and Nd isotope homogenisation is reached (Hammerli et al., 2014). In this case compostional trends in apatite (e.g., Y, Th, U, Nd, Sr, Fig. 11) across metamorphic gradients needs to be interpreted with caution as only high temperature apatite (> 500 ˚C) is equilibrated to metamorphic conditions. Early titanite seems to have formed via the reaction Quartz + Calcite + Rutile = Titanite, which is confirmed by petrographic observations where titanite overgrows rutile grains. Our element distribution calculations show that calcite can host considerable amounts of HREE. In the presence of calcite, titanite is depleted in HREE compared to titanite in calcite-absent assemblages (Fig. 7, Table 5). Hence it is inferred that some of the HREE sequestered in calcite becomes incorporated in titanite either via the above reactions, or during HREE liberation via other calcite-breakdown reactions such as decarbonatization. However, if present, xenotime is the most likely major host for HREE. The high concentrations of LREE in titanite from sample AFB59 might suggest that detrital monazite was involved in the formation of titanite, further supporting allanite and titanite formation at similar P-T conditions, as inferred by Hammerli et al. (2014a).

I observed that in most of the samples, cumulative U and Th concentrations found in the analysed minerals show poor agreement with the bulk rock U and Th content. I detected minute grains of Th, U-rich phases, probably thorite in sample AFB59 and AFB27. However due their low abundance and heterogeneous compositions, analyses of multiple grains and subsequent calculation of U and Th distributions and bulk rock budgets is challenging. When monazite is present, Th and U show a reasonable agreement with the bulk rock U and Th content (Fig. 7) because monazite incorporates significantly higher amounts of Th and U than allanite (Table 6). However, the variability of Th and U in monazite due to zoning makes it difficult to calculate U and Th budgets. Nonetheless, I conclude that the vast majority of Th and U is hosted in monazite (Figs. 5 & 6) and that the majority of Th and U in monazite-absent assemblages must be built in U-Th rich phases such as thorite.

Except for sample AFB59 and AFB27, calculated Pb budgets agree well with bulk rock Pb concentrations (Fig. 5). The discrepancy in sample AFB59 can be explained by the large range of Pb concentrations in micas (Table 4) and that calculated average values might be lower than the actual Pb concentration in micas. Due to the small grain-size and inclusions, I was not able to obtain meaningful results for K-feldspar in sample AFB27 and AFB33a. However, we assume that at least parts of the missing Pb is hosted in K-feldspar (e.g. ~ 25 µg g^{-1}) as observed in other samples (Table 3, Figs. 7, 9). Barium distributions are well constraint in samples ≥ 600 °C, whereas in lower-grade samples (e.g., AFB27 and AFB33) a considerable amount of the bulk rock Ba is unaccounted for. In sample AFB27 and AFB33a, this can be explained by the lack of data for K-feldspar which can concentrate several thousands of µg g^{-1} Ba in its crystal lattice (Table 3).

6.4 Mobile trace elements (Cs, Zn, Pb, As)

My results show that the rapid decrease of Cs in migmatites (Fig. 4) compared to lower metamorphic grades is most likely the result of Cs loss from mica (Fig. 10). Cesium decrease during high-grade metamorphism has also been previously reported (e.g., Heier and Brunfelt, 1970); in particular Bebout et al. (2007) showed that Cs loss from HP metasedimentary rocks is strongly linked with Cs loss from mica. This is consistent with our data at lower pressures, where biotite from samples <650 °C contain up 80 µg g^{-1} Cs whereas Cs concentrations in biotite from migmatites show a restricted range of 7–12 µg g^{-1}. No systematic changes of concentrations of other trace elements in mica such as Li, Ba and Rb during metamorphism was observed (Fig. 10).

The data from the northern suite (AFB) shows a decrease of As concentrations between ~450 and 500 °C, corresponding to the greenschist-amphibolite facies transition. The decrease of bulk rock As concentrations from the southern suite is less pronounced and seems to take place at higher temperatures (Fig. 4), although this is based on a fairly limted dataset. Decreasing As concentrations during metamorphism, particularly at the greenschist-amphibolite grade transition, have previously been reported (Bebout et al. 1999; Roser and Nathan 1997; Pitcairn et al., 2006). Bulk rock As loss can be explained by the relatively limited stability field to low-grade metamorphic conditions of major As hosts such as pyrite. The recrystallization of pyrite to As-depleted pyrrhotite (e.g. 2 pyrite + $2H_2O$ = 2 pyrrhotite + $2H_2S$ + O_2) during (sub-) greenschist facies metamorphism decreases the abundance of pyrite significantly (Pitcairn et al., 2006 and therein). This desulfidation reaction could lead to S loss when removed by metamorphic fluids.

Alternatively, H_2S might form fresh pyrrhotite by reacting with Fe released from silicates (Pitcairn et al., 2006). If the above reaction occurs at sub-greenschist conditions, As and possibly S are removed early in the metamorphic history of a rock. The observed As decrease in apatite (Fig. 11) with increasing metamorphic grades therefore rather reflects the As content in peak-metamorphic fluids and hence apatite did not act as As sink during the above reactions.

The continuous decrease of Pb on a bulk rock scale during metamorphism has been reported in earlier studies (e.g. Haack et al., 1984; Oliver et al. 2008). In pelitic samples (AFB33a and 94Kan38b) micas are the most important Pb hosts whereas in samples with a higher psammite component most of the Pb (>80%) is hosted in feldspars (Figs. 7 & 8). There is a continuous decrease in Pb content from micas during prograde metamorphism (Table 4, Fig. 6; see also Chapter 5), while Pb concentrations in feldspar do not seem to change with increasing temperatures (Table 3). Lead diffusion in feldspar is expected to be very slow (Cherniak, 1995) so redistribution of Pb from micas into feldspar requires recrystallization of theses phases (at least in sub-migmatitic samples). The process of Pb loss in low-grade rocks can partially be explained with decarbonatization reactions when Pb is released from calcite and subsequently removed by metamorphic fluid. Another mechanism that explains Pb loss on a bulk rock and mineral scale is the interaction of Cl-rich fluids with micas where Pb is leached out and transported in fluid as Pb–Cl species. This is consistent with the negative correlation between the Cl and Pb content of biotite (Fig. 13).

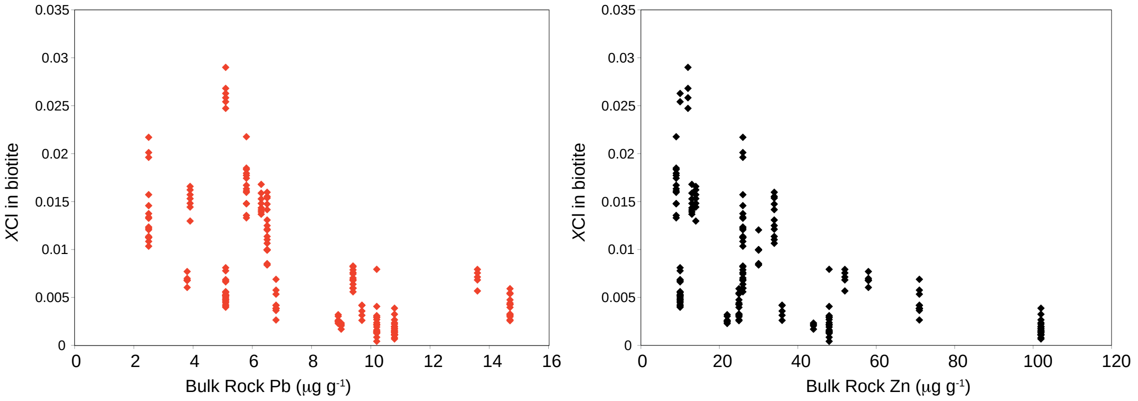

Figure 13: Bulk rock Zn and Pb vs. molar Cl content of biotite. Individual samples are vertically separated.

Finger and Schiller (2012) suggested that melt is enriched in Pb due to the incompatibility of Pb during fluid-absent melting processes. The authors argue that muscovite is an important Pb host in amphibolite facies metapelitic rocks and that during mica, and especially muscovite breakdown, considerable amounts of Pb are released to the melt. My data indicate that Pb preferentially incorporates into feldspars compared to micas (D_{Pb}=Ms_{Pb}/Kfs_{Pb} =~0.04; Table 7), so the modal abundance of micas and feldspars can strongly influence the degree of Pb liberation during melting processes. In pelitic rocks mica has an important role in hosting Pb (Figs. 7 and 9), and hence can liberate significant Pb during partial melting, whereas feldspar rich psammitic rocks may be able to retain much more Pb during partial melting.

The results from the northern prograde metamorphic suite (AFB) show that the continuous decrease of Zn during metamorphism is strongly linked with Zn decrease in biotite and muscovite where Zn occupies octahedral sites and likely preferably replaces Fe over Mg (e.g. Iltonen and Eugster, 1990). Since more than 85 % of the bulk rock Zn is hosted in biotite (in staurolite-absent rocks, Fig. 7, see also Chapter 5), Zn loss from biotite is deemed to be responsible for the decrease of Zn during metamorphism. Higher fluid/rock ratios together with elevated temperatures lead to higher Cl concentrations in biotite (see below), which correlates with lower Zn contents in biotite due to Zn-Cl-complexing in the fluid phase (Fig. 13) and potentially to a homogenization of Zn concentrations in micas (Fig. 6). Samples from the southern suite (94Kan) do not show a decrease of Zn concentrations during heating to 600 ˚C (Fig. 6), as most samples from the temperature range 550–600 ˚C contain staurolite (Fig. 6) that effectively retains most of the Zn in the rock (Fig. 7). Decrease of Zn on a bulk rock scale during metamorphism has been observed by Haack et al. (1984) and Lebedev and Nagaytsev (1982), both of whom reported Zn loss at metamorphic grades above the staurolite zone. However, other studies (e.g. Roser and Nathan, 1997; Pitcairn et al., 2006; Yang and Rivers, 2000; Garofalo, 2012) did not observe Zn depletion in biotite or bulk rock with prograde metamorphism.

Similar to Pb loss during metamorphism, my results suggest that a Cl-rich fluid is necessary to bring Zn into solution as Zn-Cl complexes via fluid-biotite interaction, which is in accordance with Ilton & Eugster (1989, 1990) who have shown that base metals partition strongly into Cl-bearing fluids. In the presence of staurolite, Zn might be sequestered in the crystal structure until staurolite decomposes and Zn is liberated, as observed in previous studies (Haack et al., (1984) and Lebedev and Nagaytsev, 1982). Both studies infer Zn transport in metamorphic fluids after staurolite breakdown, and Haack et al. (1984) infers that the decomposition of biotite (biotite + sillimanite + quartz → cordierite + K-feldspar ± garnet + H_2O) leads to Cl liberation necessary for metal complexing in high-grade rocks. Staurolite hence might be a more robust Zn host during fluid-rock interaction. However, despite lacking pelitic migmatite samples in this study, Zn loss after staurolite breakdown prior to anatexis is expected, resulting in Zn-depleted migmatites (Haack et al., 1984).

My results show that staurolite and biotite concentrate the vast majority of Zn in crustal-derived sedimentary rocks; other rock-forming minerals such as garnet (~ 15 $\mu g\ g^{-1}$) or cordierite (~ 30 $\mu g\ g^{-1}$; Bea et al., 1994) only host minor concentrations of Zn. It is yet to be investigated which mineral phases control Zn concentrations prior to biotite formation in mid-greenschist facies conditions, although chlorite is likely to be an important Zn host as Heinrichs et al. (1980) reported between 700 and 1000 μg g^{-1} Zn in chlorite in sedimentary rocks.

Biotite and muscovite from low-grade samples can contain considerable amounts (several hundreds of μg g^{-1}) of Cu while generally biotite from higher metamorphic grades contains much lower concentrations (except sample 94Kan38b). However, no Cu decrease on a bulk rock scale can be observed as only a small fraction of Cu is hosted in biotite (Table 4, Fig. 7). I was not able to identify the major Cu host in this study, but it is expected that most of the bulk rock Cu is hosted in dispersed minute grains of chalcopyrite or other sulfides (see Pitcairn et al., 2006).

6.5 Fluid flow during metamorphism

My observation of a general increase of the Cl component in apatite and biotite during prograde metamorphism (Figs. 10 & 11) indicates the presence of a Cl-rich fluid. Chlorine enrichement in apatite during metamorphism is somewhat unusual as apatite typically becomes enriched in F during prograde metamorphism (Smith and Yardley, 1999; Spear and Pyle, 2002 and therein). Smith and Yardley (1999) suggest that the release of Cl from detrital magmatic apatite could contribute to the salinity of metamorphic fluids. I have previously demonstrated that apatite in our sample suite recrystallises 500–600 ˚C (Hammerli et al., 2014a), which also corresponds to the temperature at which Cl contents of biotite and apatite increase, which argues against a detrital apatite source for the elevated Cl contents. The F/Cl ratio in biotite also decreases with increasing temperatures, which is in accord with the mechanisms described in Zhu and Sverjesky (1992) that biotite incorporates higher Cl concentrations at higher temperatures in the presence of Cl-bearing fluids. My data show a general negative correlation between Mg and Cl content in biotite, following the Mg-Cl “avoidance rules” (Fig. 14; Munoz, 1984). Conversely, the Fe-F avoidance rule is not pronounced in my samples (Fig. 14). The relatively high Ti contents of in biotite, especially from the high-grade rocks (Table 4) may affect halogen incorporation mechanisms, which may have adverse implications for the accuracy of fluid fugacity calculations (e.g. Cesare et al., 2008). Halogen contents in biotite can be used to constrain the composition of hydrothermal fluids that interacted with the rock during metamorphism (e.g., Munoz, 1984). I chose the more formal approach of Zhu and Sverjensky (1992), as described in Coulson et al. (2001), which incorporates calculated log Ks for exchange reactions between annite, phlogopite, and the OH-, Cl- and F-rich biotite endmembers to calculate HCl/H_2O and HF/HCl ratios in the fluid from the biotite compositions. Activity HCl/H_2O ratios of the fluids determined from biotite, vary up to 1.6 log units of a given metamorphic grade (Fig. 14). Variations of the calculated fugacitites within a metamorphic zone, irrespective of the metamorphic grade, is likely the result of some degree of rock buffering of fluid composition (e.g. Mora & Valley, 1989; Oliver et al., 1992).

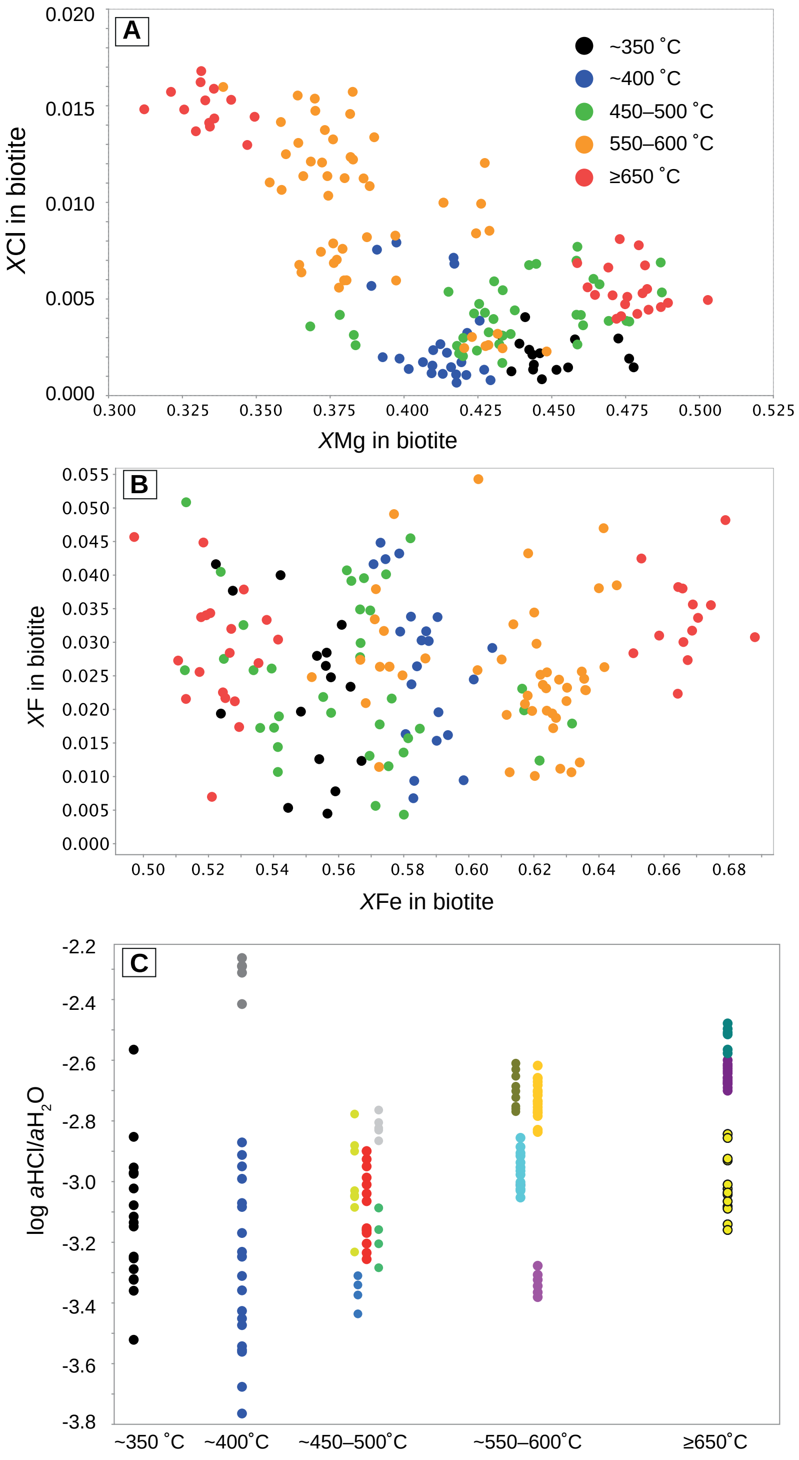

Figure 14: A) Molar fraction of Cl vs molar fraction of Mg in biotite. The negative correlation between *X*Cl and *X*Mg confirms “Mg-Cl avoidance” in biotite. B) Molar fraction of F vs. molar fraction of Fe in biotite shows a less pronounced trend of Fe-F avoidance. C) HCl/H_2O activity ratios in fluids calculated from biotite compositions vs. temperature. Each color represents a different sample.

However, the relatively large spread (-3.8 to -2.2) of calculated log aHCl/H_2O seen at low grade (≤ 400 ˚C) (Fig. 14) is replaced by progressively more homogeneous, and higher set of values at higher grades (Fig. 14) . The contraction of fugacity ratios in higher-grade rocks can be explained with higher fluid/rock ratios, as a consequence of the progressive up-temperature fluid flow. That is, at lower grades there is a tendency for inter-layer variability in halogen ratios, inherited from the protolith, to be preserved, whereas at higher grades the fluid composition across all original layers is inferred to have progressively converged on the composition of the infiltrating fluid, possibly also assisted by enhanced diffusion rates across layers at higher temperatures (Korzhinskii, 1965).

Together with increasing Cl-contents in apatite and biotite from high-grade rocks, the presence of scapolite in calcareous rocks in the Eastern Mt. Lofty Ranges strongly supports the interaction of rocks with Cl-bearing fuids (Hammerli et al., 2013). Fluid compositions in metamorphic rocks from my study site show higher HCl/H_2O activity ratios compared to fluids active during regional metamorphism of pelites in south-central Connecticut (~ -4.2 to ~ -5) or fluids typically involved in porphyry systems (~ -3.7 to ~ -5.3; e.g., Siahcheshm et al., 2012; Afshooni et al., 2013 and therein). In combination with the evidence of pervasive, up-temperature flow, this suggests that Cl-bearing fluids derived from the low metamorphic grade, little metamorphosed protoliths flowed along the metamorphic gradient towards the high temperature core.

7. Conclusions

This study suggests that metamorphism of crustal-derived metasedimentary rocks is an isochemical process for all major elements at P-T conditions similar to the middle/upper crust. The increase in the bulk chlorine content of the rocks at higher grade despite the decrease in LOI, along with the compositional homogenization of minerals and fluid, is consistent with the infiltration of a Cl-bearing fluid, even as the rocks progressively lost H_2O and CO_2. The influx of saline fluids permitted changes in LOI, Cl/H_2O, and Zn, Pb, As and Cs, but not the alkali elements, major elements or REEs. The observed As loss at the greenschist-amphibolite facies transition confirms findings of previous studies and is consistent with the recrystallization of pyrite to pyrrhotite. I also observed Cs depletion in migmatites that can be explained by the incompatibly of Cs in micas in high-grade metamorphic rocks. Significant element mobility during metamorphism is likely only achieved under conditions with high fluid flux.

Chapter 5

Metal release from biotite during prograde metamorphism as a source for Pb-Zn ore deposits

Abstract

I present a detailed study of metal mobility during regional metamorphism where up-temperature flow of a Cl-bearing fluid led to a continuous depletion of Pb and Zn on a mineral- and bulk-scale during prograde metamorphism. Biotite contains a large proportion of the total Pb and >80 % of the bulk rock Zn budget, making it the most important host of Zn in staurolite-absent metasedimentary rocks. About 75% of the Zn and 50 % of the Pb was removed from the rock during prograde metamorphism, mostly due to reactions involving biotite. Such fluid-present regional metamorphism, or broad contact metamorphism, has the potential to provide very high tonnages of base metals to mineralization sites if metamorphic fluids can be channelled into the upper crust.

1. Introduction

I examine here the potential role of base metal dissolution during metamorphism as a source of metals for orebody formation. Most of the world's largest Pb-Zn resources are Mississippi–Valley-Type (MVT) or sedimentary-exhalative (SEDEX) deposits, where mineralisation is largely hosted by carbonate and siliciclastic sedimentary rocks (sediment-hosted Pb-Zn deposits, e.g. Leach et al., 2005). Metal sources for these deposits are poorly understood, but mechanisms of circulation of metal-leaching brines through 'basement' rocks due to basin inversion or metamorphism have been suggested (e.g. Cooke et al. 1998; Leach et al., 2005; Oliver et al., 2006). Vein style epigenetic Zn-Pb deposits associated with core complex exhumation show evidence for involvement of deep-seated, possibly metamorphic fluids (Beaudoin et al., 1992). Ore deposit models for Broken Hill-type and other large stratiform and/or replacive Zn-Pb deposits in high-grade metamorphic rocks have been controversial because of uncertainties in timing and/or remobilisation of mineralisation. Some studies have demonstrated that dissolution of base-metal sulfides during high temperature metamorphism and partial melting was widespread and led to substantial modification of the pre-metamorphic orebodies (Frost et al., 2002).

There is little consensus on the mechanisms or efficiency of Pb and Zn mobility during metamorphism and related fluid flow (e.g. Haack et al., 1984; Roser and Nathan, 1997; Ague, 2003; Ague, 2011 and therein). In part, this is because studies that examine element mobility in regional metamorphic belts are plagued by uncertainty over the nature and degree of chemical variability in protolithic rocks, which in turn complicates interpretations of element mobility throughout metamorphism (e.g. Moss et al., 1995; Cullers, 2002). Tuisku et al. (1987) proposed that Zn is essentially immobile during metamorphism of pelites, but Yardley (2005) demonstrated that the nature of sedimentary protoliths strongly influences the subsequent metamorphic fluid chemical evolution, and thus the capacity for metal transport. In general, studies that address the potential for Zn and Pb mobility during metamorphism of sedimentary rocks remain contentious (e.g. Lebedev & Nagoritzi, 1980; Haack et al., 1984; Roser and Nathan et al., 1997; Pitcairn et al. 2006) with one of the reasons being the insufficient knowledge where Zn and Pb are accommodated in rocks undergoing progressive metamorphism. Other important factors that influence mass transfer include whether or not fluid flow was focussed, and whether or not fluid flowed across regional P-T gradients, such that prograde (or retrograde) reaction sequences were crossed. Although some studies have closely examined base metal distribution in different rocks at the micro-scale (e.g. Gieré et al. 2011), while others have suggested metal transfer across metamorphic gradients on the basis of bulk rock geochemistry (e.g. Masters and Ague, 2005), no study to date has combined micro-analysis of Pb and Zn in minerals with bulk geochemical changes across broad metamorphic gradients. Here we examine the geochemical variation through a package of metasedimentary rocks that experienced LP/HT prograde metamorphism and fluid flow. We address the protolith variability problem by combining the geochemistry of a large number of samples of similar sedimentary protoliths with examination of the composition of individual minerals across a range of metamorphic grades. This work demonstrates that pervasive flow of Cl-bearing fluids across prograde metamorphic gradients is capable of leaching large masses of base metals. Transport and subsequent reaction of these metal laden fluids may be crucial to the formation of economically significant Pb-Zn deposits.

2. Geological Setting

The Eastern Mount Lofty Ranges, South Australia, exposes the Kanmantoo Group metasedimentary sequence comprising siliciclastic continentally-derived sediments with minor interlayered limestone (c.f. Jago et al., 2003 and therein). The rocks underwent regional metamorphism (0.3-0.5 GPa) during the Cambro-Ordovician Delamerian Orogeny at ~ 500 Ma resulting in the formation of broad and coherent metamorphic zonation (Fig. 1) (Dymoke & Sandiford 1992; Sandiford et al., 1995; Cartwright et al., 1995 and therein). The metamorphic sequence progrades inwards from low-grade (~350–400 ˚C) greenschist facies rocks in the west to an upper amphibolite facies (~650–700 ˚C) migmatitic core in the eastern part of the orogen (Fig. 1), with an average metamorphic field gradient of ~6–7 ˚C/km (e.g. Cartwright et al., 1995).

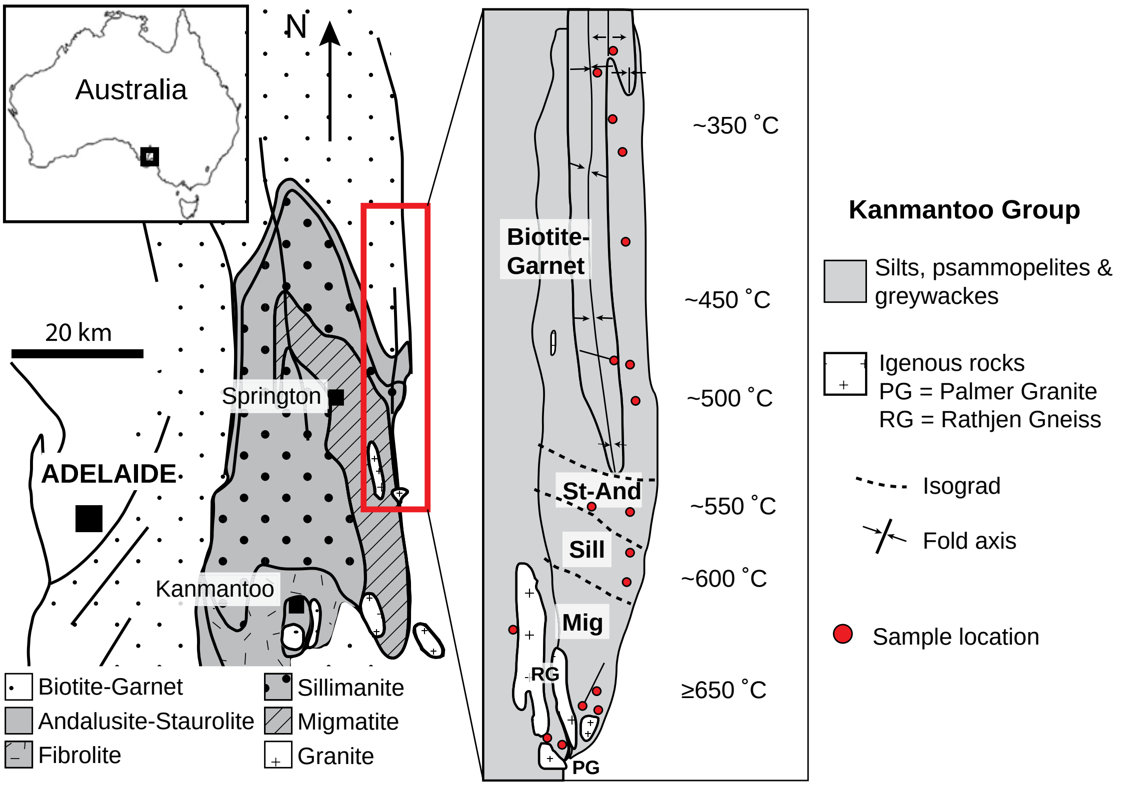

Figure 1: Map of the Eastern Mount Lofty Ranges, South Australia, showing the location of samples with respect to metamorphic zonation (modified after Dymoke and Sandiford, 1992; Oliver et al. 1998; Cartwright et al., 1995).

Peak metamorphic assemblages are well preserved and show limited retrogression. Oxygen isotope studies indicate widespread up-temperature fluid flow (fluid flow towards the high-grade centre) with an estimated total fluid flux of $10^5/m^3/m^2$ (Cartwright et al., 1995; Oliver et al., 1998). Syn-orogenic granitic plutons and widespread dolerites (now metabasites) conceivably provided the heat for high temperature metamorphism, culminating in extensive (10-25%) partial melting in the presence of excess aqueous fluid (Cartwright et al., 1995, Foden et al., 2002). This arrangement of isograds and broad, up-temperature fluid flow, in relatively homogeneous protoliths, provides an ideal study site to examine the effects of metamorphism on metal distribution and mobility.

3. Samples

We investigated a suite of Kanmantoo Group samples that record prograde metamorphic temperatures ranging from the biotite zone to the partial melting zone (~350 ˚C to ~650–700 ˚C) (Fig. 1). Thirty-five samples were analysed for their bulk rock composition, and a subset of sixteen samples were further investigated at the mineral-scale. The investigated samples have SiO_2 contents between 60 and 76 wt.% (average = 71 wt.%; see appendix), have relatively low Al_2O_3 contents (11–16 wt.%, average = 13 wt.%), and average $Fe_2O_3^{(T)}$ and MgO concentrations of 4.5 wt. % and 2 wt.%, respectively. The lowest grade samples are plagioclase-rich psammites with a small chlorite component; they represent the lowermost biotite grade indicative of temperatures around 350–400 ˚C (n=7). Samples were also examined from the biotite-garnet zone (450–500 ˚C) (n=9), and the staurolite-andalusite and sillimanite/fibrolite zone (~560–600 ˚C; n=8). Given their relatively low Fe, psammitic composition (Appendix), none of the samples studied on a mineral-scale from the biotite/garnet and staurolite zone contained garnet or staurolite, however, sillimanite/fibrolite was present in the highest-grade samples from the respective metamorphic zone. We also analysed samples from the migmatite zone (n=11), which reached peak temperatures of ~650–700 ˚C corresponding to the onset of fluid-present anatexis (Cartwright et al., 1995).

Major element concentrations in whole rock samples were measured by XRF and trace elements were analysed by LA-ICP-MS on fused discs. Major elements in minerals were determined by EPMA and trace elements where obtained by LA-ICP-MS. Zinc isotopes were analysed on a Neptune Plus MC-ICP-MS at the Australian National University. A full description of the procedure can be found in Sossi et al. (2014). Full details of the analytical procedures are outlined in the appendix.

4. Results

4.1 Bulk rock composition

Major- and rare earth element concentrations in bulk rock samples do not show systematic variations with metamorphic grades (Fig. A-2). Zinc concentrations in bulk rock samples decrease during prograde metamorphism (Fig. 2). Low-grade rocks can contain in excess of 100 µg g $^{-1}$ Zn, intermediate-grade rocks typically contain <70 µg g $^{-1}$ Zn and migmatites contain <26 µg g $^{-1}$ Zn. Zinc substitutes for Fe and Mg in minerals (reference, and see below) so to account for protolithic variations among the samples we normalise the Zn values to FeO + MgO, (see also Haack et al., 1984). We also normalise Zn contents to Al_2O_3 to evaluate variations in the pelitic components of the sample suite. Both sets of normalised Zn values show a similar trend of decreasing Zn concentrations with increasing temperature (Fig. 2).

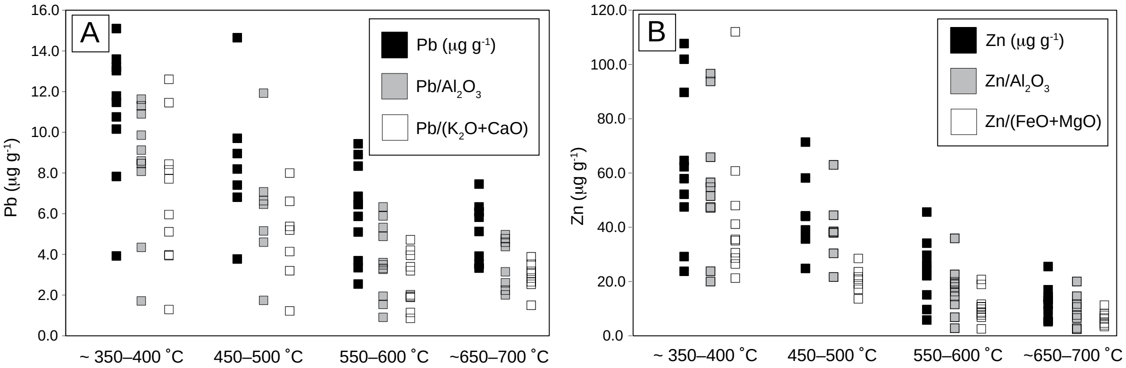

Figure 2: A) Pb, and B) Zn concentrations of bulk rock samples plotted against temperature of metamorphism. Both absolute metal (in µg g $^{-1}$) and normalised (to examine affects of protolith variation) concentrations are shown. Metal contents decrease with increasing metamorphic temperatures in both cases.

Lead concentrations also decrease with prograde metamorphism (Fig. 2), although the trend is less pronounced compared to Zn. Lowest-grade rocks contain between 8–15 µg g $^{-1}$ Pb whereas migmatites contain <8 µg g $^{-1}$ (Fig. 2). To account for protolithic variations we normalized the Pb values by dividing them by K_2O + CaO, as Pb commonly substitutes for K and Ca in silicates and carbonates, respectively (e.g. Haack et al., 1984; Cherniak, 1995). We also account for the pelitic component of the protolith by normalizing the Pb contents to Al_2O_3 (Fig. 2). Again, normalised Pb values decrease with increasing metamorphic grade.

The zinc isotope composition of a subset of four bulk rocks that record temperatures from 350°C to 600°C was measured to elucidate the mechanism of Zn fractionation. δ^{66}Zn values at low temperatures are near those of basaltic igneous rocks (≈ 0‰ vs. IRMM-3702) increasing to slightly ^{66}Zn-enriched compositions (+0.2‰) at higher temperatures. This shift is mirrored by a decrease in Zn concentration, where the highest temperature, Zn-depleted samples also exhibit the heaviest δ^{66}Zn.

4.2 Pb and Zn analysis in minerals

Micas are important hosts for a range of trace elements (e.g. Nb, Cs and Rb; Yang and Rivers, 2000). Our results show that for staurolite-absent rocks >95 % bulk-rock inventory of Zn is hosted in micas (biotite + muscovite), with >80 % of Zn hosted in biotite (Fig. 3). The total Zn accommodated in biotite decreases sharply (to 16 %) if staurolite is present, due to the great affinity of Zn for staurolite (see appendix). Zinc is also hosted in Fe-Ti oxides such as ilmenite (400–4500 µg g^{-1}) but contributes < 10% to the overall Zn budget.

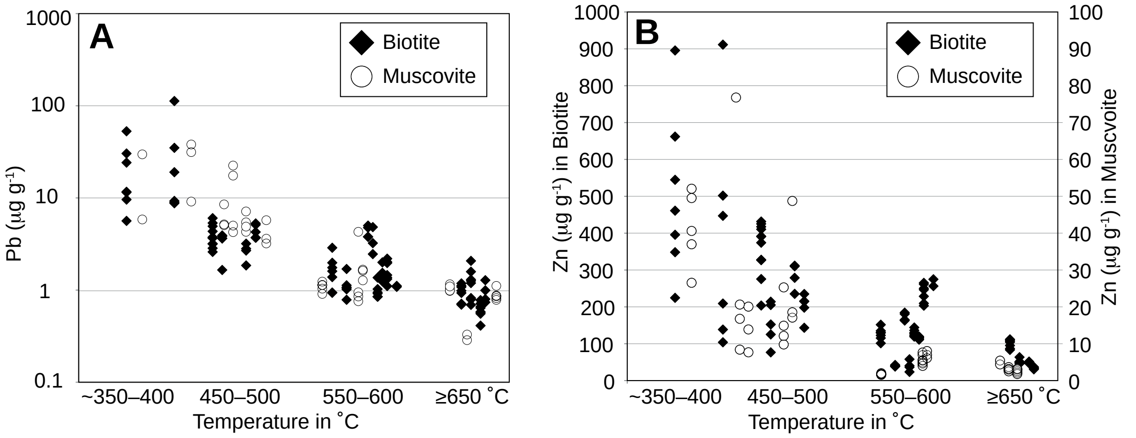

Figure 3: A) Pb and B) Zn concentrations (in µg g^{-1}) in biotite (filled diamonds) and muscovite (circles) versus metamorphic temperature. Individual samples are vertically separated.

As observed in bulk rock compositional trends, Zn concentrations in biotite and muscovite decrease with increasing temperature (Fig. 4). Biotite from low-grade samples can contain up to 900 µg g^{-1} Zn, whereas samples from intermediate metamorphic grades (~550 ˚C) contain ~ 150 µg g^{-1} Zn, and biotite from the migmatites contains the lowest Zn concentrations of ~ 50 µg g^{-1}. Zinc contents in muscovite show a similar decreasing trend from up to 600 µg g^{-1} in low-grade rocks to <5 µg g^{-1} in migmatites. The Zn content of the micas is independent of their major element composition (see appendix), as was also shown by Tischendorf et al. (2001). The large range of Zn concentrations in micas from low-grade rocks is not seen in rocks from higher metamorphic grades (> 550 ˚C), perhaps indicative of chemical homogenisation associated with up-temperature fluid flow.

Lead concentration trends in micas also show a decrease in concentration towards higher metamorphic grades (Fig. 4). Biotite in low grade samples contain 5–50 µg g^{-1} Pb, whereas biotite from high grade (>500˚C) rocks generally contain <2µg g^{-1} Pb. Biotite in low-grade rocks also show a spread of Pb concentrations (e.g. 5 – 50 µg g^{-1}), which is not seen in at higher metamorphic grades (Fig. 3). Muscovite contains ~ 6–40 µg g^{-1} Pb in low grade rocks, 3–20 µg g $^{-1}$ in intermediate grade rocks and ~ 1 μg g $^{-1}$ Pb in migmatites (Fig. 4). In low-grade rocks ~50 % of the total Pb is sequestered in mica whereas in higher-grade rocks plagioclase is the main Pb repository (Fig. 3).

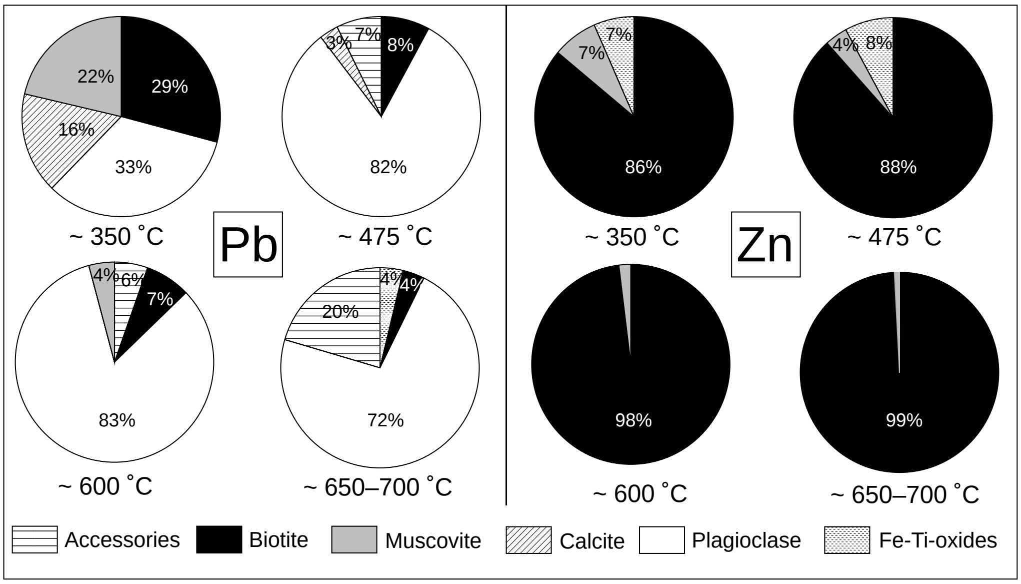

Figure 4. Pb and Zn distribution between minerals of samples at different metamorphic temperatures. Accessories are the sum of allanite, monazite, xenotime, titanite, and zircon.

4.3 Halogens in apatite and biotite

Biotite and apatite show elevated Cl concentrations in high-grade samples. The higher Cl concentrations (~0.3 vs. <0.13 wt.%) follow the predictions by Zhu and Sverjesky (1992) that biotite incorporates higher Cl concentrations at higher temperatures in the presence of Cl-bearing fluids. Apatite in low-grade samples contains <0.1 wt.% Cl whereas apatite from samples >500 ˚C contain up to 0.3 wt.% Cl and apatite grains in migmatite can incorporate ~1.2 wt.% Cl, whereas no conclusive trend of F contents in apatite with temperature can be observed (see appendix Fig. A-1). Halogen contents in biotite can be used to constrain the composition of hydrothermal fluids that interacted with the rock during metamorphism. We followed the same approach as Coulson et al. (2001), which incorporates calculated log Ks for exchange reactions between annite, phlogopite, and the OH-, Cl- and F-rich biotite endmembers to calculate HCl/H_2O and HF/HCl activity ratios in the coexisting fluid from the biotite compositions. Activity ratios HCl/H_2O spread between -3.8 and -2.2 in low-grade rocks and from -3.2 to –2.5 in migmatites, although individual migmatite samples cover samller ranges (appendix, or see Chapter 4).

5. Discussion

A fluid phase is crucial for element transport during metamorphism. Broad regional up-temperature fluid flow as reported in Cartwright et al. (1995) and Oliver et al. (1998) strongly increases the potential for element mobility in metamorphic systems. Channelized fluid flow may have a similar effect if fluid moves across P-T gradients (Masters and Ague, 2005). The relative abundance of ligands such as F^-, Cl^-, SO_3^{2-} and CO_3^{2-} in the fluid controls the complexation of cations in solution, thereby affecting their solubility transport properties. Metamorphic fluids that are poor in such ligands, or are restricted from rock interaction – particularly up-temperature gradients – are unlikely to leach significant amounts of Pb and Zn from the rock (e.g. Tuisku et al., 1987).

Apatite and biotite can be useful tracers of fluids during metamorphism (e.g., Munoz, 1989, 1992). Apatite from the studied samples show a trend of increasing Cl concentration with increasing metamorphic grade, which is in contrast to Smith and Yardley (1999) and Spear & Pyle (2002 and therein) who observed decreasing Cl contents of apatite during prograde metamorphism. We attribute this difference to the presence of a Cl-rich fluid during up temperature fluid flow in the Mt. Lofty Ranges, towards the high-grade anatectic core (Cartwright et al., 1995; Oliver et al., 1998). This is consistent with the homogenization of fugacity ratios across metamorphic gradients that can be explained with higher fluid-rock ratios, caused by up-temperature fluid flow towards the migmatitic core that also led to a homogenization of mineral compositions (Fig. 3). Further support for this premise comes from the trend of Zn isotope fractionation in the metasediments. The increase in δ^{66}Zn commensurate with loss of Zn at higher temperatures necessitates that transport was accompanied by the preferential partitioning of light Zn isotopes into the fluid phase ($\Delta^{66}Zn_{\text{biotite-fluid}}$ = -0.15‰). The type of ligands present in a hydrothermal fluid control the complexation of the transported Zn^{2+}. Ab-initio calculations indicate that the $ZnCl_4^{2-}$ species is ^{66}Zn-depleted with respect to Zn-citrate, sulphate or hexaquo species, of the order of 0.8‰ lighter at 25°C (Black et al., 2011). This would decrease to -0.13‰ at 500°C, assuming a $10^6/T^2$ dependence, a figure similar to that required to explain the δ^{66}Zn in the whole rocks. Regardless, the fluid-rock fractionation factor is maximised by Zn chloro complexes over other complexing ligands by virtue of their longer (and therefore weaker) bonds, favouring a Cl-rich fluid. The presence of saline fluids during metamorphism is also confirmed by Hammerli et al. (2013) who found strong evidence for Cl-rich bittern brine fluid circulation in the Kanmantoo Group sediments during metamorphism.

My results show that the continuous decrease of Zn concentration on a bulk rock scale with metamorphism is strongly linked with Zn loss from biotite and muscovite. Upon fluid/rock interaction, Zn strongly partitions into Cl-rich fluids compared to Fe and Mg (for which Zn substitutes in silicate minerals) (e.g. Ilton and Eugster, 1990 and therein; Nagaseki and Hayashi, 2008). Since more than 85 % of the bulk rock Zn is hosted in biotite, Zn loss from biotite is primarily responsible for the bulk rock Zn loss during metamorphism. As this study focuses on staurolite- and garnet-absent rocks, we cannot exclude that Zn behaviour would differ in pelitic rocks with higher Fe/Mg ratios and hence abundant staurolite and/or garnet. Nevertheless, staurolite is only stable over a relatively small temperature range (e.g., ~550–590 ˚C at 4 ~0.4 GPa) at low pressures (< 0.5 GPa) with staurolite breakdown to biotite occurring at temperatures below the onset of partial melting (e.g., Johnson et al., 2003). This means that even in staurolite-bearing metamorphic suites, there is a temperature window where Zn and Pb can be mobilised via fluid-biotite interaction prior to anatexis. Moreover, it is possible that the relative paucity of staurolite in these rocks is a function of Zn-loss at lower grades, as Zn tends to stabilise staurolite (e.g., Goodman, 1993).

Figure 3 shows a similar trend of Pb loss with metamorphic grade. Compared to Zn, micas are not the major Pb host in psammopelites. As most of the Pb is hosted in plagioclase, a less pronounced Pb decrease on a bulk rock scale is observed, especially once calcite disappears. However, the decrease of Pb on a bulk rock scale is likely the result of Pb loss from mica during metamorphism and decarbonisation reactions in low-grade rocks, as no systematic Pb loss of the other major Pb hosts such as plagioclase is observed.

In the Kanmantoo Group metasediments, pervasive fluid flow caused a Zn decrease of ~50 μg g $^{-1}$ and a Pb decrease of ~ 5 μg g $^{-1}$ between protoliths and their migmatitic equivalents. High-grade metamorphic anatectic rocks cover at least ~200 km^2 (e.g., Oliver et al., 1998). By using an arbitrary, but geologically feasible, thickness of the anatectic sequence of 1 km, I calculate that ~27 Mt of Zn and ~2.7 Mt of Pb were mobilized during prograde metamorphism, which is comparable to the amounts of base metals found in world class Pb-Zn deposits (e.g., Howards Pass deposit). I stress that such metal mobility is likely only achieved because of the elevated Cl content of the metamorphic fluids and pervasive nature of fluid flow that allowed fluid access to large rock volumes. This premise is consistent with results of analysis of saline fluid inclusions from quartz veins in metamorphic terranes of Yardley (2005), that show high (but variable) metal contents, and experimental studies that demonstrate an enhanced capacity of saline fluids to carry Pb and Zn (e.g., Nagaseki & Hayashi, 2008). There are likely further prerequisites to enhance the potential for ore formation via metamorphic fluids, such a short time frame for metamorphism or/and rapid uplift (Fig. 5a; Yardley & Cleverley, 2013). If the chlorine-bearing fluids evolved during metamorphism can interact with shallower parts of the crust in which sedimentation, diagenesis or vein formation is occurring, there is major potential for metal contribution into these shallower ore systems (Fig. 5).

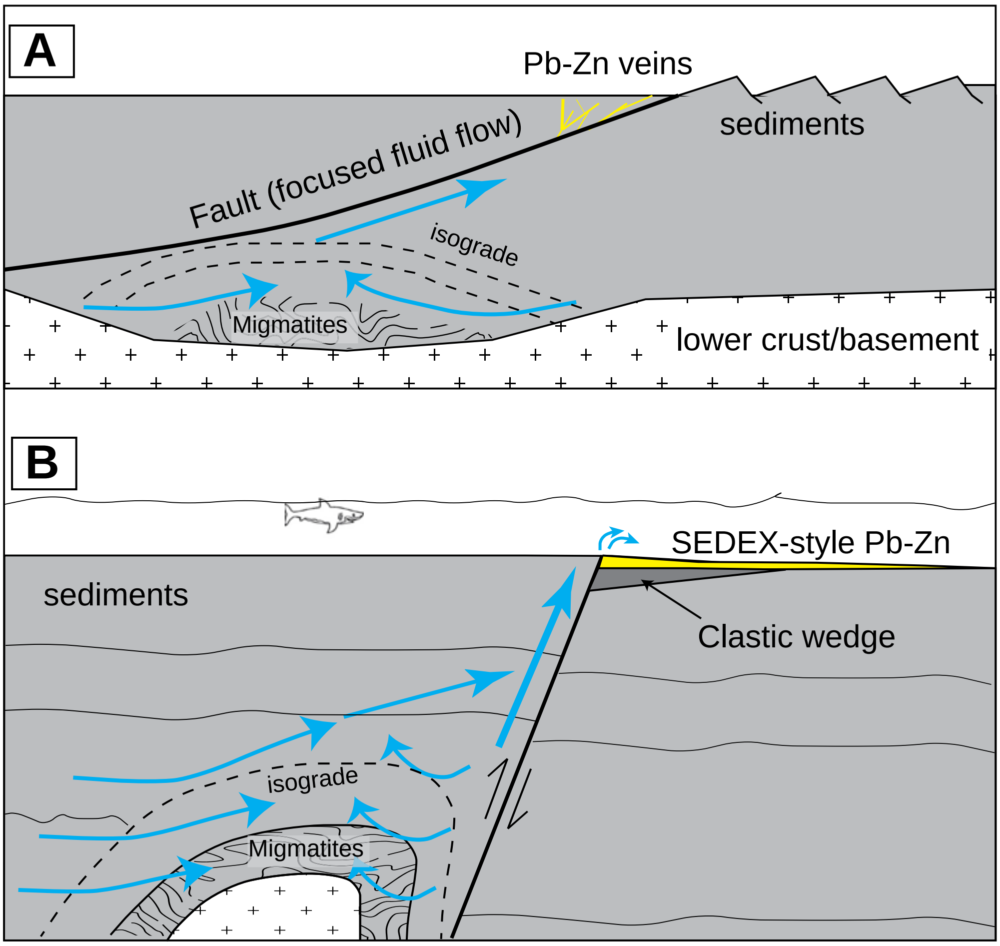

Figure 5. Models for syntectonic base metal transport and deposition in metasedimentary rock sequences. A) Syn-metamorphic exhumation of a metamorphic core complex in an extensional tectonic regime can lead to focused fluid flow along major fault zones. Changed P-T conditions and fluid mixing may lead to precipitation of Pb-Zn ore in hydrothermal veins, possibly similar to those found in the British Columbia Pb-Zn district (Beaudoin et al.,1992). B) High temperature metamorphism acts as a fluid flow pump where faults provide fluid flow paths during their activation (extension/contraction, e.g., Oliver et al., 2006) in e.g., back arc systems. Pb-Zn rich fluid exhalate ore minerals on seafloor upon P-T decrease and changing oxic condtitions/fluid mixing.

I conclude that prograde metamorphism of sedimentary rocks packages is a viable base metal source for the formation of some Pb-Zn deposits, provided that the metamorphic fluid contains sufficient Cl to effectively mobilise metals from the metamorphic system into ore-forming environments (Fig. 5). For example, syn-metamorphic exhumation of crustal rocks in British Colombia may have contributed metamorphic-derived base metals to extension-related vein systems (Beaudoin et al., 1992; Fig. 5a). Similarly, syn-contact metamorphic fluid evolution in mid-crustal rocks at Mt. Isa around 1670-1650 Ma around the Sybella Granite may have contributed to synchronous base metal deposition in the Mount Isa Group shales. The later regional Isan Orogeny at 1600 to 1580 Ma may also have provided Zn and Pb for younger SEDEX deposits in 1590 Ma sedimentary rocks at Century Mine (Fig. 5b; Feltrin et al., 2003; Oliver et al., 2006).

References

Afshooni, S.Z., Mirnejad, H., Esmaeily, D., Haroni, H.A., 2013, Mineral chemistry of hydrothermal biotite from the Kahang porphyry copper deposit (NE Isfahan), Central Province of Iran: Ore Geology Reviews, v. 54, p. 214–232.

Ague, J.J., 1994, Mass transfer during Barrovian metamorphism of pelites, South-Central Connecticut, I: Evidence for changes in composition and volume: American Journal of Science, v. 294, p. 989–1057.

Ague, J.J., 2003, Fluid infiltration and transport of major, minor and trace elements during regional metamorphism of carbonate rocks, Wepawaug Schist, Connecticut, USA: American Journal of Science, v. 303, p. 753–816.

Ague, J.J., 2011, Extreme channalization of fluid and the problem of element mobility during Barrovian metamorphism: American Mineralogist, v. 96, p. 333–352.

Aldahan, A.A., and Morad, S., 1988, Some remarks on the stability of sphene in diagenetic environments: Chemical Geology, v. 70, p. 249–255.

Armstrong, J.T., 1991, Quantitative element analysis of individual microparticles with electron beam instruments: In Electron Probe Quantitation, Heinrich, K.F.J. and Newbury, D.E., Eds., Plenum Press, pp. 261–315.

Arnold, J., and Sandiford, M., 1990, Petrogenesis of cordierite-orthoamphibole assemblages from the Springton region, South Australia: Contribution to Mineralogy and Petrology, v. 106, p. 100–109.

Audétat. A., Günther, D., Heinrich, C.A., 1998, Formation of a Magmatic Hydrothermal Ore Deposit: Insight with LA-ICP-MS Analysis of Fluid Inclusions: Science, v. 279, p. 2091–2094.

Appold, M.S., Wenz, Z.J., 2011, Composition of ore fluid inclusions from the Viburnum Trend, Southeast Missouri district, United States: Implications for transport and precipitation mechanisms: Economic Geology, v. 106, p. 55–78.

Ayres, M., and Harris, N., 1997, REE fractionation and Nd-isotope disequilibrium during crustal anatexis: constraints from Himalayan leucogranites: Chemical Geology, v. 139, p. 249–269.

Baker, D.R., 1989, Tracer versus element diffusion: Diffusional decoupling of Sr concentration from Sr isotope composition: Geochimica et Cosmochimica Acta, v. 53, p. 3015–3021.

Banks, D.A., Yardley, B.W.D., 1992, Crush-leach analysis of fluid inclusions in small natural and synthetic samples: Geochimica et Cosmochimica Acta, v. 56, p. 245¬–248.

Banks, D.A., Green, R., Cliff, R.,A., Yardley, B.W.D., 2000a, Chlorine isotopes in fluid inclusions: determination of the origins pf salinity in magmatic fluids: Geochimica et Cosmochimica Acta, v. 64, p. 1785¬–1789.

Banks, D.A., Gleeson. S.A., Green, R., 2000b, Determination of the origin of salinity in granite-related fluids: evidence from chlorine isotopes in fluid inclusions: Journal of Geochemical Exploration, v. 69, p. 309–312.

Banks, D. A., Giuliani, G., Yardley, B. W. D. & Cheilletz, A., 2000a, Emrald mineralisation in Colombia: fluid chemistry and the role of brine mixing: Mineralium Deposita, v. 35, p. 699–713.

Barbero, L., Villaseca, C., Rogers, G., and Brown, P.E., 1995, Geochemical and isotopic disequilibrium in crustal melting: An insight from the anatectic granitoids from Toledo, Spain: Journal of Geophysical Research, v. 100, p. 15745–15765.

Barrie, C.D., Boyce, A.J., Boyle, A.P., Williams, P.J., Blake, K., Wilkinson, J.J., Lowther, M., McDermott, P., Prior, D.J., 2009, On the growth of colloform textures: a case study of sphalerite from the Galmoy ore body, Irleand: Journal of the Geological Society, London, v. 166, p. 563–582.

Bea, F., Pereira, M.D., and Stroh, A., 1994, Mineral/leucosome trace-element partitioning in a peraluminous migmatite (a laser ablation-ICP-MS study): Chemical Geology, v. 117, p. 291–312.

Bea, F., 1996, Residence of REE, Y, Th and U in granites and crustal protoliths: Implications for the chemistry of crustal melts: Journal of Petrology, v. 37, p. 521–552.

Bea, F., Montero, P., 1999, Behavior of accessory phases and redistribution of Zr, REE, Y, Th, and U during metamorphism and partial melting of metapelites in the lower crust: An example from the Kinzigite Formation of Ivrea-Verbano, NW Italy: Geochimica et Cosmochimica Acta, v. 63, p. 1133–1153.

Beaudoin, G., Taylor, B.E., and Sangster, D.F., 1992, Silver-lead veins and crustal hydrology during Eocene extension, southeastern British Columbia, Canada: Geochimica et Cosmochimica Acta, v. 56, p. 3513–3529.

Bebout, G.E., Bebout, A.E., Graham, C.M., 2007, Cycling of B, Li, and LILE (K, Cs, Rb, Ba, Sr) into subduction zones: SIMS evidence from micas in high-P/T metasedimentary rocks: Chemical Geology, v. 239, p. 284–304.

Bebout, G., Ryan, J. G., Leeman, W. P., Bebout, A. E., 1999, Fractionation of trace elements by subduction-zone metamorphism effect of convergent-margin thermal evolution: Earth and Planetary Science Letters , v. 171, p. 63–81.

Berger, A., Rosenberg, C., Schaltegger, U., 2009, Stability and isotopic dating of monazite and allanite in partially molten rocks: examples from the Central Alps: Swiss Journal of Geoscience, v. 102, p. 15–29.

Bingen, B., Demaiffe, D. & Hertogen, J., 1996, Redistribution of rare earth elements, thorium, and uranium over accessory minerals in the course of amphibolite to granulite facies metamorphism: the role of apatite and monazite in orthog- neisses from southwestern Norway. Geochimica et Cosmochimica Acta, v. 60, p. 1341–1354.

Black, J. R., Kavner, A., and Schauble, E. A., 2011, Calculation of equilibrium stable isotope partition function ratios for aqueous zinc complexes and metallic zinc: Geochimica et Cosmochimica Acta, v. 75, p. 769–783.

Böhlke, J.K., Irwin, J.J., 1992, Laser microprobe analyses of Cl, Br, I, and K in fluid inclusions: Implications for sources of salinity in some ancient hydrothermal fluids: Geochimica et Cosmochimica Acta , v. 56, p. 203–225.

Bodnar, R.J., 1993, Revised equation and table for determining the freezing point depression of H_2O-NaCl solutions: Geochimica et Cosmochimica Acta, v. 57, p. 683–684.

Bons, P., D. & Gomez-Rivas, E., 2013, Gravitational fractionation of isotopes and dissolved components as a first-order process in crustal fluids: Economic Geology, v. 106, p. 1195–1201.

Bottrell, S.H., Yardley, B.W.D., Buckley, F., 1988, A modified crush-leach method fort he analysis of fluid inclusion electrolytes: Bulletin de minéralogie, v. 111, p. 279–290.

Boudreau, A. E., Love, C. & Hoatson, M. D., 1993, Variation in the composition of apatite in the Munni Munni Complex and associated intrusions of the West Pilbara Block, Western Australia: Geochimica et Cosmochimica Acta, v. 57, p. 4467–4477.

Brenan, J., 1994, Kinetics of fluorine, chlorine and hydroxyl exchange in fluorapatite: Chemical Geology, v. 110.

Brown, M., 2010, The spatial and temporal patterning of the deep crust and implications for the process of melt extraction: Philosophical Transactions of the Royal Society A Mathematical Physical and Engineering Sciences, v. 368, p. 11–51.

Brown, M., 2013, Granite: From genesis to emplacement: GSA Bulletin, v. 125, p. 1079–1113.

Bucher, K., Grapes, R., 2011, Metamorphism of Quartzofeldspathic Rocks, in: Petrogenesis of Metamorphic Rocks pp.395–412, Springer, Berlin, Germany.

Cardenas, A. A., Girty, G. H., Hanson, A. D., Lahren, M. M., Knaack, C. & Johnson, D. 1996. Assessing differences in composition between lowmetamorphic grade mudstones and high-grade schists using logratio techniques: Journalof Geology, v. 104, p. 279-93.

Carpenter, A.B., 1978, Origin and chemical evolution of brines in sedimentary basins. Oklahoma Geological Survey Circular , v. 79, p. 60–77.

Cartwright, I., Vry, J., and Sandiford, M., 1995, Changes in stable isotope ratios of metapelite and marbles during regional metamorphism, Mount Lofty Ranges, South Australia: implications for crustal scale fluid flow: Contribution to Mineralogy and Petrology, v. 120, p. 292–310.

Cartwright, I. & Oliver, N. H. S., 1992, Direction of fluid flow during contact metamorphism around the Burstall Granite, Australia: Journal of the Geological Society London, v. 149, p. 693–696.

Cartwright, I. & Oliver, N. H. S., 1994, Fluid flow during contact metamorphism at Mary

Kathleen, Queensland, Australia. Journal of Petrology, v. 35, p. 1493–1519.

Cesare, B., Satish-Kumar, M., Cruciani, G., Pocker, S., Nodari, L., 2008, Mineral chemistry of Ti-rich biotite from pegmatite and metapelitic granulites of the Kerala Khondolite Belt (southeast India): Petrology and further insights into titanium substitutions: American Mineralogist, v. 93, p. 327–338.

Cullers, R.L., 2002, Implications of elemental concentrations for provenance, redox conditions, and metamorphic studies of shales and limestones near Pueblo, CO, USA: Chemical Geology, v. 191, 305–327.

Cherniak, D.J., 1995, Diffusion of lead in plagioclase and K-feldspar: an investigation using Rutherford Backscattering and Resonant Nuclear Reaction Analysis: Contribution to Mineralogy and Petrology, v. 120, p. 358–371.

Cherniak, D.J., 2010, Diffusion in accessory minerals: Zircon, titanite, apatite, monazite and xenotime: Reviews in Mineralogy & Geochemistry, v. 72, p. 827–869.

Clemens, J.D., 2006, Melting of the continental crust: Fluid regimes, melting reactions, and source rock fertility, in Brown, M., and Rushmer, T., eds., Evolution and Differentiation of the Continental Crust: Cambridge, UK, Cambridge University Press, p. 297–331.

Condie, K.C., Belousova, E., Griffin, W.L., and Sircombe, K.N., 2009, Granitoid events in space and time: Constraints from igneous and detrital zircon age spectra: Gondwana Research, v. 15, p. 228–242.

Cooke, D.R., Bull, S.W., Large, R.R., McGoldrick, P.J., 2000, The importance of oxidized brines for the formation of Australian Proterozoic stratiform sediment-hosted Pb-Zn (Sedex) deposits, Economic Geology, v. 95, p. 1–18.

Cooke, D.R., Bull, S.W., Donovan, S., and Rogers, J., 1998, K-Metasomatism and base metal depletion in volcanic rocks from the McArthur Basin, Northern Territory–Implications for base metal mineralization: Economic Geology, v. 93, p. 1237–1263.

Corrie, S. L. & Kohn, M. J.,2008, Trace-element distributions in silicates during prograde metamorphic reactions: implications for monazite formation: Journal of Metamorphic Geology, v. 26, p. 451–464

Coulson, I.M., Dipple, G.M., and Raudsepp, M., 2001, Evolution of HF and HCl activity in magmatic volatiles of the gold-mineralized Emerald Lake pluton, Yukon Territory, Canada: Mineralium Deposita, v. 36, p. 594–606.

Cullers, R.L., 2002, Implications of elemental concentrations for provenance, redox conditions, and metamorphic studies of shales and limestones near Pueblo, CO, USA: Chemical Geology, v. 191, p. 305–327.

Davies, G.R., and Tommasini, S., 2000, Isotopic disequilibrium during rapid crustal anatexis: implications for petrogenic studies of magmatic processes: Chemical Geology, v. 162, p. 169–191.

Dorais, M.J., Wintsch, R.P., Kunk, M.J., Aleinikoff, J., Burton, W., Underdown, C., and

Kerwin, C.M., 2012, P-T-t conditions, Nd and Pb isotopic compositions and detrital zircon geochronology of the Massabesic Gneiss Complex, New Hampshire: Isotopic and metamorphic evidence for the identification of Gander Basement, Central New England: American Journal of Science, v. 312, p. 1049–1097.

Dymoke, P., and Sandiford, M., 1992, Phase relationships in Buchan facies series pelitic assemblages: calculations with application to andalusite-staurolite parageneses in the Mount Lofty Ranges, South Australia: Contribution to Mineralogy and Petrology, v. 100, p. 121–132.

Dyson I. A., Gatehouse C. G., Jago, J.B., 1996, Sequence stratigraphy of the Talisker Calc-siltstone and lateral equivalents in the Cambrian Kanmantoo Group: Geological Survey of South Australia Quarterly Geological Notes, v. 129, p. 27–41.

Ellis, D.E., 1978, Stability and phase equilibria of chloride and carbonate bearing scapolites at 750˚C and 400 bar: Geochimica et Cosmochimica Acta, v. 42, p. 1271–1281.

Evans, K., A., Powell, R. & Frost, B.R., 2013, Using equilibrium thermodynamics in the study of metasomatic alteration, illustrated by an application to serpentinites: Lithos, v. 168–169, p. 67–84.

Faryad, S.W., 2002, Metamorphic conditions and fluid compositions of scapolite-bearing rocks from the Lapis Lazuli deposit at Sare Sang, Afghanistan: Journal of Petrology, p. 43, 725–747.

Feltrin, L., Oliver, N.H.S., Kelso, I.J., and King, S., 2003, Basement metal scavenging during basin evolution: Cambrian and Proterozoic interaction at the Century Zn–Pb–Ag Deposit, Northern Australia: Journal of Geochemical Exploration, v. 78–79, p. 159–162.

Ferry, J., M., 1983, Mineral reactions and element migration during metamorphism of calcereous sediments from the Vassalboro Formation, south-central Maine: American Mineralogist, v. 68, p. 334–354.

Finger, F., Schiller, D., 2012, Lead content of S-type granites and their petrogenic significane: Contribution to Mineralogy and Petrology, v. 164, p. 747–755.

Fitzsimons, I. C. W., Kinny, P. D., Wetherley, S. & Hollings- worth, D. A., 2005, Bulk chemical control on metamorphic monazite growth in pelitic schists and implications for U–Pb age data: Journal of Metamorphic Geology, v. 23, p. 261–277.

Fisher, C.M., McFarlane, C.R.M., Hanchar, J.M., Schmitz, M.D., Sylvester, P.J., Lam, R., and Longerich, H.P., 2011, Sm-Nd isotope systematics by laser ablation-multicollector-inductively coupled mass spectrometry: Methods and potential natural and synthetic reference materials: Chemical Geology, v. 284, p. 1–20.

Fleet, M. E., 1989, Structures of sodium alumino-germanates sodalites [Na8(Al6Ge6O24)A2, A=Cl, Br, I]: Acta Crystallographica, v. 45, p. 843¬¬–847.

Foden, J.D., Elburg, M.A., Turner, S.P., Sandiford, M., O'Callaghan, J., and Mitchell, S., 2002, Granite production in the Delamarian Orogen, South Australian: Journal of the Geological

Society, London, v. 159, p. 557–575.

Foden, J., Sandiford, M., Dougherty-Page, J., and Williams, I., 1999, Geochemistry and geochronology of the Rathjen Gneiss: implications for the early tectonic evolution of the Delamarian Orogeny: Australian Journal of Earth Sciences, v. 46, p. 377–389.

Foriel, J., Philippot, P., Rey, P., Somogyi, A., Banks, D.A., Ménez, B., 2004, Biological control of Cl/Br and low sulfate concentration in a 3.5-Gyr-old seawater from North Pole, Western Australia: Earth and Planetary Science Letters, v. 228, p. 451–463.

Foster, G.L., and Carter, A., 2007, Insights into patterns and locations of erosions in the Himalaya – A combined fission-track and in situ Sm–Nd isotopic study of detrital apatite: Earth and Planetary Sciences Letters, v. 257, p. 407–418.

Foster, G.L., and Vance, D., 2006, In situ Nd isotopic analysis of geological materials by laser ablation MC-ICP-MS: Journal of Analytical Atomic Spectrometry, v. 21, p. 288–296.

Frost, B.R., Mavrogenes, J.A., and Tomkins, A.G., 2002, Partial melting of sulfide ore deposits during medium- and high-grade metamorphism: The Canadian Mineralogist, v. 40, p. 1–18.

Garcia, C.C., Lindner, H., Niemax, K., 2009, Laser ablation inductively coupled plasma mass spectrometry—current shortcomings, practical suggestions for improving performance, and experiments to guide future development: Journal of Analytical Atomic Spectrometry, v. 24, p. 14–26.

Garofalo, P.S., 2012, The composition of Alpine marine sediments (Bünderschiefer For- mation, W Alps) and the mobility of their chemical components during orogenic Metamorphism: Lithos, v. 128, p. 55–72.

Gibson, G.M. and Ireland T.R., 1996, Extension of the Delamerian (Ross) orogen into western New Zealand: Evidence from zircon ages and implications for crustal growth along the Pacific margin of Gondwana: Geology, v. 24, p. 1087–1090.

Gieré, R., and Sorensen, S.S., 2004, Allanite and other REE-rich epidote-group minerals:Reviews in Mineralogy & Geochemistry, v. 56, p. 431–493.

Giére, R., Rumble, D., Günther, D., Connolly, J., and Caddick, M.J., 2011, Correlation of growth and breakdown of major and accessory minerals in metapelites from Campolungo, Central Alps: Journal of Petrology, v. 52, p. 2293–2334.

Giére, R., Oberli, F., Meier, M., 1988: Mobility of Ti, Zr and REE – mineralogical, geochemical and isotopic evidence from the Adamello contact aureole (Italy): Chemical Geology, v. 70, p. 161.

Goff, F., Arney, B.H., & Eddy, A.C., 1982, Scapolite phenocrysts in a latite dome, northwest Arizone, U.S.A. Earth and Planetary Science Letters, v. 60, p. 86–92.

Goodman, S., 1993, Survival of zincian staurolite to upper amphibolite facies metamorphic grade: Mineralogical Magazine, v. 57, p. 736–739.

Griffin, W.L., Powell, W.J., Pearson, N.J., O'Reilly, S.Y., 2008, Glitter: Data reduction software for Laser Ablation ICP-MS, in: Sylvester, P. (Ed.), Laser Ablation ICP-MS in the Earth

Sciences: Current Practices and Outstanding Issues. Mineralogical Association of Canada, Short Course Series 40, Vancouver, pp. 308–311.

Griffin, W.L., Pearson, N.J., Belousova, E., Jackson, S.E., van Achterbergh, E., O'Reilly, S.Y., and Shee, S.R., 2000, The Hf isotope composition of cratonic mantle: LAM-MC-ICPMS analysis of zircon megacrysts in kimberlites: Geochimica et Cosmochimica Acta, v. 64, p. 133–147.

Guillong, M., Meier, D.L., Allan, M.M., Heinrich, C.A., Yardley, B.W.D., 2008, SILLS: a MATLAB-based program for the reduction of laser ablation ICP-MS data of homogeneous materials and inclusions. in: Sylvester, P. (Ed.), Laser Ablation ICP-MS in the Earth Sciences: Current Practices and Outstanding Issues. Mineralogical Association of Canada, Short Course Series 40, Vancouver, pp. 328–333.

Guillong, M., Pettke, T., 2012, Depth dependent element ratios in fluid inclusion analysis by laser ablation ICP-MS, Journal of Analytical Atomic Spectrometry, v. 27, p. 505–508.

Günther, D., Audétat, A., Frischknecht, R., Heinrich, C.A., 1998, Quantitative analysis of major, minor and trace elements in fluid inclusions using laser ablation inductively coupled plasma mass spectrometry. Journal of Analytical Atomic Spectrometry, v. 13, p. 263–270.

Haack, U., Heinrichs, H., Boness, M., Schneider, A., 1984, Loss of metals from pelites during regional metamorphism: Contributions to Mineralogy and Petrology, v. 85, p. 116–132.

Haines, P.W., Jago., J.B., Gum, J.C., 2001, Turbidite deposition in the Cambrian Kanmantoo Group, South Australia. Australian Journal of Earth Sciences, v. 48, p. 465–478.

Hammerli, J., Rusk, B., Spandler, C., Emsbo, P. & Oliver, N. H. S., 2013, In situ quantification of Br and Cl in minerals and fluid inclusions by LA-ICP-MS: A powerful tool to identify fluid sources: Chemical Geology, v. 337–338, p. 75–87.

Hammerli, J., Kemp, A.I., and Spandler, C., 2014, Neodymium isotope equilibration during crustal metamorphism revealed by in situ microanalysis of REE-rich accessory minerals: Earth and Planetary Science Letter, v. 392, p. 133–142.

Hanor, J.S., 1994, Origin of saline fluids in sedimentary basins. In Parnell ed., Geofluids; origin, migration and evolution of fluids in sedimentary basins. Geological Society Special Publications, v. 78, p. 151–174.

Hanor, J.S., 1997, Controls on the solubilization of lead and zinc in basinal brines. In Sangster, D.F., ed., Carbonated-hosted lead-zinc deposits. Society of Economic Geologists Special Publication, v. 4, p. 483–500.

Harrison, T.M., and Watson, E.B., 1984, The behavior of apatite during crustal anatexis: Equilibrium and kinetic considerations: Geochimica et Cosmochimica Acta, v. 48, p. 1467¬–1477.

Hassan, I. & Buseck, P. R., 1988, HRTEM characterization of scapolite solid solutions: American Mineralogist, v. 73, p. 119–134.

Haughton, D. R., 1970, Plagioclase-Scapolite Equilibrium: The Canadian Mineralogist, p. 854–

870.

Hauri, E., 2002, SIMS analysis of volatiles in silicate glasses, 2: isotopes and abundances in Hawaiian melt inclusions: Chemical Geology, v. 183, p. 115–141.

Hawkesworth, C.J., and Kemp, A.I.S., 2006, The differentiation and rates of generation of the continental crust: Chemical Geology, v. 226, p. 134¬–143.

Hawthorne, F. C. & Sokolova, E. 2008, The crystal chemistry of the scapolite-group minerals. 2. The origin of the I4/m ←→ P42/n phase transition and the nonlinear variations in chemical composition: The Canadian Mineralogist: v. 46, p. 1555–1575.

Heinrich, C.A., Ryan, C.G., Mernagh, T.P., Eadington, P.J., 1992, Segregation of ore metals between magmatic brine and vapor—a fluid inclusion study using PIXE microanalysis: Economic Geology, v. 87, p. 1566–1583.

Heinrich, C.A., Bain, J.H.C., Fardy, J.J., Waring, C.L., 1993, Br/Cl geochemistry of hydrothermal brines associated with Proterozoic metasediment-hosted copper mineralization at Mount Isa, northern Australia: Geochimica et cosmochimica Acta, v. 57, p. 2991–3000.

Heinrich, C.A., Günther, D., Audétat, A., Ulrich, T., Frischknecht, R., 1999, Metal fractionation between magmatic brine and vapor, determined by microanalysis of fluid inclusions: Geology, v. 27, p. 755–758.

Heinrich, C.A., et al., 2003, Quantitative multi-element analysis of minerals, fluid and melt inclusions by laser-ablation inductively-coupled-plasma mass-spectrometry: Geochimica et Cosmochimica Acta, v. 67, p. 3473–3497.

Heier K. S. and Brunfelt A. 0., 1970, Concentration of Cs in high grade metamorphic rocks. Earth Planetentary Science Letters, v. 9, p. 416- 420.

Heinrichs, H., Schulz-Dobrick, B. and Wedepohl, K.H., 1980, Terrestrial geochemistry of Cd, Bi, T1, Zn and Rb: Geochimica et Cosmochimica Acta, v. 44, p. 1519-1533.

Henderson, A.L., Foster, G.J., Najman, Y., 2010, Testing the application of in situ Sm–Nd isotopic analysis on detrital apatites: a provenance tool for constraining the timing of India–Eurasia collision. Earth and Planetary Science Letters, v. 297, p. 42–49.

Hofstra, A.H., Emsbo, P., 1993, A new method to analyze anions and cations in fluid inclusions using ion chromatography – Applications to ore genesis: Geological Society of America annual meeting, Abstracts with programs 24, A144.

Holcombe, R. J., Pearson, P. J. & Oliver, N. H. S., 1991, Geometry of a middle Proterozoic extensional decollement in northeastern Australia: Tectonophysics, v. 191, p. 255–274.

Holm, R.J., Spandlerm C., Richards, S.W., 2013, Melanesian arc far-field response to collision of the Ontong Java Plateau: Geochronology and petrogenesis of the Simuku Igneous Complex, New Britain, Papua New Guinea: Tectonophysics, v. 603, p. 189–212.

Holser, W.T., 1979, Trace elements and isotopes in evaporites, Mineralogical Society of America: Reviews in Mineralogy, v. 6, p. 295–346.

Irwin, J.J., Roedder, E., 1995, Diverse origins of fluid in magmatic inclusions at Bingham (Utah, USA), Butte (Montana, USA), St. Austell (Cornwall, UK), and Ascension Island (mid-Atlantic, UK), indicated by laser microprobe analysis of Cl, K, Br, I, Ba + Te, U, Ar, Kr, and Xe: Geochimica et Cosmochimica Acta, v. 59, p. 295–312.

Ilton. E.S. & Eugster, H.P., 1990, Partitioning o f base metals between silicates, oxides, and a chloride-rich hydrothcrmal fluid. I. Evaluation of data derived from experimental and natural assemblages. In Fluid-Mineral Interactions: a Tribute to H.P. Eugster (R.J. Spencer & I Ming Chou. cds.): Geochem. Soc, Spec. Publ. 2, pp. 157-169.

Ilton. E.S. & Eugster, H.P., 1989, Base metal exchange between magnetite and a chloride-rich hydrothcrmal fluid: Geochimica et Cosmochimica Acta, v. 53, p. 291-301.

Irwin, J.J., Reynolds, J.H., 1995, Multiple stages of fluid trapping in the Stripa granite indicated by laser microprobe analysis of Cl, Br, I, K, U, and nucleogenic plus radiogenic Ar, Kr, and Xe in fluid inclusions: Geochimica et Cosmochimica Acta, v. 59, p. 355–369.

Jago, J.B., Gum, J.C., Burtt, A.C., Haines, P.W., 2003, Stratigraphy of the Kanmantoo Group: a critical element of the Adelaide Fold Belt and the Palaeo-Pacific plate margin, Eastern Gondwana: Australian Journal of Earth Sciences, v. 50, p. 343–363.

Jambon, A., Deruelle, B., Dreibus, G. & Pineau, F.,1995, Chlorine and bromine abundance in MORB: the contrasting behaviour of the Mid-Atlantic Ridge and East Pacific Rise and implications for chlorine geodynamic cycle: Chemical Geology, v. 126, p. 101–107.

Janots, E., Engi, M., Berger, A., Allaz, J., Schwarz, J.-O., and Spandler, C., 2008, Prograde metamorphic sequence of REE minerals in pelitic rocks of the Central Alps: implications for allanite-monazite-xenotime phase relation from 250 to 610 ˚C: Journal of Metamorphic Geology, v.26, p. 509–526.

Janots, E., Brunet, F., Goffé, B., Poinssot, C., Burchard, M., and Cemic, L., 2007, Thermochemistry of monazite-(La) and dissakisite-(La): implications for monazite and allanite stability in metapelites: Contribution to Mineralogy and Petrology, v. 154, p. 1–14.

Jiang, S.Y., Palmer, M.R., Xue, C.J. & Li, Y.H., 1994, Halogen-rich scapolite-biotite rocks from the Tongmugou Pb-Zn deposit, Qinling, north-western China: Implications for the ore-forming processes: Mineralogical Magazine, v. 58, p. 543–552.

Jiang, S.-Y., Wang, R.-C., Xu, X.-S., and Zhao, K.- D., 2005, Mobility of high field strength ele- ments (HFSE) in magmatic-, metamorphic-, and submarine-hydrothermal systems: Physics and Chemistry of the Earth, v. 30, p. 1020–1029.

Johannes, W., Holtz, F., and Möller, P., 1995, REE distribution in some layered migmatites: constraints on their petrogenesis: Lithos, v.35, p.139–152.

Johnson, L., Burgess, R., Turner G., Milledge, H. J. & Harris, J. W., 2000, Noble gas and halogen geochemistry of mantle fluids: comparison of African and Canadian diamonds: Geochimica et Cosmochimica Acta, v. 64, p. 717–732.

Johnson, T.E., Brown, M., and Solar, G.S., 2003, Low-pressure subsolidus and suprasolidus phase equilibria in the MnNCKFMASH system: Constraints on conditions of regional metamorphism in western Maine, northern Appalachians: American Mineralogist, v. 88, p. 624–638.

Kharaka, Y.K., Maest, A.S., Carothers, W.W., Law, L.M., Lamothe, P.J., Fries, T.L., 1987, Geochemistry of metal-rich brines from central Mississippi Salt Dome basin, U.S.A: Applied Geochemistry, v. 4, p. 543–561.

Korh, E.A., Schmidt ,S.TH., Ulianov, A., Potel, S., 2009, Trace element partitioning in HP-LT metamorphic assemblages during subduction related assemblages during subduction-related metamorphism, Ile de Groix, France: a detailed LA-ICPMS study: Journal of Petrology, v. 50, p. 1107–1148.

Kelsey, D.E., Clark, C., and Hand, M., 2008, Thermobarometric modelling of zircon and monazite growth in melt-bearing systems: examples using modal metapelitic and metapsammitic granulites: Journal of Metamorphic Geology, v. 26, p. 199–212.

Kemp, A.I.S., Hawkesworth, C.J., Foster, G.L., Paterson, B.A., Woodhead, J.D., Hergt, J.M., Gray, C.M., and Whitehouse, M.J., 2007, Magmatic and crustal differentiation history of granitic rocks from Hf-O isotopes in Zircon: Science, v. 315, p. 980¬–983.

Kendrick, M.A., 2012, High precision Cl, Br and I determinations in mineral standards using the noble gas method: Chemical Geology, v. 292–293, p. 116–126.

Kendrick, M.A., Baker, T., Fu, B., Philips, D., Williams, P.J., 2008, Noble gas and halogen constraints on regionally extensive mid-crustal Na-Ca metasomatism, the Proterozoic Eastern Mount Isa Block, Australia: Precambrian Research, v. 163, p. 131–150.

Kendrick, M.A., Burgess, R., Pattrick, R.A.D., Turner, G., 2001, Fluid inclusion noble gas and halogen evidence on the origin of Cu-porphyry mineralizing fluids: Geochimica et Cosmochimica Acta, v. 65, p. 2651–2668.

Kendrick, M.A., Phillips, D., Wallace, M., Miller, J.McL., 2011, Halogens and noble gases in sedimentary formation waters and Zn-Pb deposits: A case study from the Lennard Shelf, Australia: Applied Geochemistry, v. 26, p. 2089–2100.

Kendrick, M.A., Burgess, R., Leach, D., Pattrick, R.A.D., 2002, Hydrothermal Fluid Origins in Mississippi Valley-Type Ore Districts: Combined Noble Gas (He, Ar,K) and Halogen (Cl, Br, I) Analysis of Fluid Inclusions from the Illinois-Kentucky Fluorspar District, Viburnum Trend, and Tri-State Districts, Midcontinent United States: Economic Geology, v. 97, p. 453–469.

Kendrick, M.A., Mark, G. & Phillips, D., 2007, Mid-crustal fluid mixing in a Proterozoic Fe oxide-Cu-Au deposit, Ernest Henry, Australia: Evidence from Ar, Kr, Xe, Cl, Br, and I: Earth and Planetary Science Letters, v. 256, p. 328–343.

Kendrick, M.A., Honda, M., Oliver, N. H. S. & Phillips, D., 2011, The noble gas systematics of late-orogenic H_2O–CO_2 fluids, Mt Isa, Australia: Geochimica et Cosmochimica Acta, v. 75, p. 1428–1450.

Kendrick, M.A., Honda, M., Pettke, T., Scambelluri, M., Phillips, D. & Giuliani, A., 2013, Subduction zone fluxes of halogens and noble gases in seafloor and forearc serpentinites: Earth and Planetary Science Letters, v. 365, p. 86–96.

Kesler, S.E., Appold, M.S., Martini, A.M., Walter, L.M., Huston, T.T., Kyle, J.R., 1995, Na-Cl-Br systematics of mineralizing brines in Mississippi Valley-type deposits: Geology, v. 23, p. 641–644.

Klemm, L., Pettke, T., Graeser, S., Mullis, J., Kouzmanov, K., 2004, Fluid mixing as the cause of sulphide precipitation at Albrunpass, Binn Valley, Central Alps: Swiss Bulletin of Mineralogy and Petrology, v. 84, p. 189–212.

Klemm, L., Pettke, T., Heinrich, C.A., 2007, Hydrothermal evolution of the El Teniente deposit (Chile): porphyry-Cu-Mo ore deposition from low-salinity magmatic fluids: Economic Geology, v. 102, p. 1021–1045.

Knesel, K.M., and Davidson, J.P., 2002,Insights into collisional magmatism from isotopic fingerprints of melting reactions: Science, v. 296, p. 2206–2208.

Korzhinskii, D.S., 1965, The theory of systems with perfectly mobile components and processes of mineral formation: American Journal of Science, v. 263, p. 193–205.

Kroslakova, I., Günther, D., 2007, Elemental fractionation in laser ablation-inductively coupled plasma-mass spectrometry: evidence for mass load induced matrix effects in the ICP during ablation of a silicate glass: Journal of Analytical Atomic Spectrometry, v. 22, p. 51–62.

Krenn, E., Ustaszewski, K., and Finger, F., 2008, Detrital and newly formed metamorphic monazite in amphibolite-facies metapelites from the Motajica Massif, Bosnia: Chemical Geology, v. 254, p. 164¬–174.

Kwak, T.A.P., 1977, Scapolite compositional change in a metamorphic gradient and ist bearing on the identification of meta-evaporite sequences: Geological Magazine, v. 114, p. 343–354.

Leach, D.L. Sangster, D.F., Kelley, K.D., Large, R.R., Garven, G., Allen, C.R., Gutzmer, J., and Walters, S., 2005, Sediment-hosted lead–zinc deposits: a global perspective: Economic Geology 100th Anniversary Volume p. 561–607.

Leach, D.L., Bradley D.C., Huston, D., Pisarevsky, S.A., Taylor, R.D.,Gardoll, S.J., 2010, Sediment-Hosted Lead-Zinc Deposits in Earth History: Economic Geology, v. 105, p. 593–625.

Lebedev V.,I., Nagaytsev YuV., 1980, Minor elements in metamorphic rocks as an ore-metal source for certain deposits: Geochemistry International, p. 17–31.

Leisen, M., Boiron, M-C., Richard, A., Dubessy, J., 2012, Determination of Cl and Br concentrations in individual fluid inclusions by combining microthermometry and LA-ICP-MS analysis: Implications for the origin of salinity in crustal fluids: Chemical Geology, v. 330–331, p. 197–206.

Lieftink, D.J., Nijland, T.G., Maijer, C., 1993, Cl-rich scapolite from Ødegårdens Verk, Bamble, Norway: Norsk Geologisk Tidsskrift, v. 73, p. 55–57.

Ludwig, K.R., 2003, Isoplot/Ex version 3.0. A geochronological toolkit for Microsoft Excel:

Berkeley Geochronological Centre Special Publication, Berkeley. 70 p.

Macera, P., Di Pisa, A., and Gasperini, D., 2011, Geochemical and Sr-Nd disequilibrium during multi-stage anatexis in a metasedimentary Hercynian crust: European Journal of Mineralogy, v. 23, p. 207–222.

Maas, R., and McCullock, M.T., 1991, The provenance of Archean clastic metasediments in the Narryer Gneiss Complex, Western Australia: Trace element geochemistry, Nd isotopes, and U-Pb ages of detrital zircons: Geochimica et Cosmochimica Acta, v. 55, p. 1915–1932.

Maboko, M.A.H., 2000, Nd and Sr isotopic investigation of the Archean-Proterozoic boundary in north eastern Tanzania: constraints on the nature of Neoproterozoic tectonism in the Mozambique Belt: Precambrian Research, v. 102, p. 87–98.

Master, R.L., and Ague, J.J., 2005, Regional-scale fluid flow and element mobility in Barrow's metamorphic zones, Stonehaven, Scotland: Contribution to Mineralogy and Petrology, v. 150, p. 1–18.

Matheson, R. S. & Searl, R. A., 1956, Mary Kathleen Uranium Deposit, Mont Isa-Cloncurry District, Queensland, Australia: Economic Geology, v. 51, p. 528–540.

McCaffrey, M.A., Lazar, B., Holland, H.D., 1987, The evaporation path of seawater and the coprecipitation of Br- and K+ with halite: Journal of Sedimentary Research, v. 57, p. 928–937.

McCubbin, F.M., Steele, A., Nekvasil, H., Schnieders, A., Rose, T., Fries, M., Carpenter, P.K., and Jolliff, B.L., 2010, Detection of structurally bound hydroxyl in fluorapatite from Apollo Mare basalt 15058,128 using TOF-SIMS: American Mineralogist, v. 95, p. 1141–1150.

McCulloch, M.T., and Bennet, V.C., 1994, Progressive growth of the Earth's continental crust and depleted mantle: Geochemical constraints: Geochimica et Cosmochimica Acta, 58, 4717–4738.

McDonough, W. F. & Sun, S. S., 1995, The composition of the Earth: Chemical Geology, v. 120, p. 223–253.

McFarlane, C.R.M., and McCulloch, M.T., 2007, Coupling of in-situ Sm–Nd systematics and U–Pb dating of monazite and allanite with applications to crustal evolution studies: Chemical Geology, v. 245, p. 45–60.

McLennan, S.M., Taylor, S.R., McCulloch, M.T., and Maynard, J.B., 1990, Geochemical and Nd-Sr isotopic composition of deep-sea turbidites: Crustal evolution and plate tectonic associations: Geochimica et Cosmochimica Acta, v. 54, p. 2015–2050.

Moecher, P. D. & Essene, E. J., 1991, Calculation of CO_2 activities using scapolite equilibria: constraints on the presence and composition of a fluid phase during high grade metamorphism: Contribution to Mineralogy and Petrology, v. 108, p. 219¬–240.

Moecher, P. D., Valley, J.W., Essene, E. J., 1991, Extraction and carbon isotope analysis of CO_2 from scapolite in deep crustal granulites and xenoliths: Geochimica et Cosmochimica Acta, v. 58, p. 959–967.

Moldovanyi, E.P., Walter, L.M., 1992, Regional trends in water chemistry, Smackover Formation, Southwest Arkansas: Geochemical and physical controls: American Association of Petroleum Geologists Bulletin, v. 76, p. 864–894.

Montel, J-M., 1993, A model for monazite/melt equilibrium and application to the generation of granitic magmas: Chemical Geology, v. 110, p. 127–146.

Mora, C. I. & Valley, J. W., 1989, Halogen-rich scapolite and biotite: Implications for metamorphic fluid-rock interaction: American Mineralogist, v. 74, p. 721–737.

Morad, S., 1988, Diagenesis of titaniferous minerals in Jurassic sandstones from the Norwegian Sea: Sedimentary Geology, v. 57, p. 17–40.

Moss, B.E., Haskin, L.A., Dymek, R.F., Shaw, D.M., 1995, Redetermination and reevaluation of compositional variations in metamorphosed sediments of the Littelton Formation, New Hampshire: American Journal of Science, v. 295, p. 988–1019.

Moss, B.E., Haskin, L.A., Dymek, R.F., 1996, Compositional variations in metamorphosed sediments of the Littleton Formation, New Hampshire, and the Carrabassett Formation, Maine, at sub-hand specimen outcrop, and regional scales: American Journal of Science, v. 296, p. 473–505.

Mottl, M.J., Holland, H.D., 1978, Chemical exchange during hydrothemal alteration of basalt by seawater 1. Experimental results for major and minor components of seawater, Geochimica et cosmochimica Acta, v. 42, p. 1103–1115.

Munoz, J. L. & Swenson, A., 1981, Chloride-hydroxyl exchange in biotite and estimation of relative HCl/HF activities in hydrothermal fluids: Economic Geology, v. 76, p. 2212–2221.

Munoz, J.L., 1992, Calculation of HF and HCl fugacities from biotite compositions: revised equations: Geological Society of America, Abstracts with Programs 26, p. 221.

Munoz, J.L., 1984, F–OH and Cl–OH exchange in micas with applications to hydrothermal ore deposits, in Bailey, S.W., ed., Micas. Reviews in Mineralogy, Mineralogical Society of America, v. 13, p. 469–494.

Nagaseki, H., and Hayashi, K., 2008, Experimental study of the behavior of copper and zinc in a boiling hydrothermal system: Geology, v. 36, p. 27–30

Nahnybida, T., Gleeson, S. A., Rusk, B. G. & Wassenaar, L. I., 2009, Cl/Br ratios and stable chlorine isotope analysis of magmatic–hydrothermal fluid inclusions from Butte, Montana and Bingham Canyon, Utah: Mineralium Deposita, v. 44, p. 837–848.

Neumann, N.L., Gibson, GM. & Southgate, P.N., 2009, New SHRIMP age constraints on the timing and duration of magmatism and sedimentation in the Mary Kathleen Fold Belt, Mt Isa Inlier, Australia: Australian Journal of Earth Sciences, v. 56, p. 965–983.

Nutman, A.P., 2007, Apatite recrystallisation during prograde metamorphism, Cooma, southeast Australia: implications for using apatite-graphite association as a biotracer in ancient metasedimentary rocks: Australian Journal of Earth Sciences, v. 54, p. 1023–1032.

Offler, R. and Fleming, P. D., 1968, A synthesis of folding and metamorphism in the Mt Lofty

Ranges, South Australia: Journal of the Geology Society of Australia, v. 15, p. 245-266.

Oliver, N.H.S., Dipple, G.M., Cartwright, I., and Schiller, J., 1998, Fluid flow and metasomatism in the genesis of the amphibolite-facies, pelite-hosted Kanmantoo copper deposit, South Australia: American Journal of Science, v. 298, p.181–218.

Oliver, N. H. S., Cartwright, I., Wall, V. J. & Golding, S. D.,1993, The stable isotope signature of kilometer-scale fracture-dominated metamorphic fluid pathways, Mary Kathleen, Australia: Journal of Metamorphic Geology, v. 11, p. 705–720.

Oliver, N.H.S., Pearson, P. J., Holcombe, R. J. & Ord, A.,1999, Mary Kathleen metamorphic-hydrothermal uranium - rare-earth element deposit: ore genesis and numerical model of coupled deformation and fluid flow: Australian Journal of Earth Sciences, v. 46, p. 467–483.

Oliver, N.H.S., Valenta, R. K. & Wall, V. L., 1990, The effect of heterogeneous stress and strain on metamorphic fluid flow, Mary Kathleen, Australia, and model for large-scale fluid circulation: Journal of Metamorphic Geology, v. 8, p. 311–331.

Oliver, N.H.S., Rawling, T. J., Cartwright, I. and Pearson, P., 1994, High-temperature fluid-rock interaction and scapolitization in an extension-related hydrothermal system, Mary Kathleen, Australi: Journal of Petrology, p. 1455–1491.

Oliver, N.H.S. & Wall, V. J., 1987, Metamorphic plumping system in Proterozoic calc-silicates, Queensland, Australia: Geology, v. 15, p. 793–796.

Oliver, N.H.S., Wall, V. J. & Cartwright, I., 1992, Internal control of fluid compositions in amphibolite-facies scapolitic calc-silicates, Mary Kathleen, Australia: Contributions to Mineralogy and Petrology, v. 111, p. 94–112.

Oliver, N.H.S., Cleverley, Geordie, M., Pollard, P.J., Fu, B., Marshall, L.J., Rubenach, M.J., Williams, P.J. and Baker, T., 2004, Modeling the Role of Sodic Alteration in the Genesis of Iron Oxide-Copper-Gold Deposits, Eastern Mount Isa Block, Australia: Economic Geology, v. 99, p. 1145–1176.

Oliver, N.H.S., 1995, Hydrothermal history of the Mary Kathleen Fold Belt, Mt Isa Block, Queensland: Australian Journal of Earth Sciences, v. 42, p. 267–279.

Oliver, N.H.S., McLellan, J.G., Hobbs, B.E., Cleverley, J.S., Ord, A., and Feltrin, L., 2006, Numerical models of extensional deformation, heat transfer, and fluid flow across basement-cover interfaces during basin-related mineralization: Economic Geology, v. 101, p. 1–31.

Oliver, N.H.S., McLellan, J.G., Hobbs, B.E., Cleverley, J.S., Ord, A., and Feltrin, L., 2006, Numerical models of extensional deformation, heat transfer, and fluid flow across basement-cover interfaces during basin-related mineralization: Economic Geology, v. 101, p. 1–31.

Oliver, N.H.S., 1996, Review and classification of structural controls on fluid flow during regional metamorphism: Journal of metamorphic Geology, v. 14, p. 477–492.

Oliver N. H. S., Butera K. M., Rubenach M. J., Marshall L. J., Cleverley J. S., Mark G., Tullemans F. and Esser D., 2008, The protracted hydrothermal evolution of the Mount Isa Eastern Succession: a review and tectonic implications: Precambrian Research, v. 163, p. 108–130.

Orville, P. M., 1995, Stability of scapolite in the system Ab-An-NaCl-$CaCO_3$ at 4 kb and 750 °C: Geochimica et Cosmochimica Acta, v. 39, p.1091–1105.

Page, R. W, 1983, Chronology of magmatism, skarn formation, and uranium mineralization, Mary Kathleen, Queensland, Australia: Economic Geology, v. 78, p. 838–853.

Pan, Y., Fleet, M.E. & Ray, G. E., 1994, Scapolite in two Canadian gold deposits: Nickel Plate, British Columbia and Helmo, Ontario: The Canadian Mineralogist, v. 32, p. 825–837.

Pan, Y. & Fleet, M.E., 2002, Compositions of the Apatite-Group Minerals: Substitution Mechanisms and Controlling Factors: Reviews in Mineralogy and Geochemistry, v. 48, p. 13–49.

Pan, Y., Dong, P., 2003, Bromine in scapolite-group minerals and sodalite: XRF microprobe analysis, exchange experiments, and application to skarn deposits: Canadian Mineralogist, v. 41, p. 529–540.

Papike, J. J. & Zoltai, T., 1965, The crystal structure of a marialite scapolite: The American Mineralogist, v. 50, p. 641–655.

Patchett, P.J., and Ruiz, J., 1989, Nd isotopes and the origin of Grenville-aged rocks in Texas: implications for Proterozoic evolution of the United States mid-continent region: Journal of Geology, v. 97, 685–695.

Paterson, B.A., Rogers, G., Stephens, W.E., 1992, Evidence for inherited Sm–Nd isotopes in granitoid zircons: Contribution to Mineralogy and Petrology, v. 111, p. 378–390.

Patino Douce, A.E., and Harris, N., 1998, Experimental constraints on Hymalayan anatexis: Journal of Petrology, v. 39, p. 689–710.

Pearce, N. J. G., Perkins, W. T., Abell I., Duller, G. A. T., and Fuge, R., 1992, Mineral microanalysis by laser ablation inductively coupled plasma mass-spectrometry. Journal of Analytical Atomic Spectrometry, v. 7, p. 53–57.

Perini, G., Cesare, B., Gómez-Pugnaire, M.T., Ghezzi, L., and Tommasini, S., 2009, Armouring effects on Sr-Nd isotopes during disequilibrium crustal melting: the case study of frozen migmatites from El Hoyazo and Mazarrón, SE Spain: European Journal of Mineralogy, v. 21, p.117¬–131.

Pettke, T., Oberli, F., Audétat, A., Guillong, M., Simon, A.C. Hanley, J.J., Klemm, L.M., 2012, Recent developments in element concentration and isotope ratio analysis of individual fluid inclusions by laser ablation single and multiple collector ICP-MS: Ore Geology Reviews, v. 44, p. 10–38.

Pettke, 2008, Analytical protocols for element concentration and isotope ratio measurements in fluid inclusions by LA-(MC)-ICP-MS. in: Sylvester, P. (Ed.), Laser Ablation ICP-MS in the Earth Sciences: Current Practices and Outstanding Issues. Mineralogical Association of Canada, Short Course Series 40, Vancouver, pp. 189–212.

Pichavant, M., Montel, JM., and Richard, L.R., 1992, Apatite solubility in peraluminous liquids: Experimental data and an extension of the Harrison-Watson model: Geochimica et

Cosmochimica Acta, v. 56, p. 3855–3861.

Pietranik, A., Slodczyk, E., Hawkesworth, C.J., Breitkreuz, C., Storey, C.D., Whitehouse, M., and Milke, R., 2013, Heterogeneous zircon cargo in voluminous late Paleozoic rhyolites: Hf, O isotope and Zr/Hf records of plutonic to volcanic magma evolution: Journal of Petrology, v. 10, p. 1–19.

Pitcairn, I.K., Teagle, D.A.H., Craw, D., Olivo, G.R., Kerrich, R., and Brewer, T.S., 2006, Sources of metals and fluids in orogenic gold deposits: Insights from the Otago and Alpine Schists, New Zealand: Economic Geology, v. 101, p. 1525–1546.

Pitcairn, I.K., Olivio, G.R., Teagle, D.A.H., Craw, D., 2010, Sulfide evolution during prograde metamorphism of the Otago and Alpine Schists, New Zealand: The Canadian Mineralogist, v. 48, p. 1267–1295.

Plank, T., Langmuir, C.H., 1998, The geochemical composition of subducting sediment and its consequences for the crust and mantle: Chemical Geology, v. 145, p. 325–394.

Pollard, P.J., 1997, Cloncurry Base Metals and Gold, Final Report, Volume 1 , AMIRA P438.

Pollard P.J., Geordie, M. & Mitchell L.C., 1998, Geochemistry of Post-1540 Ma Granites in the Cloncurry District, Northwest Queensland: Economic Geology, v. 93, p. 1330–1344.

Pyle, J.M., Spear, F.S., Rudnick, R.L,, McDonough, W.F., 2001, Monazite–xenotime–garnet equilibrium in metapelites and a new monazite–garnet thermometer: Journal of Petrology, v. 42, p. 2083-2107.

Ramsay, C.R. & Davidson, L.R., 1970, The origin of scapolite in the regionally metamorphosed rocks of Mary Kathleen, Queensland, Australia: Contribution to Mineralogy and Petrology, v. 25, p. 41–51.

Preiss, W.V., 2000, The Adelaide Geosyncline of South Australia and ist significance in Neoproterozoic continental reconstruction: Precambrian Resreach, v. 100, p. 21–63.

Price, J.R., Velbel., M.A., and Patino, L.C., 2005, Allanite and epidote weathering at the Coweeta Hydrologic Laboratory, western North Carolina, U.S.A.: American Mineralogist, v. 90, p. 101–114.

Rapp, R.P., and Watson, E.B., 1986, Monazite solubility and dissolution kinetics: implications for the thorium and light rare earth chemistry of felsic magmas: Contributions to Mineralogy and Petrology, v.94, 304–316.

Rapp, J.F., Klemme, S., Butler, I.B., Harley, S.L., 2010: Extremely high solubility of rutile in chloride and fluoride-bearing metamorphic fluids: An experimental investigation: Geology, v.38, p. 323–326.

Rittenhouse, G., 1967, Bromide in oilfield waters and its use in determining possibilities of origins its waters: American Association of Petroleum Geologists Bulletin, v. 51, p. 2430–2440.

Roedder, E., 1971, Fluid-inclusion evidence on the environment of formation of mineral deposits of the southern Appalachian valley: Economic Geology, v. 66, p. 777–791.

Ronov A., B., Migdisov A., A., Lobach-Zhuchenko, S., B., 1977, Regional metamorphism and sediment composition evolution: Geochemistry International, v. 14, p. 90–110.

Roser, B.P., Nathan, S., 1997, An evaluation of elemental mobility during metamorphism of a turbidite sequence (Greenland Group, New Zealand): Geological Magazine, v. 134, p. 219–234.

Rubatto, D., Williams, I.S., and Buick, I.S., 2001, Zircon and monazite response to prograde metamorphism in the Reynold Ranges, central Australia: Contribution to Mineralogy and Petrology, v. 140, p. 458–468.

Rubatto, D., 2002, Zircon trace element geochemistry: partitioning with garnet and the link between U–Pb ages and metamorphism: Chemical Geology, v. 184, p. 124–138.

Rubatto, D. & Hermann, J., 2007, Experimental zircon/melt and zircon/garnet trace element partioning and implications fort he geochronology of crustal rocks: Chemical Geology, v. 241, p. 38–61.

Rubenach, M. J., Foster, D. R., Evins, P. M., Blake, K. L. & Fanning, C. M., 2008, Age constraints on the tectonothermal evolution of the Selwyn Zone, Eastern Fold Belt, Mount Isa Inlier. Precambrian Research, v. 163, p. 81–107.

Rusk, B., Koenig, A., Lowers, H., 2011, Visualizing trace element distribution in quartz using cathodoluminescence, electron microprobe, and laser ablation-inductively coupled plasma-mass spectrometry: American Mineralogist, v. 96, p. 703–708.

Rusk, B., Reed, M., 2002, Scanning electron microscope-cathodoluminescence analysis of quartz reveals complex growth histories in veins from the Butte porphyry copper deposit, Montana: Geology, v. 30, p. 727–730.

Rusk, B.G., Reed, M.H., Dilles, J.H., Klemm, L.M., Heinrich, C.A., 2004, Compositions of magmatic hydrothermal fluids determined by LA-ICP-MS of fluid inclusions from the porphyry copper–molybdenum deposit at Butte, MT: Chemical Geology, v. 210, p. 173–199.

Ryan, C.G., Heinrich, C.A., Mernagh, T.P., 1993, PIXE microanalysis of fluid inclusions and ist application to study ore metal segregation between magmatic brine and vapor. Nuclear Instruments and Methods in Physics Research. Section B: beam interactions with Materials and Atoms 77 (1–4), 463–471.

Sandiford, M., Fraser, G., Arnold, J., Foden, J., and Farrow, T., 1995, Some causes and consequences of high-temperature, low-pressure metamorphism in the eastern Mt Lofty Ranges, South Australia: Australian Journal of Earth Sciences, v. 42, p. 233–240.

Satish-Kumar, M., Hermann, J., Tsunogae, T. & Osanai, Y., 2006, Carbonation of Cl□rich scapolite boudins in Skallen, East Antarctica: evidence for changing fluid condition in the continental crust: Journal of metamorphic Geology, v. 24, p. 241–261.

Sawyer, E.W., 1991, Disequilibrium melting and the rate of melt-residuum separation during migmatization of mafic rocks from the Grenville Fron, Quebec: Journal of Petrology, v. 32, p 701–738.

Sawyer, E.W., Cesare, B., and Brown, M., 2011, When the continental crust melts: Elements, v. 7, p. 229-234.

Schwarcz, H.P., 1966, Chemical and mineralogic variations in an arkostic quartzite during progressive burial regional metamorphism: Geological Society of America Bulletin, v. 77, p. 509–532.

Seo, J.H, Guillong, M., Aerts, M., Zajacz, Z., Heinrich, C.A., 2011, Microanalysis of S, Cl, and Br in fluid inclusions by LA-ICP-MS: Chemical Geology, v. 284, p. 35–44.

Sha, P. 2013, Genesis of the Elaine Cu-Au-REE-U deposit., Mary Kathleen Fold Belt, North Queensland. Honors Thesis, James Cook University (Unpublished).

Shaw, D. M., 1960a, The geochemistry of scapolite Part 1. Previous Work and General Mineralogy: Journal of Petrology, v. 1, p. 218–260.

Shaw, D. M., 1960b, The geochemistry of scapolite Part 2. Trace elements, petrology, and general geochemistry: Journal of Petrology, v. 1, p. 261–285.

Shaw, D.M., 1954, Trace elements in pelitic rocks I, II. Geological Society of America Bulletin, v. 65, p. 1151–1167.

Siahcheshm, K., Calagari, A.A., Abedini, A., Lentz, D.R., 2012, Halogen signatures of biotites from the Maher-Abad porphyry copper deposit, Iran: Characterization of volatiles in syn- to post-magmatic hydrothermal fluids: International Geology Review, v. 54, p. 1353–1368.

Siemann, M. G. & Schramm, M., 2002, Henry's and non-Henry's law behaviour of Br in simple marine systems: Geochimica et Cosmochimica Acta, v, 66, p. 1387–1399.

Smith, M.P., Yardley, B.W.D., 1999, Fluid evolution during metamorphism of the Otago Schist, New Zealand: (II) Influence of detrital apatite on fluid salinity: Journal of Metamorphic Geology, v. 17, p. 187–193.

Sokolova, E. & Hawthorne, F. C., 2008, The crystal chemistry of the scapolite-group minerals. 1. Crystal structure and long-range order: The Canadian Mineralogist, v. 46, p. 1527–1554.

Sossi, P.A., Halverson, G.P., Nebel, O., and Eggins, S.M., 2014, Combined separation of Cu, Fe and Zn from rock matrices and improved analytical protocols for stable isotope analysis: Geostand. Geoanal. Res. Accepted

Spandler, C., O'Neill, H.St.C., 2010, Diffusion and partition coefficients of minor and trace elements in San Carlos olivine at 1,300°C with some geochemical implications: Contributions to Mineralogy and Petrology, v. 159, p. 791–818.

Spandler, C., Hermann, J., Arculus, R., and Mavrogenes, J., 2003, Redistribution of trace elements during prograde metamorphism from lawsonite blueschist to eclogite facies; implications for deep subsduction-zone processes: Contribution to Mineralogy and Petrology, v. 146, p. 205–222.

Spandler, C., Pettke, T., Rubatto, D., 2011, Internal and external fluid sources for eclogite-facies veins in the Monviso meta-ophiolite, Western Alps: Implications for fluid flow in subduction zones: Journal of Petrology, v. 52, p.1207–1236.

Spear, F.S., and Pyle, J.M., 2002, Apatite, monazite, and xenotime in metamorphic rocks. In: Kohn, M.J., Rakovan, J., Hughes, J.M. (Eds.), Phosphates: Geochemical, Geobiologi- cal, and Materials Importance. Reviews in Mineralogy and Geochemistry. Mineralogical Society of America, Washington, D. C., pp. 293–335.

Spear, F.S., 2010, Monazite-allanite phase relations in metapelites: Chemical Geology, v. 279, p. 55–62.

Stevens, G., Clemens, J.D., and Droop, G.T.R., 1997, Melt production during granulite-facies anatexis: experimental data "primitive" metasedimentary protoiths: Contribution to Mineralogy and Petrology, v. 128, p. 352–370.

Stoffell, B., Appold, M.S., Wilkinson, J.J., McClean, N.A., 2008, Geochemistry and evolution of Mississippi Valley-Type mineralizing brines from the Tri-State and northern Arkansas districts determined by LA-ICP-MS microanalysis of fluid inclusions: Economic Geology v. 103, p. 1411–1435.

Svensen, H., Jamtveit, B., Yardley, B., Engvik, A.K., Austrheim, H., Broman, C., 1999, Lead and bromine enrichment in eclogite-facies fluids: Extreme fractionation during lower-crustal hydration: Geology, v. 27, p. 467–470.

Taylor, S.R. and McLennan, S.M., 1985, The continental crust: its composition and evolution. Blackwell, Oxford, 312 pp.

Teertstra, T. K. & Sherriff, B. L., 1997, Substitutional mechanisms, compositional trends and the end-member formulae of scapolite: Chemical Geology, v. 136, p. 223¬¬–260.

Tischendorf, G., Förster, H.-J., Gottesmann, B., 2001, Minor- and trace-element composition of trioctahedral micas: a review: Mineralogical Magazine, v. 65, p. 249–276.

Tuisku, P., Ruostesuo,P., and Häkkinen, A-M., 1987, The metamorphic behaviour and petrogenetic significance of zinc in amphibolite facies, staurolite-bearing schists, Puolankajärvi Formation, Central Finland: Geochimica et Cosmochimica Acta, v., 51, p. 1639–1650.

Turner, S., Haines, P., Foster, D., Powell, R., Sandiford, M., and Offler R., 2009, Did the Delamarian Orogeny start in the Neoproterozoic?: The Journal of Geology, v. 117, p. 575¬–583.

van Achterbergh E., Ryan C.G., Jackson S.E., and Griffin, W.L., 2001, Data reduction software for LA-ICP-MS. In: Sylvester P (ed) Laser-ablation-ICPMS in the earth sciences: principles and applications. Mineralogical Association of Canada, Short Course 29, pp 239–243.

Vanko, D.A., Bonnin-Mosbah, M., Philippot, P., Roedder, E., Sutton, S.R., 2001, Fluid inclusions in quartz from oceanic hydrothermal specimens and the Bingham, Utah porphyry-Cu deposit: a study with PIXE and SXRF: Chemical Geology, v. 173, p. 227–238.

Viets, J.G., Hofstra, A.H., Emsbo, P., 1996, Solute compositions of fluid inclusions in sphalerite from North American and European Mississippi Valley-Type ore deposits: Ore fluids derived from evaporated seawater, Society of Economic Geologists Special Publication, v. 4, p. 465–482.

Wade, B.P., Barovich, K.M., Hand, M., Scrimgeour, I.R., and Close, D.F., 2006, Evidence for early

Mesoproterozoic arc magmatism in the Musgrave Block, central Australia: Implications for Proterozoic crustal growth and tectonic reconstructions of Australia: Journal of Geology, v. 114, p. 43-63.

Walter, L.M., Stuebler, A.M., Huston, T.J., 1990, Br-Cl-Na systematics in Illinois basin fluids: Constraints on fluid origin and evolution: Geology, v. 18, p. 315–318.

Warren, J.K, 1997, Evaporites, brines and base metals: Fluids and 'the evaporite that was': Australian Journal of Earth Sciences, v. 44, p. 149–183.

Weinberg, R., 1999, Mesoscale pervasive felsic magma migration: alternatives to dyking: Lithos, v. 46, p. 393–410.

Wendlandt, E., DePaolo, D.J., and Baldridge, W.S., 1993, Nd and Sr isotope chronostratigraphy of Colorado Plateau lithosphere: implications for magmatic and tectonic underplating of the continental crust: Earth and Planetary Science Letter, v. 116, 23–43.

Whalen. J. B., Currie, K. L. & Chappell, B. W., 1987, A-type granites: geochemical characteristics, discrimination and petrogenesis: Contribution to Mineralogy and Petrology, v. 95, p. 407–419.

White, A., 1959, Scapolite-bearing marbles and calc-silicate rocks from Tungkillo and Milendella, South Australia: Geological Magazine, v. XCVI, p. 285–307.

Wilkinson, J.J., Stoffell, B., Wilkinson, C.C., Jeffries, T.E., Appold, M.S., 2009, Anomalously metal-rich fluids form hydrothermal ore deposits: Science, v. 323, p. 764–767.

Wing, B.A., Ferry, J.M., and Harrison, T.M., 2003, Prograde destruction and formation of monazite and allanite during contact and regional metamorphism of pelites: petrology and geochronology: Contribution to Mineralogy and Petrology, v. 145, p. 228–250.

Wodzicki, A., 1971, Migration of trace elements during contact metamorphism in the Santa Rosa Range, Nevada, and ist Bearing on the origin of ore deposits associated with granitic intrusion,: Mineralium Deposita, v. 6, p. 49–64.

Wolf, M.B., and London, D., 1995, Incongruent dissolution of REE- and Sr-rich apatite in peraluminous granitic liquids: Differential apatite, monazite, and xenotime solubilities during anatexis: American Mineralogist, v. 80, p. 765–775.

Xiao, Y., Hoefs. J. & Kronz, A., 2005, Compositionally zoned Cl-rich amphiboles from North Dabie Shan, China: Monitor of high-pressure metamorphic fluid/rock interaction processes: Lithos, v. 81, p. 279–295.

Yang, Y.H., Sun, J.F., Xie, L.W., Fan, H.R., and Wu, F.Y., 2008. In situ Nd isotopic measurement of natural geologic materials by LA-MC-ICPMS: Chinese Science Bulletin, v. 53, p. 1062–1070.

Yang, P., and Rivers, T., 2000, Trace element partitioning between coexisting biotite and muscovite from metamorphic rocks, Western Labrador: Structural, compositional and thermal controls: Geochimica et Cosmochimica Acta, v. 64, p. 1451–1472.

Yardley, B.W.D., 2005, Metal concentrations in crustal fluids and their relatioships to ore formation: Economic Geology, v. 100, 613–632.

Yardley, B.W.D., and Cleverley, J.S., 2013, The role of metamorphic fluids in the formation of ore deposits. In: Jenkin, G. R. T., Lusty, P. A. J., Mcdonald, I., Smith, M. P., Boyce, A. J. & Wilkinson, J. J. (Eds.), Ore Deposits in an Evolving Earth, Geological Society, London, Special Publications, 393.

Yardley, B.W.D., Banks, D.A., Bottrell, S.H., Diamond, L.W., 1993, Post-metamorphic gold-quartz veins from N.W. Italy: the composition and origin of the ore fluid: Mineralogical Magazine, v. 57, p. 407–422.

Yardley, B. W. D., 1997, The evolution of fluids through the metamorphic cycle. In: Fluid flow and transport in rocks, mechanisms and effect, ed. Jamtveit, B and Yardley, B. W. D. Chaoman & Hall, 99–121.

Yardley, B.W.D., 1989, An Introduction to Metamorphic Petrology, Longman Scientific & Technical, New York.

Zeng, L., Saleeby, J.B., and Asimow, P., 2005, Nd isotope disequilibrium during crustal anatexis: A ercord from the Goat Ranch migmatite complex, southern Sierra Nevada batholith, California: Geology, v. 33, p. 53–56.

Zhang, Y., 2010, Diffusion in Minerals and Melts: Theoretical Background: Reviews in Mineralogy & Geochemistry, v. 72, p. 5–59.

Zhang, K-J., Zhang, Y-X., Li, B., and Zhong, L-F., 2007, Nd isotopes of siliciclastic rocks from Tibet, western China: Constraints on provenance and pre-Cenozoic tectonic evolution: Earth and Planetary Science Letters, v. 257, p. 604–616.

Zheng, J., Griffin, W.L., O'Reilly, S.Y., Lu, F., Yu, C., Zhang, M., and Li, H., 2004, U-Pb and Hf-isotope analysis of zircons in mafic xenoliths from Fuxian kimberlites: evolution of the lower crust beneath the North China craton: Contribution to Mineralogy and Petrology, v. 148, p. 79–103.

Zhu, C., and Sverjensky, D.A., 1991, Partitioning of F-Cl-OH between minerals in hydrothermal fluids: Geochimica et Cosmochimica Acta, v. 55, p. 1837–1858.

Appendix

Chemical Geology 337-338 (2013) 75–87

Contents lists available at SciVerse ScienceDirect

Chemical Geology

journal homepage: www.elsevier.com/locate/chemgeo

In situ quantification of Br and Cl in minerals and fluid inclusions by LA-ICP-MS: A powerful tool to identify fluid sources

Johannes Hammerli [a,*], Brian Rusk [a,1], Carl Spandler [a], Poul Emsbo [b], Nicholas H.S. Oliver [a]

[a] School of Earth and Environmental Sciences, James Cook University, Townsville, 4811, Australia
[b] US Geological Survey, Mail Stop 973, Denver Federal Center, Denver, CO, 80225 USA

ARTICLE INFO

Article history:
Received 1 September 2012
Received in revised form 3 December 2012
Accepted 4 December 2012
Available online 13 December 2012

Editor: J. Fein

Keywords:
LA-ICP-MS
Bromine
Chlorine
Fluid inclusions
Scapolite
MVT

ABSTRACT

Bromine and chlorine are important halogens for fluid source identification in the Earth's crust, but until recently we lacked routine analytical techniques to determine the concentration of these elements in situ on a micrometer scale in minerals and fluid inclusions. In this study, we evaluate the potential of in situ Cl and Br measurements by LA-ICP-MS through analysis of a range of scapolite grains with known Cl and Br concentrations. We assess the effects of varying spot sizes, variable plasma energy and resolve the contribution of polyatomic interferences on Br measurements. Using well-characterised natural scapolite standards, we show that LA-ICP-MS analysis allows measurement of Br and Cl concentrations in scapolite, and fluid inclusions as small as 16 μm in diameter and potentially in sodalite and a variety of other minerals, such as apatite, biotite, and amphibole. As a demonstration of the accuracy and potential of Cl and Br analyses by LA-ICP-MS, we analysed natural fluid inclusions hosted in sphalerite and compared them to crush and leach ion chromatography Cl/Br analyses. Limit of detection for Br is ~8 μg g^{-1}, whereas relatively high Cl concentrations (>500 μg g^{-1}) are required for quantification by LA-ICP-MS. In general, our LA-ICP-MS fluid inclusion results agree well with ion chromatography (IC) data. Additionally, combined cathodoluminescence and LA-ICP-MS analyses on natural scapolites within a well-studied regional metamorphic suite in South Australia demonstrate that Cl and Br can be quantified with a ~25 μm resolution in natural minerals. This technique can be applied to resolve a range of hydrothermal geology problems, including determining the origins of ore forming brines and ore deposition processes, mapping metamorphic and hydrothermal fluid provinces and pathways, and constraining the effects of fluid–rock reactions and fluid mixing.

Journal of
METAMORPHIC GEOLOGY

J. metamorphic Geol., 2014, **32,** 93–112 doi:10.1111/jmg.12060

Cl/Br of scapolite as a fluid tracer in the earth's crust: insights into fluid sources in the Mary Kathleen Fold Belt, Mt. Isa Inlier, Australia

J. HAMMERLI,[1] C. SPANDLER,[1] N. H. S. OLIVER[1] AND B. RUSK[2]
[1]*School of Earth and Environmental Sciences, James Cook University, Townsville, 4811, Australia (johannses.hammerli@my.jcu.edu.au)*
[2]*Department of Geology, Western Washington University, Washington, DC, 98225, USA*

ABSTRACT A combination of analytical methods, including trace element analysis of Br in scapolite by LA-ICP-MS, was employed to unravel the fluid–rock interaction history of the Mary Kathleen Fold Belt of northern Australia. Halogen ratios in the metamorphic and hydrothermally derived scapolite from a range of rock-types record interaction between the host rocks and magmatic-hydrothermal fluids derived from granite plutons and regional metamorphism. The results show that halite-dissolution supplied at best only minor chlorine to fluids in the Fold Belt. Chlorine/bromine ratios in metamorphic scapolite indicate that fluids were dominantly derived from basinal brines formed from sub-aerial evaporation of seawater beyond the point of halite saturation. This bittern fluid infiltrated the underlying sedimentary sequences prior to regional metamorphism. Zoned scapolite in a major late metamorphic mineralized shear-zone records three discrete pulses of magmatic and metamorphic fluid, and it is suggested that fluid mixing may have assisted mineralization along and around this shear-zone. As a crucial prerequisite for halogen fluid tracer studies using scapolite, we find in our samples that Cl and Br do not fractionate when incorporated in scapolite. Furthermore, unaltered rims of heavily retrogressed scapolite show indistinguishable Cl/Br signatures compared with fresh grains from the same sample indicating retrograde metamorphism did not significantly affect Cl and Br signatures in scapolite group minerals.

Key words: bromine and chlorine; fluid sources; halogens; hydrothermal fluids; Mary Kathleen; scapolite.

Earth and Planetary Science Letters 392 (2014) 133–142

Contents lists available at ScienceDirect

Earth and Planetary Science Letters

www.elsevier.com/locate/epsl

Neodymium isotope equilibration during crustal metamorphism revealed by in situ microanalysis of REE-rich accessory minerals

J. Hammerli[a,*], A.I.S. Kemp[a,b], C. Spandler[a]

[a] *School of Earth and Environmental Sciences, James Cook University, Townsville, Australia*
[b] *Centre for Exploration Targeting, University of Western Australia, Perth, Australia*

ARTICLE INFO

Article history:
Received 7 November 2013
Received in revised form 3 February 2014
Accepted 5 February 2014
Available online 4 March 2014
Editor: T.M. Harrison

Keywords:
Nd isotope equilibration
laser ablation MC-ICP-MS
accessory minerals
anatexis

ABSTRACT

Radiogenic isotopes are widely used to investigate crustal evolutionary processes, however recent claims of Nd and Sr isotope disequilibrium during anatexis question the reliability of such information. We have conducted an in situ Sm–Nd isotope study of apatite, allanite, titanite, xenotime and monazite in metasedimentary rocks of different metamorphic grade to test Nd isotope equilibrium during metamorphism. Our results show that apatite retains an original, probably detrital, highly variable Nd isotopic signature until at least 500 °C before being isotopically homogenised, irrespective of textural context within the rock. Once equilibrated, apatite retains its Nd isotope signature throughout anatexis. In contrast, allanite and titanite are equilibrated at temperatures as low as 350–400 °C. REE-rich accessory minerals in high-grade rocks (∼600 °C) show very similar initial εNd values at the time of metamorphism. We conclude that under these metamorphic conditions Nd isotope disequilibrium between crustal melts and metasedimentary sources is unlikely. Intra-grain Nd isotope zoning of monazite indicates that partial melting was open system, involving the injection of externally-derived melt into migmatites. This process, likely to be common in anatectic terranes but not always obvious at hand-specimen scale or from bulk rock geochemical data, can produce isotope variation that could potentially be misinterpreted as disequilibrium between the melt and its protolith.

This publication has been removed due to copyright restrictions